JPL NO. 9950-324

DOE/JPL 954786-79/[illegible]7
DISTRIBUTION CATEGORY UC-63
FR-79-10052

DEVELOPMENT OF PULSED PROCESSES FOR THE MANUFACTURE OF SOLAR CELLS

FINAL REPORT
APRIL 1979

THE JPL LOW-COST SILICON SOLAR ARRAY PROJECT IS SPONSORED BY THE U.S. DEPARTMENT OF ENERGY AND FORMS PART OF THE SOLAR PHOTOVOLTAIC CONVERSION PROGRAM TO INITIATE A MAJOR EFFORT TOWARD THE DEVELOPMENT OF LOW-COST SOLAR ARRAYS. THIS WORK WAS PERFORMED FOR THE JET PROPULSION LABORATORY, CALIFORNIA INSTITUTE OF TECHNOLOGY, BY AGREEMENT BETWEEN NASA AND DOE.

(NASA-CR-153188) DEVELOPMENT OF PULSED PROCESSES FOR THE MANUFACTURE OF SOLAR CELLS Final Report, Apr. 1979 (Spire Corp., Bedford, Mass.) 238 p HC A11/MF A01
N80-23771
Unclas
CSCL 10A G3/44 19282

Prepared Under Contract No. 954786 for:

JET PROPULSION LABORATORY
CALIFORNIA INSTITUTE OF TECHNOLOGY
PASADENA, CA 91103

spire

DOE/JPL 954786-79/02
Distribution Category UC-63
FR-79-10052

DEVELOPMENT OF PULSED PROCESSES FOR THE MANUFACTURE OF SOLAR CELLS

Final Report
April 1979

Contract 954786

Submitted to:
JET PROPULSION LABORATORY
California Institute of Technology
Pasadena, CA 91103

Prepared by: John
Principal Investigator

Approved by: Allen R. Kirkpatrick
Program Manager

SPIRE CORPORATION
Patriots Park
Bedford, MA 01730

ACKNOWLEDGMENT

Contributions to this program have been made by many individuals at Spire Corporation. The program manager was A. R. Kirkpatrick, and the principal investigator was J. A. Minnucci. The project team was staffed as follows:

P.H. Rose, Ion Implanter Design
A.C. Greenwald, Electron Beam Processing
R.C. Thomas, Solar Cell Processing
G.A. Landis, SAMIS Analysis

The considerable contributions by other technical staff and support personnel at Spire and at Jet Propulsion Laboratory, particularly R. H. Josephs and D. Fitzgerald, Technical Managers, are gratefully acknowledged.

ABSTRACT

This report describes the results of a one and half year program to develop the processes required for low-energy ion implantation for the automated production of silicon solar cells.

The program included (1) demonstrating state-of-the-art ion implantation equipment and designing an automated ion implanter, (2) making efforts to improve the performance of ion-implanted solar cells to 16.5 percent AM1, (3) developing a model of the pulse annealing process used in solar cell production, and (4) preparing an economic analysis of the process costs of ion implantation and furnace annealing.

During the program, phosphorus ions at an energy of 10 keV and dose of 2×10^{15} cm^{-2} were implanted in silicon solar cells to produce junctions, while boron ions at 25 keV and 5×10^{15} cm^{-2} were implanted in the cells to produce effective back surface fields. An ion implantation facility with a beam current up to 4 mA and a production throughput of 300 wafers per hour was designed and installed. A design was prepared for a 100-mA, automated implanter with a production capacity of 100 MW_e per year.

Two process sequences were developed which employ ion implantation and furnace or pulse annealing. The JPL-Solar Array Manufacturing Industry Simulation (SAMIS) computer program was used to determine costs for junction formation by ion implantation and various furnace annealing cycles to demonstrate cost effectiveness of these methods.

TABLE OF CONTENTS

TABLE OF CONTENTS (Concluded)

LIST OF FIGURES

LIST OF FIGURES (Continued)

LIST OF FIGURES (Continued)

LIST OF FIGURES (Concluded)

LIST OF TABLES

LIST OF TABLES (Concluded)

SECTION 1
INTRODUCTION

This is the final report after phase II of an 18-month contract which was performed for the JPL-LSA project to develop ion implantation, pulse processes, and process equipment. Development was directed towards an extremely abbreviated process sequence for the manufacture of solar cells. This process sequence does not include any thermal heat treatments or wet chemistry. The emphasis of the second phase of the contract is upon pulse process development and demonstration of the technology.

Under a previous contract(1), it was demonstrated that silicon solar cells can be fabricated very rapidly without furnace treatments, wet chemistry, or gas atmosphere operations if ion implantation is employed in conjunction with pulse annealing. The deliverable solar cells were 2 x 2 cm demonstration devices with efficiencies up to 12.3 percent AM1. Under phase I of this contract(2), ion-implanted, pulse annealed cells were delivered with efficiencies up to 15 percent AM1. Implanted, furnace annealed cells were delivered with an average efficiency of 15 percent AM1 and peak efficiencies greater than 16.5 percent AM1 for 7.6-cm (3-inch) diameter solar cells.

Efforts in pulse process development were concentrated on establishing the pulsed electron beam parameters necessary to anneal 7.6-cm (3-inch) diameter solar cells with a single pulse. Demonstration of this technology was accomplished by delivery of five hundred 7.6-cm diameter solar cells with ion-implanted, pulsed electron beam annealed junctions and back surface fields. The average efficiency of these pulse annealed cells was 12 percent.

The program at Spire also emphasized resolving the questions regarding the hardware and economics of ion implantation for automated production. It involved introducing cost-effectively to the solar cell structure by implantation, such high-efficiency characteristics as back surface fields and shallow junctions.

Ion implantation and pulse annealing hardware problems were also addressed under this contract. A junction processor, to date only a concept, is an integrated ion implanter and pulse annealer. Two of the components of such a junction processor were pursued at two levels of detail:

- Ion Implanter — A detailed design was prepared for a 100 mA ion implanter with ten, 10 mA ion sources.
- Pulse Annealer — Functional requirements were identified for a pulsed electron beam processor capable of a throughput of at least 1,800 wafers per hour.

SECTION 2
TECHNICAL DISCUSSION

2.1 ION IMPLANTATION EQUIPMENT FOR SOLAR CELL PRODUCTION

2.1.1 General Considerations

Ion implantation machines remain versatile, sophisticated, and expensive capital equipment. A typical machine for semiconductor industry production will provide spectroscopically pure ion beams of most of the elements on the periodic table at any energy from 25 to 200 or more keV. Ion doses between 10^{11} and 10^{17} ions/cm^2 are delivered accurately and with virtually complete uniformity and reproducibility. Because of their versatility and their cost, these implanters are not economic for solar cell production purposes, not even at 1979 levels. However, the limitations are associated with the available machines and not with the process of ion implantation. The correction of implantation machine inadequacies has been addressed in this program.

The general configuration of an ion implanter is shown in Figure 2-1. Among factors which must be considered in the design of ion implantation equipment specifically for solar cells are the following:

1. Ion species requirements
2. Ion purity requirements
3. Ion energy requirements
4. Ion dose requirements
5. Dose uniformity/reproducibility requirements
6. Ion beam/substrate geometry

Both n- and p-type dopants have been implanted to form a high-performance n^+/pp^+ silicon solar cell structure. The use of phosphorus (P) and boron (B) ions was found adequate for high efficiency CZ solar cells. Aluminum (Al) can also be substituted for boron for BSF application. Ions other than P, B, and Al, however, are not needed from ion implanters for processing silicon solar cells, and significant machine cost savings can be achieved by dedicating each machine to production of a single ion species.

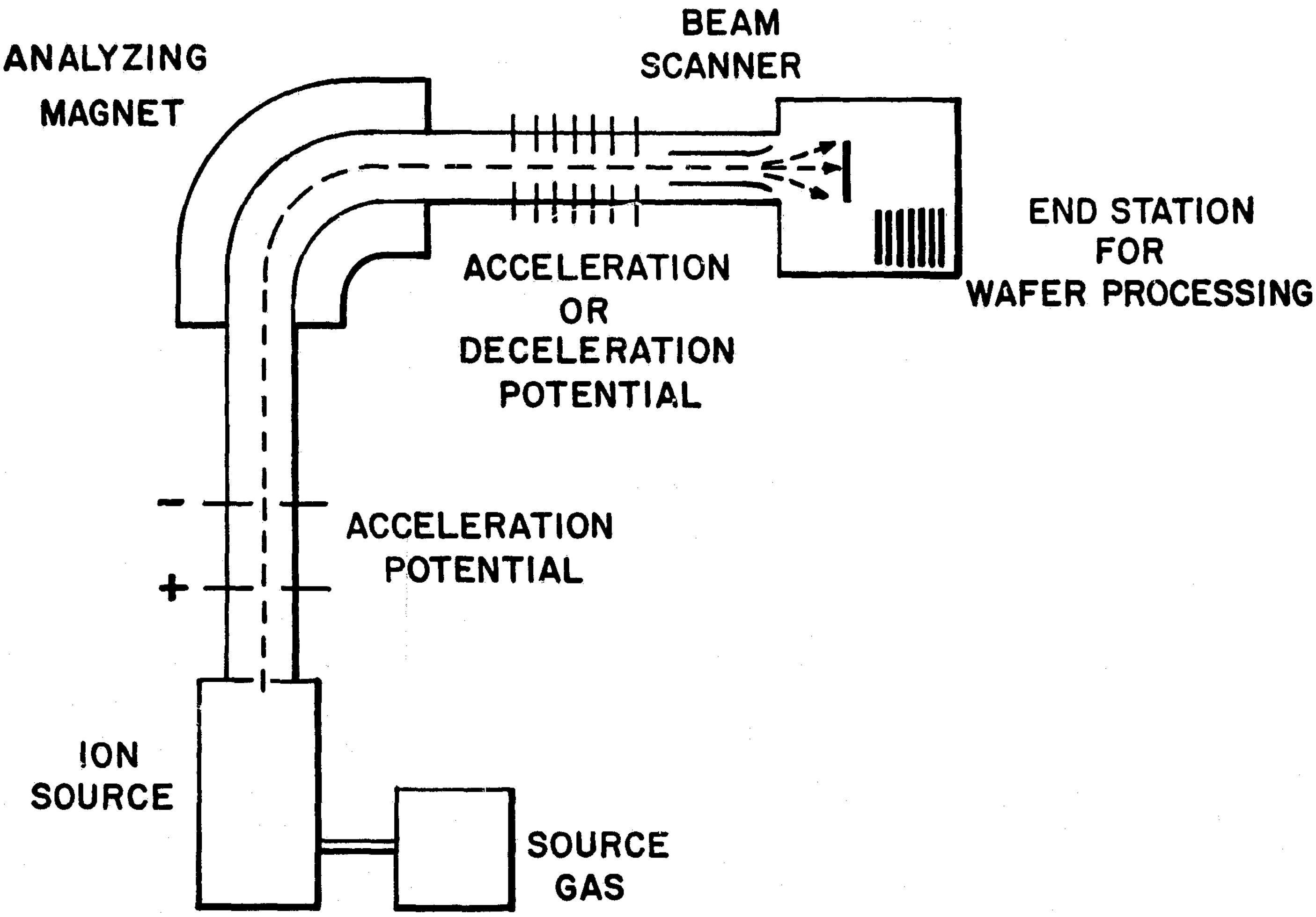

FIGURE 2-1. TYPICAL ION IMPLANTER CONFIGURATION

At present, ion implantators for the semiconductor industry produce spectroscopically pure dopant. Before being directed onto the material being processed, the ion beam undergoes mass separation, so that only a particular isotope of the desired element is actually implanted. Major simplification of implanter design will result if mass separation were not required, in which case small amounts of unavoidable impurities in the beam would also be implanted. A degree of control might be established over the choice of the major impurity components, so if the effect upon performance of the solar cell device could be made benign, implantation without beam analysis might be used in production.

Most ion implantation equipment now in use operates inefficiently or not at all at ion energies below roughly 25 keV, yet lower energies are desirable for very shallow junction solar cells. As shown in Figures 2-2 and 2-3, the projected range — and resultant junction depth — are proportional to the ion energy. Shallow-junction solar cells are best prepared by low energy ions which are typically in the 10 keV range.

Ion doses (particles/cm^2) were optimized under this contract and found to require relatively high doses, at least by conventional semiconductor industry standards as shown below:

Junction implants	-	$2.5 \times 10^{15}\ {}^{31}P^{+}\ cm^{-2}$ @ 10 keV
Back surface field implants	-	$5.0 \times 10^{15}\ {}^{11}B^{+}\ cm^{-2}$ @ 25 keV

These implant doses and ion energies are not consistent with today's ion implanters which are commonly used in the 50 - 100 keV range for doses less than 10^{14} ions per square centimeter. Implanters for low-dose applications have low beam currents, a few hundred microamperes maximum or less, and are capable of processing solar cells slowly because of the beam limitations. Machines with higher currents in the milliampere range now exist, but to achieve good uniformity and avoid excessive wafer heating at high ion energies, these machines have not been designed to utilize the available beam current efficiently. Typically the wafers are loaded onto a rotating disc in a batch mode, the entire disc is then placed in the vacuum load-lock and rotated during implantation. Recent implanters that have been introduced to the market are described in detail in Section 2.1.2.

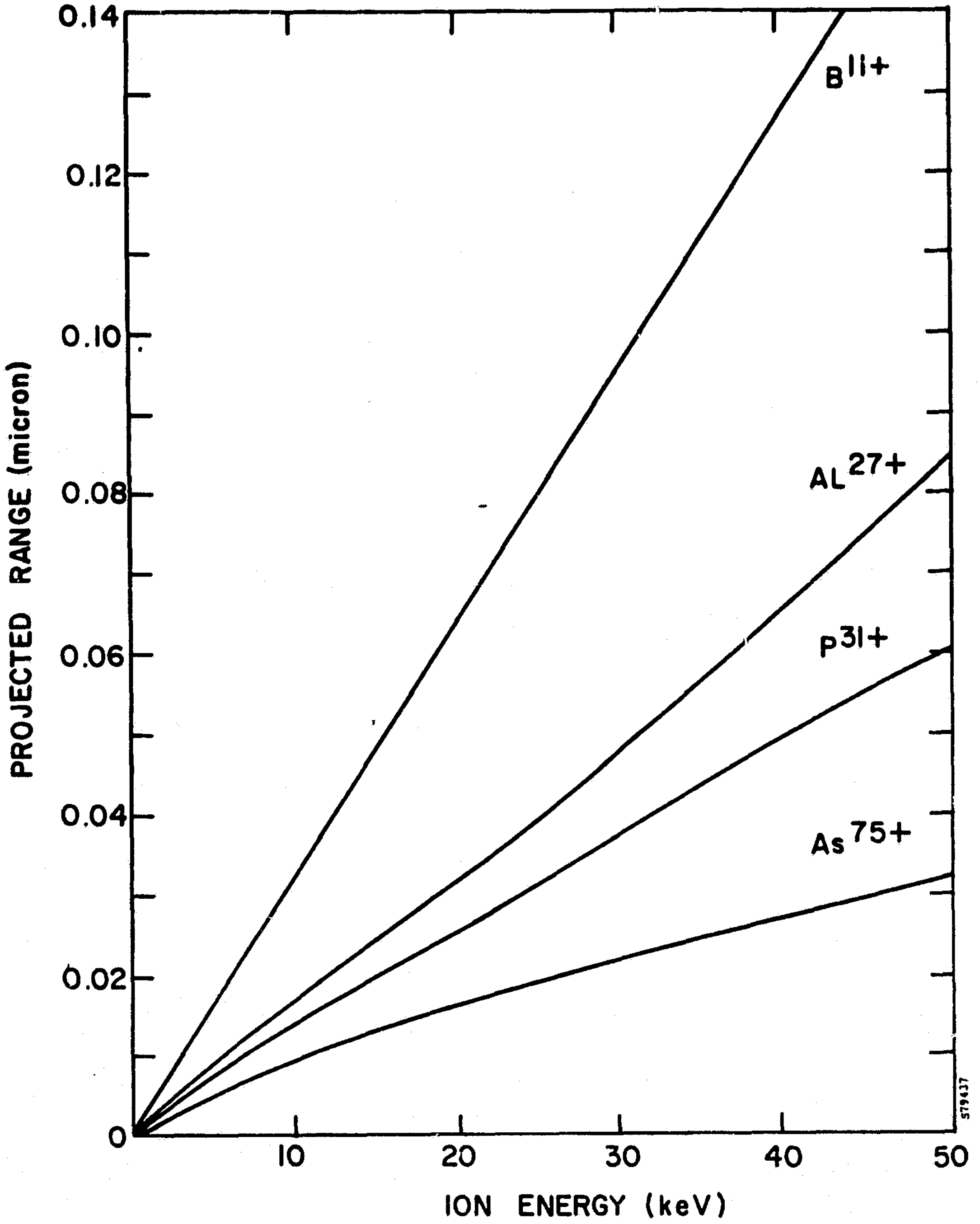

FIGURE 2-2. PROJECTED RANGE FOR P^+, B^+, As^+, AND Al^+ INTO SILICON

2.1.2 State-of-the-Art Survey

The present generation of high-current ion implanters is targeted at the pre-deposition process applications. These machines offer nominal beam currents of up to 10 mA of phosphorus and 5 mA of boron over an energy range of 10 - 80 keV.

Machines with phosphorus beam currents of 10 mA are now available from the Extrion division of Varian and from Nova Associates, but for solar cell application, these machines offer no throughput advantages over the solar cell implanter installed at Spire, and described in Section 2.1.2. Wafer throughput is not higher than earlier machines because of their load-lock wafer transport and poor beam utilization. The typical throughput and machine specifications for the NOVA NV-10 are shown in Figure 2-3 and Table 2-1.

Neither of the new generation ion implanters is well suited for solar cell application because of:

1. Wafer transport systems designed for ±1 percent dose uniformity. This contract has shown ±10 percent dose uniformity is sufficient for 16.5 percent efficiency CZ solar cell processing. The machine manufacturers have traded off possible throughput improvement for dose uniformity presently thought necessary for pre-dep application.
2. High machine costs because of their built-in versatility to implant ions with masses up to arsenic and at energies between 10 and 80 keV.

Less expensive machines can be assembled if dedicated implanters are specified for production use. Single ion species at a single energy significantly reduces the implanter cost.

If the requirements for mass-analyzed ion beams can be relaxed for solar cell manufacturing, implantation equipment can be greatly simplified, with reduced capital equipment costs the result. Examples of such simplified equipment (if the process sequence can be modified and successfully demonstrated) include:

1. Hollow cathode, ion sources — Without mass analysis these sources, originally developed for ion thrusters, can deliver ampere-level beams over a large area. Typical current densities are 3 mA/cm^2 at 1 - 2 keV. By controlling the purity of the ion source material, nonintentional ion species can be

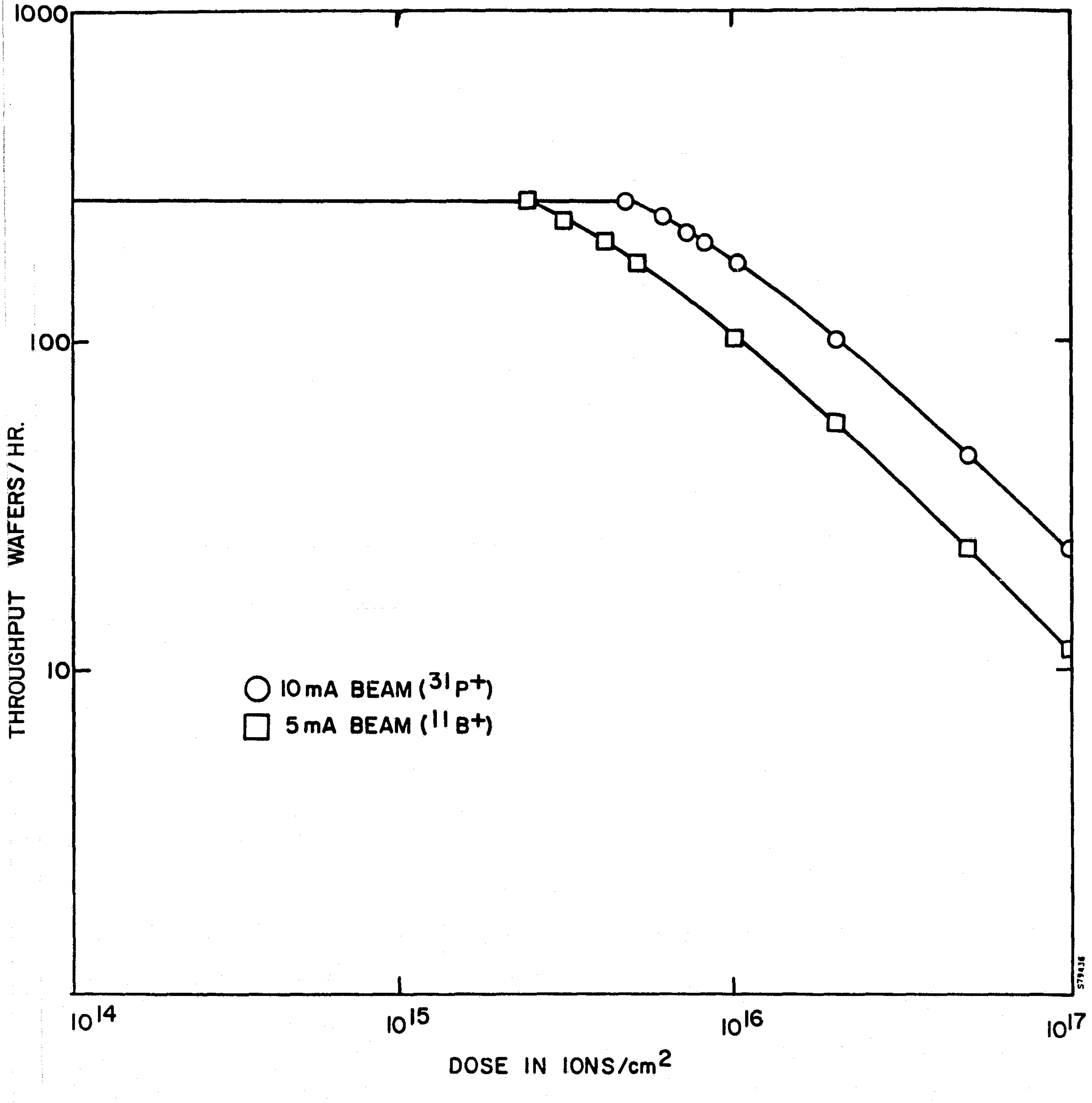

FIGURE 2-3. TYPICAL PRE-DEP ION IMPLANTER THROUGHPUT

TABLE 2-1. MACHINE SPECIFICATIONS FOR NOVA NV-10 IMPLANTER (3)

Beam Energy:	10 - 60 keV
Beam Currents	B^+ - 5 mA, P^+ 10 mA
Wafer Throughput:	
$2 \times 10^{15}\ {}^{31}P^+$ @ 10 mA	270 wafers/hr
$5 \times 10^{15}\ {}^{11}B^+$ @ 5 mA	130 wafers/hr
Doping Uniformity:	0.5% (3-inch wafers) 0.8% (4-inch wafers)
Wafer Holding Capability	18 (3-inch) 13 (4-inch) 10 (5-inch)
Ion Mass Range:	1 - 125 amu
Mass Resolution:	150
Vacuum System	Cryopumps
Ion Source:	Freeman with gas or solid source

controlled. This method of implantation, although not mass-analyzed, will be usable provided the implant anneal is done properly as discussed below.

2. Liquid metal ion sources — Charged particles are produced with high beam currents of aluminum, gallium, and other metals. Sources with 2.5 mA beam currents are now commercially available for gallium. The source provides 0.1 - 10.0 keV ions from a jet of liquid metal directed into a plasma.

For each of these methods of ion implantation, the purity specifications of the ion beams can be relaxed significantly if pulse heating is used to anneal the implantation damage and to activate the implanted ions. The ion source purity requirements can be lessened for pulse annealing because spurious dopants contained within the source materials when implanted cannot diffuse more rapidly than the aluminum during transient heating and rapid quenching. In contrast, furnace annealing requires long times (typically 15 - 30 minutes) at an elevated temperature, allowing fast diffusing impurities to migrate to the bulk silicon. For example, titanium, a common impurity found in most aluminum material, has a diffusion coefficient larger than aluminum. The effect of spurious contaminants, which include magnesium, iron, and titanium, on solar cell performance is a net reduction of carrier lifetimes, diffusion lengths, and solar cell current.

An approximation of the spurious ions that would be implanted along with the desired species can be obtained by simply scanning through the mass range of an implanter. This data does not include ions with mass numbers greater than the highest mass capacity of the electromagnet. Examples of mass spectra for the Extrion 200-1000WF are shown in Figures 2-4 and 2-5 for boron (BF_3 source gas), and phosphorus (PH_3 source gas). The mass spectra are strongly dependent on the history of the ion source.

2.1.3 High-Current Solar Cell Implanter

A dedicated solar cell implanter has been designed and fabricated in conjunction with Varian/Extrion Division. The design has adapted state-of-the-art implanter equipment technology to solar cell production requirements. An end station wafer processor was selected which utilizes a high percentage of available beam currents to achieve a throughput of up to 300 wafers per hour for junction implants. The machine

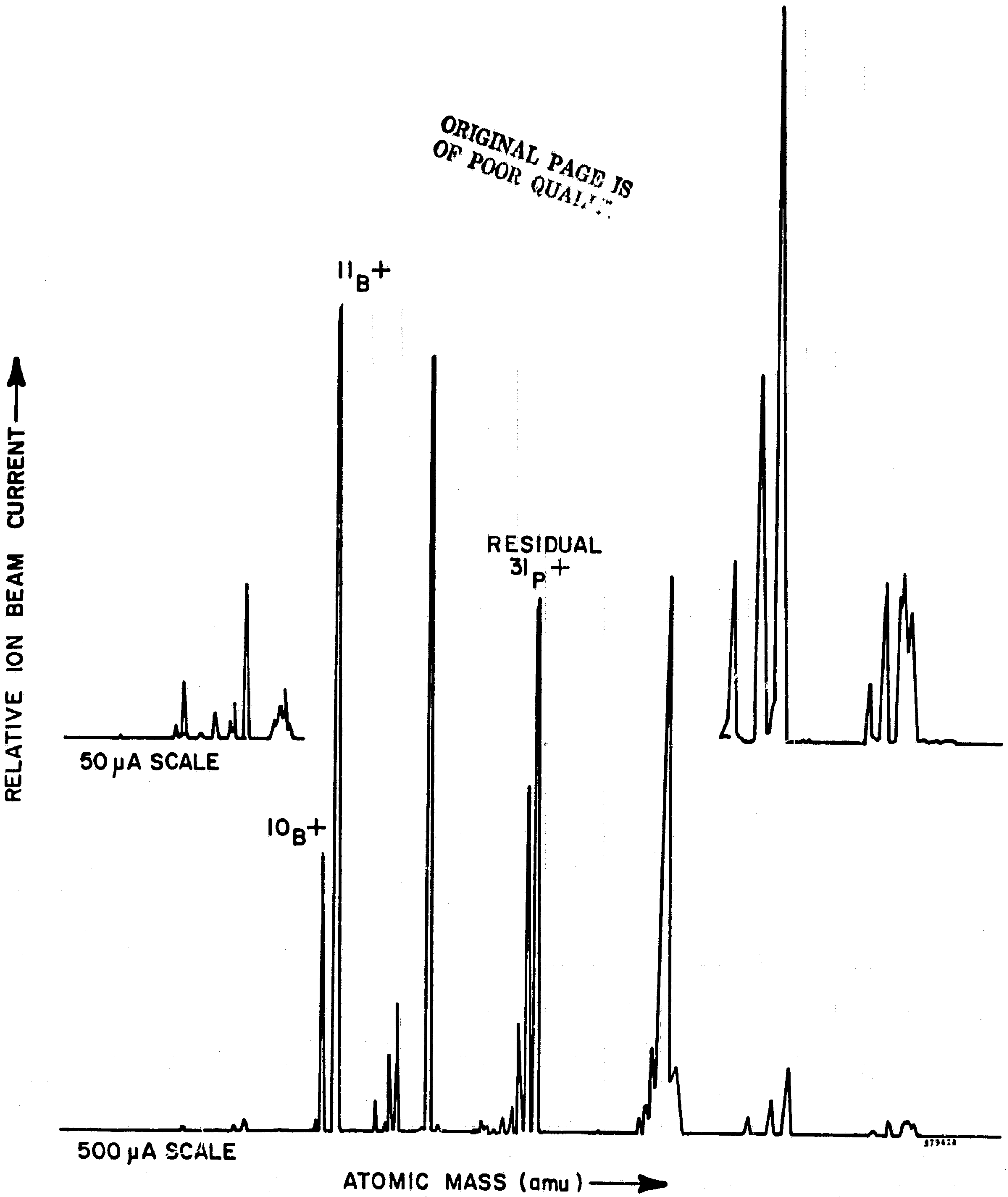

FIGURE 2-4. MASS SPECTRUM FOR BF_3 IN VARIAN/EXTRION 200-1000WF IMPLANTER

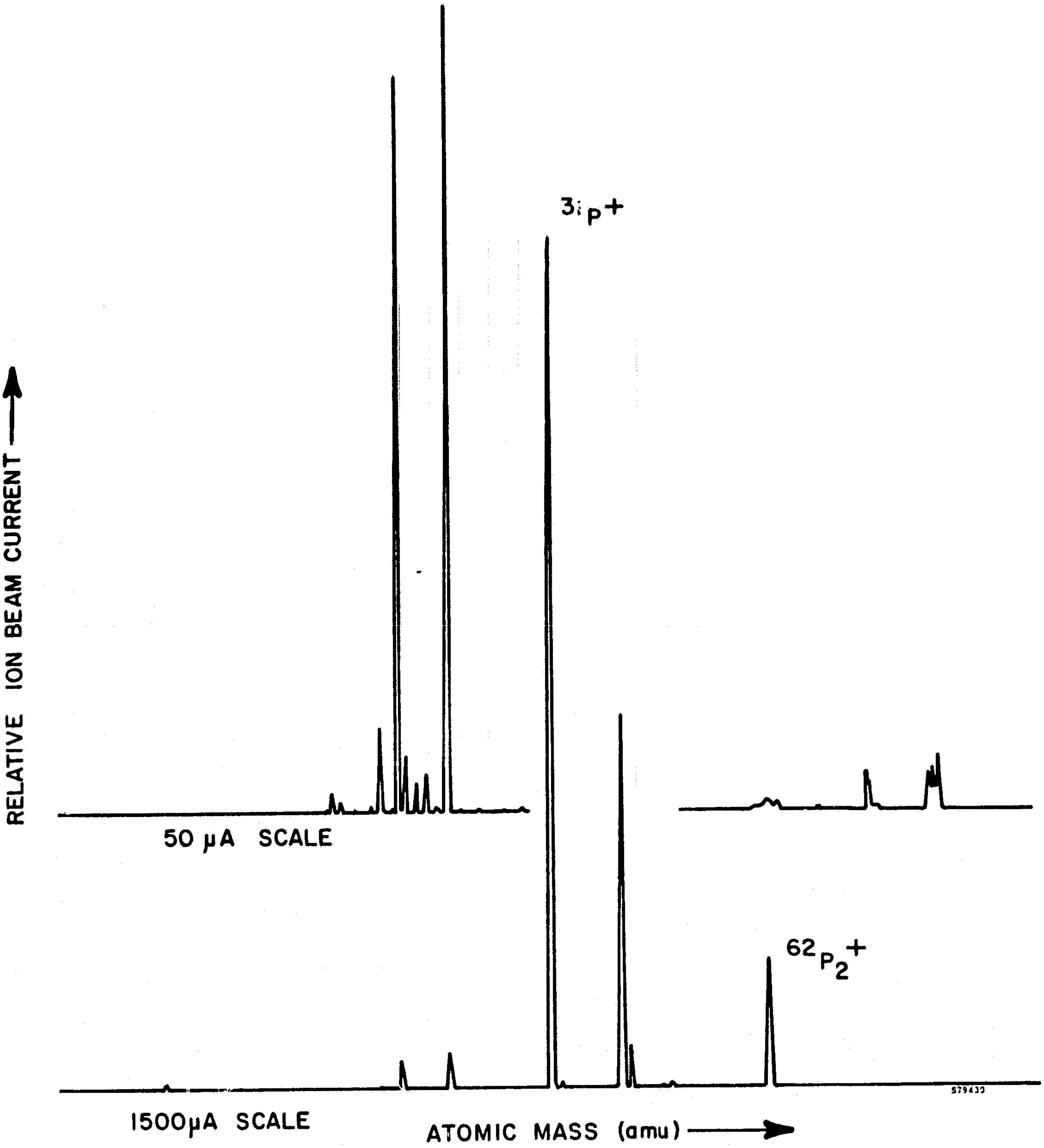

FIGURE 2-5. MASS SPECTRUM FOR PH_3 IN VARIAN/EXTRION 200-1000WF IMPLANTER

operates over a low ion energy range from 5 to 50 keV, which is of interest for shallow junction, high-efficiency solar cell processing. Other unique features of this implanter (shown in Figure 2-6 and 2-7) include:

- Rotation of the wafer during implantation at the rate of one rotation per second to produce uniform doping of texturized surfaces
- Elimination of fixture shadowing because of the absence of holding devices
- Continuous wafer processing rather than batch loading, and
- Magnetic field oscillation of the ion beam to provide the necessary implant dose uniformity.

Other implanters with beam currents comparable to those of the solar cell process machine in general have much lower throughput capability because of wafer station design. For example, a high-current implanter capable of processing at 200 keV would not be designed to implant individual wafers in a few seconds because at 200 keV, a 10^{15} ion/cm^2 implant carries sufficient energy to raise the temperature of a silicon wafer 250 micrometers thick by approximately 750°C. Aside from the problems encountered in trying to anneal the radiation damage remaining after implant, the transport and handling of high-temperature wafers would be impractical. To speed processing with the high-current machine, many wafers usually are implanted over a relatively long period of time through batch loading. However, the solar cell implanter is designed for low ion energies, and at 10 keV, a 10^{15} ion/cm^2 implant increases the temperature of a wafer 250 micrometers thick by only 37°C.

Figure 2-8 illustrates the wafer holding mechanism which rotates the wafer at one revolution per second in the ion beam during implant. Wafer rotation in combination with off-axis tilt is an important function for a number of reasons, including:

1. The total forward surface of the wafer is implanted without regions being shadowed because of the holding mechanism.
2. Silicon material with irregular surface features or a texturized surface is multidirectionally implanted to avoid gaps from shadowing.
3. Circumferential uniformity over the implanted wafer is assured regardless of any lack of symmetry in the ion beam itself.

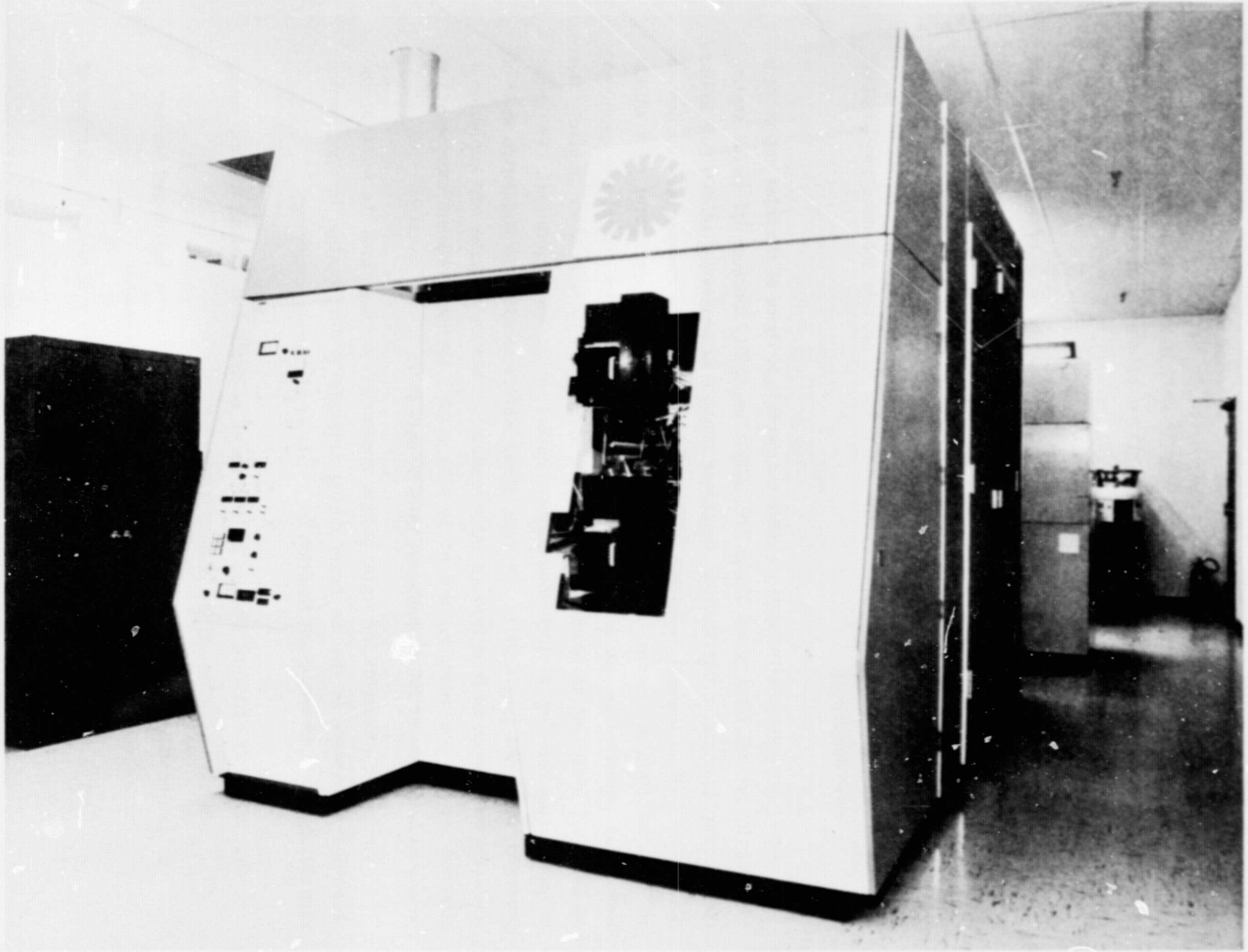

FIGURE 2-6. HIGH-CURRENT SOLAR CELL IMPLANTER

ORIGINAL PAGE IS
OF POOR QUALITY

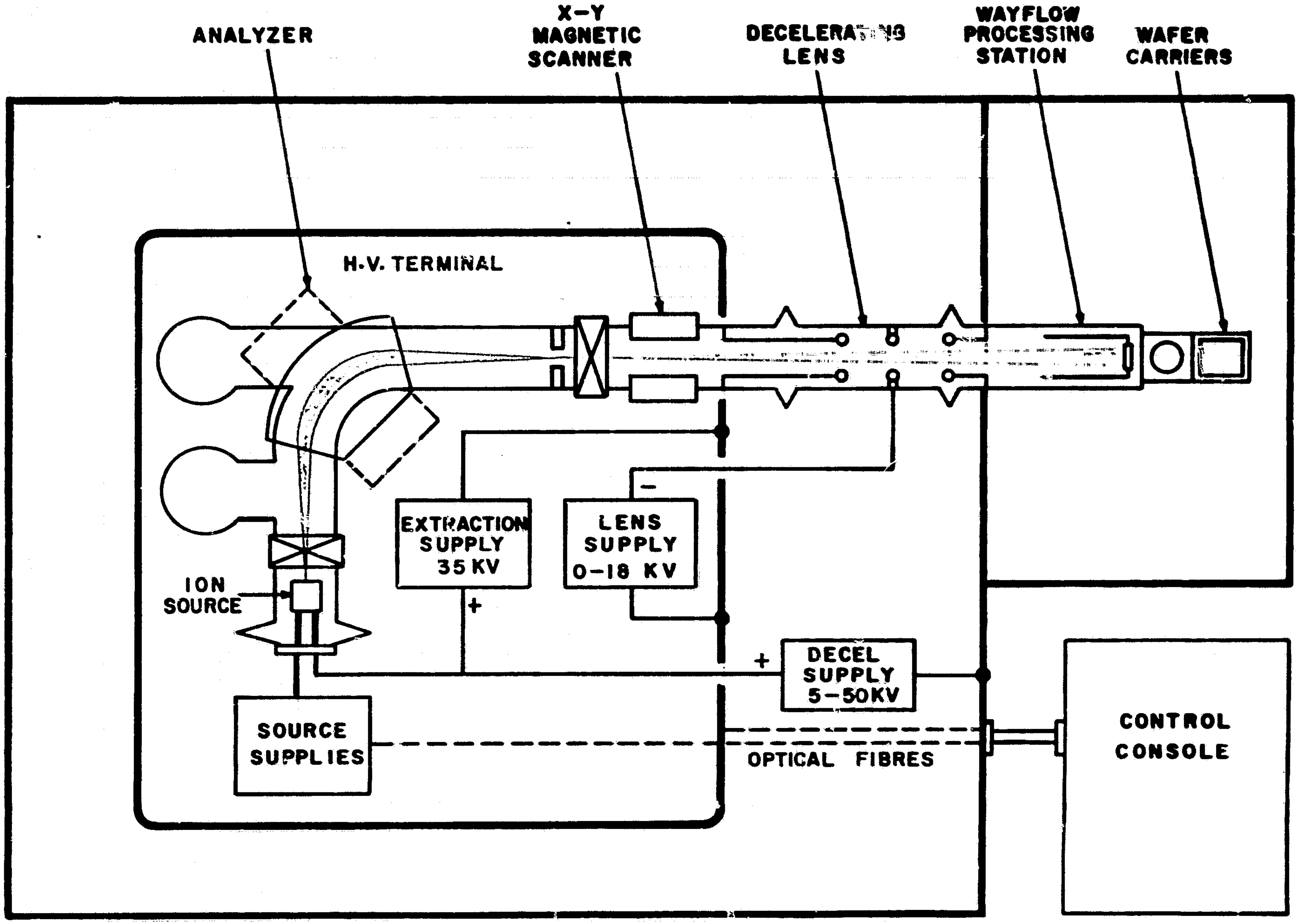

FIGURE 2-7. SOLAR CELL ION IMPLANTER

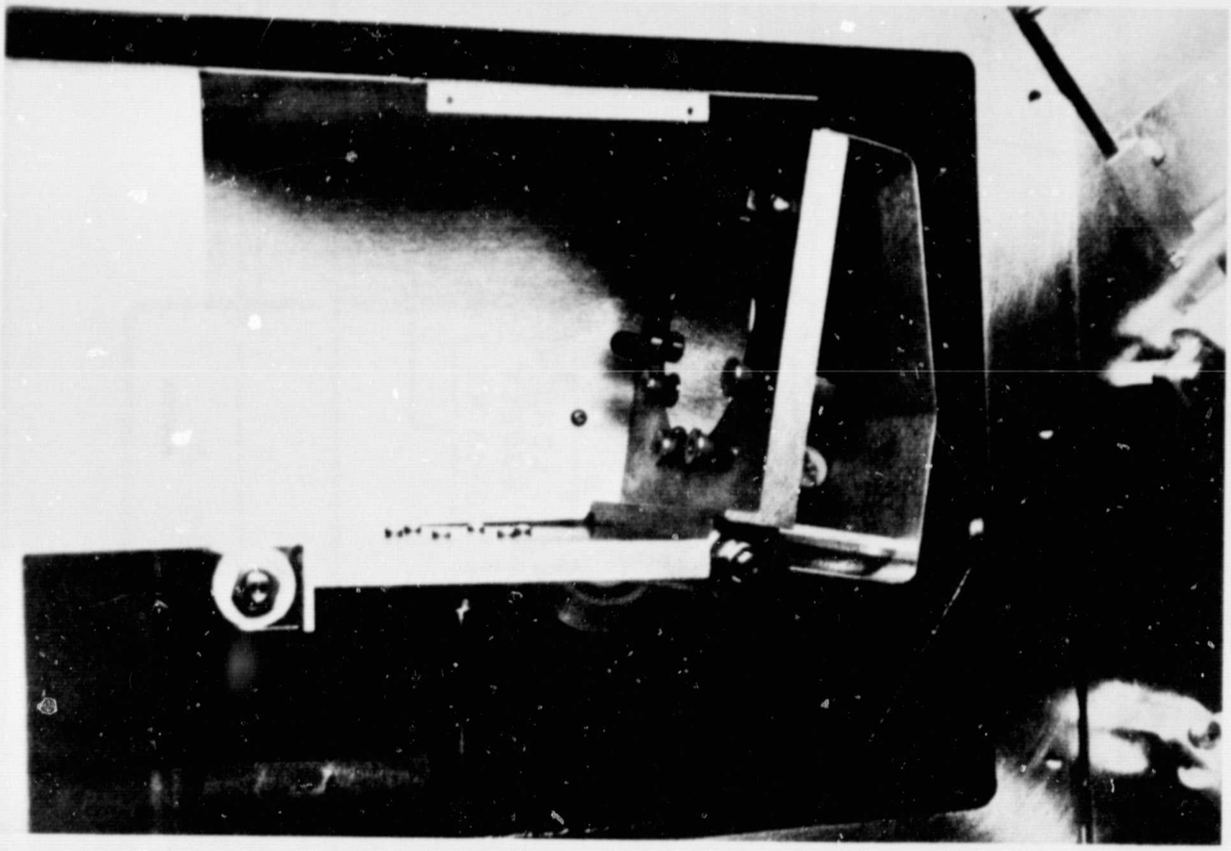

FIGURE 2-8. WAFER HOLDER/ROTATOR FOR SOLAR CELL IMPLANTS

Beam currents are above the minimum required for the end station limited throughput of 300 three-inch wafers per hour, as shown in Table 2-2. If operated to capacity on a multiple-shift basis, this implanter could produce junction implants (at a dose of 2×10^{15} phosphorus ions per square centimeter at 10 keV) at a rate equal to approximately 1 MW_e of peak power of high-performance solar cell product per year.

Operational parameters for the high-current solar cell implanter were developed to provide adequate implant dose uniformity. A target uniformity variation was specified to be ±10 percent across the wafers with diameters of 7.6 cm. The requirement of ±10 percent uniformity was placed on both the phosphorus ($^{31}P^+$) junction implants and the boron ($^{11}B^+$) back surface field implants.

The final implanter setup parameters were determined by considering the dose uniformity variables of ion energy, ion species, degree of overscan, and scan frequency. Table 2-3 shows the specified implant parameters utilized to manufacture the 1,000 solar cells delivered to JPL. Figure 2-9 shows the resultant implant dose uniformity achieved for boron implants, Figure 2-10 shows the uniformity for phosphorus junction implants, and Figure 2-11 shows the uniformity for arsenic implants. Both sets of implant parameters result in dose variations within the uniformity goal of ±10 percent. Quantitative measurements of the neutral beam component have shown this nonscanned component to be the major contributor in the uniformities of ±10 percent which remain constant for wafer sizes up to 10-cm diameter.

2.1.4 Ion Implanter Design

The implanter described in Section 2.1.2 can serve immediate needs for implanted solar cell process development. But if implantation is to be practical for use as the central element for automated production to meet the mid-1980 objectives, dedicated machines with higher beam currents and faster throughput characteristics must be developed. The engineering design of such a solar cell production implanter was completed. The production implanter can operate continuously at delivered beam current levels of not less than 100 mA. (The operational characteristics of the most recently developed high-current implanter, the dedicated solar cell implanter and an automated production implanter are compared in Table 2-4.) As shown in Table 2-4, solar cell product throughput of one automated production implanter machine in full operation will be approximately 100 MW_e peak output per year.

TABLE 2-2. PERFORMANCE CHARACTERISTICS FOR THE VARIAN/EXTRION 200-1000WF IMPLANTER

Species	Dose (ions/cm^2)	Required Minimum Beam Current* (mA)	Machine Design Specification (mA)
$^{11}B^+$	1×10^{15}	1.0	0.7
$^{31}P^+$	1×10^{15}	1.0	1.0
	2×10^{15}	2.1	1.0
$^{75}As^+$	1×10^{15}	1.0	1.0

Beam Energy (keV)	Actual Beam Current (mA)		
	$^{11}B^+$	$^{31}P^+$	$^{75}As^+$
5	0.89	-	-
10	0.89	4.2	2.5
15	0.95	2.4	1.6
20	0.95	2.2	1.2
25	0.96	2.0	1.1
30	0.96	2.0	1.1
35	0.96	2.0	1.1
40	0.96	2.1	1.1
45	0.96	2.2	1.2
50	0.95	2.3	1.2

* These beam currents provide 7-sec implants; an additional 5 sec is allowed for wafer transport.

TABLE 2-3. HIGH-CURRENT IMPLANTER SETUP PARAMETERS

Ion	Energy (keV)	Dose (cm^{-2})	Scanning External Magnetic Field Frequency (Hz)*		Overscan (%)
			X	Y	
$^{11}B^+$	25	5×10^{15}	8	6	30
$^{31}P^+$	10	2.5×10^{15}	8	6	20

*All electromagnets are driven by a sine-wave modulated power supply.

SHEET RESISTANCE MAP

Signetics Corp., June 5, 1978, 21:24
U3385, Spire's Boron Implant Wafer #1184-11

Parameters

CF = 4.500
FPP Spacing = 0.025 in.
Current = 1050.0 microamperes
Contour Integral = 1 percent
Wafer Diameter = 3 in.
Measured Uniformity = 96.82 ohms/sq ± 7.50 percent
Implant = 5×10^{15} $^{11}B^{+}$ cm^{-2}, 25 keV (100) Si

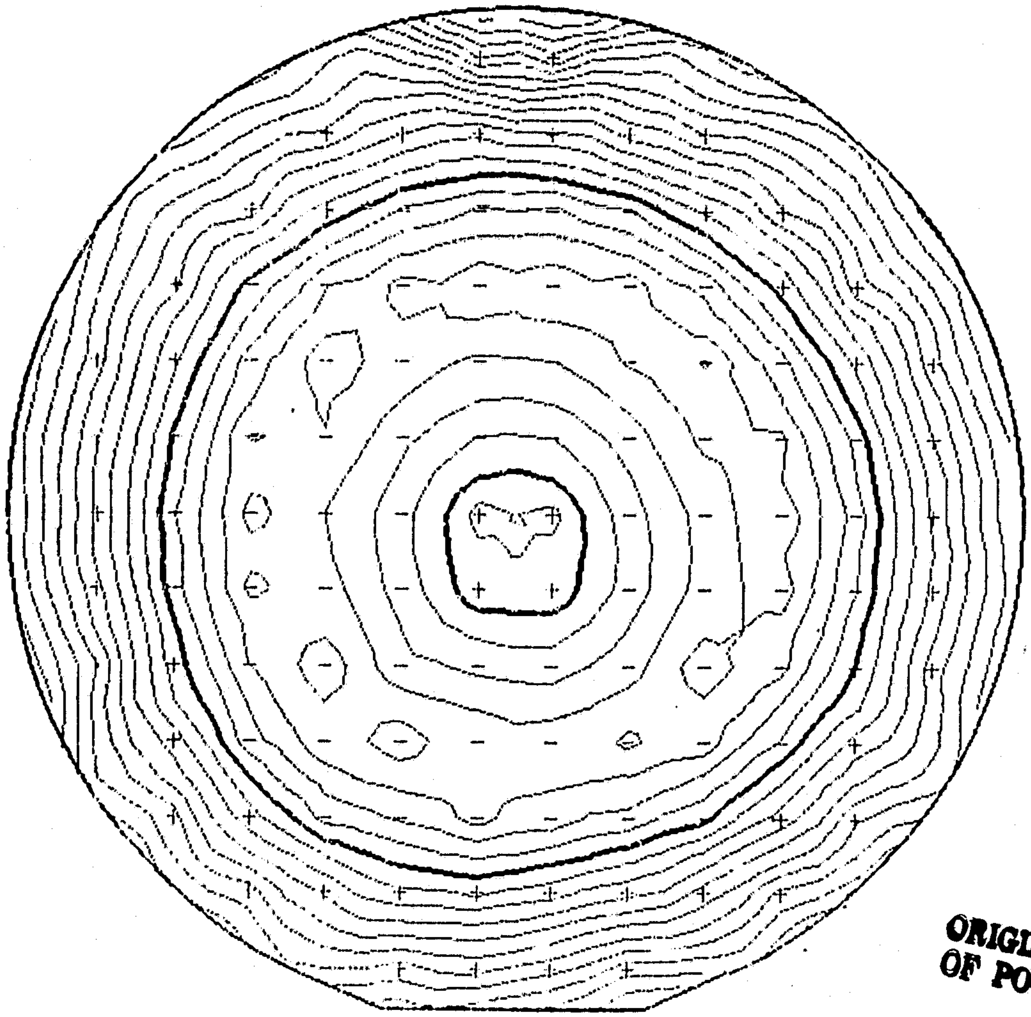

FIGURE 2-9. SHEET RESISTANCE CONTOUR MAP FOR STANDARD BORON IMPLANTS AFTER ANNEALING

SHEET RESISTANCE MAP

Signetics Corp., July 12, 1978, 19:40
U3421, Spire's Phosphorus Implant Wafer #1184-8

Parameters

CF = 4.5
FPP Spacing = 0.250 in.
Current = 3000 UA
Contour Integral = 1 percent
Wafer Diameter = 3 in.
Measured Uniformity = 45.71 ohms/sq ± 7.81 percent
Implant = $2\times10^{15}\ {}^{31}P^{+}\ cm^{-2}$, 10 keV (100) Si

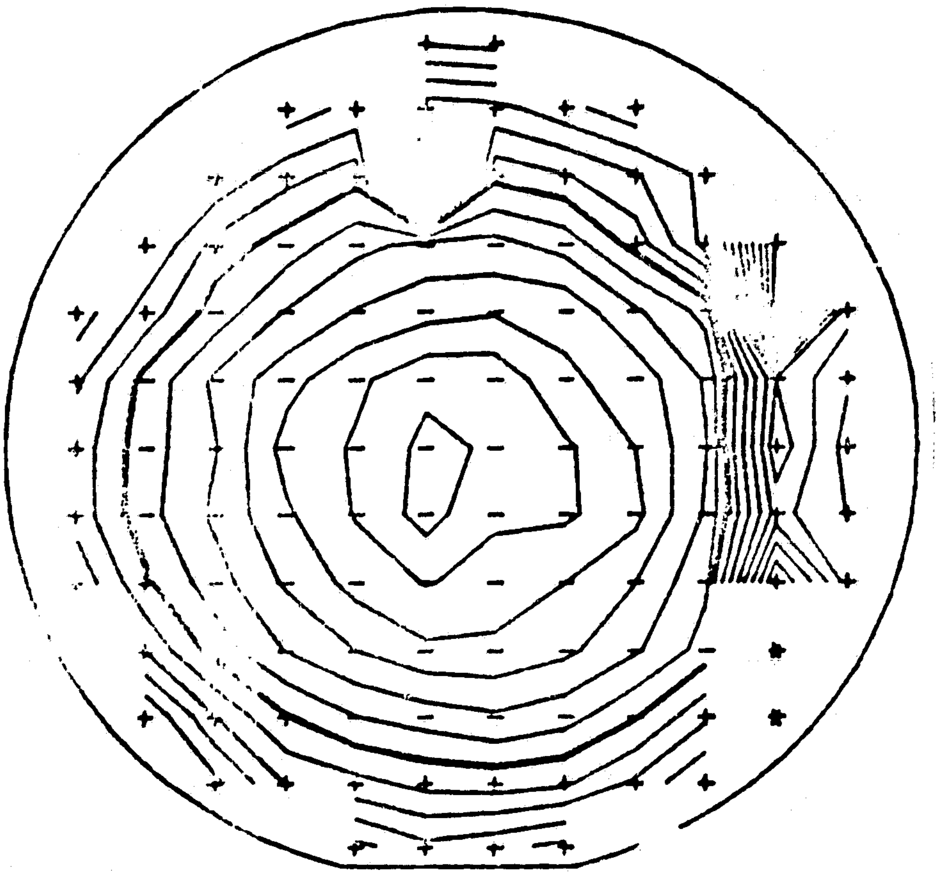

FIGURE 2-10. SHEET RESISTANCE CONTOUR MAP FOR STANDARD PHOSPHORUS IMPLANTS AFTER ANNEALING

SPIRE 03/26/80 ARSENIC

WAFER NO. 2782-1

AVERAGE R(SHEET)=50.5 OHMS/SQUARE

STD. DEV. = +/-3.64 RANGE =+/- 7.28 OHMS/SQUARE

VOC. MAP ***

ORIGINAL PAGE IS OF POOR QUALITY

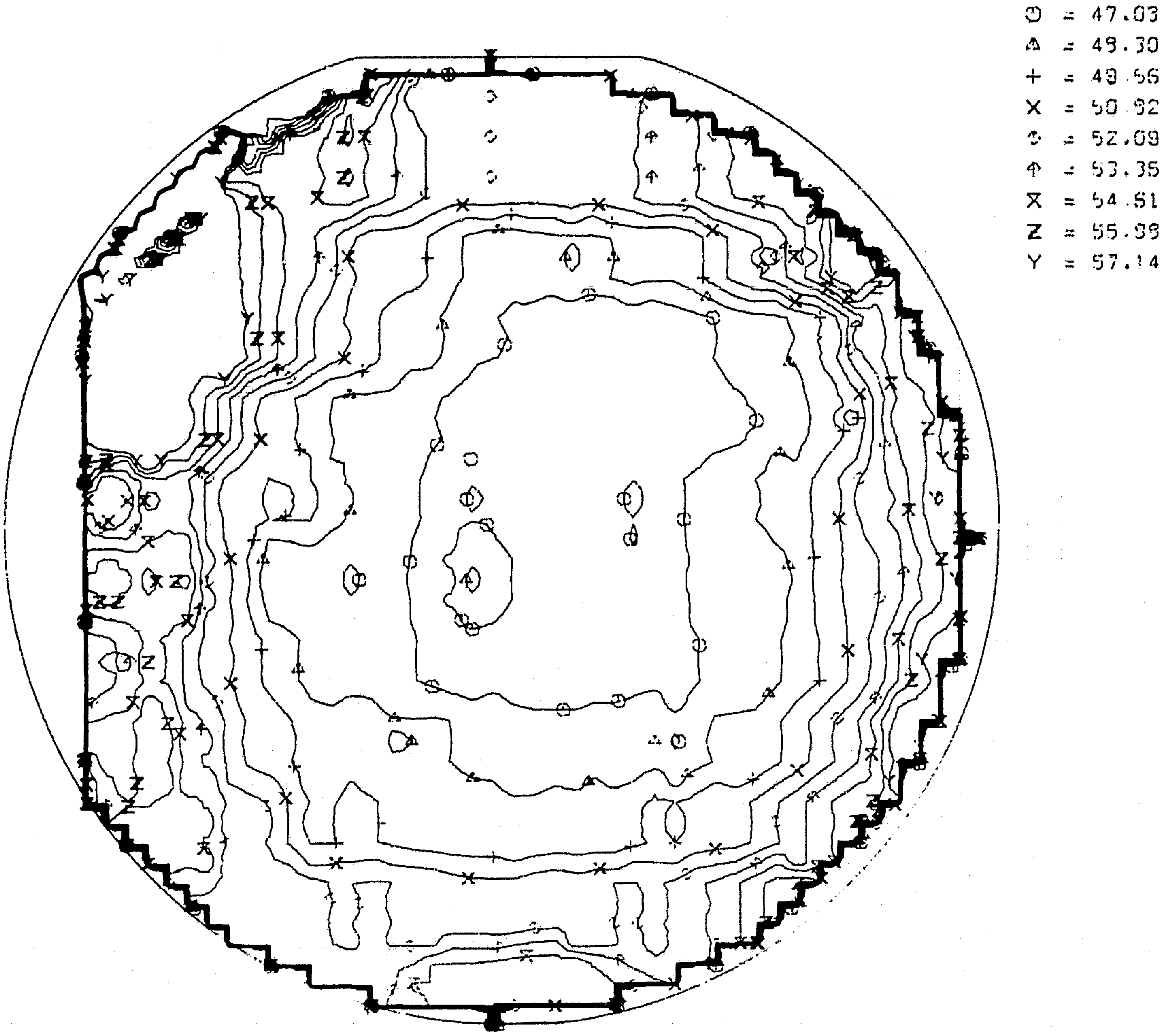

FIGURE 2-11. SHEET RESISTANCE CONTOUR MAP FOR STANDARD ARSENIC IMPLANTS AFTER FURNACE ANNEALING

TABLE 2-4. COMPARISON OF ION IMPLANTATION EQUIPMENT FOR SOLAR CELL JUNCTION IMPLANTS

Specification	Pre-Dep Implanter NOVA Assoc. (NV-10)	State-of-the Art Solar Cell Process Implanter (Extrion 200-1000WF)	Advanced Solar Cell Automated Production Implanter
Process Mode	Batch	Continuous	Continuous
Carrier	None	Cassette	Platen
Phosphorus Beam Current	10 mA @ 10 keV	4 mA @ 10 keV	100 mA @ 10 keV
Beam Utilization Efficiency (%)		15	83
Throughput (3" wafers/hr)	270	300	35,000
Solar Cell Product Per Year	100 kW_e	1 MW_e	100 MW_e

A set of functional requirements for an automated production implanter were defined to meet the objectives shown in Table 2-5. The design provides continuous, uniform, reproducible, high-volume throughput. The production implanter system as shown in Figure 2-12 includes multiple ion sources (10), a beam extraction and acceleration stage, an ion-beam mass analysis system, a magnetic beam-scanning with a material processing chamber complete with load/unload systems, and conveyors with vacuum load-locks to allow for the continuous flow of material through the system.

The material to be processed must fit inside the boundaries of the 21-centimeter-by-21-centimeter carriers are used to transport substrates through the system. The implanter design includes power supply systems for the ion sources, analyzing magnet, and scanner system. These units can be linked together by the signals from the instrumentation for beam current measuring, which will include Faraday cages and multichannel current metering. The dose monitoring system will be cpable of measuring the uniformity of the dose provided by each ion source system. The dose may be preset, with the dose controller then automatically keeping the dose within specification of +10 percent. The machine must be fully automated; i.e., only one control is to be needed to

TABLE 2-5. PRODUCTION IMPLANTER PERFORMANCE SPECIFICATIONS

Ion Species:	$^{31}P^+$, $^{75}As^+$, $^{11}B^+$ (Single machine may be dedicated to only one ion)
Ion Energy:	Fixed within the range 10 - 30 keV
Beam Current:	Minimum 100 mA of $^{31}P^+$
Analyzed Beam Purity:	Resolution of 0.5 amu at mass 31
Beam Uniformity/Reproducibility:	Not worse than ±10% over all material area processed
Substrate Throughput:	Variable - minimum of 500 cm^2/sec at 1×10^{15} ions/cm^2
Materials to Be Processed:	Silicon wafers, ribbon, or sheet to maximum individual-item dimensions of 20 x 20 cm
Surfaces to Be Implanted:	Planar and texturized
Processing Mode:	Continuous flow
Operational Mode:	Continuous throughout routine and predictable component failure maintenance

start or stop the implanter once the setup conditions have been satisfied. A minicomputer will be used to link together the various subsystems and to provide controls, displays, and data logging.

Ion Sources

The ion sources (Figure 2-13 shows one such source that is suitable for high throughput) are Feeeman sources with an exit aperture 75 mm long by 2 mm wide. The arc chamber is made of molybdenum shaped to focus the beam from the ion source into the magnet gap with very little loss of beam. The ion sources are designed to operate with phosphorus vaporizer sources. It will be possible safely to remove an ion source from the system for maintenance and replacement while the machine is running. The source gas feeds, roughing system, and power supplies are to be independent of each other. Each source module is completely interlocked to prevent accidental operational errors or dangerous situations. The sources are designed to operate for 24 hours with a

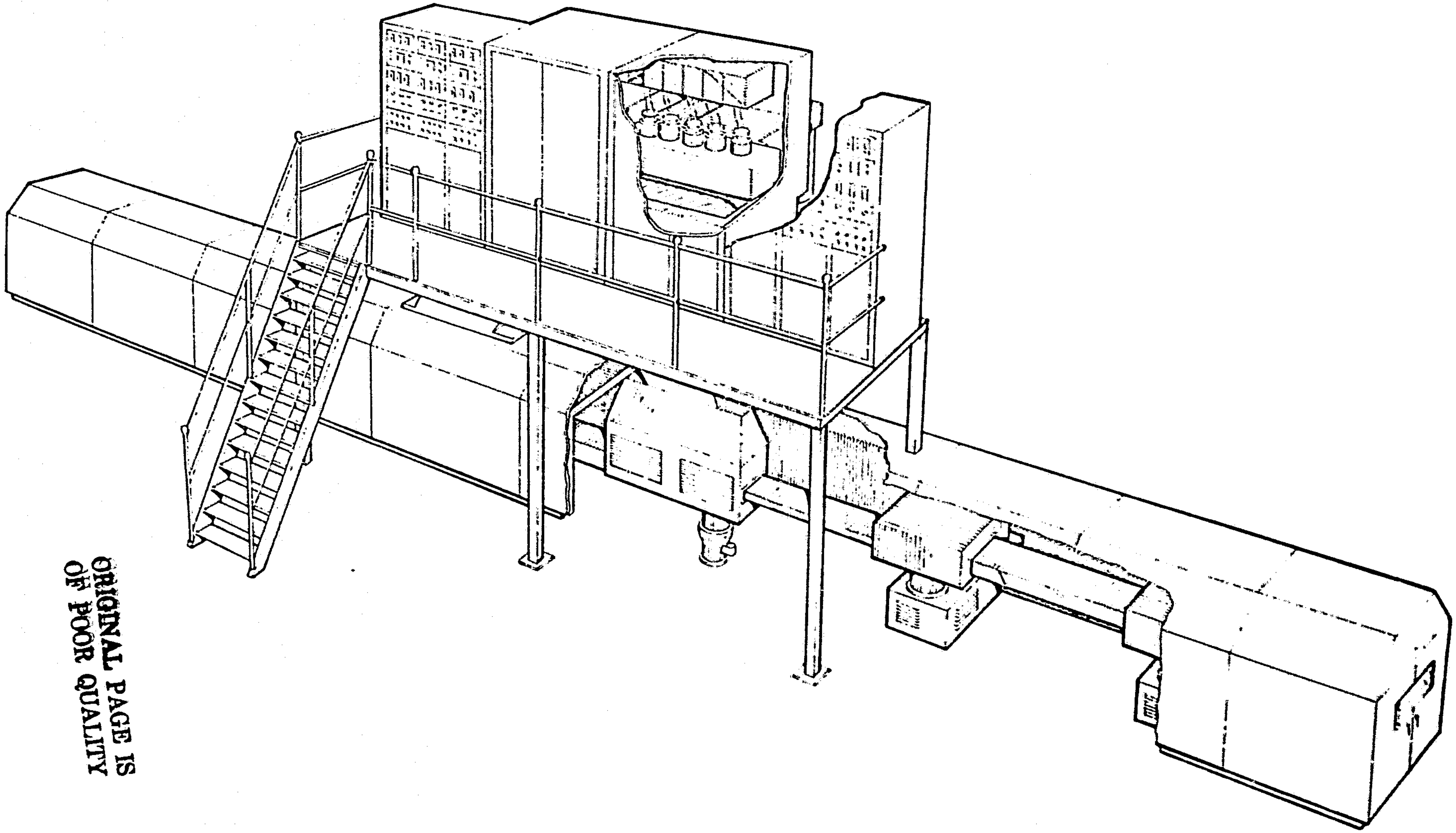

FIGURE 2-12. SYSTEM DRAWING FOR 100-mA AUTOMATED PRODUCTION IMPLANTER

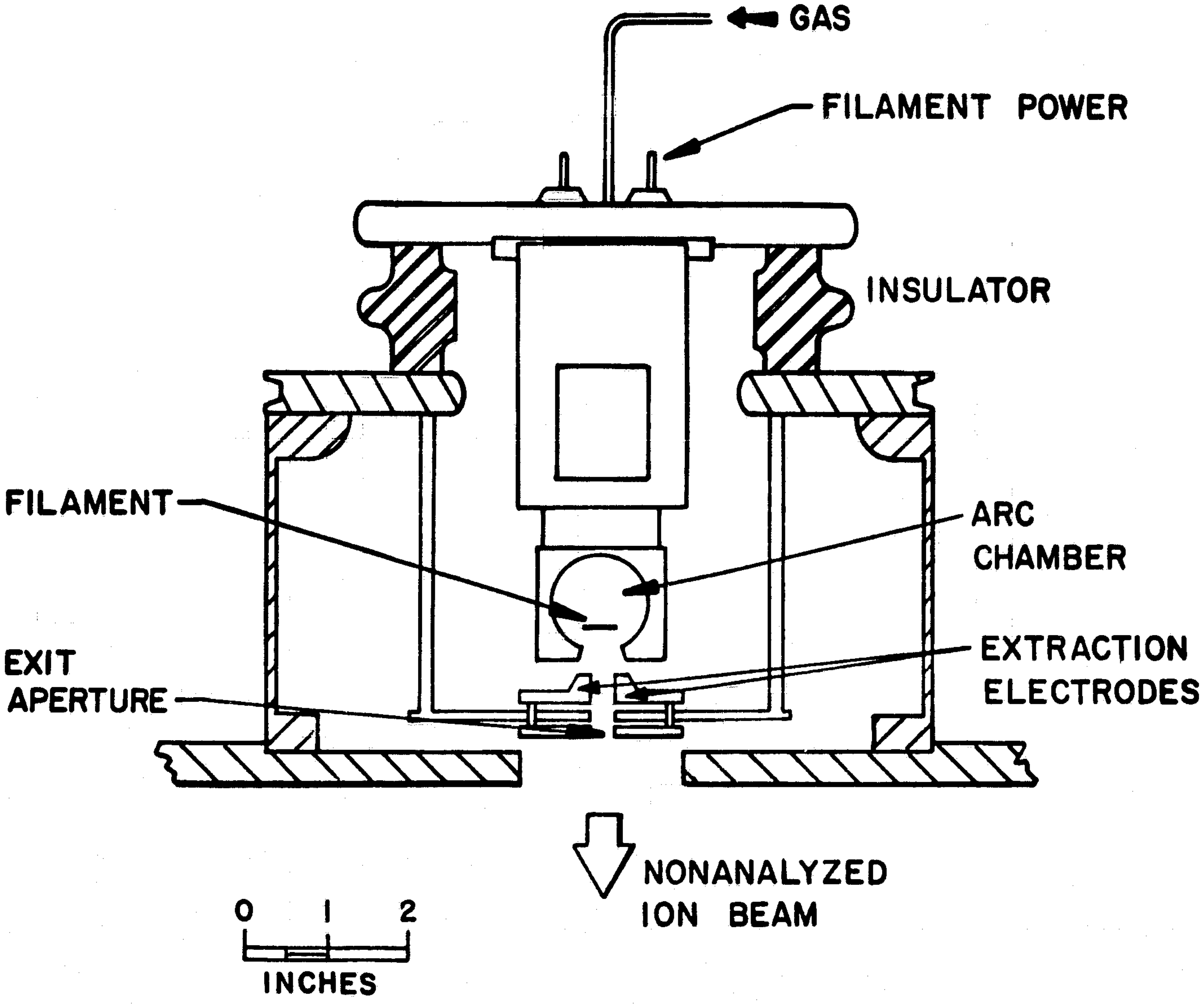

FIGURE 2-13. FREEMAN ION SOURCE CROSS SECTION

probability of failure of less than 1 percent. The sources are to be removed for filament replacement and maintenance within this 24-hour period. Each source is to be controlled by its own servo-loop with monitoring instructions from the main control computer. All control signals and displays will be optically isolated.

Each ion source is designed to provide 20 mA of analyzed $^{31}P^{+}$ beam. To process texturized or low-grade surface substrates, five sources will implant at an angle of +15° to normal and five at -15° to normal. During machine operation with a total beam current of 100 mA, three sources will operate at 16 mA each and at +15°, while three others will operate at the same current level at -15°. The additional 4 mA will be made up by a seventh source, which will provide the fine-dose control. The remaining three sources will be in various stages of programmed maintenance. At any given time the combination of the 16-mA sources and one 4-mA source will be providing the total of 100 mA of analyzed beam.

Acceleration System

The extraction or acceleration system involves a single-gap geometry with a negatively biased electrode to trap electrons. The extraction power supply for each of the 10 ion sources is to be rated at 50 mA of continuous current. The supplies for each source will be independently controlled and may be varied ±2 percent about the predetermined value, so that the position of the beam in the analyzing slit region can be optimized. To minimize neutral beam formation, a series of restrictions or apertures, one for each source, is to be placed ahead of the analyzer entrance pole face. After initial adjustment, the mechanical components can be removed for changing or cleaning and returned to the original position with a jig.

Mass Analyzing System

The ion beam will enter the analyzer pole face perpendicularly (see Figure 2-14). The magnet pole deflection angles (there are two poles, one deflecting at ±45° and the other at ±30°) and pole face angles will be chosen to focus the beam on the target at an angle of ±15°. The focusing system is to be such that the beam will focus in the analyzing slits and in an orthogonal direction on the target. The radius of curvature of the beam trajectory in the magnetic field will be 30 cm.

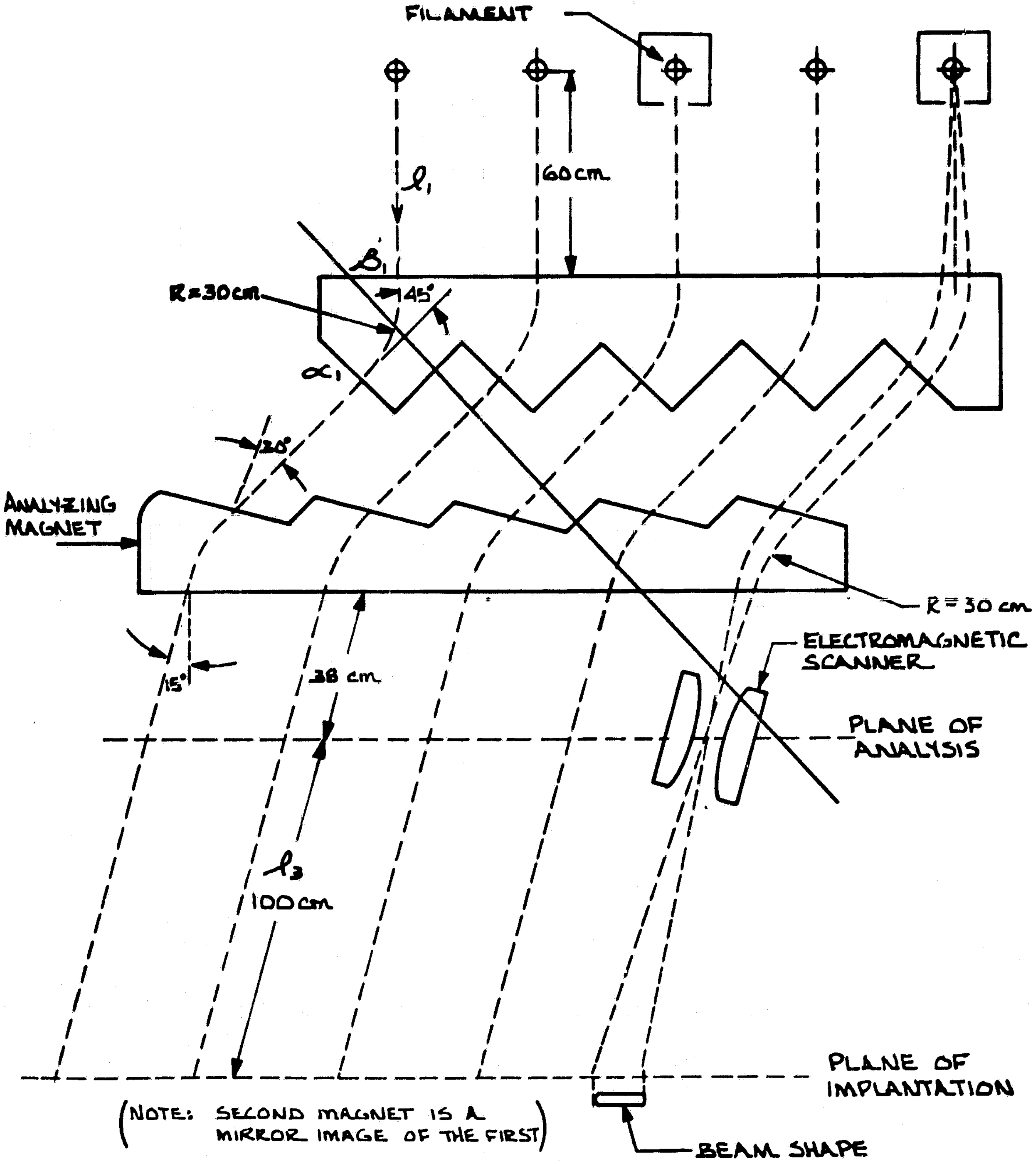

FIGURE 2-14. SCHEMATIC DIAGRAM OF THE BEAM TRAJECTORY THROUGH THE ANALYZING AND SCANNING SYSTEM

Ion-Beam Scanning System

A magnetic ion-beam scanning system with a laminated core will be utilized and, to minimize the power required to scan the ion beam, the magnetic field gap will be located in the region of the crossover. The minimum gap between the poles of the scanning magnet will be 10 mm and the deflection angle will be $\pm 5^{\circ}$. The magnet iron and drive coils will be shielded from the ion beam and located in the vacuum of the analyzer tank. A scan generator is to be provided which can be adjusted to produce the correct waveform to satisfy uniformity requirements. This part of the system will provide a ±5 percent uniformity of dose. A wide-band amplifier will be employed to drive the system. The mean position of the scanning magnet is to be 1,200 mm below the exit of the analyzing magnet. Each scanner coil and magnet will be removable for repair, and will be coded and pinned to prevent replacement into an incorrect location. To change a scanner magnet the main vacuum system will have to be vented to atmospheric pressure.

Process Chamber

The implant process chamber is to be provided with a chain drive substrate carrier system. Carriers are to be fed onto this chain at two levels from the entrance lock, one 15 mm below the other (see Figure 2-15). Three carriers at a time will pass through each level with a gap of 45 mm between the groups of three on the same level. The chamber is to be provided with a series of mechanical beam gates provided with Faraday cages. A set of eight slits is to be used for beam dose uniformity measurement and for scan adjustment. The beam gates are to be driven by stepping motors under control of the central computer. Cooling is to be provided for all parts of the system where necessary.

Control Console

The implanter control console will be connected to the implanter by armored cables. The console will consist of three 6-foot-high cabinets connected together and provided with a desk. The console will provide a main operator control panel to enable and operator to start up, process, and shut down the machine without any other actions. Two display panels will indicate the status of the ion sources and of the vacuum system. The display will be such that a fault condition is indicated by both a red light and an audible alarm. The computer system is expected to be a Digital Equipment Corporation

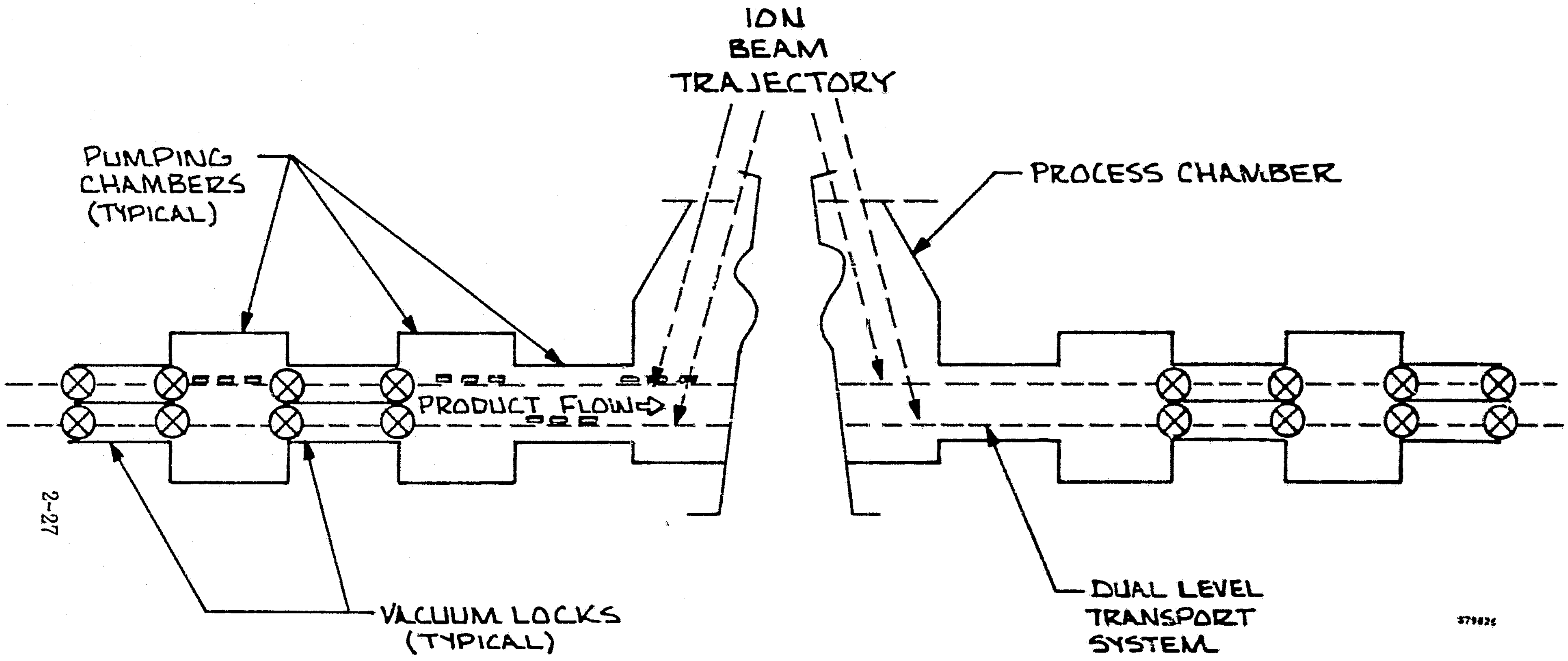

FIGURE 2-15. MATERIAL TRANSPORT SYSTEM

PDP/11. The unit selected for the prototype implanter system will be suitable for software development and will include:

- 11/34A CPU (32 KW of memory)
- Serial line unit
- Real-time clock
- RL11 - AK disk control/drive (5 megabytes)
- RL01 - AK drive (5 megabytes)
- LA11 - PA printer

All communication from the implanter subsystems to the computer will be via optical isolators, as shown in Figure 2-16.

Software

The system is to be designed to minimize the initial software requirements. The control circuitry will be designed so that the servo-loops are at the lowest level. Software programs will be written initially for:

- Uniformity measurement (but not to adjust the scanner waveform automatically)
- Dose calculation and adjustment of the scanned source current to give the correct dose
- Vacuum system control
- Transport system control and synchronization
- Monitoring variables such as the status of locks, temperature levels, and carrier speeds
- Data logging
- Displays for the CRT system for use in diagnostics
- Troubleshooting routines
- Start-implant and stop-implant programs.

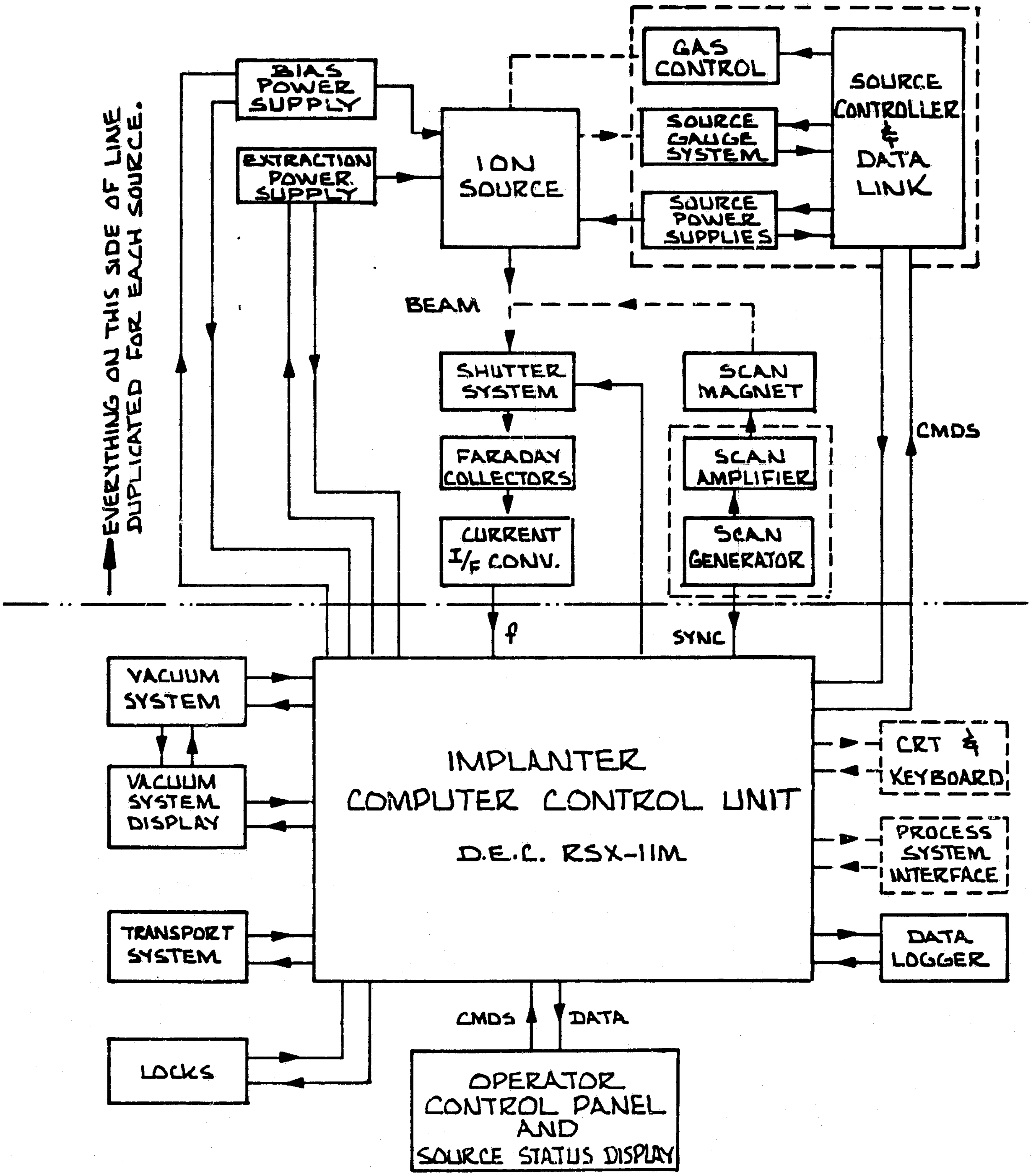

FIGURE 2-16. IMPLANTER CONTROL SYSTEM BLOCK DIAGRAM

Facility Requirements

Based upon the present design, the facility requirements for installation and operation of the prototype solar cell production implanter are as listed in Table 2-6. The size and weight of the solar cell implanter will be compatible with a typical semiconductor production area. The power, cooling, and other requirements will be met by standard industrial facilities. Overall dimensions are given in Figure 2-17.

2.1.5 Manufacturing Cost

Estimated costs to manufacture the solar cell production implanter in 1978 dollars are summarized in Table 2-7. Costing is based upon experience with present generation implanters which are much smaller, but more versatile and complex. Profit to be expected by the machine manufacturer is not indicated. Costs for units subsequent to the prototype model assume that at least 10 machines will be constructed over a period of several years, and engineering changes will be incorporated as a result of operational experience.

TABLE 2-6. FACILITY REQUIREMENTS FOR PROTOTYPE SOLAR CELL PRODUCTION IMPLANTER

Item	Requirement
Power	200 kVA, three-phase, four-wire, grounded neutral plus equipment ground
Water	5 kg/cm^2 (75 psig) maximum inlet pressure; 2.8 kg/cm^2 (40 psig) minimum differential pressure between inlet and outlet; flow rate 140 l/sec (35 gpm); Maximum inlet temperature 27°C (80°F)
Compressed Air	4.7 - 7 kg/cm^2 (60-100 psig) for pneumatic valves
Dry Nitrogen	1.9 l/sec (4 cfm) continuous flow at transport system entrance and exit
Ventilation	565 l/sec (1,200 cfm) exhaust
Site Preparation	For unit shown in Figure 2-17.

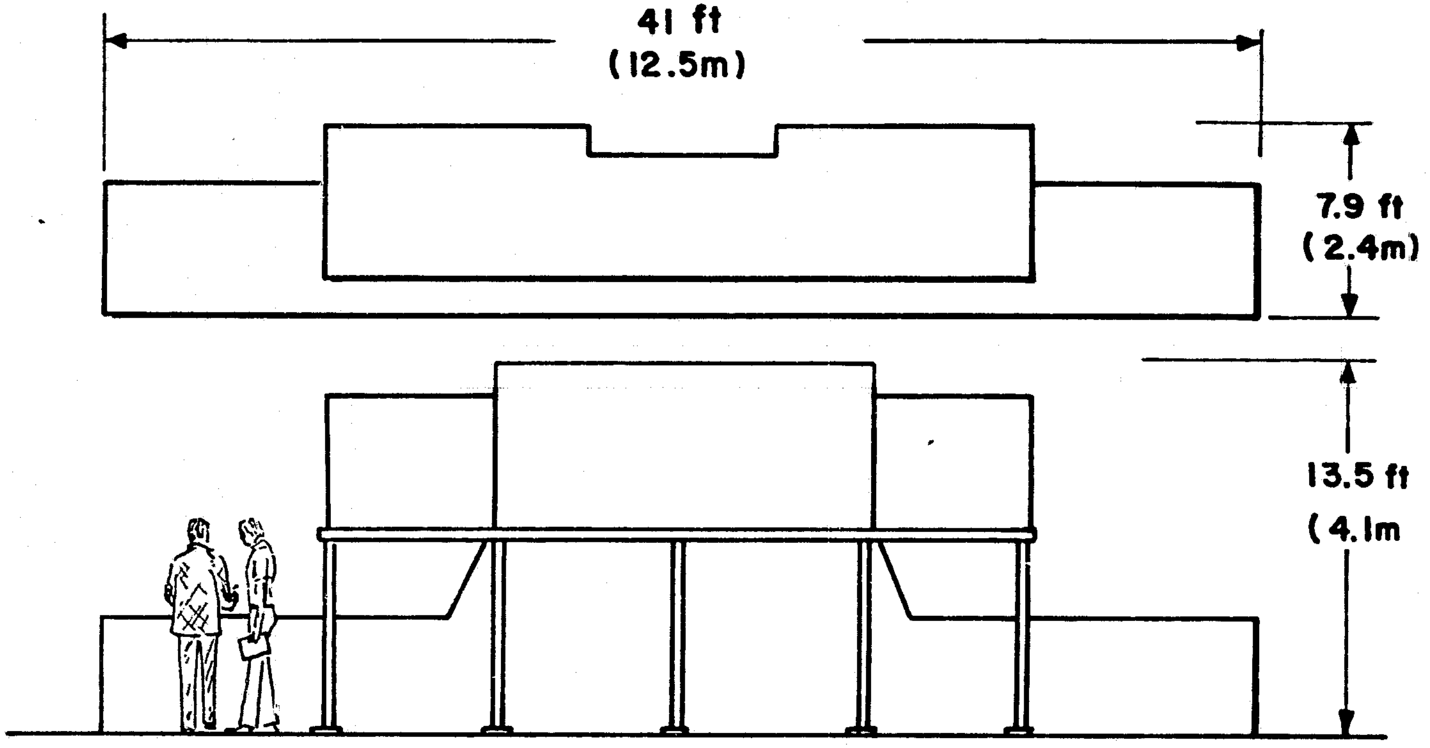

TOTAL WEIGHT : 23.5 TONS (21,000 kg)
MAGNET WEIGHT: 10 TONS (9,070 kg)

FIGURE 2-17. FACILITY REQUIREMENTS AND OVERALL DIMENSIONS FOR AN AUTOMATED PRODUCTION IMPLANTER

TABLE 2-7. ESTIMATED MANUFACTURING COSTS OF SOLAR CELL PRODUCTION IMPLANTERS

			Cost (1978 $)	
	Item		Prototype Unit	Subsequent Units
1.	Construction Management		$ 100,000	$ 10,000
2.	Engineering		400,000	38,000
3.	Documentation		(Included in item 2)	14,000
4.	Material and Subassembly Labor			
	- Control Console	18,000		
	- Entrance and Exit Vacuum Assembly	197,000		
	- Analyzing Magnet	78,000		
	- Magnet Power Supply	129,000		
	- Ion Sources	20,000		
	- Implanter Vacuum Chamber	107,000		
	- Diffusion Pumps	15,000		
	- Mechanical Pumps	8,000		
	- Miscellaneous	18,000		
	Subtotal		590,000	400,000
5.	Other Manufacturing Costs		59,000	40,000
6.	Assembly on Site		32,000	20,000
7.	Test and Qualification		40,000	20,000
8.	Software Development		60,000	10,000
	Totals		$1,281,000	$552,000

2.2 SOLAR CELL DEVELOPMENT

2.2.1 Background

To assess the technical status of ion implantation for silicon solar cells and to integrate implantation processing into a simplified, automated production process for the highest efficiency cells, the following tasks were performed under this contract:

1. Improvement of cell design, structure, and performance using implantation for n^+ and p^+ dopant introduction.
2. Assessment of the relative performance of otherwise identical cells with diffused and ion implanted junctions.
3. Integration of high-performance cell structures into an abbreviated implantation/ pulse energy processing sequence being developed for low-ccst, automated production.

2.2.2 Ion Implantation Parameter Selection

To utilize ion implantation in manufacturing solar cells, process parameters must be selected for both junction and back surface field layers. These parameters include ion species, ion dose, ion energy, beam current, angle of incidence, substrate temperature, and dose uniformity both wafer to wafer and within the wafer.

Junction Layer for n^+/pp^+ Structures

Selection of implant parameters for junction introduction is one of the critical design elements for high efficiency solar cells. The parameters are interdependent with subsequent annealing processes and contact grid design. Because implant parameters are flexible, both concentration and dopant location can be easily controlled; however, implanted dopant profiles are quite different from the theoretical predictions for low-energy ions in crystalline materials.

Desirable characteristics of a solar cell junction layer are quite well known. These are summarized below:

1. A relatively shallow junction is necessary for good blue response. Typically, the desired junction depth is from 0.1 to 0.3 micrometers for highest efficiency. Either phosphorus ($^{31}P^+$) or arsenic ($^{75}As^+$) can be used as an

n-type dopant with implantation. Arsenic has an inherent advantage over phosphorus for producing shallow junctions because its larger atomic size results in less penetration. However, more experimental effort has been carried out to date with phosphorus implantation, in part because successful annealing of the implantation damage has been achieved.

2. The peak dopant concentration should fall continuously from the surface. In practice, this is quite difficult to accomplish without using oxide or nitride layers as preabsorbers. However, these layers can result in knock-on oxygen or nitrogen implants. Furthermore, the use of an absorber increases the implant dose required and reduces implanter throughput.

3. Retrograde fields in depth must be avoided. It is necessary to minimize the channeling of ions along crystal axis which can produce a second peak in the implanted/annealed dopant profile. Reduction of channeling is achieved by intentionally misaligning the ion beam and the silicon wafer by 7 to 15°.

Back Surface Field Layer for n^+/pp^+ Structures

Selection of implant parameters for back surface layers depends upon the solar cell design requirements. For silicon with resistivities greater than 10 ohm-cm and with high minority carrier lifetime, the p^+ layer can act as a high-low junction or back surface field (BSF). For lower lifetime silicon of 1.0 ohm-cm resistivity, the p^+ layer only provides a heavily doped layer for ohmic contacts.

Choice of the implanted p^+ ion species depends on its intended function. For BSF's, either $^{11}B^+$ or $^{27}Al^+$ ions are effective with proper annealing procedures. For simple ohmic contact $^{11}B^+$, $^{27}Al^+$, or $^{49}BF_2^+$ can be used. The advantage of $^{49}BF_2^+$ molecular ions is that higher beam currents and therefore higher throughputs can be realized.

Because the depth of implanted ions and the p-p^+ junction location does not necessarily have to be shallow in this case, higher ion energies have been used. However, as with junction implants, channeling must be avoided to prevent retrograde electric fields. A second requirement is the desirability to maintain the peak dopant level at or near the back surface. Both channeling and surface dead layers due to retrograde fields can be minimized by selecting a relatively high anneal temperature which redistributes the implanted boron ions by diffusion.

Boron implants for p^+ back surface fields have been successfully included in high efficiency cell structures. The back surface field effect was first demonstrated under this program by the use of boron ion implantation and furnace annealing. Back surface field effects, after optimized furnace annealing of boron implants, increase V_{oc} from 550 mV to 600 mV. Pulse-annealed, boron-implanted back surface fields have also been demonstrated to be effective in increasing the V_{oc} of 10-ohm-cm, crucible grown silicon substrates from 550 mV to 570 mV. 5×10^{15} cm^{-2} boron ions were implanted at 25 keV into the back surface of each wafer. The implants were then pulse-annealed using a fluence of approximately 0.3 cal/cm^2 for a 0.1-microsecond, pulsed electron beam.

2.2.3 Junction Contact Design

Ion implantation provides good control of dopant density and hence sheet resistance of the junction layers. The cell structure design must include contacts which are optimized for the junction formation process being utilized — which in our case was implantation — with a given sheet resistance. Preliminary anneal test matrix results showed that for high-dose, low energy implants, the junction would have a sheet resistance of 50-ohms/square when most of the implant was electrically activated. Our grid design was then based on a 50-ohm/square layer which has a metallurgical junction depth of 0.28-micron. For evaluation of implantation, evaporated TiPdAg was selected because of its proven stability and its characteristically narrow line widths. Work by other LSA contractors has been focused on thick-film Ag contact application to implanted junctions; however, thick-film contacts generally require high temperature sintering to lower the bulk silver conductivity and shunting of the junction occurs due to Si:Ag reactions. Significant development of thick-film metallizations is required before this contact system can be applied to shallow, relatively high sheet resistance junctions.

The sheet resistance of an implanted phosphorus layer can be arbitrarily reduced by increased implant dose ($ions/cm^2$), but implanter throughput must then be traded off with implant dose. As can be calculated from the data in Table 2-2, doses of 2.5×10^{15} require 2.6 mA of phosphorus ion to process at a rate of 300 wafers per hour. Any change in implant dose will decrease the machine's throughput linearly.

The remainder of this section presents the analysis used to optimize TiPdAg contacts for implanted junction layers which were then annealed by pulsed electron beams and by furnace processing.

The losses of cell power output due to the front contacts can be assumed to result from four sources:

1. Shadowing of cell area by metal
2. Resistive losses in line and buss grids
3. Sheet resistance losses on the silicon front surface implanted layer
4. Contact resistance

For simplicity, the cross section of a contact grid line is assumed to be ohmic. Most patterns can be analyzed by conceptually breaking them down into many simple geometries, and summing the losses from each of these units to find the loss for the whole cell(4). The simplest such geometry, the rectangular unit, is shown in Figure 2-18. Other simple units may be triangular or trapezoidal.

For analysis, power loss due to resistance is taken to be I_2R, integrated over the appropriate area(5,6). For example, in the case of the rectangular unit:

P_r = Power loss due to resistance in the line

$$= \int I^2 \, dR$$

$$dR = \rho_m \frac{dx}{WT}$$

so

$$P_r = \frac{I_o^{\,2} \rho_m D^2 L^3}{3\, WT}$$

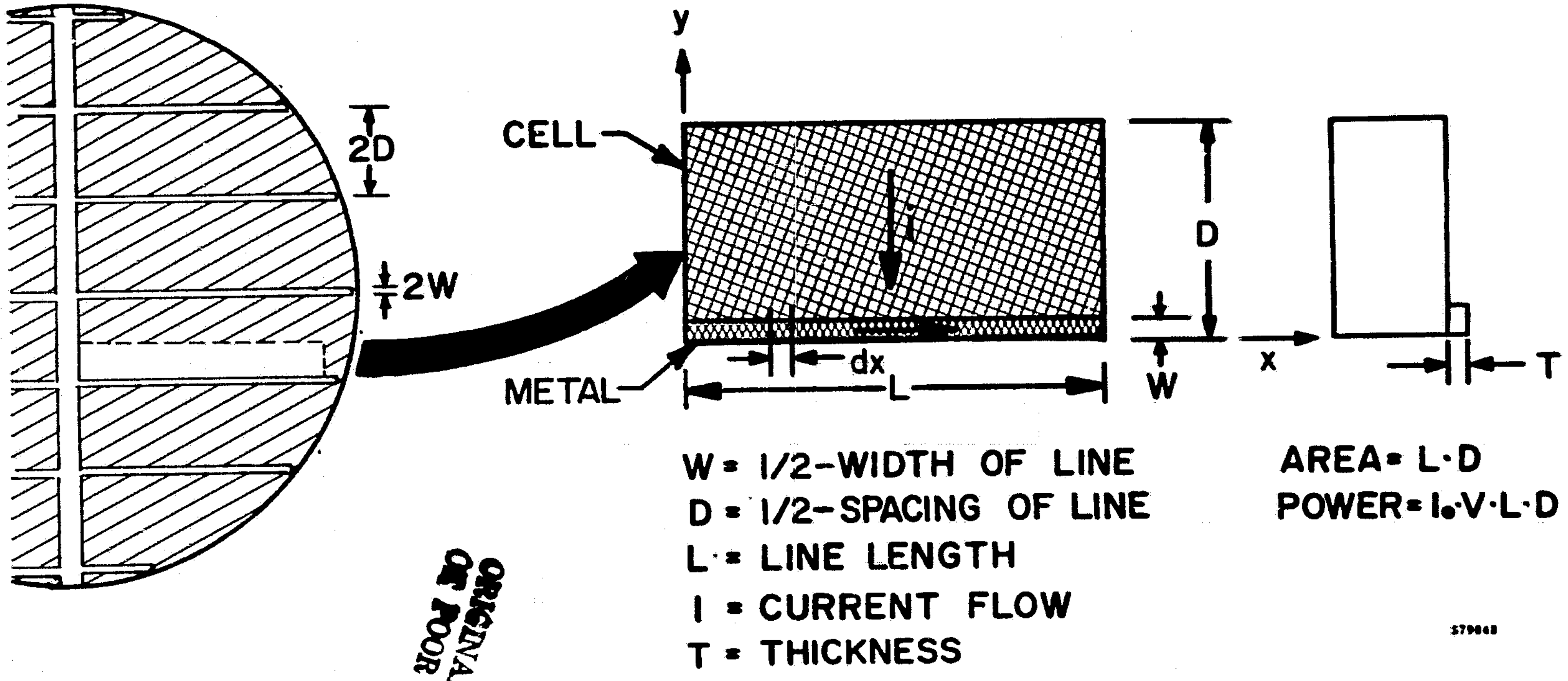

FIGURE 2-18. GENERALIZED RECTANGULAR GEOMETRY UNIT CELL

P_o = Power loss due to sheet resistance

$$= \int_A I^2 \, dR$$

$$dR = R_{sh} \frac{dy}{dx}$$

$$dI = I_o y \, dx \qquad \text{(current assumed to flow perpendicularly to contact)}$$

$$P_i = 1/3 \; R_{sh} \; I_o^2 D^3 L$$

P_c = Power loss due to contact resistance

$$= \frac{I_o{}^2 R_c D^2 L}{W}$$

To find the losses as a fraction of total possible power from this area, divide by the total power, $I_o VLD$. To this must be added the fractional loss due to shadowing:

P_s = Fractional loss due to shadowing = W/D

To find the total fractional power loss:

$$\overline{P}_s = \frac{I_o \; DL^2 \; \rho_m}{3 \; WTV} + \frac{R_{SH} \; I_o \; D^2}{3V} + \frac{I_o \; R_c \; D}{WV} + \frac{W}{D}$$

where:

I = current flow
W = half-width of line
L = line length
D = half-spacing of line
ρ_m = metallization resistivity in ohm-cm
R_{SH} = implanted layer sheet resistivity in ohm/square
R_c = contact resistance in ohm-cm^2 (assumed ohmic)
V = operating voltage
I_o = operating current production density in A/cm^2
T = metallization thickness

Several linearizing assumptions are made regarding the independence of the operating point on grid pattern. As long as power loss in the contact is low, which is true for any case likely to be considered, these assumptions will not affect the results. It is possible to reduce metal-to-silicon contact resistance to low levels by the proper choice of contact metals and sintering cycle, so contact resistance has been assumed to be negligible for grid configuration analysis.

Note that if the line half-width and spacing could both be decreased while metal thickness is held constant, the total losses would uniformly decrease. This implies that the metallization lines should be designed as thin as the appropriate technology allows. In fact, since metal thickness cannot be much larger than line width, extremely thin lines are not practical. As indicated in Figure 2-19, this constraint added, lines of width less than about 15 micrometers prove to lose efficiency. The initial cell grid pattern selected is based on a total line width of 35 micrometers.

Since loss is also directly dependent on line length, loss can be minimized by lowering the length. This is done by increasing the number of output terminals. The advantage of adding output terminals levels out at around three to four terminals. Four terminals have been selected for the designs used in this program.

A computer program was written to calculate the power losses of various metallization patterns using the approach outlined above. Line spacings were optimized while other parameters were held constant. This program was used both the design optimum grid patterns, and to graph the effects of variations in cell process parameters (such as line width and sheet resistivity) as an aid in cell design.

Several different grid patterns were analyzed for this study. In order to take maximum advantage of very narrow line widths, patterns were designed specifically to reduce the distance traveled along the line to an output terminal. This permits extremely narrow lines to be used without excess loss due to resistance. Figure 2-20 shows one solar cell with the Spire "Starburst" contact pattern selected for use on 3-inch-diameter implanted cells. Total power losses by the contact grid (shadow and resistive) are predicted to be slightly less than 5 percent.

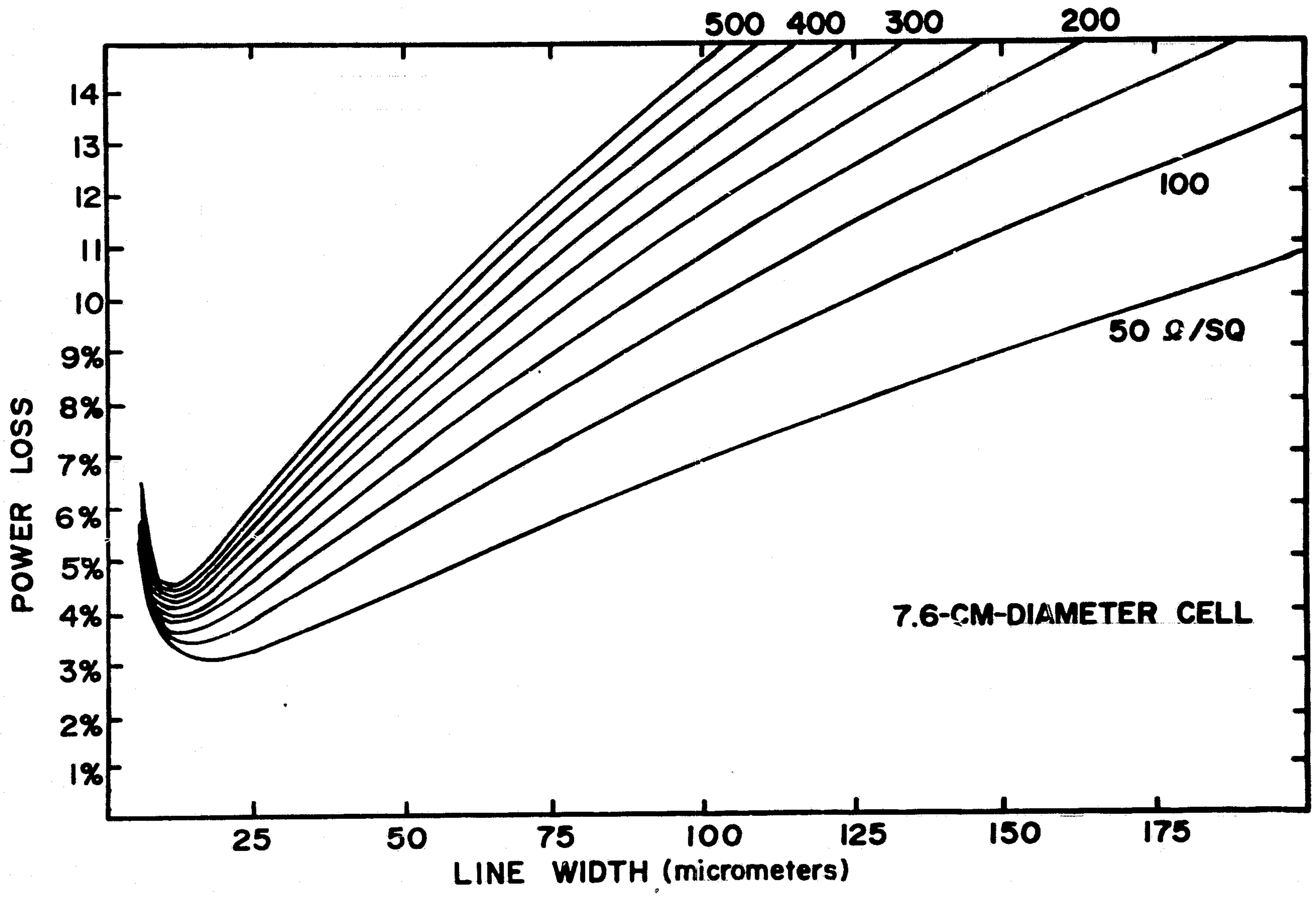

FIGURE 2-19. PERCENT OF TOTAL CELL POWER LOST BY RESISTANCE AND SHADOWING VERSUS LINE WIDTH FOR SEVERAL SHEET RESISTANCES

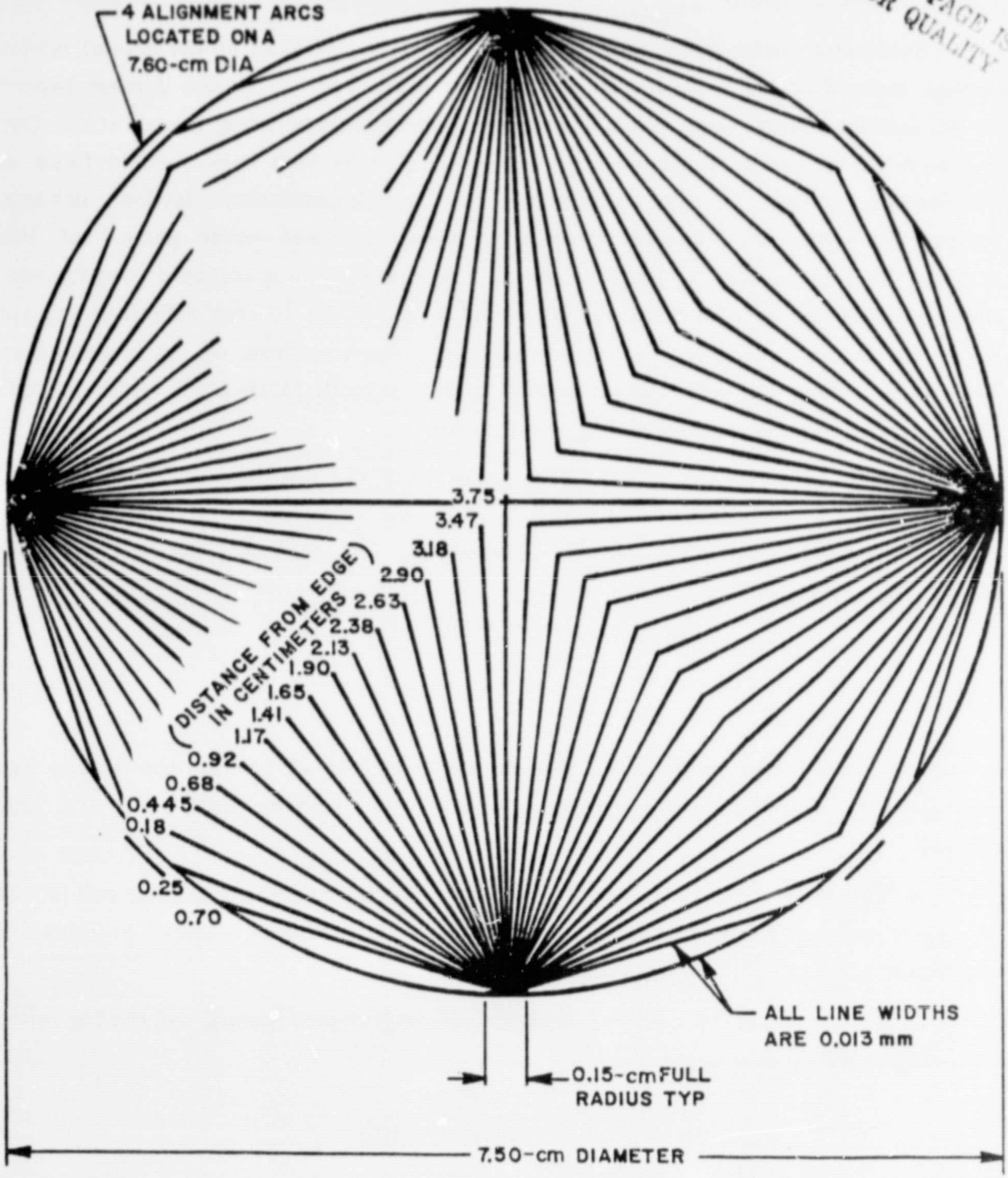

FIGURE 2-20. OPTIMIZED FRONT CONTACT METALLIZATION PATTERN FOR 7.6-cm CELLS (R_{sh} = 50 ohms/square)

2.2.4 Furnace Annealing

Successful device optimization requires adequate annealing of the crystal lattice damage induced by ion implantation. The characteristics of the lattice damage depend on the implant energy, dose, and temperature of the substrate during implantation. One key element in manufacturing high-efficiency solar cells with back surface fields in Czochralski silicon is the annealing of ion implantation lattice damage. Performance-optimized annealing procedures were developed under phase I of this contract for simultaneous n^+ junction and p^+ BSF annealing in a standard tube furnace. However, these procedures were not optimized with respect to cost effectiveness, but rather for demonstrating high-efficiency solar cell manufacturing by ion implantation. For example, cells with efficiencies as high as 16.5 percent (AM1-28°C) were produced using the very long anneal schedule described below.

The objective of the effort under phase II of the contract was to reduce the process time at temperature while maintaining cell efficiency. For reference, the performance-optimized anneal process element was specified and verified by other contractors as follows:

2 hours - 550°C
15 minutes - 850°C
2 hours - 550°C

A furnace temperature programmer was not used, so that all heating and cooling was rapid and typical of the manual transfer of quartz wafer holders into and out of a tube furnace.

A furnace anneal matrix was designed and utilized for processing solar cell lots of 20 wafers each. The test matrix for furnace anneal optimization is shown in Table 2-8 and Figure 2-21.

Cycle 4 in Table 2-8 refers to temperature-programmed heating and cooling rates; the cycle is defined as follows:

1. 550°C - 1 hour (solid phase epitaxial regrowth)
2. Heated at 13.6°C/min to 850°C
3. 850°C - 15 min (activation of implanted species to substitutional lattice sites)
4. Cool at 3.3°C/min to 550°C
5. 550°C - 1 hour (lifetime enhancement)

TABLE 2-8. FURNACE ANNEAL SCHEDULES FOR IMPLANT ANNEAL OPTIMIZATION

Lot No.	Anneal Cycle	Time at Temperature (minutes) 550°C	850°C	550°C	Total Time
1754	Standard	120	15	120	225
1755	1	0	15	120	135
1756	2	0	15	60	75
1757	3	0	15	0	15
1758	4	ramp	ramp	60	272
1910	5	0	15	30	45
1826	6	60	15	60	135
1825	7	60	15	0	75

Cycle 5 in Table 2-8 refers to a commercial belt furnace commonly used for metal sintering processes with a hydrogen atmosphere. Belt furnaces can be designed and fabricated for large production rates with tantalum chambers and chain drives to minimize contamination by nonintentional dopants. Further discussion of the feasibility and economics of belt furnace annealing is included in Section 3 which presents a SAMIS analysis of each anneal cycle.

The starting silicon material for this furnace anneal test matrix was characterized as follows:

Specification	Range
Resistivity:	10 ohm-cm and 1 ohm-cm ±25%
Diameter:	7.62 cm
Thickness:	300 micrometers ±10%
Orientation:	(100)
Surfaces:	Etched to remove saw damage
Growth:	Czochralski
Type:	p-Boron doped

All the material was processed as shown in Table 2-9.

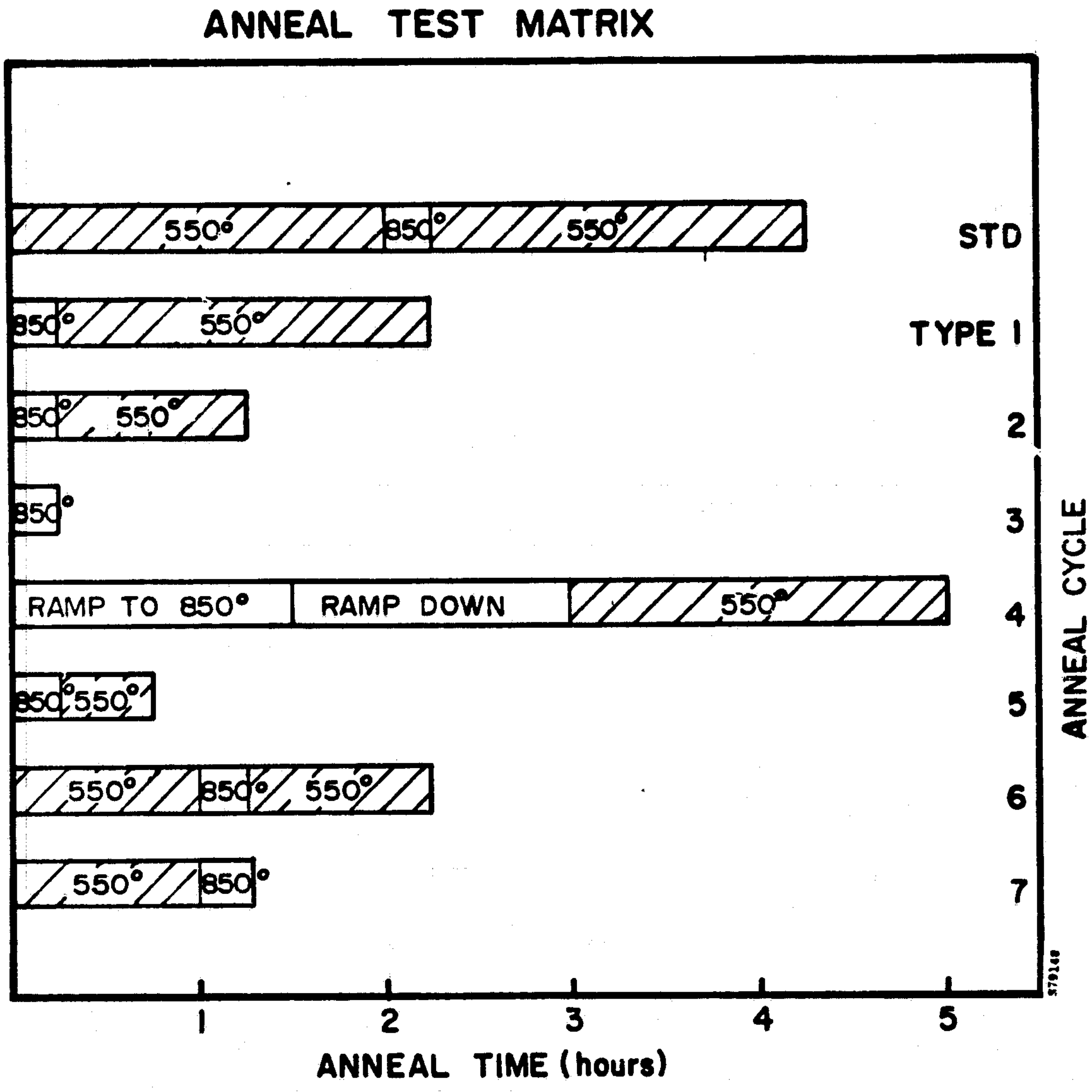

FIGURE 2-21. FURNACE CYCLES SELECTED FOR COST-PERFORMANCE OPTIMIZATION FOR ION IMPLANTATION ANNEALING (Note: All temperatures shown are °C)

TABLE 2-9. PROCESS SEQUENCE FOR ION-IMPLANTED, n^+/pp^+, HIGH-EFFICIENCY SOLAR CELLS

Silicon Material	10-ohm-cm, (100), CZ, p-type, 300 micrometers thick, flash etched
<u>Process Sequence</u>	
Implant:	Junction - 2 x 10^{15} $^{31}P^+$ cm^{-2}, 10 keV, 10° Back surface field - 5 x 10^{15} $^{11}B^+$ cm^{-2}, 25 keV, 10°
Implant Uniformity:	No worse than ±10 percent across wafer Approximately ±1 percent wafer to wafer
Anneal:	Simultaneous phosphorus and boron implant anneal in nitrogen (see Table 2-8 for process specifications)
Clean:	Buffered HF Deionized water rinse
Front Metallization:	Evaporate 400A Ti + 400A Pd + 1,000 Ag Define Spire Starburst pattern with standard Kodak KTFR process Electroplate 12 micrometers of Ag
Clean:	Buffered HF Deionized water rinse
Back Metallization:	Evaporate 400A Ti + 400A Pd + 1 micrometer of Ag
AR Coating:	Evaporate 700A TiO_2
Sinter:	400°C - 10 minutes in nitrogen
Test:	AM1 I-V and spectral response

The results of the anneal matrix are shown in Table 2-10 for 10-ohm-cm Czochralski silicon. These experiments have shown that significant time can be saved in furnace anneal process requirements with no average performance loss. Specifically, the Type 2 anneal, which consists of 15 minutes at 800°C followed by 60 minutes at 550°C, is as effective as the 255-minute baseline process. The results, which are summarized in Tables 2-10, 2-11, and 2-12, show that high-efficiency cells are obtainable with 10-ohm-cm silicon when processed with ion-implanted junctions and BSF's. The BSF increases open-circuit voltage of cells processed with 10-ohm-cm material from 550 mV typical of 10-ohm-cm material to 585 mV. Both absolute spectral response and external quantum efficiency are shown for each anneal type in Figures 2-22 and 2-23.

2.2.5 Belt Furnace Hardware

As described in Section 2.2.4, an anneal test matrix was designed and carried out to develop a more cost-effective furnace annealing cycle for solar cell manufacturing. Belt furnaces with in-line material transport are now commonly used in the thick-film hybrid circuit industry for sintering noble metals in hydrogen/nitrogen atmospheres. Experiments have been conducted to determine if:

1. Solar cell performance can be maintained in a belt furnace.
2. The use of cracked ammonia or hydrogen atmosphere in the belt furnace can eliminate the need for HF etching to remove oxides normally found in nitrogen atmosphere annealing.

Cost estimates for belt furnaces with throughputs of 50 and 125 cm^2/sec have been prepared. The furnace for implant annealing is designed to reproduce closely the 850°C - 15 minute plus 550°C - 60 minute cycle now being used at Spire for tube furnace annealing. An outline drawing of a 125 cm^2/sec belt furnace is shown in Figure 2-24. In each furnace, 4.3m is allowed for entrance and exit material-handling to eliminate oxygen and water vapor from the hot zone and to allow stacking of the silicon carbide, duramic, or other high-temperature carrier platens. As shown in Figure 2-24, two transport speeds are required. One transport system operates at 12 cm/sec for the initial transfer of the wafer carriers and for stacking the carriers into modules before entrance into the furnace hot zone. The modules, with dimensions of 20 x 20 x 20 cm, will contain 64 carriers each with a capacity of 400 cm^2 of silicon. Stacking the carriers into such

TABLE 2-10. AVERAGE PERFORMANCE CHARACTERISTICS FOR ION-IMPLANTED n^+/pp^+ SOLAR CELLS

			Average Performance					
			(AM0-25°C)					(AM1-28°C)
Lot No.	Anneal Cycle	Wafer Resistivity (ohm-cm)	V_{oc} (V)	I_{sc} (A)	FF	P_{max} (W)	Eff. (%)	Eff. (%)
1754	S	10	0.587 (0.2)	1.760 (1.5)	0.74 (3.1)	0.766 (3.8)	12.4	14.6
1755	1	10	0.585 (0.3)	1.753 (1.3)	0.74 (1.4)	0.761 (2.4)	12.3	14.6
1756	2	10	0.586 (0.3)	1.744 (1.4)	0.75 (1.3)	0.767 (1.8)	12.4	14.7
1757	3	10	0.579 (0.8)	1.703 (8.2)	0.69 (14)	0.682 (19)	11.1	13.0
1758	4	10	0.567 (0.2)	1.710 (2.5)	0.72 (10)	0.699 (13)	11.3	13.4
1910	5	10	0.581 (0.4)	1.709 (1.0)	0.74 (1.4)	0.738 (2.1)	12.0	14.1
1826	6	10	0.586 (0.4)	1.732 (1.9)	0.71 (2.8)	0.720 (4.3)	11.7	13.8
1825	7	10	0.585 (0.7)	1.741 (0.2)	0.73 (1.5)	0.743 (2.4)	12.0	14.2

Notes: Percent standard deviation is shown in parentheses (%).
Data represents average of 20 cells for each anneal cycle.

TABLE 2-11. ABSOLUTE SPECTRAL RESPONSE FOR ION-IMPLANTED n^+/pp^+ SOLAR CELLS

Lot No.	Anneal Cycle	Average Spectral Response (mA/mW)							
		450nm	500nm	600nm	700nm	800nm	900nm	950nm	1000nm
1754	S	0.190 (10.8)	0.271 (8.2)	0.375 (5.6)	0.439 (6.2)	0.482 (6.3)	0.508 (5.3)	0.493 (6.5)	0.326 (6.7)
1755	1	0.194 (10.1)	0.275 (7.9)	0.371 (4.2)	0.429 (4.2)	0.468 (4.3)	0.487 (4.7)	0.467 (6.3)	0.301 (8.2)
1756	2	0.183 (9.2)	0.266 (6.6)	0.372 (4.2)	0.434 (3.8)	0.473 (3.9)	0.496 (3.8)	0.473 (5.0)	0.307 (6.6)
1757	3	0.183 (22.2)	0.259 (19.1)	0.358 (16.8)	0.419 (17.2)	0.454 (17.7)	0.477 (16.0)	0.465 (15.0)	0.311 (11.6)
1758	4	0.173 (10.7)	0.256 (9.4)	0.374 (4.1)	0.451 (3.2)	0.496 (4.2)	0.520 (3.6)	0.499 (4.7)	0.319 (5.2)
1910	5	0.183 (9.2)	0.266 (6.6)	0.372 (4.2)	0.434 (3.8)	0.473 (3.9)	0.496 (3.8)	0.473 (5.0)	0.307 (6.6)
1826	6	0.147 (13.5)	0.216 (12.7)	0.323 (10.2)	0.398 (7.6)	0.448 (6.5)	0.469 (5.6)	0.456 (7.2)	0.305 (8.6)
1825	7	0.182 (22.3)	0.256 (20.9)	0.341 (20.2)	0.391 (19.8)	0.426 (19.5)	0.440 (19.2)	0.422 (19.5)	0.277 (19.9)

Notes: Percent standard deviation is shown in parentheses (%).
Data represents average of 20 cells for each anneal cycle.

TABLE 2-12. EXTERNAL QUANTUM EFFICIENCY FOR ION-IMPLANTED n^+/pp^+ SOLAR CELLS

Lot No.	Anneal Cycle	External Quantum Efficiency (carriers collected/photon) 450nm	500nm	600nm	700nm	800nm	900nm	950nm	1000nm
1754	S	0.524	0.672	0.775	0.778	0.747	0.700	0.643	0.404
1755	1	0.535	0.682	0.768	0.760	0.725	0.671	0.610	0.373
1756	2	0.504	0.650	0.767	0.783	0.753	0.701	0.634	0.384
1757	3	0.504	0.642	0.740	0.742	0.704	0.657	0.607	0.386
1758	4	0.477	0.635	0.773	0.799	0.769	0.716	0.651	0.396
1910	5	0.504	0.660	0.769	0.769	0.773	0.683	0.617	0.381
1826	6	0.405	0.536	0.668	0.705	0.694	0.646	0.595	0.378
1825	7	0.502	0.635	0.705	0.693	0.660	0.606	0.551	0.343

modules is required to minimize the overall length of the belt furnace. The second transport system within the hot zone of the furnace operates at 0.2 cm/sec for a total time of 75 minutes. The load on the furnace heating elements will be 48 lb/linear ft, typical of existing furnace conveyors. Major system parameters for a 125 cm^2/sec belt furnace are outlined in Table 2-13.

Discussions with several belt furnace manufacturers have shown that Duramic and Al_2O_3 carriers have been used in semiconductor processing. The carriers have been utilized to prevent contamination of the silicon wafers from the belts. One manufacturer is also working on automatic handlers which allow integration of wafers such that they are loaded onto alumina carriers before loading into the furnace. The only problem identified to date is possible sodium contamination of the aluminaboats; but this could be eliminated by careful specification of the ceramic material. A possible sequence is given in Table 2-14 and shown diagrammatically in Figure 2-25.

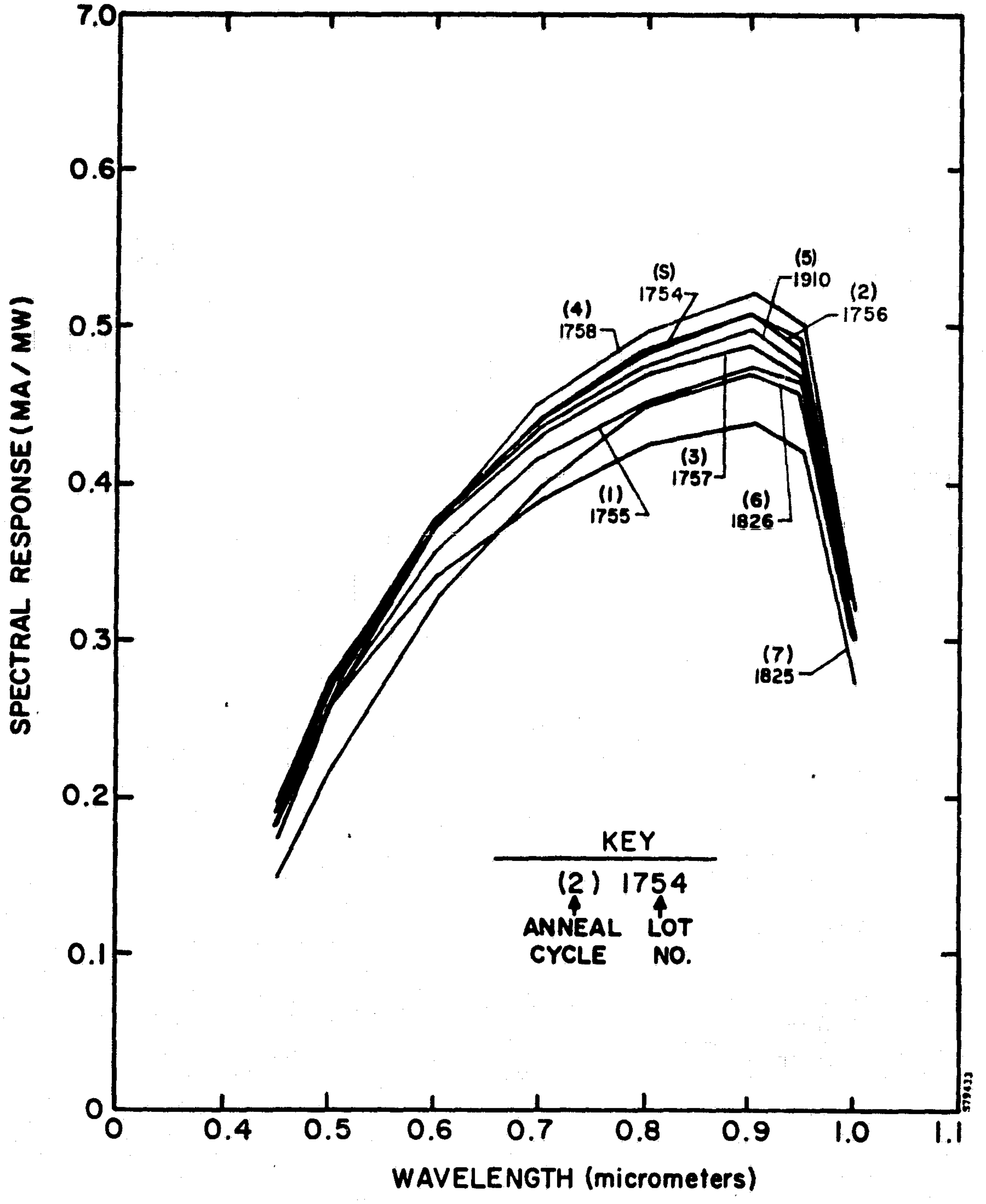

FIGURE 2-22. ABSOLUTE SPECTRAL RESPONSE FOR IMPLANT ANNEAL TEST MATRIX

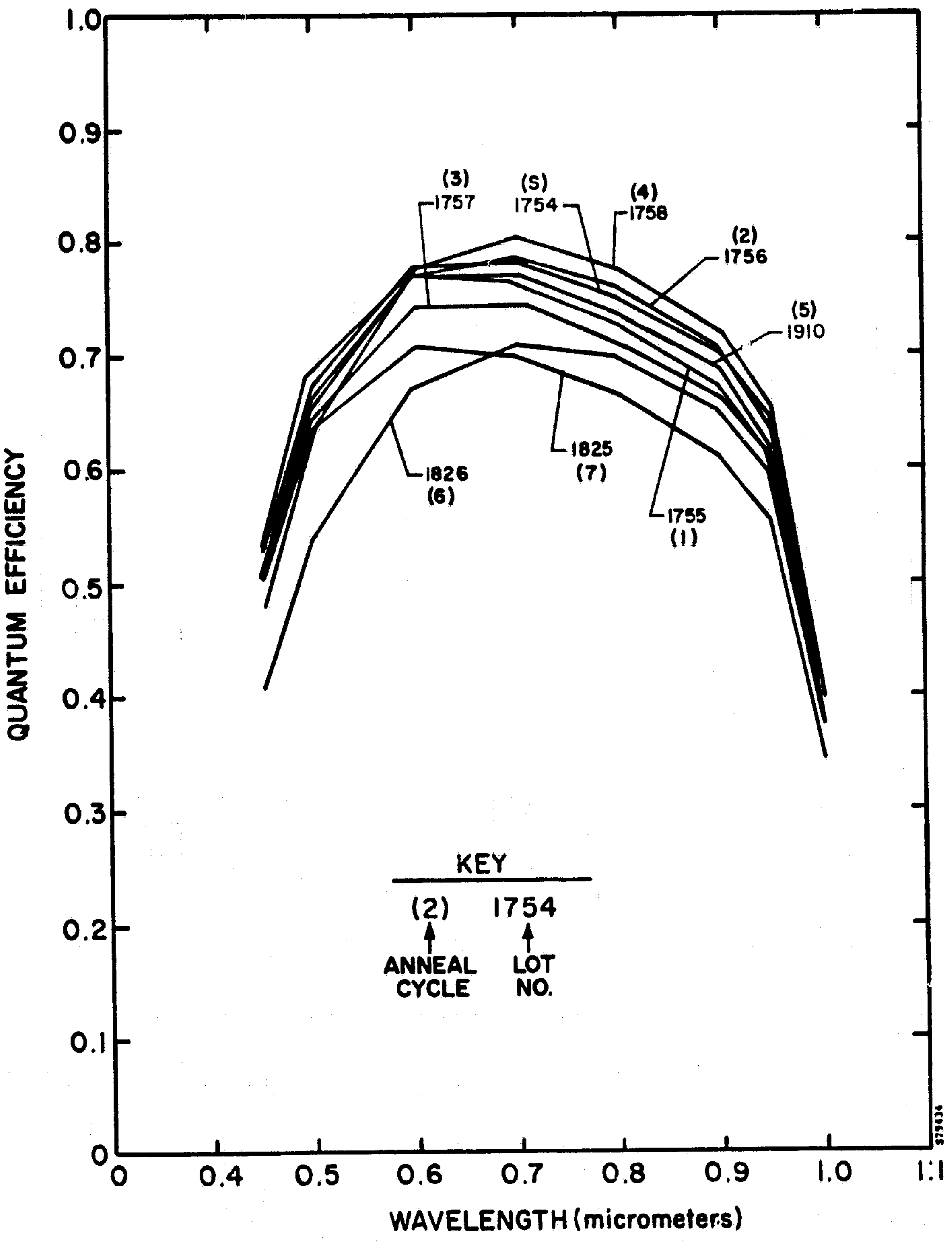

FIGURE 2-23. EXTERNAL QUANTUM EFFICIENCY FOR IMPLANT ANNEAL TEST MATRIX

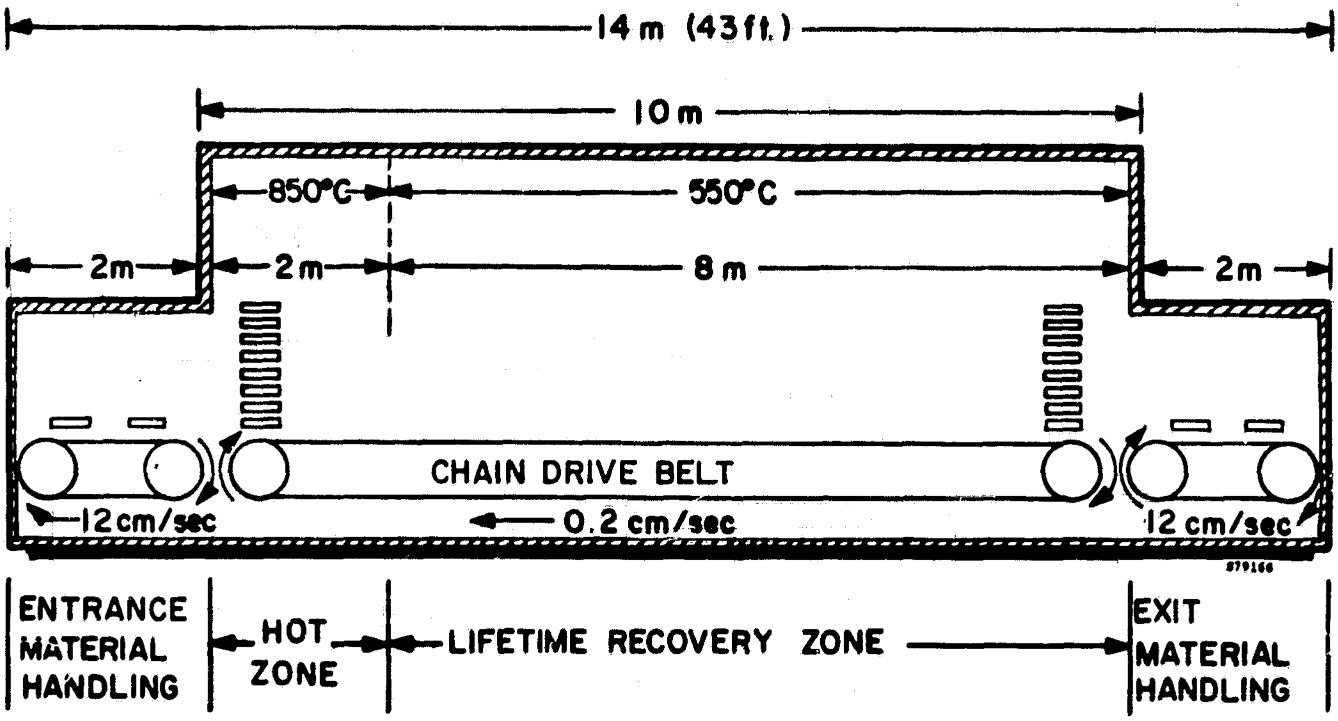

FIGURE 2-24. SCHEMATIC FOR 125 cm^2/sec BELT FURNACE FOR IMPLANT ANNEALING

TABLE 2-13. FUNCTIONAL REQUIREMENTS FOR 125 cm^2/sec BELT FURNACE FOR IMPLANT ANNEALING

Item	Specification
Belt width:	63 cm
Belt speed:	0.2 cm/sec (loading)
Silicon carrier size:	20 x 20 x 0.3 cm thick
Module size:	20 x 20 x 20 cm (64 carriers/module)
Carrier material:	Silicon carbide, duramic, or equivalent
Throughput:	125 cm^2/sec
Mass loading:	24 kg/linear meter

TABLE 2-14. SEQUENCE OF OPERATION FOR AUTOMATED BELT FURNACE ANNEALING

1. Dump wafers into machine cassette
2. Dump carriers into machine cassette
3. Integrate wafer/carrier (W/C)
4. Inject W/C into machine cassette
5. Transfer full cassettes to load
6. Eject W/C's together
7. Transfer W/C's to furnace belt
8. Shuttle full cassette into position
9. Exchange full and empty cassettes
   Reset shuttle by operator
10. Transfer W/C's off furnace belt and align
11. Inject W/C's into machine cassettes
12. Shuttle empty into position
13. Exchange full and empty cassettes
    Reset shuttle by operator
14. Transfer full cassettes to be segregated
15. Eject W/C to segregate station
16. Inject wafer to machine cassette
17. Inject carrier to machine cassette
18. Dump wafers into plastic cassette
19. Dump carriers into plastic cassette
20. Clean carriers in HF

Offline storage is possible between manual transfers.

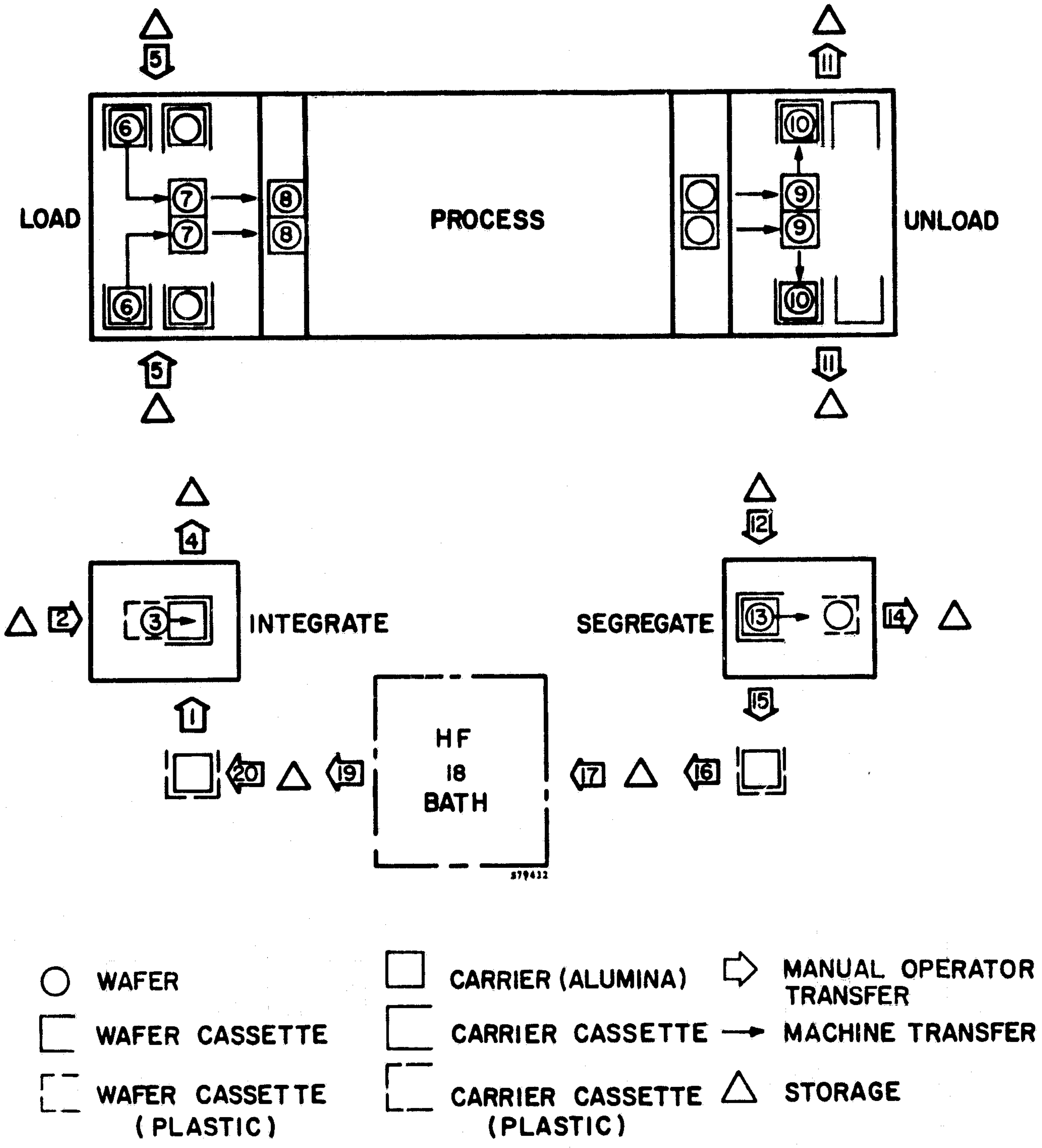

FIGURE 2-25. PROCESS SEQUENCE FOR AUTOMATED LOADING OF A BELT FURNACE FOR IMPLANT ANNEAL (Source: Watkins-Johnson)

2.2.6 Pulse Annealing

There are four general types of directed energy sources for annealing ion implantation lattice damage in semiconductors. Each has been at least demonstrated, some have been developed to the point of feasibility, but none of the methods has been optimized for application to semiconductor manufacturing. The four general types of directed energy sources are listed in Table 2-15 with some of their characteristics.

Under this contract, we have shown feasibility of pulsed electron beam annealing of wafers up to 7.6-cm (3-inch) diameter with a single pulse. Figure 2-26 shows the 7.6-cm diameter pulsed electron beam anneal signature on a 10-cm ion implanted wafer. We have also demonstrated pulsed laser annealing with anneal diameters up to 5.0 cm (2 inches) with a single pulse. Figures 2-27a and b show the annealed sheet resistance uniformities which were used as a figure of merit for each annealing process evaluated for this application.

As shown in Table 2-15, laser annealing did not produce junction layers with sheet resistances as low as the values typical of pulsed electron beam annealing. This may be due to less efficient energy coupling of the laser beam into the implanted silicon lattice. The measurements across the anneal signature are shown below:

Anneal Process	Anneal Energy	Typical Sheet Resistance (ohms/square)	Anneal Diameter (cm)
Furnace	850°C - 15 min	48 ± 8%	7.6
Pulsed Electron Beam	1.0 J/cm^2	38 ± 21%	7.6
Pulsed Nd:YAG Laser	2.6 J/cm^2	53 ± 13%	5.0
Pulsed Nd:YAG Laser	3.0 J/cm^2	50 ± 10%	5.0
Pulsed Nd:YAG Laser	3.3 J/cm^2	45 ± 10%	5.0

TABLE 2-15. DIRECTED ENERGY SOURCE CHARACTERISTICS

Characteristic	Source			
	Lasers		Electron Beam	
	Pulsed	Scanned	Pulsed	Scanned
1. Energy efficiency	low	low	high	high
2. Beam area	small	small	large	arbitrary
3. Beam optics	conventional	conventional	E-M difficult	E-M depends on current
4. Method of anneal	LPE SPE	SPE	LPE SPE	SPE
5. Rep. rate capability	Limited by Nd:YAG crystal heating	NA	good	NA
6. Typical beam energy	3.0 J/cm^2*	—	1.0 J/cm^2	—
7. Typical junction sheet resistance for 2.5×10^{15} $^{31}P^+$ implant	45 - 50 ohms/square	—	35 - 40 ohms/square	—

* Higher energy density is required for lasers than electron beam due to reflection losses and the energy coupling mechanism.

ORIGINAL PAGE IS
OF POOR QUALITY

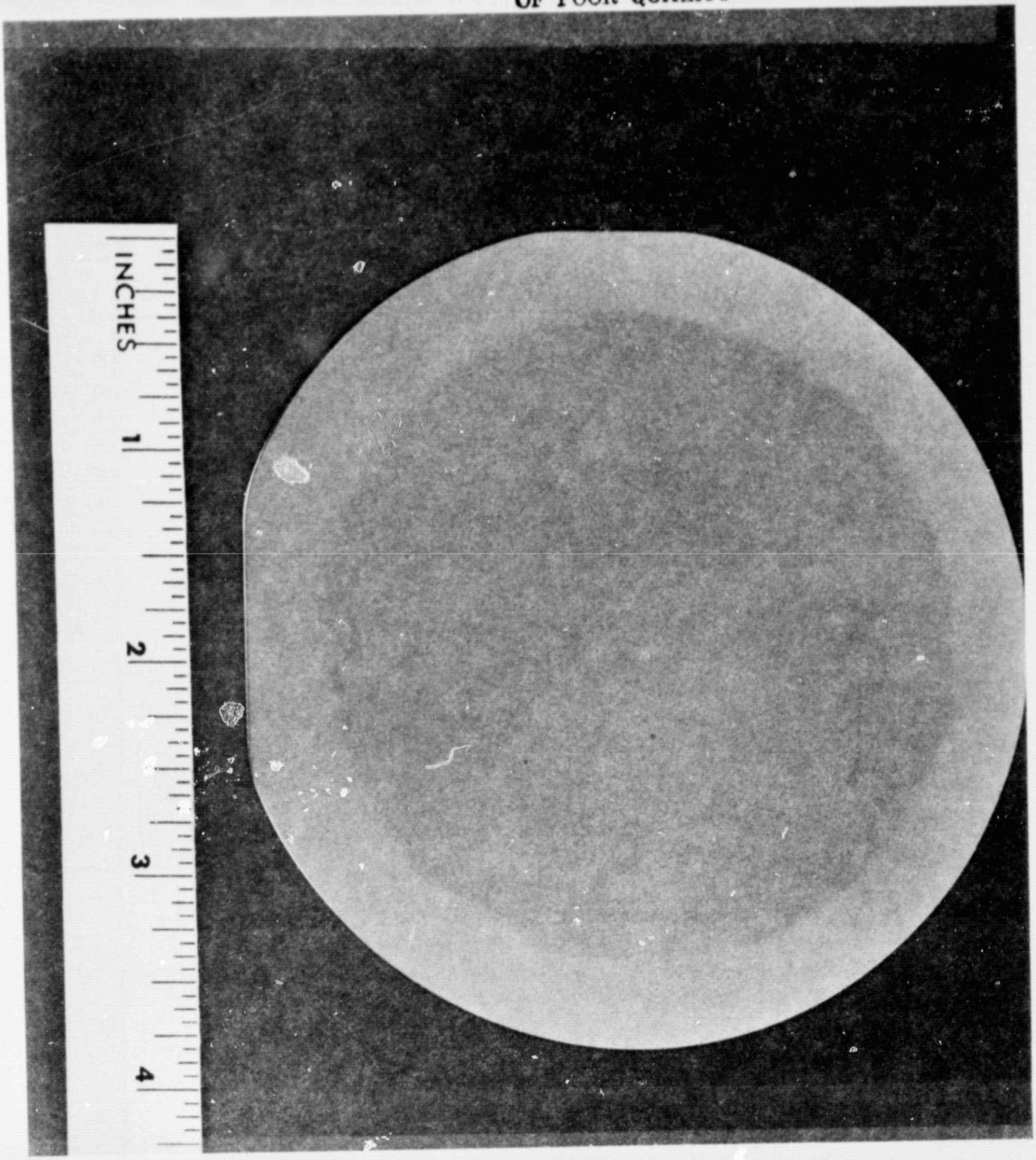

FIGURE 2-26. 7.6-cm PULSED ELECTRON BEAM SIGNATURE

SPIRE 06/22/79 ARSENIC RS

WAFER NO. 2055-6

AVERAGE R(SHEET)=34.5 OHMS/SQUARE

STD. DEV. = +/-3.73 RANGE =+/- 7.45 OHMS/SQUARE

IMPLANT CONDITIONS-

TILT= 7 ENERGY= 25KEV

ANNEAL SPEC- PEBA 280

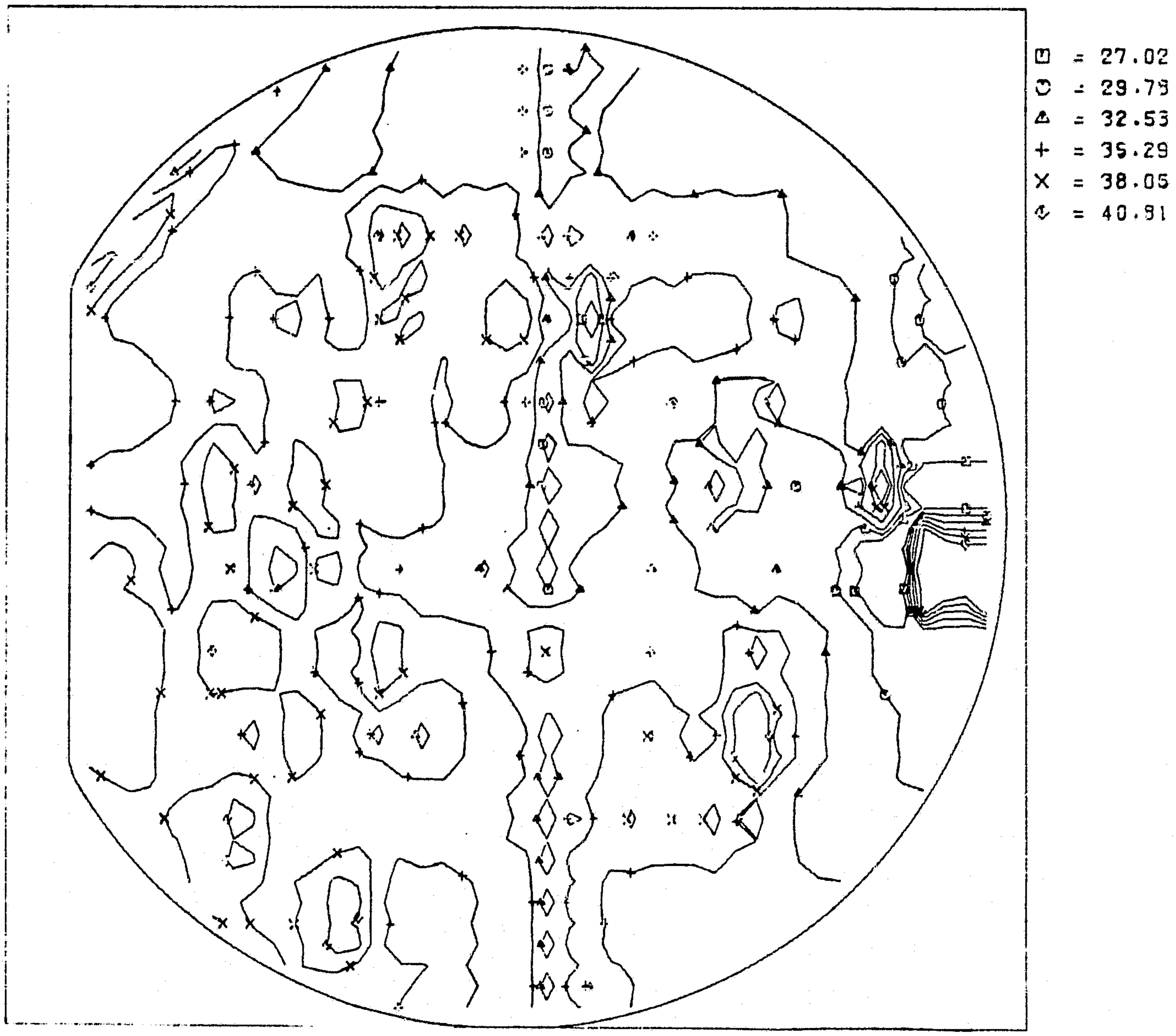

FIGURE 2-27a. SHEET RESISTANCE CONTOUR MAP FOR ION-IMPLANTED/PULSED ELECTRON BEAM ANNEALED (SINGLE-PULSE) JUNCTION

SPIRE 05/29/79 PHOSPHOROUS

WAFER NO. 2030-3 1.2 PERCENT

AVERAGE R(SHEET)=48.5 OHMS/SQUARE

STD. DEV. = +/-2.56 RANGE =+/- 5.13 OHMS/SQUARE

IMPLANT CONDITIONS-

TILT=10 ENERGY= 10KEV FLUENCE=2.50E15 /CM2

IMPLANT SPEC- ANNEAL SPEC- LASER

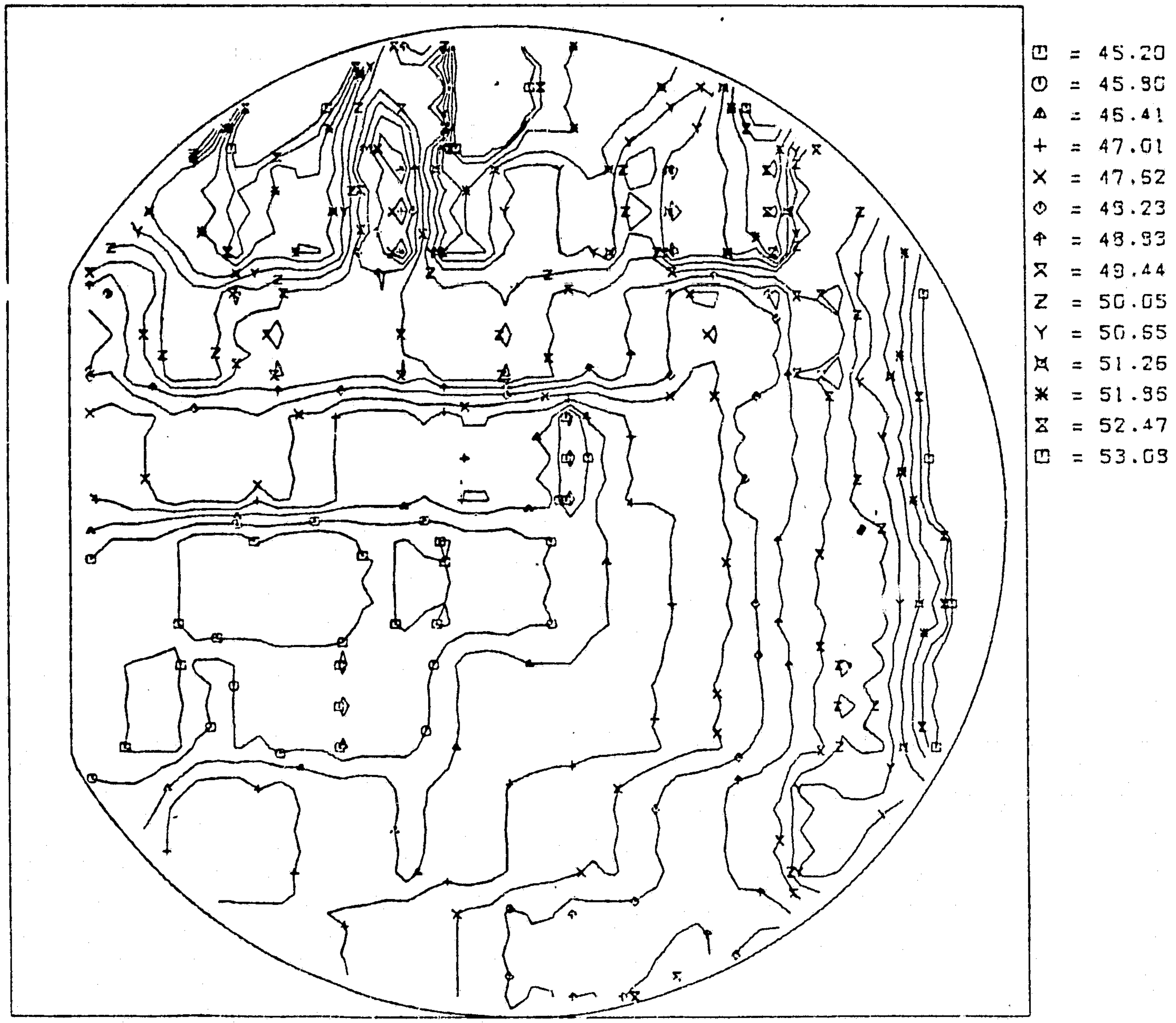

FIGURE 2-27b. SHEET RESISTANCE CONTOUR MAP FOR ION-IMPLANTED/LASER ANNEALED (SINGLE-PULSE) JUNCTION ON 5-cm WAFERS

An evaluation of directed energy sources was conducted by using both pulsed lasers and pulsed electron beams to anneal junction implants in solar cells. A schematic of the processing is shown in Figure 2-28. All back surface fields were implanted and then furnace annealed prior to implantation of the junction layer. As outlined in the processing schematic, two lasers were used. One laser was a Quantronix System and the other was unidentified. Spire Corporation performed the electron beam annealing and the furnace annealing of the control slices. All of the wafers were then shipped to Optical Coating Laboratory Inc. (OCLI) for TiPdAg contacts, AR coatings, and AM0 measurements.

The results of this annealing process test matrix are summarized in Tables 2-16, 2-17, and 2-18. The general trends were as follows:

1. Furnace annealing resulted in highest peak and average short-circuit current, open-circuit voltage and fill-factor.
2. Pulsed electron beam annealing resulted in better short-circuit current and open circuit voltage when compared with laser annealing. This may be due to better activation of the implanted phosphorus.
3. Pulsed laser annealing yielded better fill-factors than pulsed electron beam annealing. This effect may be related to fewer residual defects in the solar cell junction depletion layer.
4. Typical spectral response for each of the anneal processes tested is shown in Figure 2-29. In general, the furnace annealed cells had better red response and as a result, higher short circuit current.

More detailed solar cell performance data for laser, e-beam and furnace annealing is given in Appendix B of this report.

2.3 PROCESS DEVELOPMENT

A high-efficiency, n^+/pp^+ solar cell design and process specification has been developed under this program. The baseline process specification includes requirements on starting material, surface preparation, implant parameters, furnace annealing conditions, and the contact mask design.

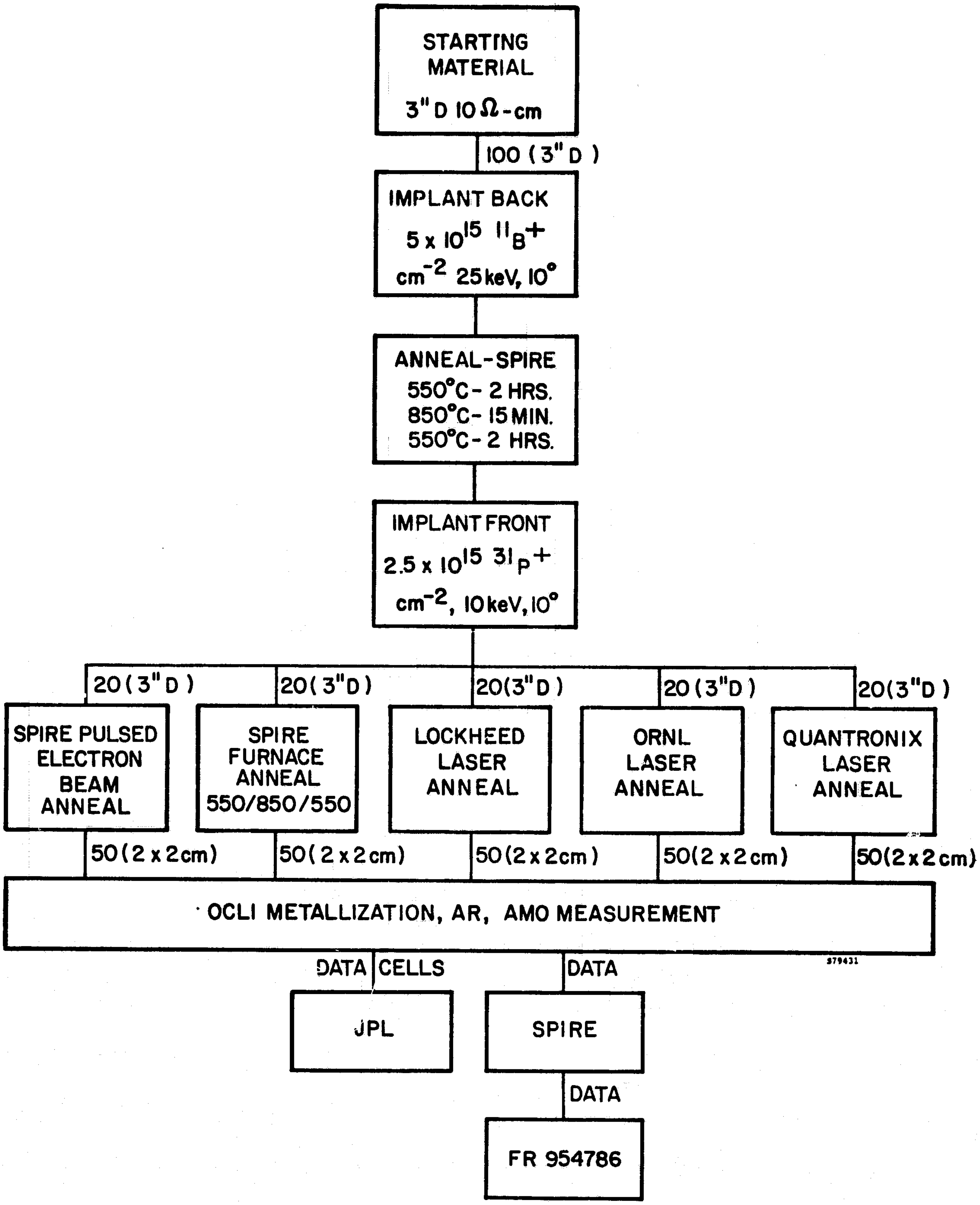

FIGURE 2-28. PROCESS SCHEMATIC FOR PULSE ANNEAL PROCESS EVALUATION

TABLE 2-16. PULSE ANNEALER PARAMETERS USED FOR JUNCTION LAYER COMPARISONS

	Value	
Parameter	Laser (Quantronix)	E-beam (Spire)
Pulse width (nanoseconds)	120 - 150	100
Wavelength/energy	1.06 microns	12 keV
Beam energy (J/cm^2)	3	1
Average power	10 watts	NA
Repetition rate	5 kHz	NA
Annealing rate	0.5 cm^2/sec	NA
Operational mode	Step and repeat	Single shot
Laser mode	Single	NA

TABLE 2-17. AVERAGE SOLAR CELL PERFORMANCE FROM A COMPARISON OF LASER AND ELECTRON BEAM ANNEALING PROCESSES

		AM0-15°C			AM1-28°C
Lot No.	Anneal	I_{sc} (A)	V_{oc} (V)	P_{max} (mW)	Eff. (%)
1497	E-beam (Spire)	0.150 (1.3)	0.577 (5.4)	60.1 (5.1)	13.1
1499	Laser (Quantronix)	0.141 (1.6)	0.569 (3.8)	61.4 (1.1)	13.3
1501	Laser (Lockheed)	0.125 (20.0)	0.486 (67.0)	41.2 (14.0)	9.0
1502	Furnace	0.156 (2.5)	0.588 (8.1)	66.5 (7.0)	14.5

Note: Standard deviation is shown in parentheses.

TABLE 2-18. MEASURED MINORITY CARRIER LIFETIME FOR ION-IMPLANTED LASER, E-BEAM AND FURNACE ANNEALED SOLAR CELLS

Cell	Anneal	Lifetime (Microseconds)
1497-3	E-beam (Spire)	3.3
1497-4	"	3.0
1499-6	Laser (Quantronix)	4.2
1499-18	"	4.8
1501-6	Laser (Lockheed)	4.7
1501-34	"	4.8
1502-1	Furnace (Spire)	2.8
1502	"	1.9

The cell structure employs an implanted junction and implanted back surface field (BSF), starting with 10-ohm-cm, (100) oriented, Czochralski-grown silicon. The front contact, as was described in Section 2.2.4, has been designed specifically for implanted junction layer characteristics such as sheet resistance and junction depth. The metallization system employed was TiPdAg. Experience with this contact metallurgy and mask design indicates that ultimate line widths of 25 micrometers can be fabricated. Metallization line widths of 25 micrometers and of this design result in shadowing of only 4 percent of the cell active area, so that nearly ideal performance of the structure can be at least measured.

The baseline structure is shown in Figure 2-30; the p^+ layer provides an effective BSF which increases both V_{oc} and the voltage at the maximum power point. For example, V_{oc} for a simple n^+/p solar cell under one-sun, AM0-25^{o}C conditions is 550 mV; with the inclusion of an effective BSF, the V_{oc} is increased to 600 mV.

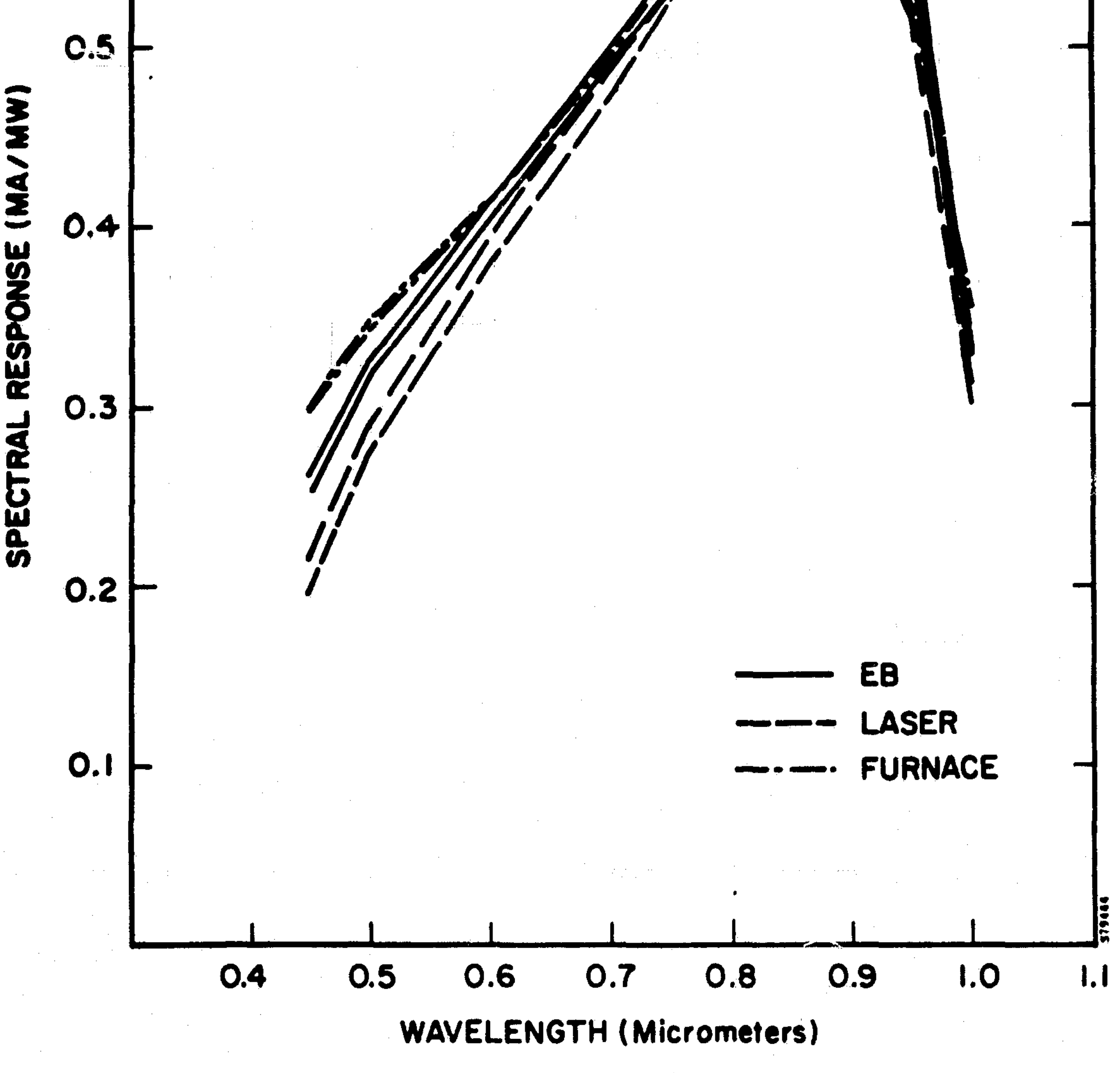

FIGURE 2-29. SPECTRAL RESPONSE FOR ION-IMPLANTED/PULSE AND FURNACE ANNEALED SOLAR CELLS

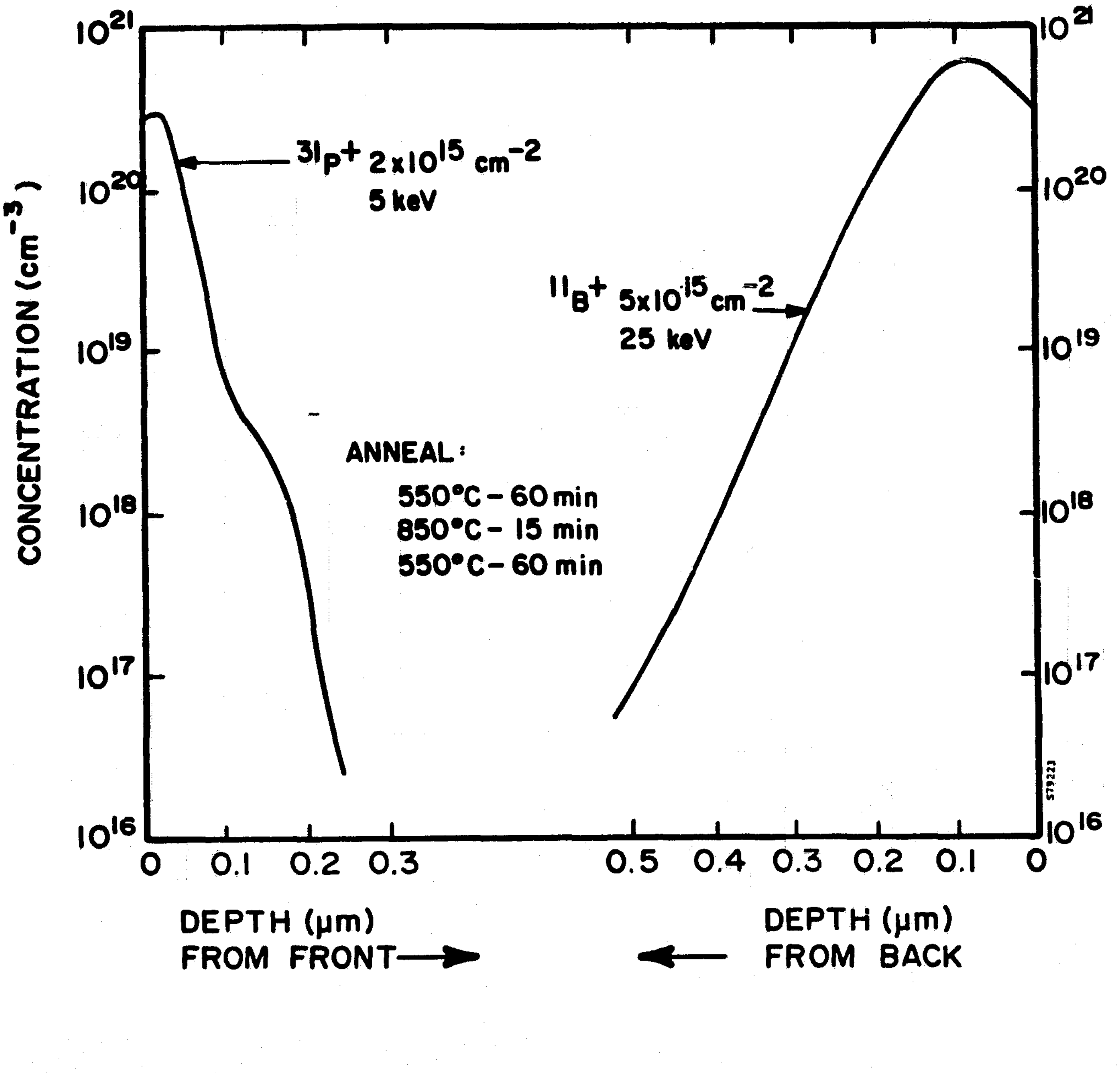

FIGURE 2-30. BASELINE PROCESS ION-IMPLANTED n^+/pp^+ SOLAR CELL STRUCTURE

The process shown schematically in Figure 2-31 does not include edge etching, nor does it include an aluminum alloyed BSF; the absence of these steps greatly simplifies the production process. During this contract effort, both float-zone and Czochralski-grown silicon materials were evaluated by the use of this baseline process. The characteristics of the materials were as follows:

Growth Technique	Defect Density (no./cm^2)	Resistivity (ohm-cm)	Surfaces	Thickness (micrometers)
Float-zone	0	1	Polished	450
Float-zone	400	10	Polished	450
Czochralski	400	1	Polished	450
Czochralski	400	10	Polished	450
Czochralski	400	10	Polished	375
Czochralski	400	10	Etched	300
Cast	—	5	Etched	375

No advantages in improved efficiency were noted for float-zone material over Czochralski-grown material when processed according to this specification. Higher efficiencies were measured for wafers 450 micrometers thick than for those 300 micrometers thick, but the cost-effectiveness of increased wafer thickness has not yet been determined. Extensive data was collected during the manufacture of 500 deliverable cells, starting with 300-micrometer, etched wafers. The performance distributions are presented in Section 2.4.

2.4 SOLAR CELL PERFORMANCE STATUS

The baseline cell process, as was outlined in Table 2-9, was developed for application to single crystal, Czochralski silicon material. This section reviews the measured cell performance for three types of process variations:

1. n^+/pp^+ implanted/furnace annealed cells using 7.6-cm diameter single crystal wafers
2. n^+/pp^+ implanted/pulsed electron beam annealed cells using 7.6-cm diameter single crystal wafers
3. $n^+p(p^+)$ implanted/furnace annealed cells using 5 x 5 cm SILSO polycrystalline sheet material.

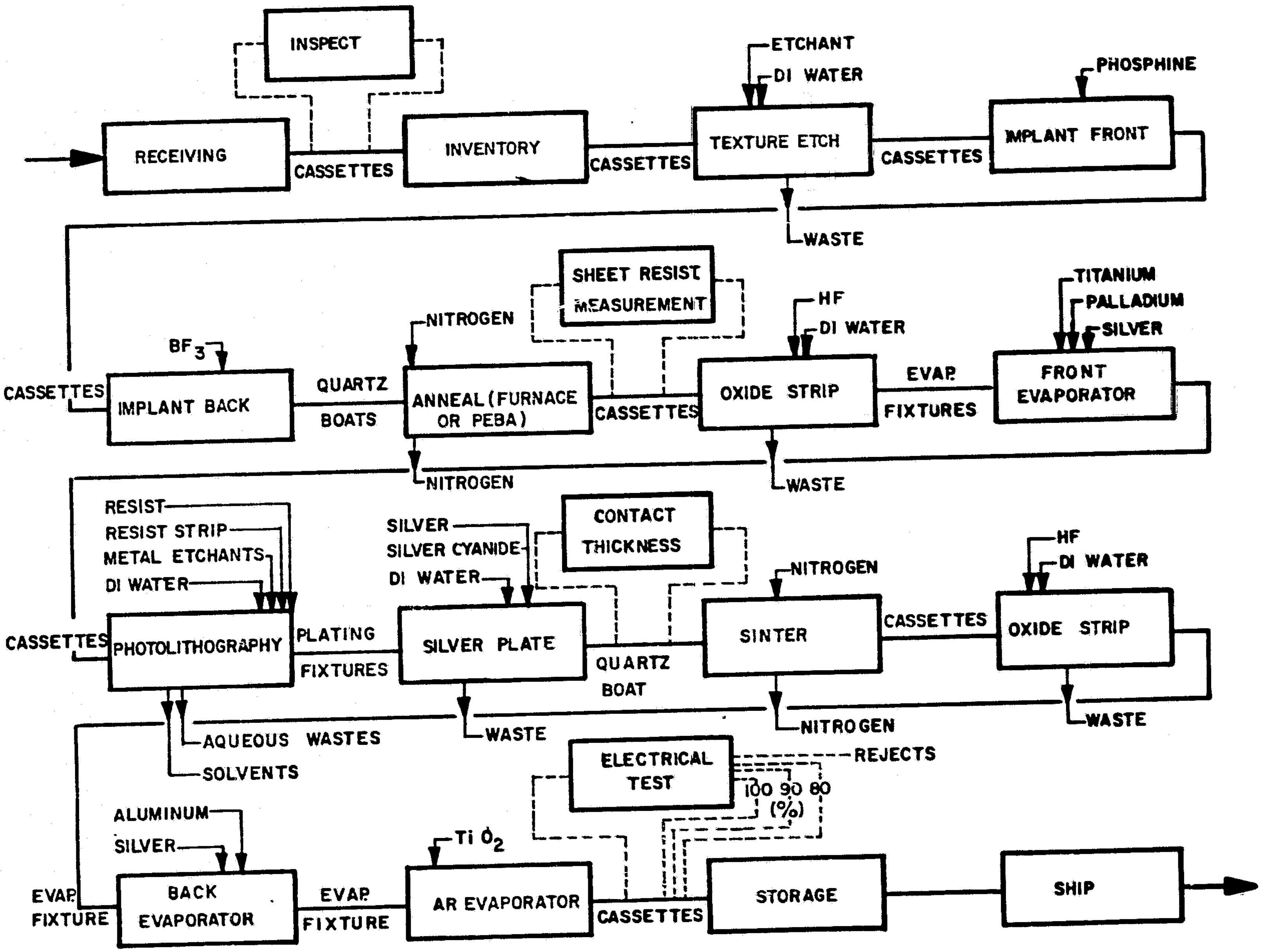

FIGURE 2-31. PROCESS SCHEMATIC FOR ION-IMPLANTED n^+/pp^+ SOLAR CELLS

2.4.1 Implanted/Furnace Annealed Cell Performance

Based upon experience with the high-current ion implanter, manufacturing and quality control procedures were determined for cell processing, and 660 wafers with diameters of 7.6 cm were implanted for complete processing into solar cells using furnace annealing. The characteristics of the starting material are summarized below:

	Resistivity (ohm-cm)	Thickness (μm)	Orien-tation	Surface	Growth Technique	No. of Wafers Started
Type A	10	300	(100)	Bright-Etched	Czochralski	600
Type B	10	450	(100)	Front-Polished Back-Etched	Czochralski	60

Both types were Czochralski, semiconductor-grade silicon wafers. All the wafers were implanted, using the JPL-LSA, high-current ion implanter, to provide both junction and back surface field regions. The ion dose uniformity across each wafer was between ± 7 percent and ± 10 percent. This level of uniformity did not produce a measurable performance loss when compared with cell characteristics produced with a dose uniformity controlled to better than ± 1 percent.

The remaining cell processing included furnace annealing, TiPdAg contacts, and AR coating; no edge etching or other treatments were used to isolate the edges of the cells. The process was as outlined in Table 2-9 . Out of the 660 wafer starts, 80 wafers were broken during handling and 60 were electrical rejects. The cause of these rejects was surface plating of silver along the cell edge, which caused a reduction of the internal cell shunt resistance and curve fill factor.

The average and peak characteristics for the five hundred 7.6-cm diameter cells delivered to JPL are as shown in Table 2-19. Performance distributions of I_{sc}, V_{oc}, I_{490}mV, and efficiency are shown in Figure 2-32. The highest cell efficiency was measured to be 14.1 percent (AM0-25°C) at Spire, as shown in Figure 2-33. JPL's AM1-28°C measurement is shown in Figure 2-34.

TABLE 2-19. SUMMARY OF PERFORMANCE CHARACTERISTICS FOR 500 7.6-cm DIAMETER ION-IMPLANTED, FURNACE ANNEALED CELLS

		Measured (AM0-25°C) Characteristics		
	Parameter	Average	Peak	Std. Deviation
	V_{oc} (mV)	594	600	2.8
	I_{sc} (mA)	1780	1955	74
	I_{490} (mA)	1611	1780	82
AM0	Efficiency (%)	12.8	14.1	0.65
AM1	Efficiency (%)	15.0	16.5	(Measured at JPL)

2.4.2 Cast Polycrystalline Silicon Solar Cells

Non-single-crystal silicon materials such as sheet and ribbons present no particular problems for implantation processing. Considerations of grain boundary diffusion effects, preferential dopant collection in grain boundaries are minimized for properly conducted implantation, and implant damage annealing procedures. As a part of this program, the baseline processes was shown feasible for manufacturing ion-implanted cells from cast polycrystalline sheet silicon.

The starting material was manufactured by Wacker Chemical Corporation under the trade name of SILSO. This material is characterized by a large grain structure, as shown in Figure 2-35, and was produced by casting boron-doped, 5-ohm-cm silicon in a suitable mold.

The cell process incorporated ion implantation for the introduction of n^+/pp^+ structure. The process used for the manufacture of the 100 cells delivered to JPL is outlined below:

1. Saw to 5 x 5 cm.
2. Etch to remove saw damage.
3. Implant Front: 2×10^{15} $^{31}P^+$ cm^{-2}, 10 keV, 10°.
4. Implant Back: 5×10^{15} $^{11}B^+$ cm^{-2}, 25 keV, 10°.
5. Anneal: 550°C - 2 hr, 850°C - 15 min, 550°C - 2 hr.
6. HF clean.
7. Front contact metallization: TiPdAg.
8. Back contact metallization: TiPdAg.
9. AR evaporation: TiO_2.

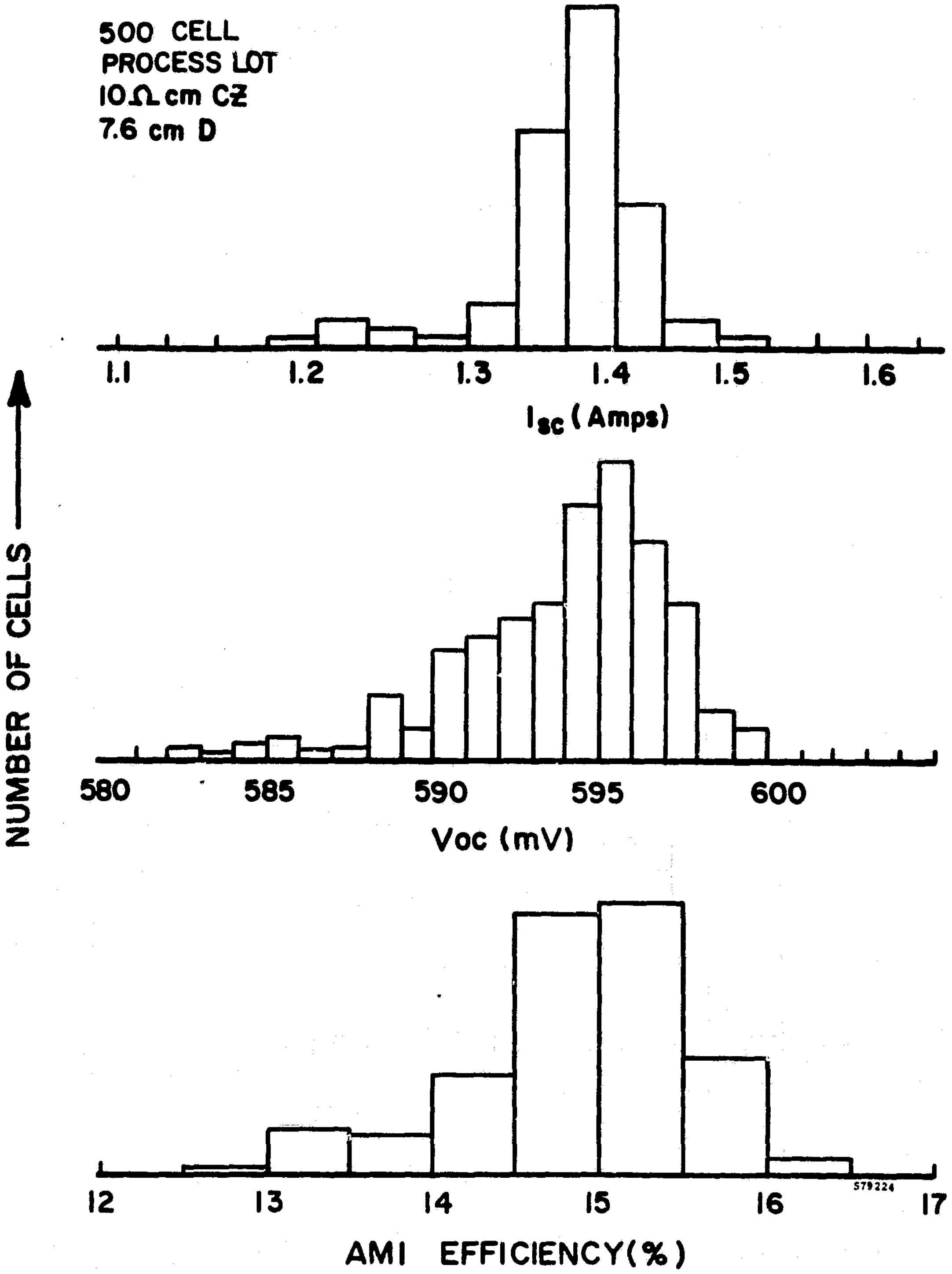

FIGURE 2-32. PERFORMANCE DISTRIBUTIONS FOR ION-IMPLANTED/ FURNACE ANNEALED SOLAR CELLS WITH 7.6-cm DIAMETERS

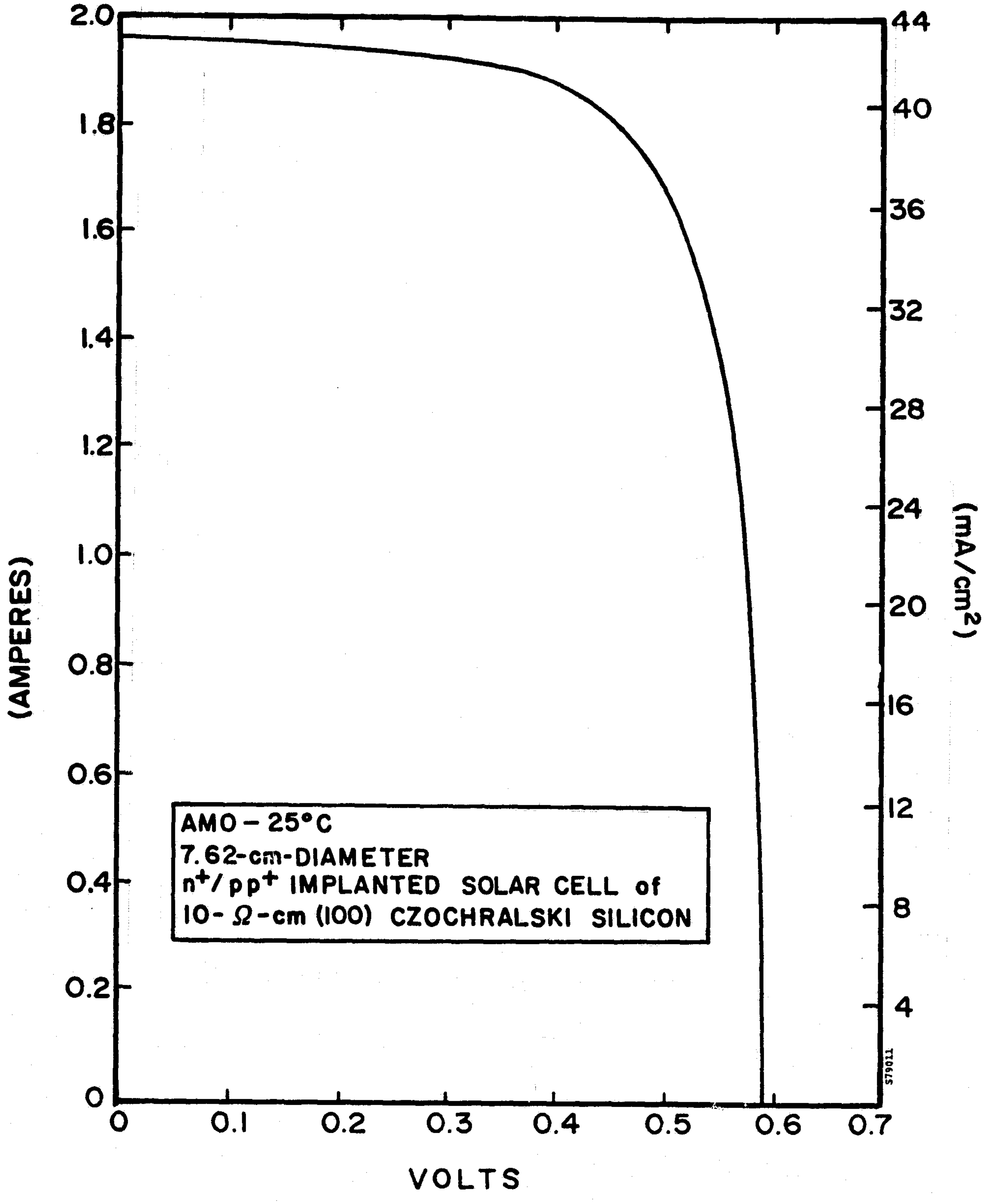

FIGURE 2-33. I-V CHARACTERISTICS FOR 7.62-cm DIAMETER, IMPLANTED, FURNACE ANNEALED SOLAR CELL

JET PROPULSION LABORATORY
PHOTOVOLTAIC MFG AND TEST PROJECT GROUP

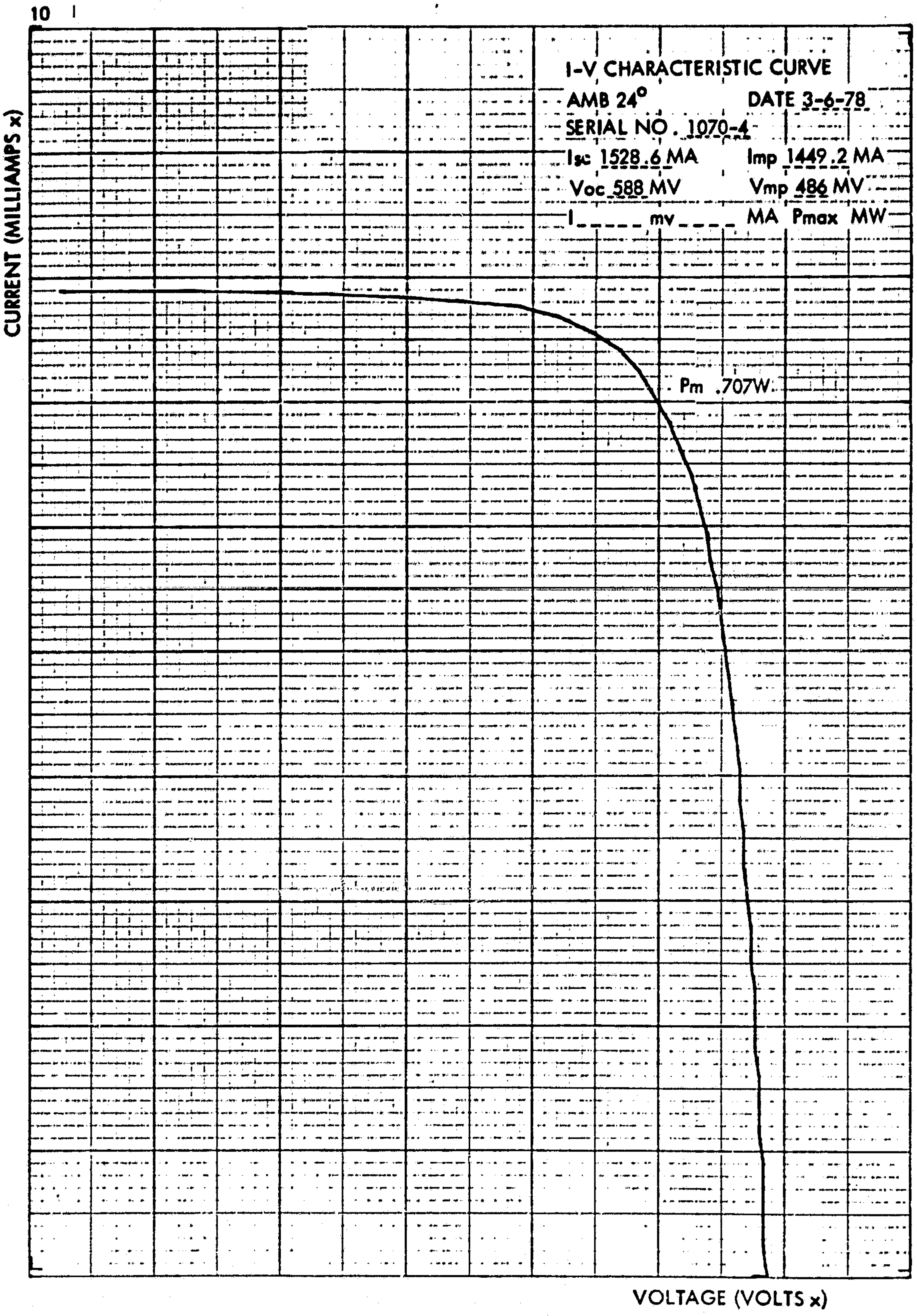

I-V CHARACTERISTIC CURVE
AMB 24° DATE 3-6-78
SERIAL NO. 1070-4
Isc 1528.6 MA Imp 1449.2 MA
Voc 588 MV Vmp 486 MV
I____ mv____ MA Pmax MW

FIGURE 2-34. AM1-28°C, I-V CHARACTERISTICS FOR 7.62-cm DIAMETER, FURNACE ANNEALED SOLAR CELLS

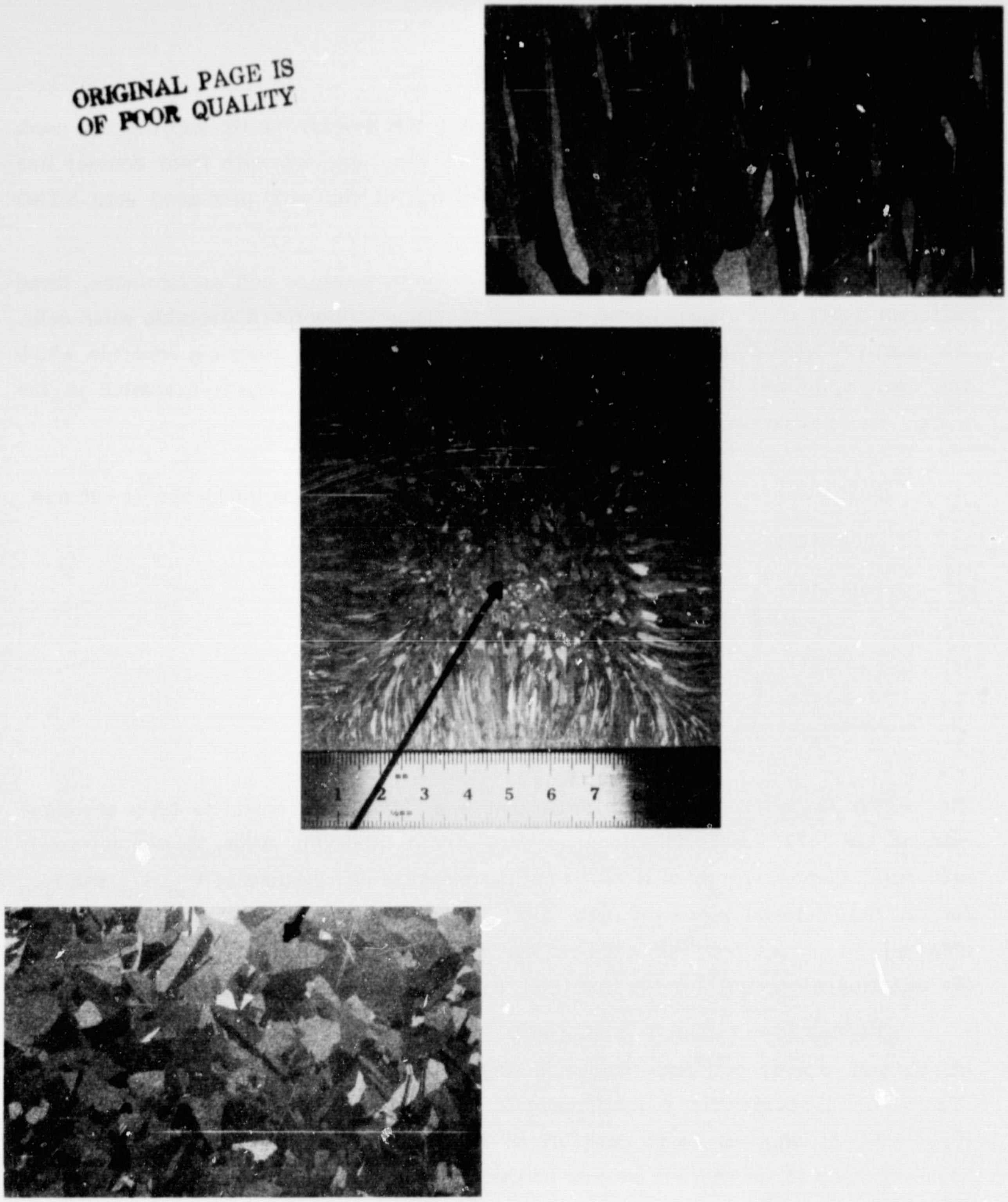

S79001P

FIGURE 2-35. TYPICAL GRAIN CONFIGURATION OF POLYCRYSTALLINE SILSO WAFER

Insufficient time was available to optimize this process for the sheet silicon used, but efficiencies up to 10.3 percent (AM1-$28^{\circ}C$) were obtained with front contact line widths of 75 micrometers. Figure 2-36 shows one of the cells processed with SILSO material.

To assess the effect of the p^+ layer on polycrystalline cell performance, three different types of p^+ layers were employed to manufacture the deliverable solar cells. All junctions were formed by ion implantation and a furnace annealing schedule which had been optimized for Czochralski silicon. The various p^+ layers evaluated in the n^+/pp^+ device structure were formed as follows:

Lots 1584: evaporated aluminum alloy (5 micrometers thick), $850^{\circ}C$ - 30 min
Lot 1473: no p^+
Lots 1469: Implant - $5x10^{15}\ {}^{11}B^+\ cm^{-2}$, 25 keV, 10°
1470: Anneal - $500^{\circ}C$ - 2 hr
1471: $850^{\circ}C$ - 15 min
1472: $550^{\circ}C$ - 2 hr
1474:

The results from this comparison show that a p^+ layer is essential to form an ohmic contact, Lot 1473, processed without an implanted or alloyed p^+ layer, showed extremely poor curve factors. Figure 2-37 shows the performance distributions of V_{oc}, I_{sc}, and I_{450} for all the material processed with a p^+ layer. The highest cell performance was obtained with implanted ${}^{11}B^+$ back surface layers, as shown in Figure 2-38. Details of the cell results were given in the first interim report for this contract.

Although the implanted or alloyed p^+ layers can provide back surface field (BSF) effects and improve cell performance in single-crystal solar cells, the minority carrier lifetime of SILSO material is insufficient to allow the BSF effects to be demonstrated. Higher cell efficiencies would therefore be attainable with polycrystalline silicon that has been doped to 1.0 ohm-cm because of the higher open circuit voltages which would be realized.

The most notable performance deficiency measured for the deliverable cells was the internal shunting of cell output power by individual grains which appear to have extremely high doping or contaminant concentration. Such heavily doped grains can occur during the casting process, and are a result of the segregation of impurities during

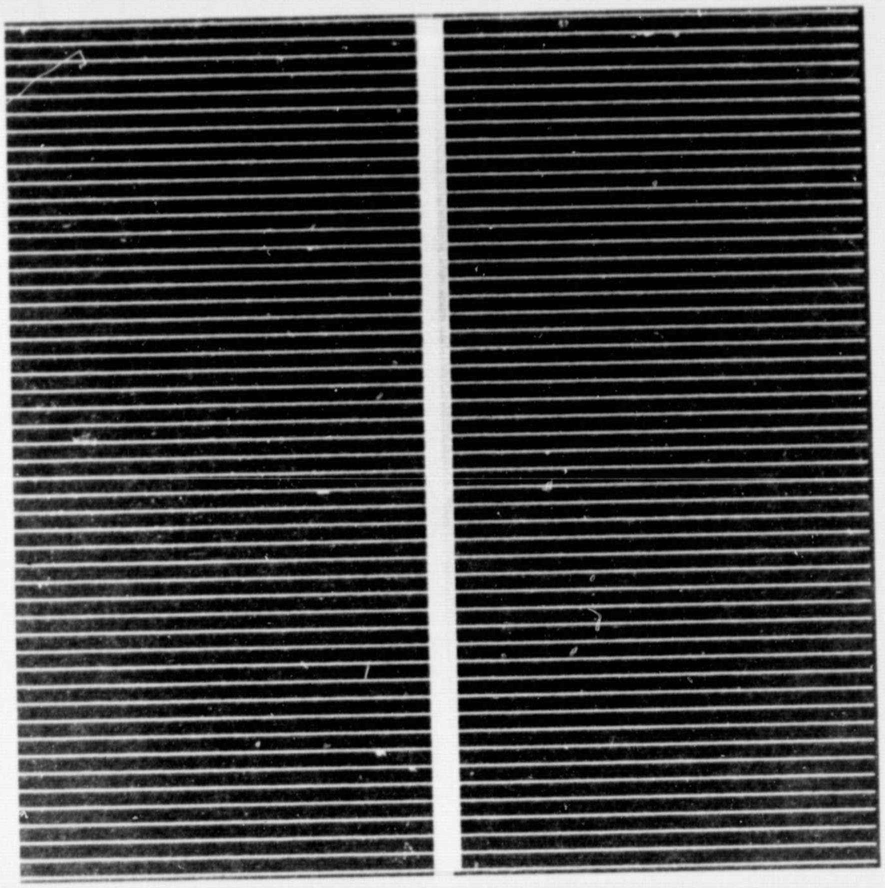

FIGURE 2-36. POLYCRYSTALLINE SHEET SILICON (SILSO) SOLAR CELL

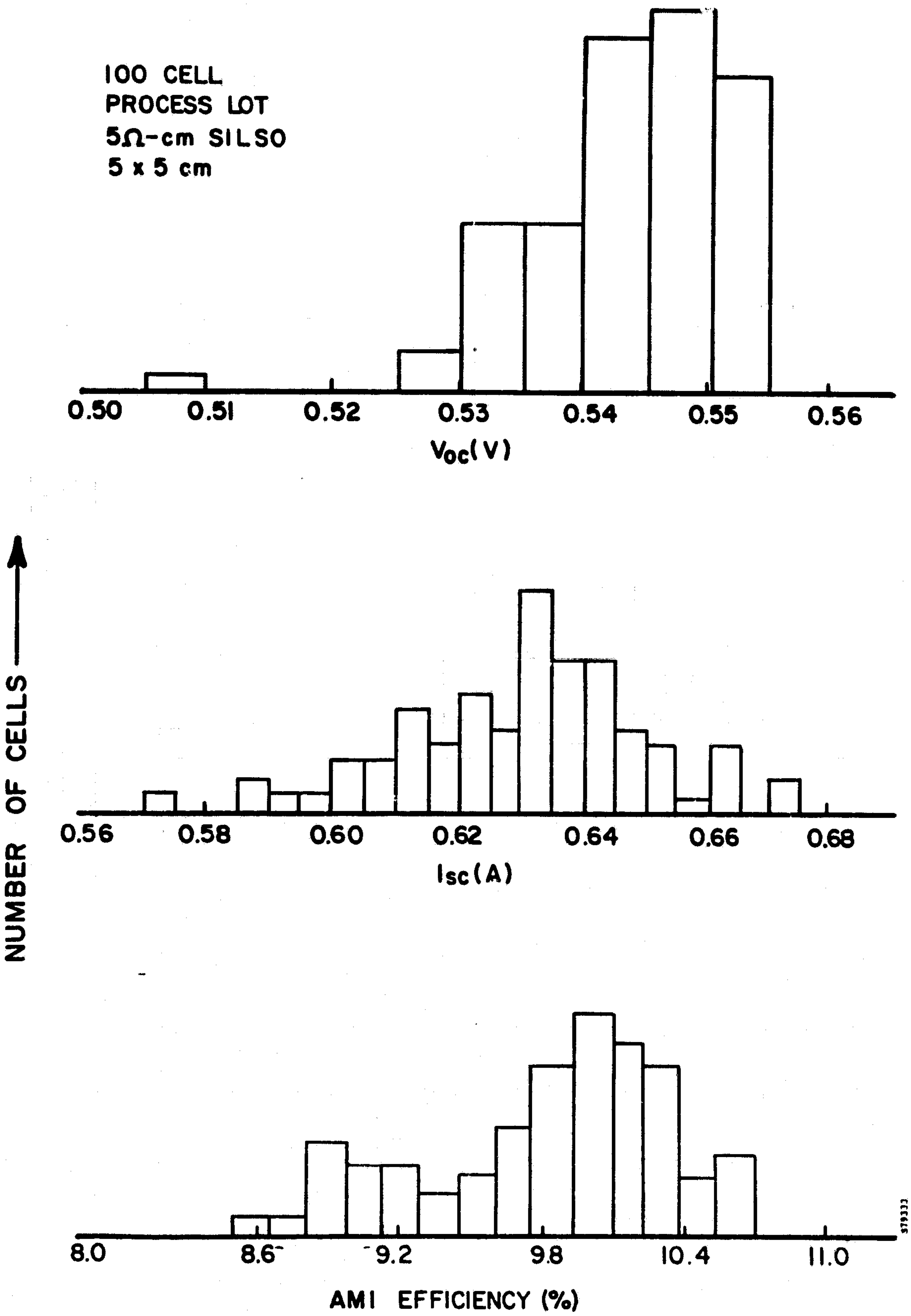

FIGURE 2-37. PERFORMANCE DISTRIBUTIONS FROM ION IMPLANTED/ FURNACE ANNEALED SILSO SOLAR CELLS

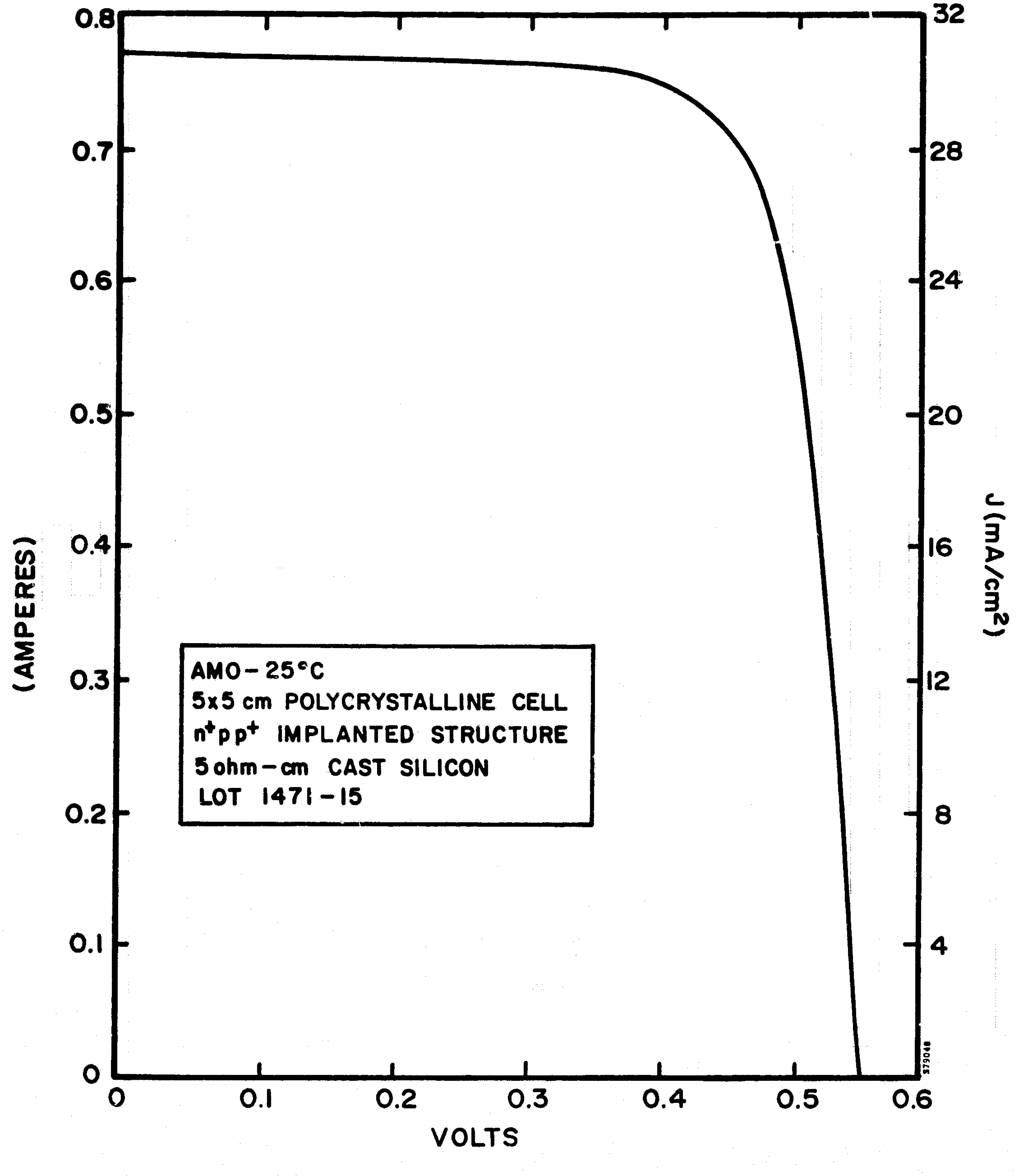

FIGURE 2-38. I-V CHARACTERISTICS FOR 5x5 cm ION IMPLANTED, FURNACE ANNEALED n$^+$/pp$^+$ POLYCRYSTALLINE SOLAR CELL

solidification of the molten silicon. The presence of the highly doped grains is delineated during electroplating of the front contact grids. During the electroplating process, any highly doped silicon regions act as conductors and cause silver to be electrodeposited from the bath onto the silicon.

2.4.3 Ion Implanted/Pulse Annealed Cell Performance

Phase II of this contract emphasized development of suitable pulsed electron beam parameters to anneal 7.6-cm diameter wafers with a single pulse. The details of the beam development effort are given in Section 2.4.4.

For both beam development and cell processing, the standard junction implant of $2.5 \times 10^{15}\ {}^{31}P^{+}\ cm^{-2}$ at 10 keV was used. Figure 2-39 shows a contour map of one pulse annealed wafer; these contour maps were used for electron beam diagnostic purposes during the contract effort. Because of the high transient temperatures of the junction layer during pulse anneal, the average sheet resistance of pulse annealed junctions is lower than furnace annealed junctions. The difference in sheet resistance as shown in Figure 2-40, is attributed to more complete activation of the implanted phosphorus ions; the nonuniformity of furnace annealed junctions is due to the neutral beam component of the ion implanter.

After a suitable 7.6 cm electron beam was developed, 500 implanted/pulse annealed cells were processed to compare performance with furnace annealed cells and to determine the reproducibility levels. Although significant effort went into beam development, the laboratory-type machine limitations resulted in less than desirable uniformity and reproducibility as described in Section 2.4.4. Some beam development efforts were continued while the 500 cells were being annealed which resulted in an overall improvement in cell efficiency with experience as shown in Figure 2-41. The average cell performance for each lot of 25 wafer starts is shown in Table 2-20. Figure 2-42 presents the distribution of cell performance. The best average lot cell performance was 12.3 percent (AM1-28°C) for ion implanted pulse annealed solar cells, while the peak cell efficiency was 13.9 percent (AM1-28°C) for cell no. 2138-2. Figure 2-43 shows the AM0-25°C I-V characteristics for the best cell. Two performance limiting mechanisms were noted: lower V_{oc} and lower I_{sc} when compared with equivalently processed furnace annealed cells.

SPIRE 06/22/79 ARSENIC RS

WAFER NO. 2055-6

AVERAGE R(SHEET)=34.5 OHMS/SQUARE

STD. DEV. = +/-3.73 RANGE =+/- 7.45 OHMS/SQUARE

IMPLANT CONDITIONS-

TILT= 7 ENERGY= 25KEV

ANNEAL SPEC- PEBA 280

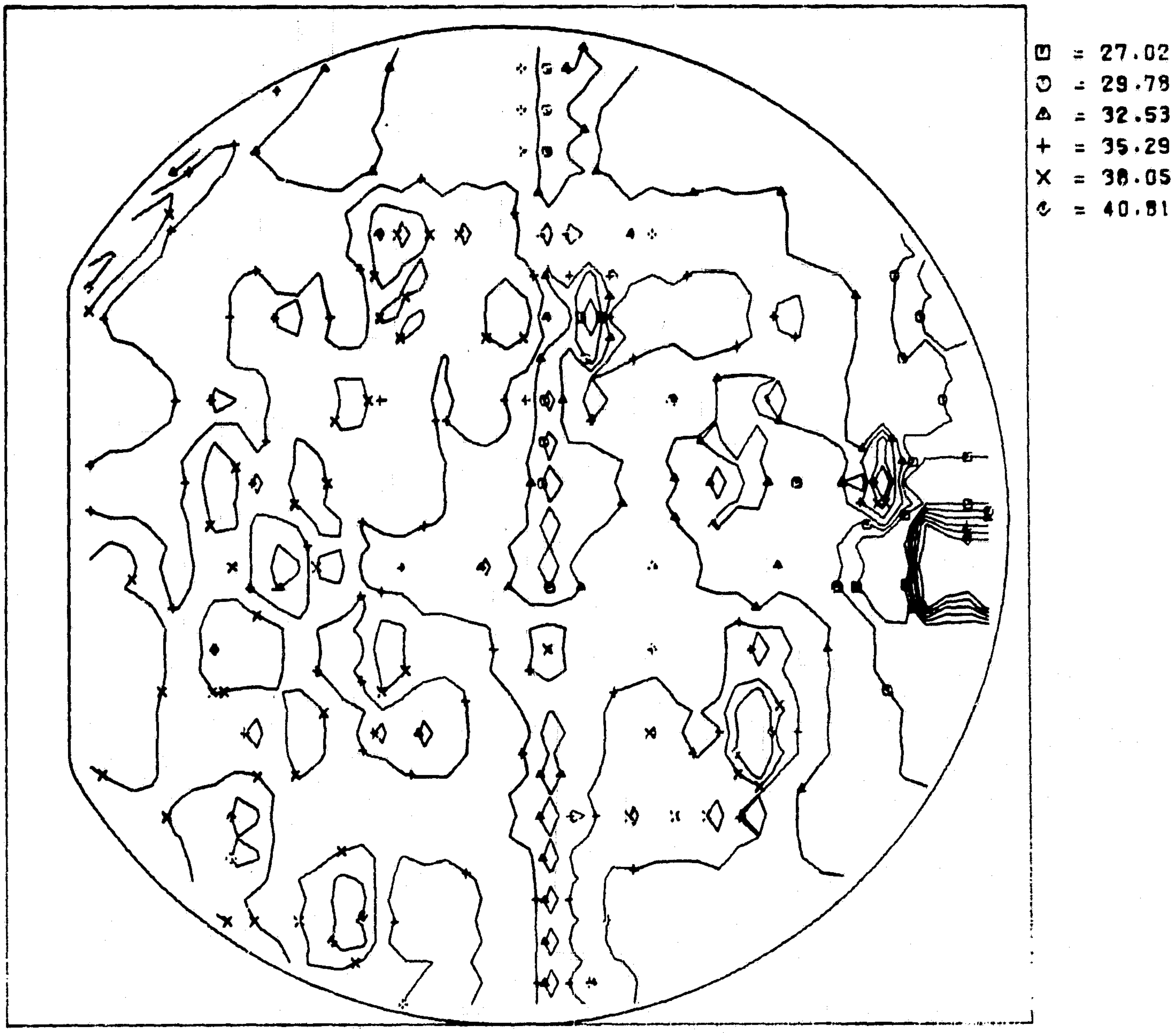

FIGURE 2-39. SHEET RESISTANCE CONTOUR MAP OF ION IMPLANTED/ SINGLE PULSE ANNEALED JUNCTIONS

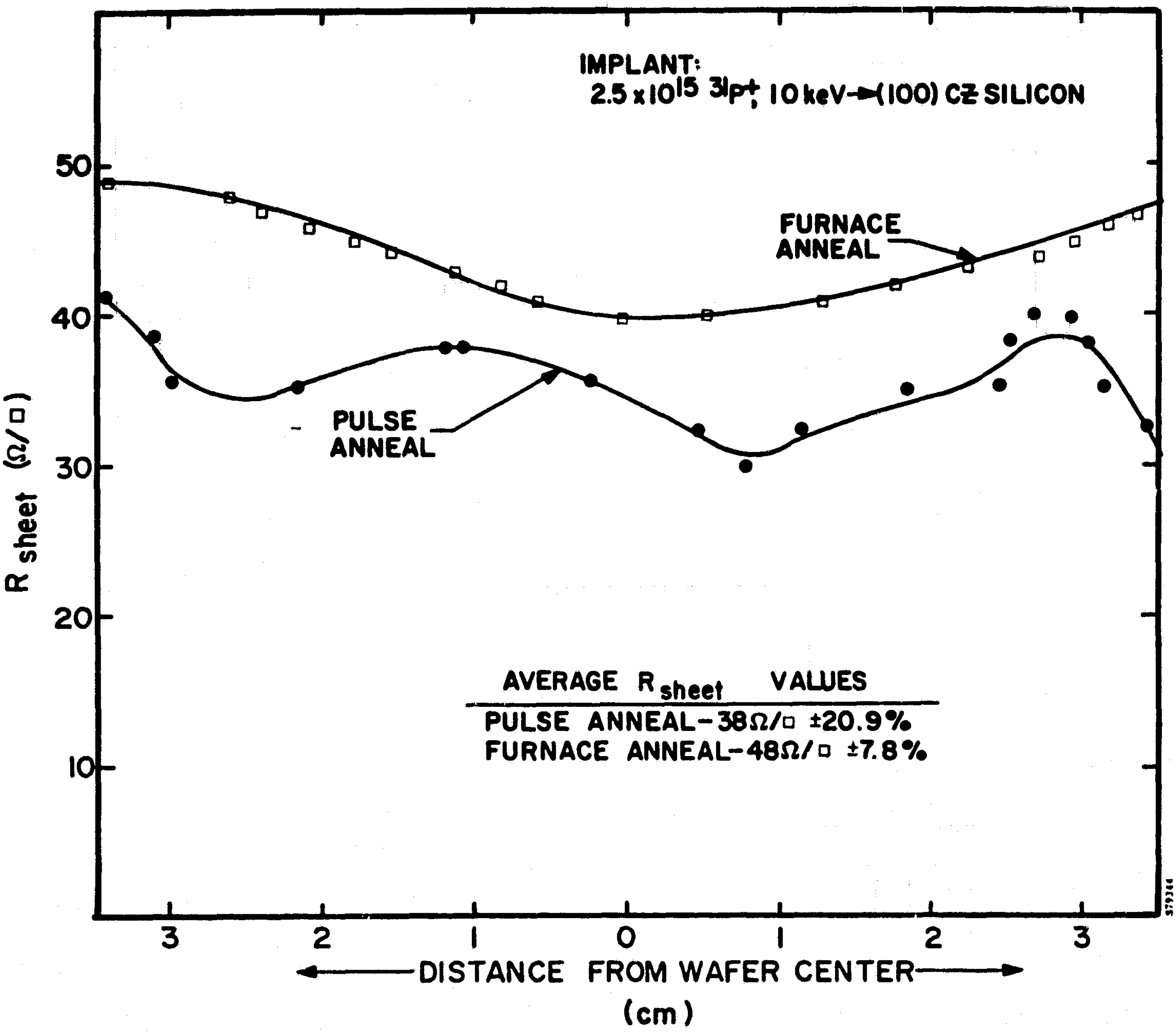

FIGURE 2-40. MEASURED SHEET RESISTANCE ACROSS 7.6-cm IMPLANTED JUNCTIONS

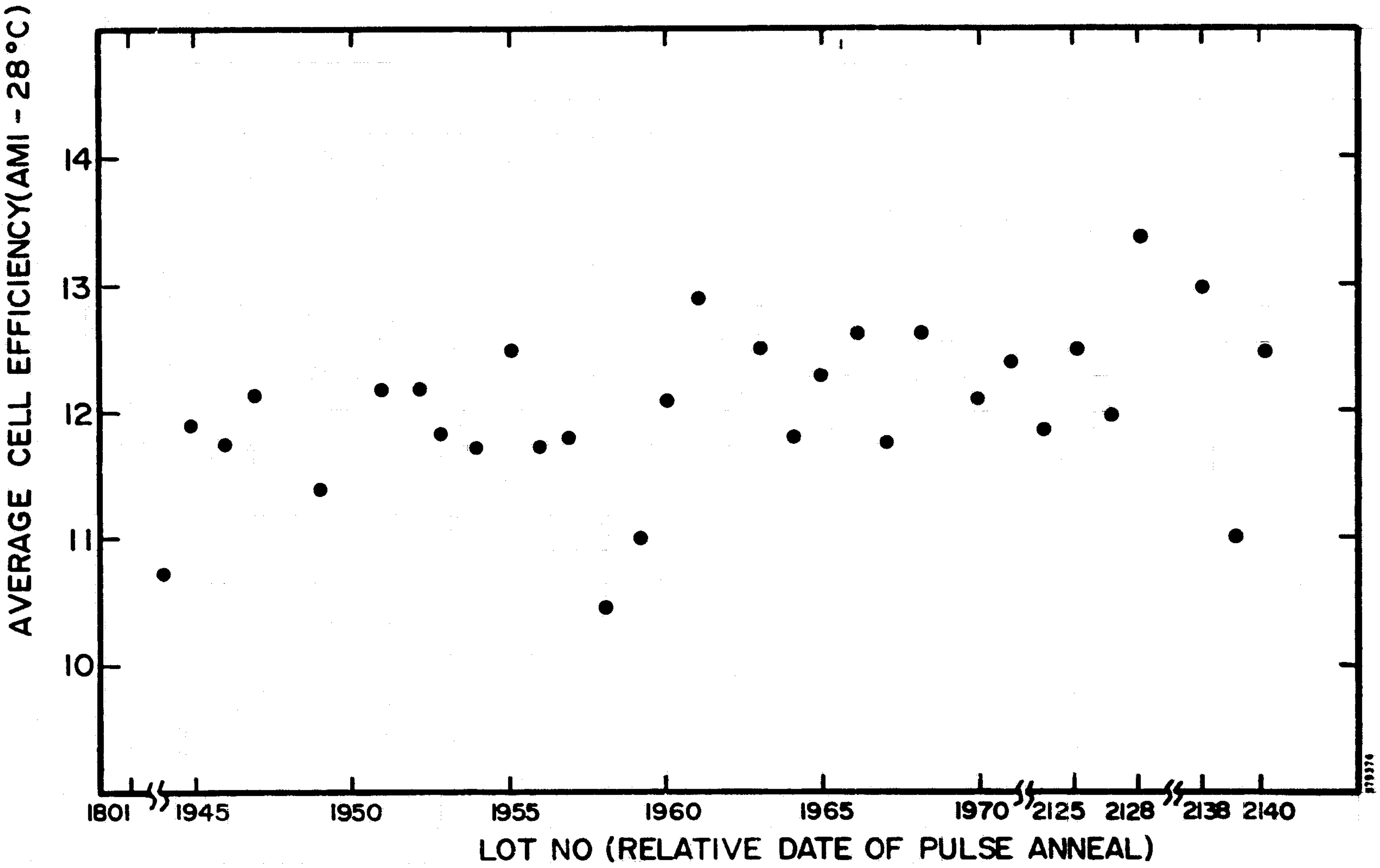

FIGURE 2-41. HISTORY OF PULSE ANNEALED CELL EFFICIENCY DURING BEAM DEVELOPMENT

TABLE 2-20. AVERAGE PERFORMANCE SUMMARY BY PROCESSING LOT NUMBER FOR IMPLANTED/PULSE ANNEALED SOLAR CELLS

Lot No.	P_{max}(W) AM0-25°C	Efficiency (%) AM1-28°C
1944	0.560	10.7
1945	0.624	11.9
1946	0.600	11.5
1947	0.636	12.2
1949	0.595	11.4
1951	0.638	12.2
1964	0.617	11.8
1965	0.645	12.3
1966	0.661	12.6
1967	0.618	11.8
1968	0.660	12.1
1970	0.630	12.1
1971	0.647	12.4
2125	0.619	11.8
2126	0.653	12.5
2127	0.627	12.0
2128	0.669	13.4
2138	0.681	13.0
2139	0.573	11.0
1952	0.637	12.2
1953	0.616	11.8
1954	0.614	11.7
1955	0.653	12.5
1956	0.614	11.7
1957	0.615	11.8
1958	0.541	10.4
1959	0.576	11.0
1960	0.640	12.2
1961	0.672	12.9
1963	0.654	12.5
1950	0.629	12.0
1948	0.568	11.0
2140	0.653	12.5
1801	0.627	12.0

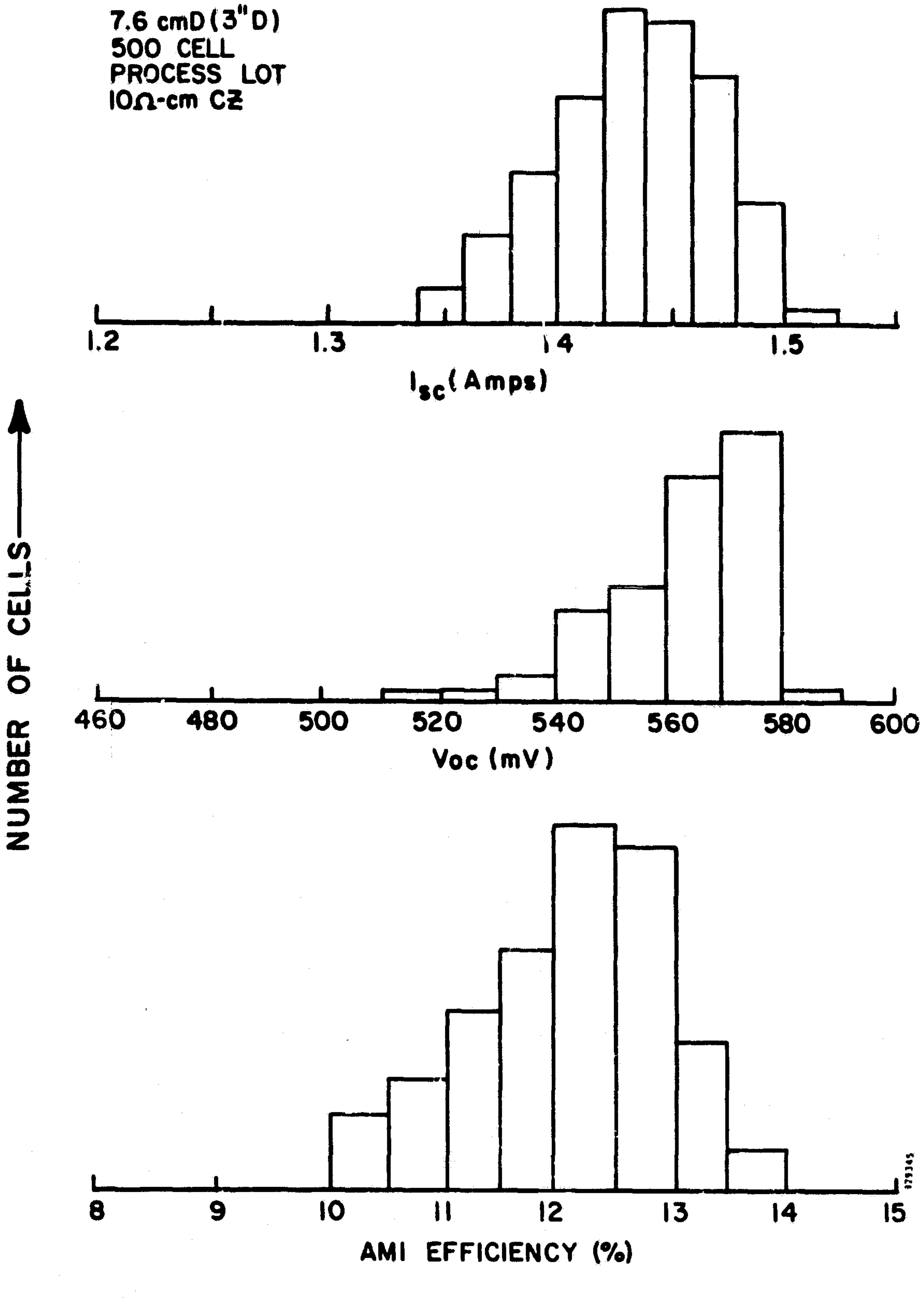

FIGURE 2-42. PERFORMANCE DISTRIBUTIONS FOR ION IMPLANTED/ PULSE ANNEALED SOLAR CELLS

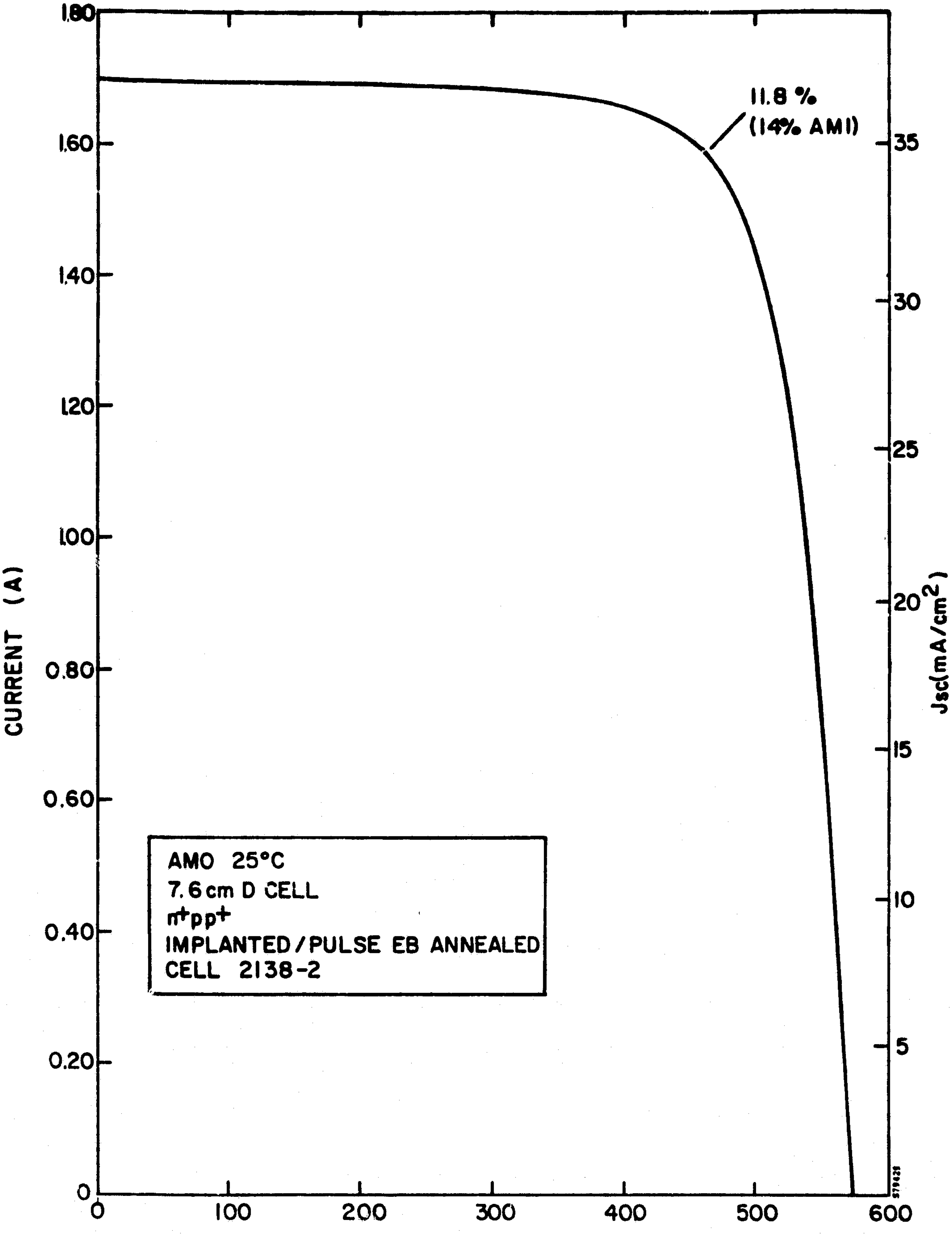

FIGURE 2-43. I-V CHARACTERISTICS FOR THE BEST ION IMPLANTED/ PULSE ANNEALED SOLAR CELLS

C-2

The performance limiting mechanism was not isolated, but is believed to be due to both poor red response and point defects in the junction depletion layer caused by rapid thermal quenching following deposition of the pulsed electron beam. Figure 2-44 and 2-45 show typical, and average spectral reponse and quantum efficiency for pulse annealed and furnace annealed junctions. Better blue repsonse is attributed to more complete activation of the implanted phosphorus ions. No mechanism was identified to rationalize the decreased red response that was measured.

Because point defects have low activation energies for annealing, some post-pulse thermal furnace annealing experiments were conducted. Figure 2-46 shows the results following non-equilibrium furnace heat treatment. In most processing sequences, this heat treatment would be integral to such steps as contact and AR sintering.

The uniformity of the 7.6-cm pulsed electron beam utilized for implant annealing was also checked by photolithographic processing of five 2 x 2 cm cells on one 7.6-cm wafer. Figure 2-47 shows the AM0-25°C characteristics for each of the five cells cut from a single wafer. As shown in this figure, efficiencies varied between 11.1 percent and 12.9 percent (AM1-28°C) within a single wafer.

2.4.4 Limitations of Existing Pulsed Electron Beam Hardware

This section reviews the methods used to generate large area electron beams and then identifies the likely beam characteristics which limited solar cell performance reported in Section 2.4.3.

One machine configuration for generating 7.6-cm diameter electron beams is a single cathode-anode system where the silicon wafer is the anode. However, to achieve the uniformity necessary for implant annealing, it has been found necessary to drift the electron beam beyond a transparent mesh anode. The extra drift distance, above the cathode-anode gap, allows strong self-interactions in the multikiloampere electron beam to disrupt unstable perturbations and improve uniformity. At minimum drift distances, the parallel conducting planes formed by the anode and sample reduce the self-radial electric field of the beam and the self-magnetic field then causes the electron beam to focus. At larger drift distances, the radial electric field is sufficient to force the outer electrons near the beam edge to the vacuum chamber walls. As a compromise, to maintain high fluence, high current electron beams with adequate uniformity, the geometry of PEBA for large diameter beams requires a partially focusing short drift distance.

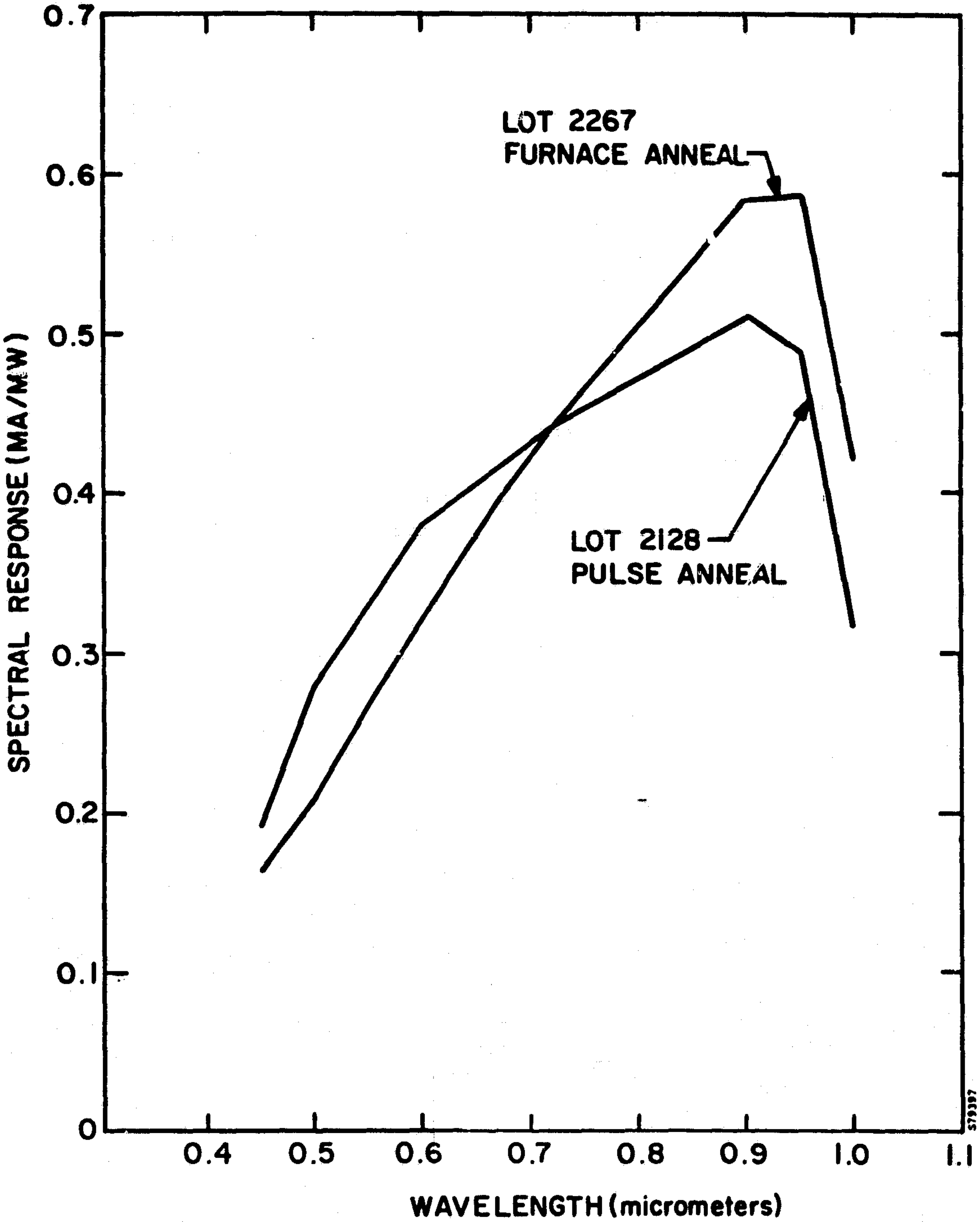

FIGURE 2-44. AVERAGE SPECTRAL RESPONSE OF TYPICAL PROCESSING LOTS FOR BOTH PULSE AND FURNACE ANNEAL

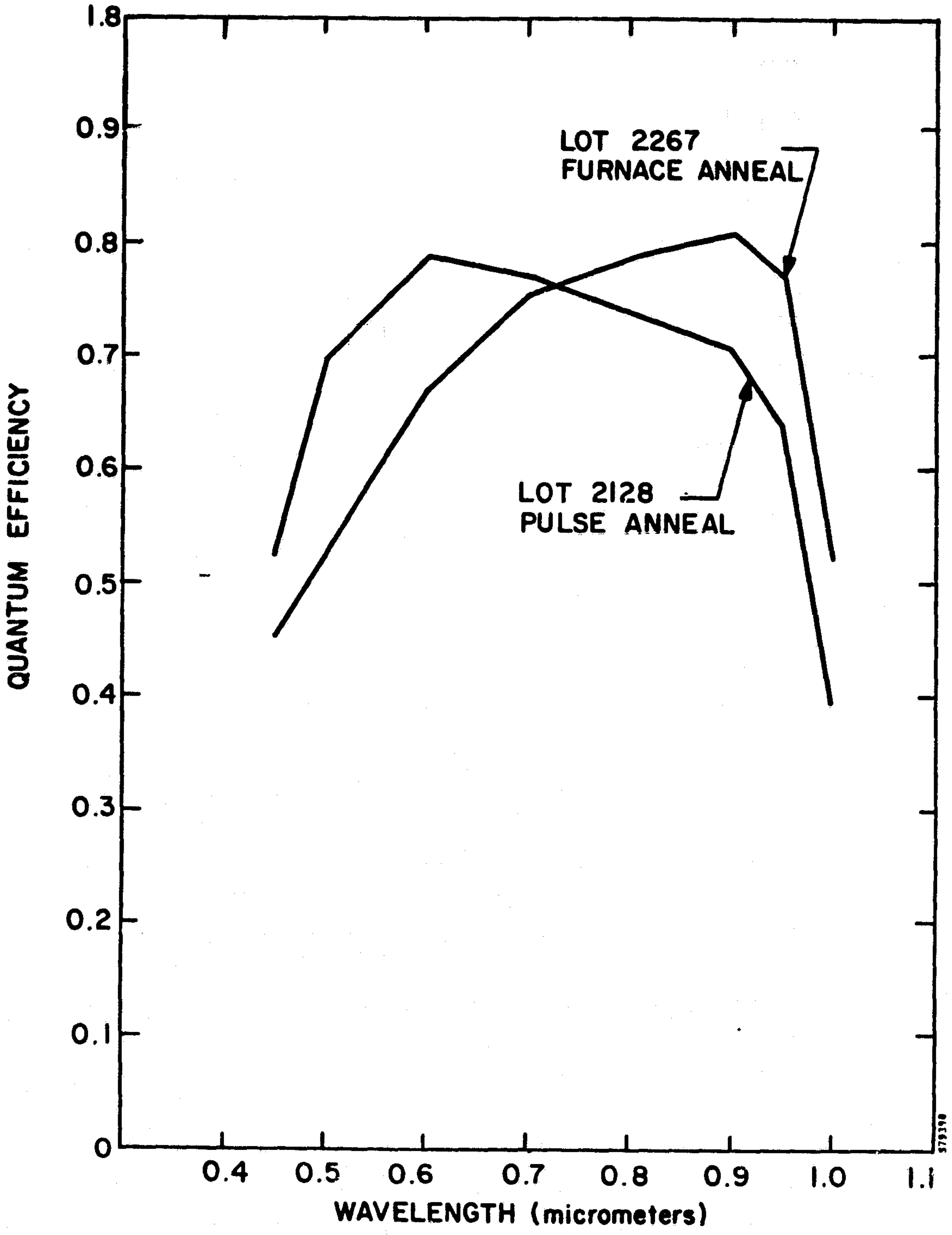

FIGURE 2-45. AVERAGE INTERNAL QUANTUM EFFICIENCY OF TYPICAL PROCESSING LOTS FOR BOTH PULSE AND FURNACE ANNEAL

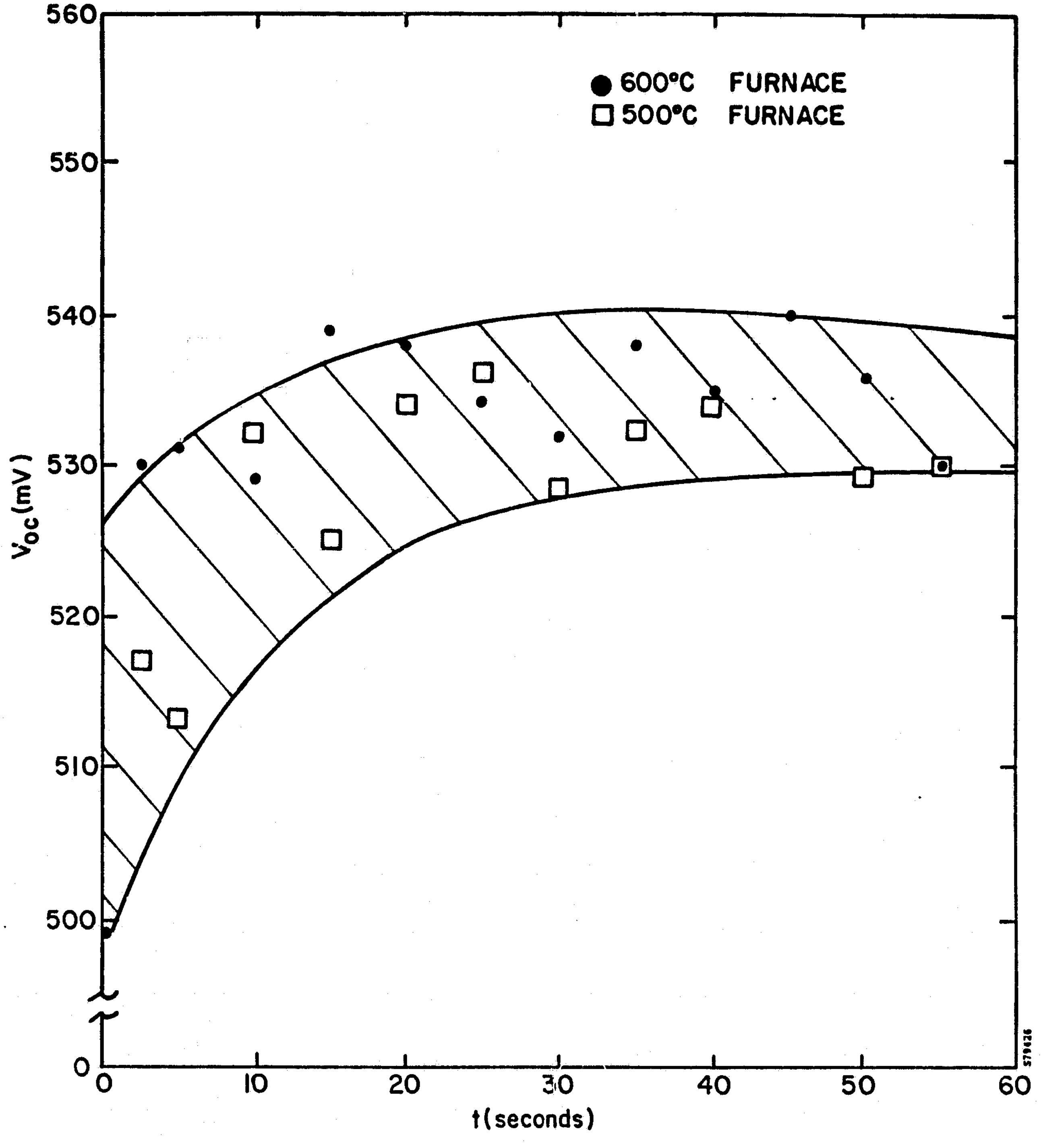

FIGURE 2-46. MEASURED V_{oc} (AM0-25°C) FOR POST-PULSE FURNACE ANNEALING (Point probe, before AR coating)

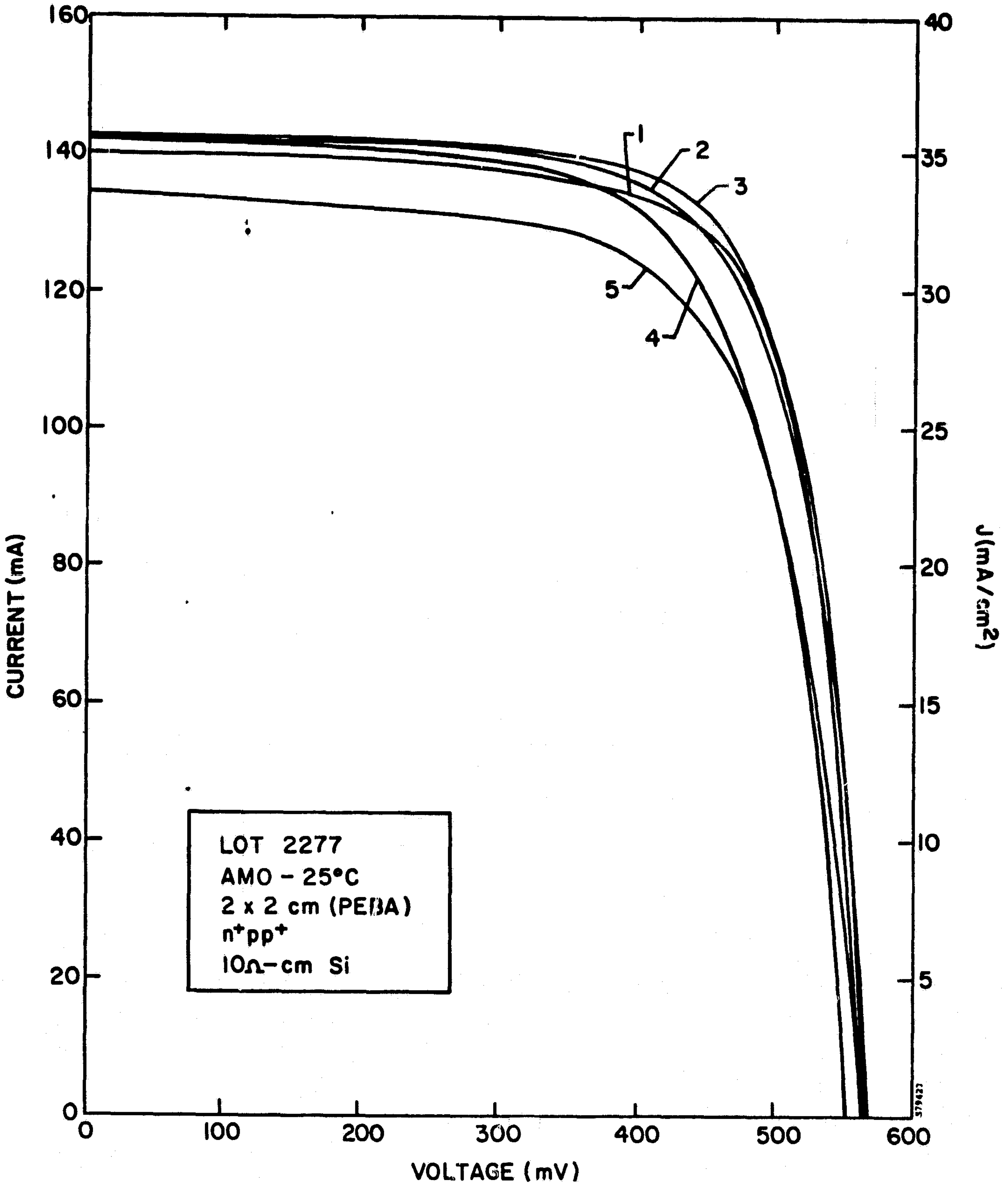

FIGURE 2-47. I-V CHARACTERISTICS OF FIVE 2x2 cm CELLS CUT FROM A SINGLE 7.6-cm DIAMETER, PULSE ANNEALED WAFER

Focusing implies that the initial cathode diameter be larger than the sample (wafer) diameter. Cathodes with OD of 3.5, 4, 4.5, 5 and 6 inches were tested. The minimum cathode-anode gap is fixed by a pulse shortening mechanism and the maximum gap is determined by the initial diode impedance and maximum diode (electron energy) voltage allowed. The sample to anode distance is fixed by aforementioned conditions on self-electric fields. Experimental geometry was, therefore, limited and after testing at different charging voltages on the energy storage capacitor/transmission line the 4-inch (10 cm) cathode was chosen as optimal. Measured diode voltage and current traces for two similar pulses are shown, with calculated decoded electron energy spectra, in Figure 2-48.

The diode current is identical for the two pulses. The diode voltage is also identical, but noise in oscillograph traces introduces a random baseline shifting error in the digitizing equipment. This error is increased when the voltage trace is corrected for inductance effects (L dI/dt) in the diagnostics. The final variation is about ±5 percent in total energy and average electron energy. The variation in total charge in the beam is due to the assumption in the numerical analysis code that the electron beam current is cut off when the voltage goes to zero. The calculated depth dose profiles of these electron energy spectra, for an angle of incidence of 60°, are shown in Figure 2-49. They are similar except for changes near the surface.

2.5 PULSED ENERGY PROCESSING SEQUENCE

The application of ion implantation to solar cell processing requires an annealing technique to remove the inherent radiation damage to the silicon lattice. One approach to annealing ion implantation damage is to utilize pulsed energy deposition. In this technique, a pulsed energy source, such as an electron or laser beam, is directed onto the surface to be heated. Almost all the energy carried by source is deposited into the first few micrometers of the surface being processed, resulting in momentary, high-temperature transients. A mechanism which can explain the annealing effects obtained by pulsed energy transients has been identified and is described in Appendix C. Pulsed energy sources can replace the thermal operations ordinarily performed in a furnace. The potential advantages of pulsed energy processing can be separated into technical and cost categories and are summarized as follows:

Technical Advantages:

1. Higher efficiency cells may be achievable. Better lattice regrowth occurs with pulse annealing, as will be discussed. Rapid dopant diffusion during

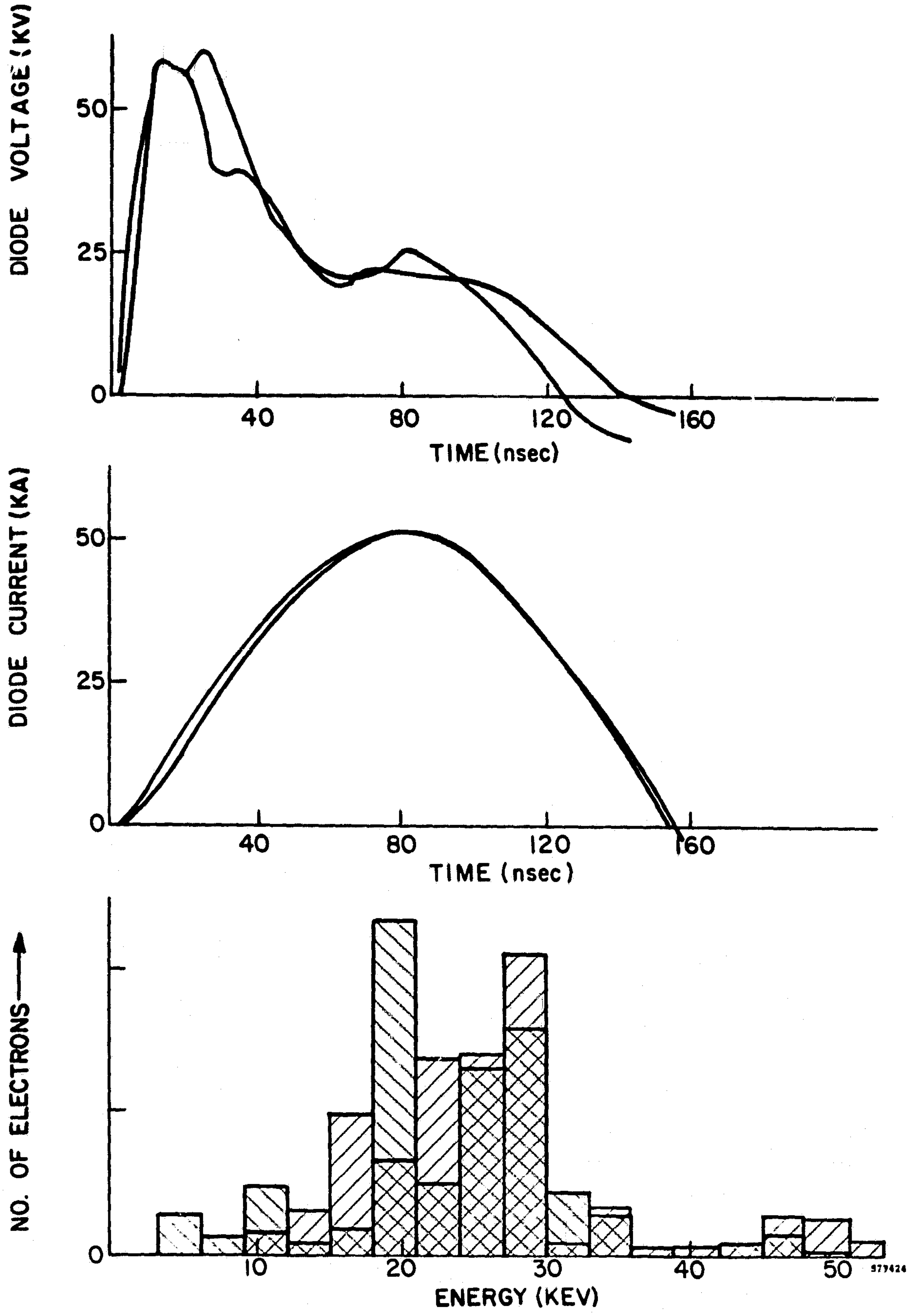

FIGURE 2-48. ELECTRON BEAM CHARACTERISTICS FOR TWO SEQUENTIAL PULSES

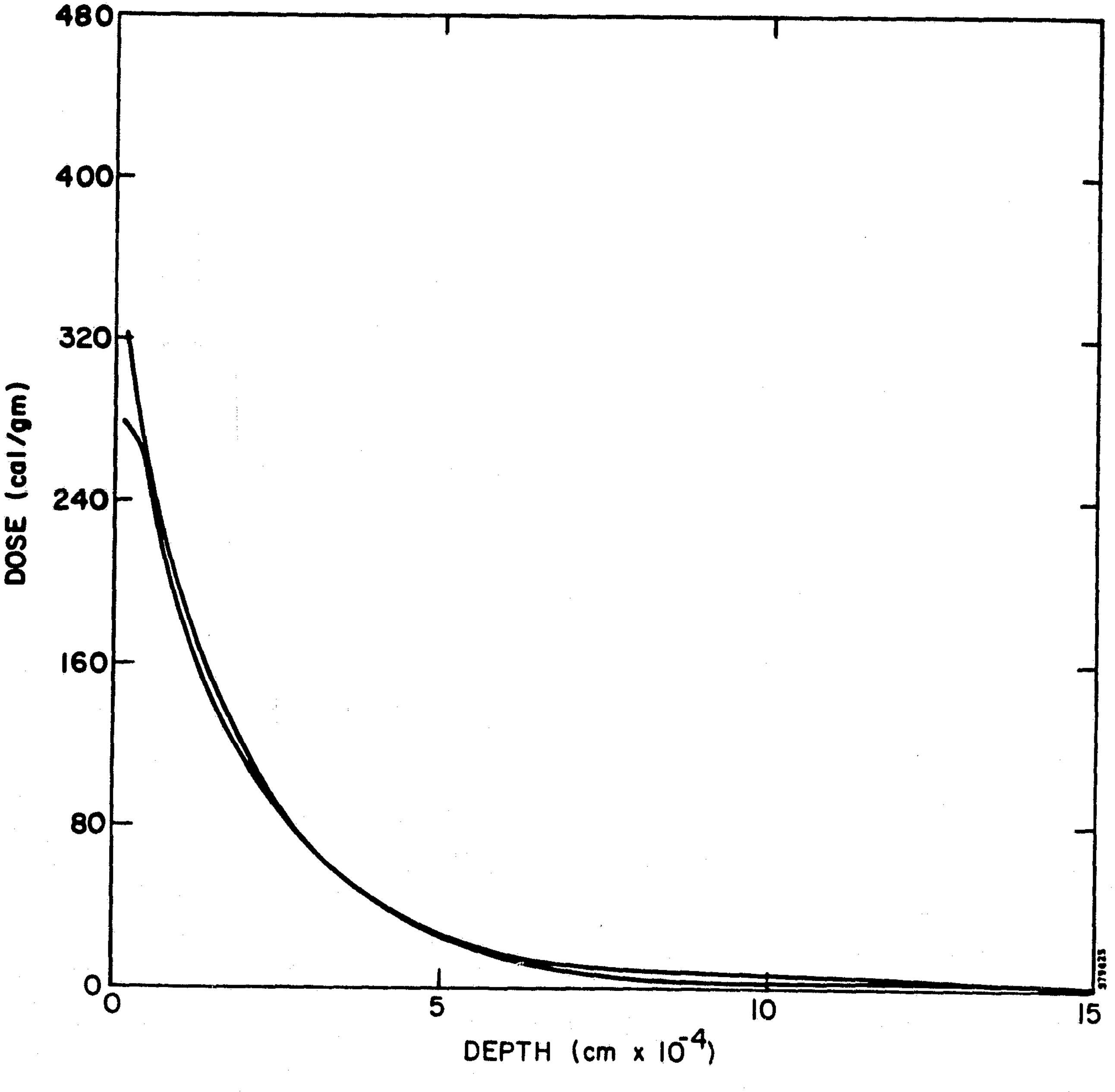

FIGURE 2-49. DEPTH-DOSE PROBE FOR TWO SEQUENTIAL ELECTRON BEAM PULSES

annealing may result in a better junction profile. During pulse processing, the bulk silicon is never brought to a high temperature, thereby precluding lifetime degradation by thermally induced defects.

2. Pulse processing may prove advantageous for fabricating cells from advanced polycrystalline sheet materials. Transient, surface heating will minimize grain boundary effects such as the diffusing of dopants and contact metallization. Also, thermally unstable materials and substrates can be processed.

3. Pulse annealing facilities, analogous to ion implantation facilities, are amenable to in-line processing for automation. Also, pulse annealing is a vacuum process, and is compatible with ion implantation equipment.

Cost Advantages:

1. The cost of pulse processing should be considerably less than conventional processing, because no wet chemistry or forming gases are required. Furthermore, pulse processing is an efficient use of input utility supplied power significantly reducing solar cell pay-back time.

2. Capital equipment costs for pulse processing will be less than those associated with diffusion processing or ion implantation with annealing furnaces. Since the projected size of a pulse annealer is comparable to a 100-mA implanter, relatively small building space is required. In-line annealing should also reduce the number of silicon carrying cassettes thereby reducing cost.

3. Since the process is amenable to automation and compatible with ion implantation, common cassettes can be implemented.

4. Reduced capital equipment requirements allow production scale-up to be achieved relatively easily.

Other Advantages:

1. Reduced environmental impact can be expected due to the elimination of wet chemistry, forming-gas processes, and waste treatment facilities.

The above advantages, in addition to the characteristics of line-of-sight ion beam and electron beam processing, eliminate the need for edge treatments for junction and BSF isolation. The following process sequence has been selected as one which could be utilized in an in-line, all vacuum process:

1.	Etch	Texturize or flash, plasma assisted
2.	Implant BSF p^+	5×10^{15} $^{11}B^+$ or $^{27}Al^+$ cm^{-2} at 25 keV (±10% dose tolerance) at 3-4 mA/cm^2 current density. Mass analysis may not be required for BSF aluminum processing.
3.	Pulse anneal BSF	0.2-cal/cm^2, 100-ns pulsed electron beam at 10 keV, in the liquid-phase epitaxy mode.
4.	Implant junction n^+	2×10^{15} $^{31}P^+$ cm^{-2} at 10 keV (±10% dose tolerance) at 3-4 mA/cm^2 current density.
5.	Pulse anneal junction	0.2-cal/cm^2, 100-ns pulsed electron beam at 10 keV, in the liquid-phase epitaxy mode.
6.	Deposit back contact	400A Al plus base metal for conductance. Method to be determined.
7.	Deposit front contact grid	400A Ta, Mo, W, with 10 micron Cu, Ag written by charged particle or ink jet technology.
8.	Deposit AR coating	Plasma assisted Si_3N_4 chemical vapor deposition

A few of the process steps listed above require proof of feasibility for solar cell production. These steps include a method for additive contact printing such as charged particle writing and ink jet writing (step 7). The BSF-implant parameters also require optimization for pulse anneal processing (step 2), including the parameters for the ion species, $^{11}B^+$ and $^{27}Al^+$, as well as the molecular implants, $^{49}BF_2^+$ and AlH_x^+. The advantage of molecular implants is the higher available beam currents from Freeman-type ion sources. For example, Figure 2-50 shows the mass-analyzed ion beam spectrum for BF_3 gas in a hot-filament, Freeman-type ion source. Approximately 40 percent more ion beam current, and therefore, greater throughput is available for $^{49}BF_2^+$ than for $^{11}B^+$ ions. Pulse annealing $^{49}BF_2^+$ implants (step 3) has yet to be investigated for activating boron ions as a BSF, while diminishing the effects caused by

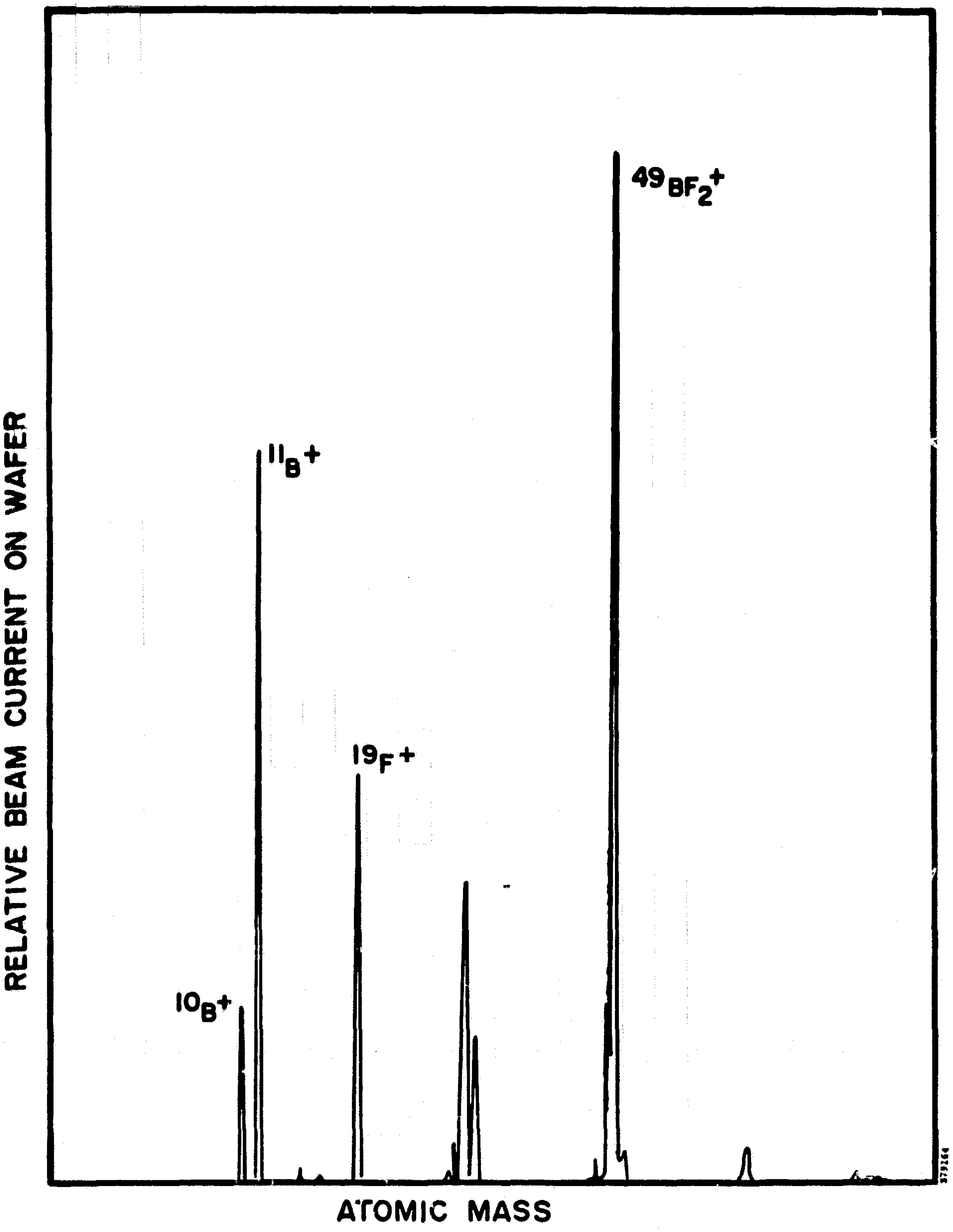

FIGURE 2-50. RELATIVE ION BEAM CURRENT ON WAFER FROM FREEMAN ION SOURCE WITH BF_3 GAS FEED

retention of the fluorine atoms in the silicon lattice. In previous studies, furnace annealing has been found to be inadequate for activating BF_2 for the following two reasons: (1) high current implants of $^{11}B^+$ or $^{49}BF_2^+$ at room temperature do not produce a totally amorphous region, and therefore such implanted boron atoms become difficult to activate electrically with furnace techniques(7) as shown in Figure 2-51a; and (2) retention of fluorine is evident in the thermal annealing of $^{49}BF_2^+$ implants as shown in Figure 2-51b.

2.6 PULSED ELECTRON BEAM MACHINE DESIGN

2.6.1 Functional Requirements for Pulsed Electron Beam Processor

The functional requirements for the electron beam processor have been defined, as listed in Table 2-21, to represent the minimum performance objectives to be met. These functional requirements will provide continuous, uniform, reproducible annealing throughput at a rate compatible with that of a 100-mA ion implanter. In addition to being compatible with the ion implanter throughput, the design philosophies of the prototype electron beam processor are similar to those of the ion implanter. A particularly important aspect is that the prototype pulser has multiple electron beam sources analogous to the ion sources of the 100-mA implanter. Multiple sources allow for system redundancy for reliability, continuous processing, and ease of maintenance. The available fluence, or energy deposited per square centimeter, is adjustable over a range so that liquid-phase epitaxial regrowth can be utilized for pulse annealing with this processor.

Each of the major subsystems for the electron beam processor is shown diagrammatically in Figure 2-52. Approximately 20 electron sources are required. The functional requirements of the major subsystems are as follows:

Variable High-Voltage Power Supply

A variable high-voltage power supply will provide basic electrical energy for the pulse electron beam processor. The power supply will be powered by conventional 110 volts, 60 Hz AC. The high-voltage generation range of the supply will be between 50 and 300 kilovolts. The current which it can supply will be up to 10 milliamperes. Power supply regulation in both current and voltage will be ±2 percent.

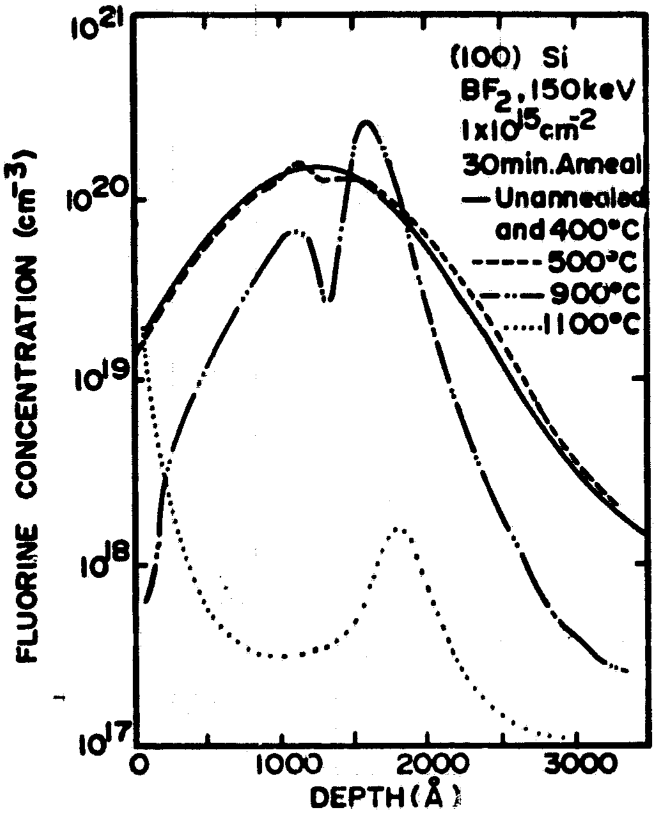

FIGURE 2-51a. FLUORINE ATOMIC PROFILES OBTAINED FROM SIMS MEASUREMENTS ON (100) Si IMPLANTED AT ROOM TEMPERATURE WITH A 1x10^{15}-cm^2 FLUENCE OF BF$_2^+$ (See Ref. 7)

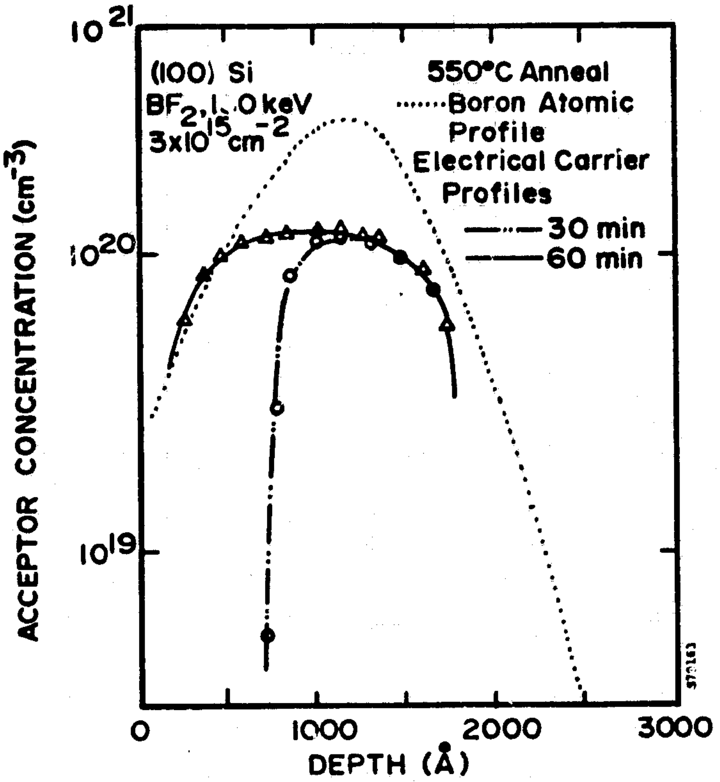

FIGURE 2-51b. NET ACCEPTOR CONCENTRATION PROFILE OBTAINED FROM A HIGH-FLUENCE BF$_2^+$ IMPLANT AND 500°C ISOTHERMAL ANNEAL (See Ref. 7)

TABLE 2-21. FUNCTIONAL REQUIREMENTS FOR PROTOTYPE PULSED ELECTRON BEAM PROCESSOR

(Compatible with 100-mA Implanter Throughput)

Item	Requirement
Energy Source:	Electrons
Electron Energy:	Multispectral components: Maximum 50 keV Average 10-15 keV
Fluence:	Less than 0.5 cal/cm^2
Electron Beam Current Density:	Less than 1,000 A/cm^2
Electron Beam Pulse Width:	Between 1.0 and 0.1 microsecond
Beam Uniformity/ Reproducibility	No worse than ±10 percent over all material procesed; no material fractured, and all material annealed.
Substrate Throughput:	Variable, minimum of 1,000 cm^2/sec per unit
Materials To Be Handled:	Silicon wafers, ribbon sheet, etc., to maximum individual item dimension of 20 cm x 20 cm
Surfaces To Be Processed:	Planar and texturized
Processing Mode:	Continuous flow
Operational Mode:	Continuous throughput, routine operations, predictable component failure, and easy maintenance.

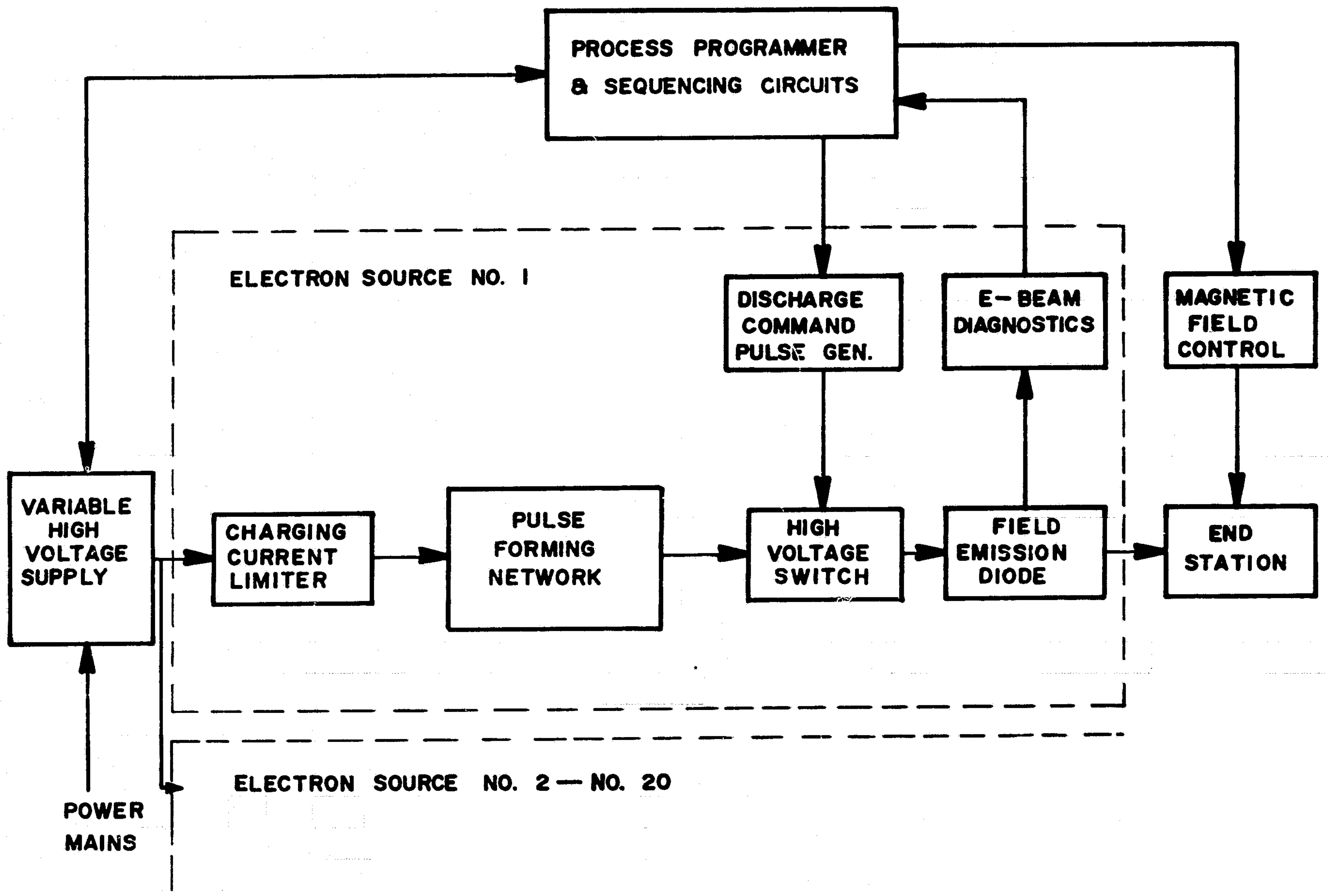

FIGURE 2-52. ELECTRON BEAM PROCESSOR SYSTEM ELEMENTS

Charging Current Limiter

Charging of the pulse forming network (PFN) of the pulsed electron beam sources will be from the high-voltage power supply through a charging current limiter. This limiter is necessary to prevent power supply burnout should shorting occur within the high-voltage PFN. This charging current limiter will be a high-power resistor of 10,000-ohm, 100-watt continuous power.

Pulse Forming Network

A PFN capable of being charged to a high voltage will be the basic energy store from which the electron beam pulse energy is extracted. This PFN will be a transmission line geometry with an impedance of between 1 and 50 ohms. The voltage to which this transmission line will be charged is between 50 and 300 kilovolts, compatible with the high-voltage power supply.

High-Voltage Switch

A command switch is required for discharge of the PFN once it has been charged by the high-voltage power supply. This switch will consist of a trigatron geometry with high-voltage spark initiation occurring on the ground side of the system, i.e., the diode. The trigatron switch will be initiated with a high-voltage pulse not less than 10 percent of the transmission line charging voltage. Switch jitter will be controlled to within ±1 microsecond.

Field Emission Diode

Energy from the PFN will be switched via a trigatron to the field emission diode. The field emission diode will consist of a vacuum coax region, a dielectric high-voltage insulating structure, a field/plasma emission cathode, and a transmission anode. Associated with the diode will be fast, high-voltage diagnostics consisting of a return current shunt and a capacitive voltage monitor, both built into the vacuum coax wall. These diagnostics will be calibrated for performance at the levels of processing.

End Station

The end station subsystem will be compatible with that of the 100-mA automated production ion implanter, that is, the vacuum interlocks and silicon transport will be identical to those used by the ion implanter. An additional requirement, however, is the presence of a 1 - 10 kilogauss magnetic field normal to the surface of the silicon to be processed. This will be provided for all electron sources by one large electromagnet. Vacuum requirements for the electron beam processor will also be compatible with that of the ion implanter. When final integration processor and implanter are accomplished, a common vacuum and silicon transport system will be used.

Process Programmer and Sequencer Controls

A microprocessor control console will be used to monitor and control the electron beam processor parameters and timing sequences. Eventually, this will be linked with the console of the 100-mA, automated production ion implanter. The processor will initiate a discharge upon command, via an intermediate voltage pulse generator which breaks down the trigatron switch in the high voltage system. The control console will also record the response of the diagnostics for the field emission diode such that beam parameters are precisely monitored on a pulse-to-pulse basis. The magnetic field parameters in the transport system will also be programmable.

The electron beam source will become a basic building block in the automated processing line to be developed to achieve 1986 and greater production goals. The processor described will satisfy the requirements of an ion implanter with 100 milliamperes of current and a throughput of 500 cm^2/sec for junction implants. Individual electron beams, similar to the case of ion sources, will be provided by transmission line pulse forming networks. This approach offers advantages similar to those of the multisource ion implanter. Electron beam source redundancy and off-line startup are achieved. The reliability of moderate level individual sources is improved, and the entire system reliability, reproducibility, and duty cycle are thereby enhanced.

2.6.2 Step and Repeat Pulse Annealing for 20 x 20 cm Areas

Separate electron beam pulses which anneal ion implantation damage in silicon can be overlapped leaving the region at the intersection annealed and undamaged. A pattern with a maximum dimension less than 3.8 cm was replicated over a 7.6-cm diameter implanted wafer, sufficient for a solar cell demonstrating that the technique will work on larger areas.

There are two approaches to large-area annealing with a circular electron beam pattern. The simpler method is to move the sample material beneath the beam in such a manner that eventually the entire area is in the beam. The disadvantage of this technique is that 40 percent of the surface is pulsed two or three times (with a square packing pattern), so that excessive diffusion of the implanted dopant in this multiply heated region may adversely affect the solar cell output. The alternative approach, chosen for this study, is the create a noncircular beam (i.e., square) by the use of a mask which can define an area for annealing with minimal overlap and dopant diffusion. A mask is necessary because the beam is focused and contains a very high current; therefore, a pattern generated at the cathode will not propagate to the silicon sample in a uniform corresponding pattern.

The experimental configuration was as shown in Figure 2-53. The beam mask was fashioned from a high-density graphite sheet 0.5 mm thick. This materials shows high resistance to damage from melting or spalling from pulsed, high-power electron beams and has negligible x-ray yield (i.e., it is suitable for production line machines). The mask was held in place and grounded through electrically conductive grease to the sample holder. Figure 2-54 shows various details of the edge configuration for the mask. With the mask touching the sample, a thin crack in the wafer at the carbon-silicon-vacuum interface always developed, independent of the geometry shown in Figure 2-55. The damage is believed to result from a vacuum problem, since with the mask in contact with or close to the wafer the region between the two is not effectively pumped. With a slight enhancement of pressure (due to the grease), the electron beam arcs to the interface point. When the mask was raised off the surface by about 0.5 mm (see Figure 2-54), the damage was prevented. Irregularities in the edge of the annealed pattern on the implanted wafer, as shown in Figure 2-55, were less than 0.5 mm, and inside this edge the anneal was uniform. The pattern can be replicated, as shown in Figure 2-56, without cracking the sample.

2.6.3 Solid Phase Epitaxial Regrowth Annealing

An alternative approach to annealing large-area sheet materials is to develop a lower temperature pulse annealing technique, based upon solid phase epitaxial regrowth of the crystal structure(8), which would use multiple pulses at lower fluence. This technique would prevent diffusion of the implanted dopant and allow the use of overlapping beams without masks. Here, the percentage of overlap from one pulse to the next is high, exceeding 90 percent, so that each point on the silicon surface would be pulsed 10 or more times. The technique was tested using a fluence of 0.6 joule/cm^2, compared to 1 joule/cm^2 for the liquid phase epitaxial annealing normally used, for 10 successive shots. The sample showed little electrical activation of the implanted dopant

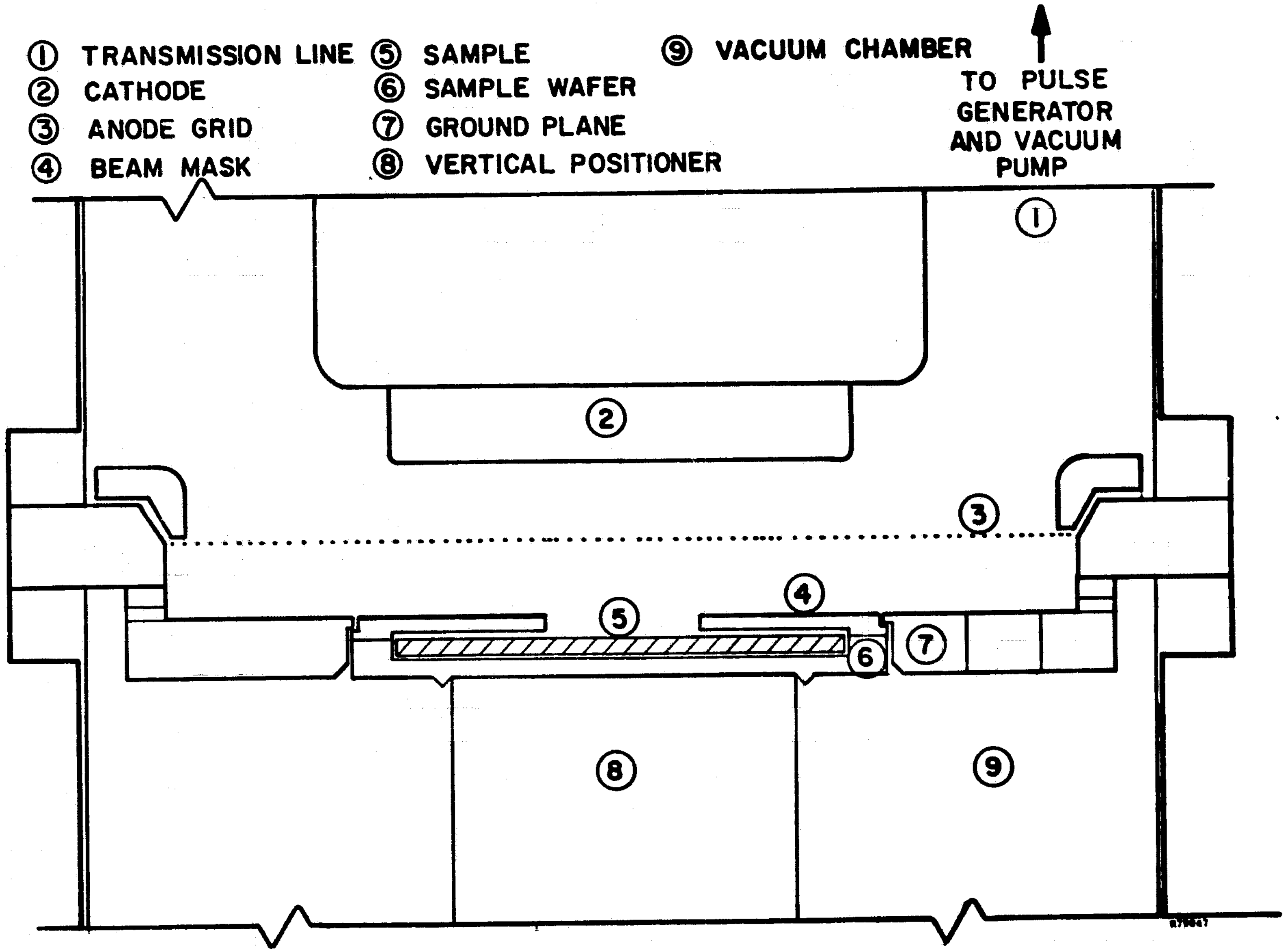

FIGURE 2-53. SCHEMATIC OF MASK EXPERIMENTS FOR PROCESSING DISCRETE ANNEAL AREAS WITHIN IMPLANTED WAFERS

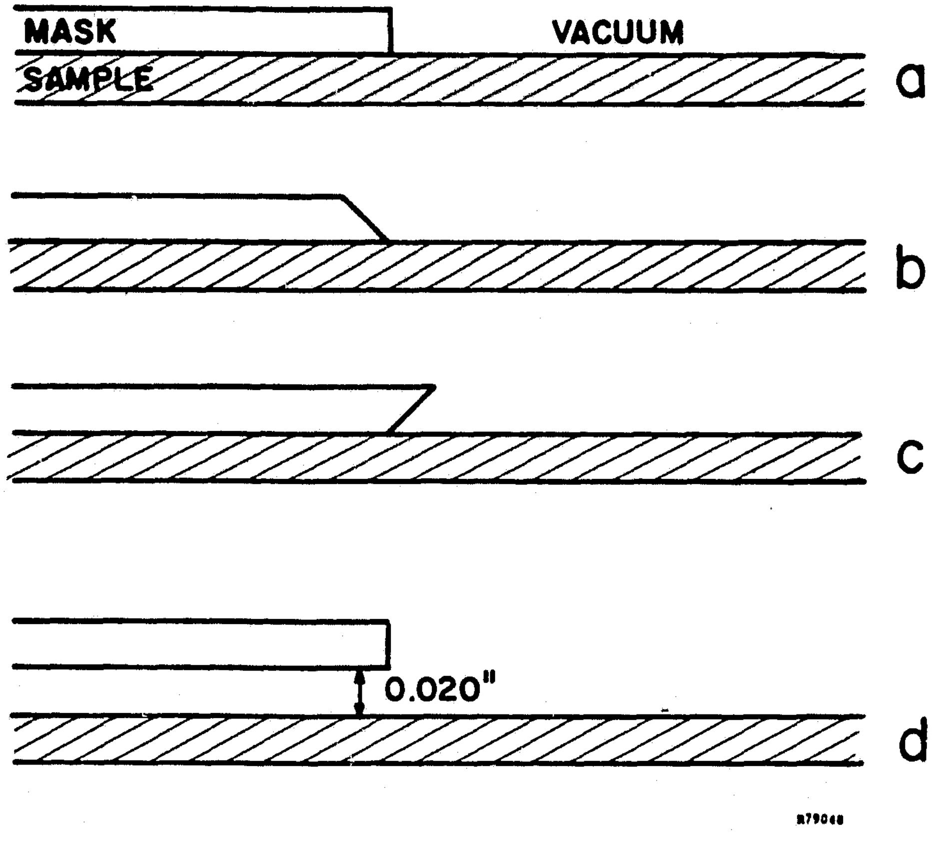

FIGURE 2-54. SCHEMATIC REPRESENTATION OF MASK EDGE DETAILS FOR PULSED ELECTRON BEAM PROCESSING

FIGURE 2-55a. MICROPHOTO OF EDGE OF ANNEAL PATTERN USING CARBON MASK 0.5 mm (0.02 inch) OFF WAFER SHOWING UNIFORMLY SHARP CONTOUR CHANGE

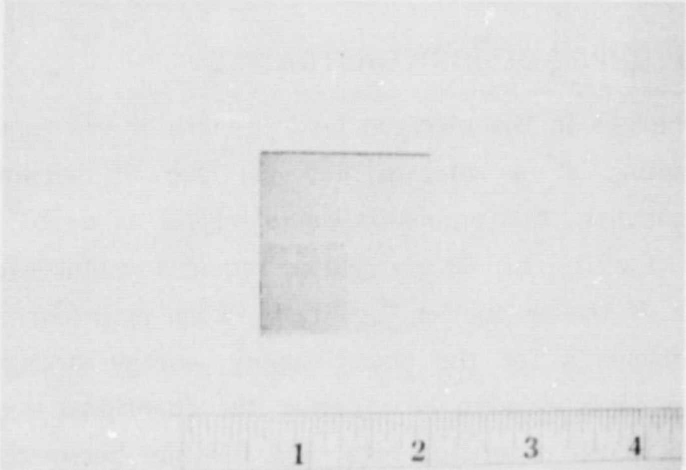

FIGURE 2-55b. SQUARE PATTERN ANNEAL (1 PULSE) COVERING ONE-QUARTER OF SAMPLE

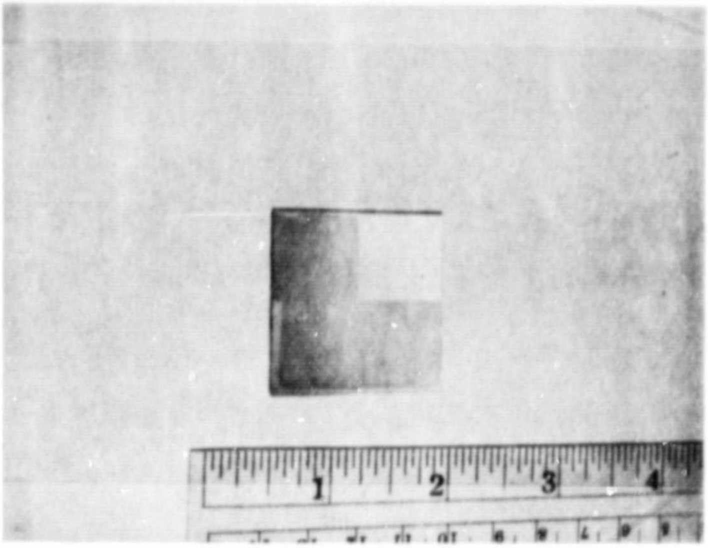

FIGURE 2-56. PHOTOGRAPH OF STEP AND REPEAT ANNEAL PATTERN ON 4 x 4 cm ION-IMPLANTED SILICON SHEET

after 1 pulse but nearly complete annealing after 10 pulses. The point probe open-circuit voltage under AM0 illumination was 480 mV compared to 520 mV from a single pulse anneal and 540 mV after furnace annealing. Results would improve with optimization of the technique.

2.7 PULSER THROUGHPUT DESIGN CONSTRAINTS

Significant changes in the electron beam generator are required to build a pulse processor for annealing at a rate of 600 cm^2/sec of ion-implanted silicon. At 50 cm^2/pulse for annealing, this processor would trigger at 4×10^8 times per year. The existing laboratory facility at 50 cm^2/pulse requires maintenance every $1 - 2 \times 10^3$ pulses. The lifetime of the production facility between maintenance downtime is a key requirement. Requirements for the power supply, energy storage, switch, and beam cathode-anode components capable of meeting the functional requirements for beam fluence, pulse width, pulse repetition rate, and lifetime between periods of scheduled maintenance have been identified.

If a single large pulse is no longer suitable (i.e., a beam 20 x 20 cm square is not considered feasible because of the extremely high currents that must be switched) and given that step and repeat annealing is a realistic process to consider, the energy of a single pulse is variable. The fluence, or energy per unit area, must remain constant, but the diameter of the electron beam can vary. The economic balance between a smaller number of high-energy electron beam geneators and many smaller, but simpler beam generators is being determined but is outside the scope of this effort. Here, we note the technical benefits of using smaller, lower energy beams:

- The lifetime of a high-current switch increases as the energy per pulse decreases.
- The transmission lines, or replacement components, will have a greater lifetime and smaller size. Volume scales roughly as the square of the energy in a pulse.
- The anode may not be needed, focusing may not be required, contamination can be reduced, and the mask (described in Section 2.7.2) may not be necessary.

The assumption of approximately constant fluence is based upon fixed material properties and a narrow range of acceptable pulse widths. Too short a pulse and the silicon will crack due to shock, while too long a pulse will allow significant energy to be diffused thermally into the wafer, leading to very deep junctions and lower solar cell performance. The acceptable range for electron beam pulse width is about 10 ns to 200 ns for annealing ion implantation damage to the silicon crystal by liquid phase epitaxy. No successful annealing, with any technique, fall outside this range, as shown in Figure 2-57. Spire Corporation has available an electron beam generator (the SPI-PULSE 600) with a 40-ns pulse width. It stores 20 percent of the energy of the existing pulse annealing equipment at the same charging potential in 1/20 of the volume. It was used to answer the question on the suitability of lower energy beams for implant annealing. For comparison, commercially available equipment currently used for semiconductor processing has a pulse width 100-150 ns long and is adjustable, but has a maximum fluence of only 0.1 joule/cm^2 per pulse, an order of magnitude too small.

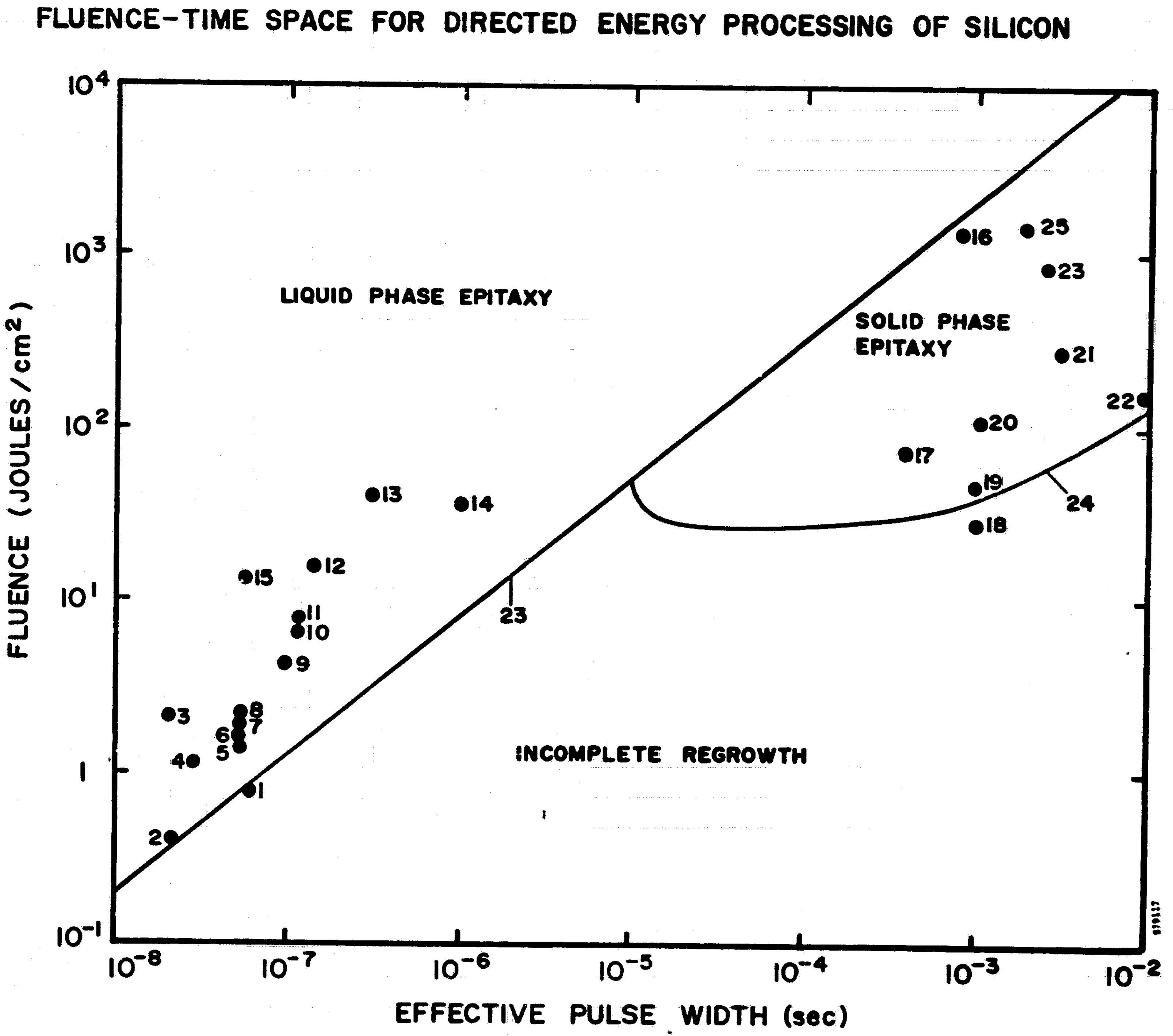

FIGURE 2-57. SUMMARY OF EXISTING EXPERIENCE ON THE USE OF PULSED ENERGY ANNEALING OF ION IMPLANTATION DAMAGE (Note: Numbers beside data points are referenced on p. 2-109)

REFERENCES FOR DATA POINTS OF FIGURE 2-57

No.	First Author	Journal	Laser
1	Kirkpatrick	IEEE Trans. ED-24, 429 (1978)	e-beam
2	Shtyrkov	Sov. Phys. Semicond. 9, 1309 (1975)	Nd:YAG
3	Revesz	Appl. Phys. Lett. 33, 431 (1978)	Ruby
4	Narayan	J. Appl. Phys. 49, 3912 (1978)	Ruby
5	Young	Appl. Phys. Lett. 32, 139 (1978)	Ruby
6	Lysenko	Sov. Phys. Semicond. 11, 1327 (1977)	Ruby
7	Foti	J. Appl. Phys. 49, 2569 (1978)	Ruby
8	Foti	Phys. Lett. 65A, 430 (1978)	Ruby
9	Kutukova	Sov. Phys. Semicond. 10, 265 (1976)	Ruby
10	Celler	Appl. Phys. Lett. 32, 464 (1978)	Nd:YAG
11	Beri	Appl. Phys. Lett. 33, 137 (1978)	Ruby
12	Bean	Appl. Phys. Lett. 33, 227 (1978)	Nd:YAG
13	Celler	Appl. Phys. Lett. 32, 464 (1978)	CO_2
14	Kistemaker	(Unpublished) FOM-42.593, AMOLF-77/260 (Amsterdam) (1977)	Nd:YAG
15	Greenwald	(Unpublished) Spire Corp. (1978)	CO_2
16	Gat	Appl. Phys. Lett. 32, 276 (1978)	Ar
17	Gat	Appl. Phys. Lett. 33, 389 (1978)	Kr
18	Minnucci	(Unpublished) Spire Corp. (1976)	Ruby
19	Minnucci	(Unpublished) Spire Corp. (1976)	Nd:YAG
20	Kachurin	Sov. Phys. Semicond. 11, 1178 (1977)	Flash lamp
21	Antonenko	Sov. Phys. Semicond. 10, 81 (1976)	Ruby
22	Kachurin	Sov. Phys. Semicond. 10, 1128 (1976)	Ar
23	Greenwald	(Unpublished) Spire Corp. (1978)	e-beam
24	Williams	Appl. Phys. Lett. 33, 542 (1978)	Ar
25	Auston	Appl. Phys. Lett. 33, 539 (1978)	Ar

Approximately 250 pulses using implanted silicon samples for diagnostic instruments as targets were processed with the 1-inch diameter SPI-PULSE 600 facility. A typical electron energy spectrum, reduced from measurements of the diode voltage and current, is shown in Figure 2-58. The average electron energy and fluence at the sample are comparable to results on the larger facility. The implant anneal pattern on a wafer is shown in Figure 2-59.

Electrical solar cell measurements of these samples showed very low open-circuit voltages, less than 400 mV. The loss of V_{oc} is believed to be caused by point defects below the junction region in the pulse annealed ion-implanted silicon. This region is heated but not melted during pulsed processing, and therefore the rapid quenching can introduce defects in the material. One solution to this problem is to use a more shallow deposition profile (reducing heating below the junction) of electron beams with a grazing angle of incidence. This profile is achieved in the larger pulse anneal facility by focusing the beam and causing it to rotate in a magnetic field. On the smaller facility, focusing the electron beam (but maintaining constant fluence at the sample) increased the open-circuit voltage V_{oc} to 480 mV. A suitable magnet was not available, but it is believed that the use of magnetic fields would increase the electrical performance of a pulse anneal to the level seen on the larger facility.

Because the electrical performance of implanted silicon samples annealed by the lower energy beam was less than the performance of samples annealed by the standard beam used to date, a second series of experiments was performed on the SPI-PULSE 6000 facility, using an aperture at the anode to reduce beam size. The experimental apparatus was similar to that shown in Figure 2-53, except that the carbon mask was placed next to the anode or used in place of the anode. The mask had circular holes with various diameters. The important physical difference in location of the mask is that the propagation of a smaller diameter, low-current beam from the anode to the sample shows less self-interaction than the larger, high-current beam and in effect resembles a small electron beam generator. Experimental results showed the lack of beam self-focusing. The electron beam fluence was too low with the standard beam in the diode. Increasing the charging voltage in the energy storage capacitor increased both the current and average electron energy in the apertured beam, which did anneal the ion-implant damage but with poor electrical results, similar to those from the smaller facility. Increasing the current density without focusing by decreasing the cathode diameter from 7.6 to 5.0 cm increased the diode impedance. The charging voltage was then adjusted to maintain approximately the same electron energy spectrum, and samples were adequately

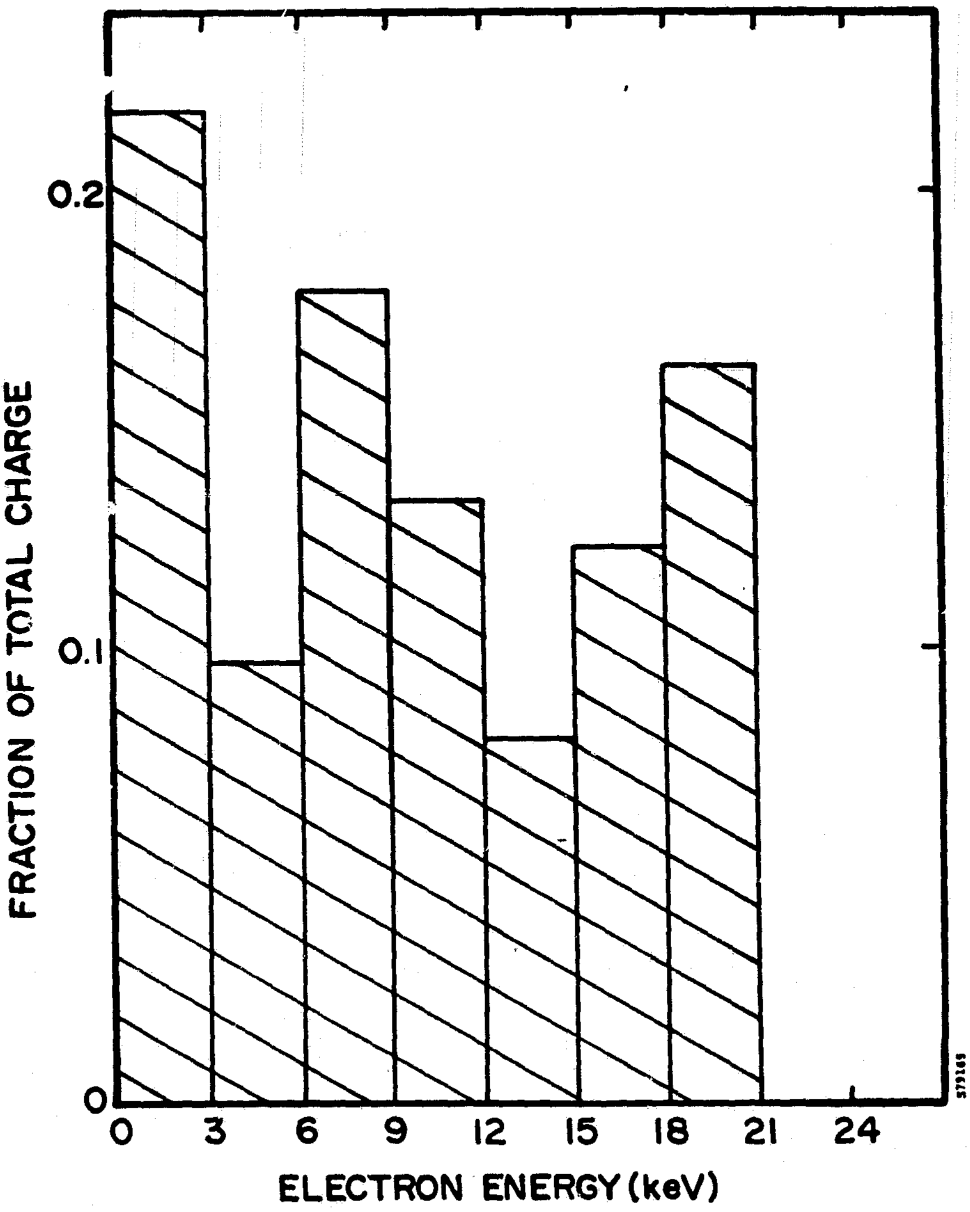

FIGURE 2-58. ELECTRON BEAM ENERGY SPECTRUM FOR 1-INCH DIAMETER SPI-PULSE 600 PULSED ELECTRON BEAMS

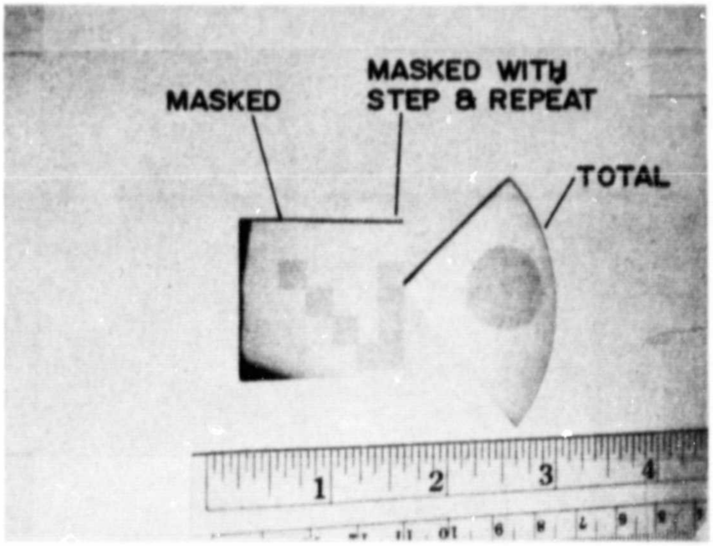

FIGURE 2-59. TYPICAL PULSED ELECTRON BEAM ANNEAL SIGNATURE FOR OVERLAP PULSES FOR STEP AND REPEAT OPERATION OF SPI-PULSE 600

annealed with the small aperture in place. The carbon mask could not be used as an anode when the diameter of the opening greatly exceeded the cathode-anode gap.

As a result of these experiments the following conclusions were drawn with respect to the design of the pulse forming network (PFN):

- With constant fluence at the silicon wafer, and with constant electron energy spectrum, the diameter of the pulsed beam may be varied.
- There is no minimum beam diameter or total energy except as implied by the criterion of large angles of incidence of the electrons at the sample surface.
- The anode is essential for the propagation of the electron beams of interest for annealing when the current at the appropriate electron energy (10 - 12 keV) exceeds the space charge limiting value of approximately 5 amperes.

2.7.1 Power Supplies for Pulsed Electron Beam Processors

Power supplies for pulse processor applications must be chosen primarily on the basis of the maximum voltage required to charge the energy storage capacitor, and the maximum necessary charging current for the required repetition rate. The latter is a function of both the capacitance of the store and the pulse repetition rate. For one-of-a-kind experiments and single shot processing, Van de Graaff generators, operable up to 400 kVdc and 50 microamperes, have proven useful. Repetitive processing at intermediate rates of about 10 cm^2 of annealed surface per second requires a power supply with a 1 mA current at 300 - 400 kV, while final processing goals of 600 cm^2/sec may require supply currents up to 100 mA. Output currents of this magnitude place exceedingly harsh demands on all but the most carefully designed high-voltage power supplies.

Two categories of commercially available supplies will be useful for these higher current applications. Gas-insulated, multistage Crockroft-Walton high frequency (30 kHz) driven units can supply the 1 - 2 mA currents required for intermediate processing applications of up to 50 cm^2/sec. The inherent compactness of the high-voltage multiplier section in the Crockroft-Walton supply allows its installation directly inside the enclosure of large PFN's like the SPI-PULSE 6000, which are generally operated in a high-pressure, insulating gas environment. The need for high-voltage supply cables and feedthrough bushings from supply to energy store is thus eliminated. In addition, the ability to control the supply output voltage with a small control voltage makes such supplies ideal for programmed repetitive charging cycles.

A single multistage Crockroft-Walton power supply cannot provide the 100-mA charging currents necessary for the final processing goal of 600 cm^2/sec. For this more demanding application, a 60-Hz transformer-rectifier supply appears necessary. This type of supply must generally be mounted externally and connected to the PFN with a high-voltage cable because of its large size. There appears to be little advantage to using gas-insulated high frequency supplies when external mounting is required. Many traditionally designed and well tested oil-immersed power supplies are commercially available at costs lower than Crockroft-Walton supplies rated at the same voltage and current. The most critical component of external power supplies is in fact the connecting cable and feedthrough bushing to the high-pressure capacitor. The highest voltage levels of 400 kVdc used in pulse annealing applications appears to be within the limits of state-of-the-art technology in this area.

The relative costs of the supplies discussed in this section are summarized in Table 2-22.

2.7.2 Pulse Forming Network

Experimental work to date at Spire has demonstrated the usefulness of existing coaxial-charge-store pulse forming networks (PFN's) for PEBA applications. In particular, the incorporation of a DC charged, solid dielectric energy store into the PFN allows control of beam energy at a level of precision not generally obtainable with dynamically charged gas or liquid dielectric energy stores. Such precision is essential for the reproducibility of the pulse processing of ion-implanted silicon.

The major drawback of solid dielectrics has generally been their lack of self-reparability in the event of high-voltage breakdown of the insulator. Nevertheless, capacitor prototypes developed at Spire using advanced manufacturing techniques and optimized dielectric materials have not yet experienced volume puncture after more than 10^3 shots at the designed charging voltage of 400 kV.

TABLE 2-22. COMPARATIVE SPECIFICATIONS AND COSTS FOR POWER SUPPLIES FOR PULSE PROCESSOR APPLICATIONS

Power Supply	Representative Commercial Unit	Voltage (Current)	Annealing Rate	Approx. Cost
High Frequency Crockroft-Walton Multiplier	Deltaray S-400	400 kV (1 mA)	10 cm^2/sec	$10,000
Transformer-Rectifier	Hippotronics 2300	300 kV (10 mA)	100 cm^2/sec	$9,000
Transformer-Rectifier	Universal Voltronics BAL-300	300 kV (100 mA)	600 cm^2/sec	$20,000
Transformer-Rectifier	Universal Voltronics	450 kV (80 mA)	600 cm^2/sec	$50,000

Operation of such energy storage capacitors at lower voltages near 100 kV will greatly increase the projected lifetime. We estimate a minimum of $10^7 - 10^8$ shots, based on available lifetime data from pulsed capacitor manufacturers. Experiments to date indicate that successful anneals at these lower voltages should be possible.

Another source considered possible for use as a PFN energy store involves the use of several commercial, low-inductance capacitors available at rated voltages up to 100 kV. The chief advantage of lower system cost is offset by the increased system inductance, which leads to longer risetime of the electron beam pulse. Total energy store charging voltage will generally be lower, in the 50 - 100 kV range, so that capacitor lifetime can be enhanced by major voltage derating. Preliminary estimates, based on a system using eight rectangular 100-kV, 20-nanohenry, 0.3-microfarad capacitors, indicate that risetimes on the order of two or three times longer than those achievable with existing coaxial PFN's should be possible. It is not yet known whether the increased risetimes will influence the pulse annealing mechanism.

2.7.3 High Voltage Switching

Large-scale pulse annealing processors will require reliable, long-lifetime, high-voltage switches for activation of the electron beam pulse. This relatively underdeveloped area of technology will be an extremely critical one in any final processor design for production applications.

Continuous-duty switching problems occur because electrode materials deteriorate in time with the necessary current levels. Degradation of the insulating medium, usually a gas between the switch electrodes, can also occur. Various investigators elsewhere have identified important high-voltage pulsed switch parameters, but design criteria have by no means been optimized.

Switch experiments planned on existing Spire high-repetition-rate pulser facilities are aimed at selecting the best switch design for our specific pulseforming network and pulse annealing applications.

2.7.4 Scanning DC Electron Beam Annealing

As part of the determination of the manufacturing feasibility of pulse annealing, DC, or continuous, electron beam scanning has been assessed as an alternative method of directed annealing. Calculations were performed to evaluate the feasibility of annealing large silicon sheets on a suitable platen or carrier. Input data for the calculation was as follows:

Material:	Polycrystalline sheet silicon
Thickness:	0.38 mm (0.015 inch)
Size:	20 x 20 cm
Transfer rate:	30 cm/sec
Cassette:	Silicon carbide or equivalent
Electron beam:	20 cm long x 0.5 to 50 cm wide

This calculation assumes that the final temperature is 1412°C (the melting point for silicon), but none of the material is melted. It was concluded that, on the time scales of interest, the temperature profile throughout the depth of the material is nearly uniform and the flow of heat in the direction of motion is small. The calculation of heat input (average heat capacity x total mass x temperature rise) is accurate enough for initial design parameters. The transfer of heat by radiation to the surrounding space or conduction to the wafer cassette is small but nonnegligible compared to the thermal input.

<u>Approximate Calculations</u>

The average heat capacity from 298°K to 1685°K for crystalline silicon, based upon the integration of the equation for heat capacity given by Runyan, is 0.916 joule/g°C.(9)

The sheet is 380 micrometers (0.015 inch) thick, and its mass per unit area is 8.88 g/cm^2.

The fluence required to reach melt temperature (neglecting heat flow) is 112.8 J/cm^2.

The total beam power required at 600 cm^2/sec is approximately 68 kW.

One-Dimensional Solution to Heat Flow in a Moving Slab

The silicon slab is very thin compared to its length or width or distance traveled in one second. For an approximate pulse width of 15 msec (equivalent to the time that any point on the surface is irradiated by the electron beam), the characteristic depth to which heat is transported by thermal diffusion for a semi-infinite slab would be:

$$x \sim (4Kt)^{1/2} = (4 \times 0.224 \text{ cm}^2/\text{sec} \times 0.015 \text{ sec})^{1/2} = 0.116 \text{ cm} \qquad (1)$$

This is approximately three times the width of the slab, justifying the assumption of a uniform temperature profile throughout the thickness of the slab.

To compute the flow of heat along the slab, on neglecting edge effects since there is no variation in depth $\hat{z}$ or thickness $\hat{y}$, the problem is one-dimensional in the direction of motion of the slab, $\hat{x}$. For a thin, infinitely long rod with a perimeter p and cross-sectional area w — moving in the direction $\hat{x}$ at a constant velocity u, with the point at x = 0 held at a fixed temperature T_1 — the temperature profile is given by Carlsaw and Jaeger:

$$T = T_1 \exp \frac{u - (u^2 + 4K\nu)^{1/2}}{2K} x \qquad (2)$$

$K = \kappa/\rho C$ = thermal diffusivity

κ = thermal conductivity

ρ = density

C = heat capacity

$\nu = Hp/\rho Cw$

p = perimeter

w = cross-sectional area

H = surface conductance

The rate of heat loss from the surface of the rod is assumed to be proportional to H $(T-T_o)$, where T_o is the temperature of the surroundings and T varies with x. The units of H are in watts/cm^2•deg. For this problem, the rod has one dimension equal to the thickness of the slab (0.015 inch) while the other dimension $\Delta \rightarrow 0$. Therefore:

$$w = (0.5p - d)\,d$$

$$p = 2\,(d + \Delta)$$

or

$$\nu = H\Delta/\rho cw = H\Delta/\rho c\Delta d = H/\rho Cd$$

Typical values for H for aluminum-aluminum contacts in vacuum, for parts with a fine surface finish but not "optically flat", is approximately 30 BTU/hr-ft^2-°F at 10 PSI pressure between the two surfaces. On assuming this behavior is similar for both rough-cut silicon wafers and ribbon with a silicon carbide "flat" holder and also on assuming a pressure of 0.1215 PSI and $H \propto P^{2/3}$, then $H \sim 9.0 \times 10^{-4}$ W/cm^2 - °C. (Note: Data is taken from the <u>Handbook of Heat Transfer</u>.) Another approximation would assume purely radiative heat transfer as T^4 with a maximum value of 45.7 W/cm^2, which, divided by the temperature, gives $H \sim 0.027$ W/cm^2 - °C. The radiation treatment does not follow from the linear heat loss rate with temperature used to develop Equation (2), which overestimates the cooling.

The value of ν can now be estimated at between 0.011 and 0.33 sec^{-1}. The value of $K\nu$ is at most 0.074 cm^2/sec compared to 900 cm^2/sec^2 for u^2. Therefore, Equation (2) can be simplified:

The value of can now be estimated at between 0.011 and 0.33 sec^{-1}. The value of K is at most 0.074 cm^2/sec compared to 900 cm^2/sec^2 for u^2. Therefore, Equation (2) can be simplified:

$$\frac{u - (u^2 + 4K\nu)^{1/2}}{2K}\, x \equiv -\nu x/u \qquad (3)$$

$$T \equiv T_1 \exp\,(-\nu x/u)$$

where:

$$0.011 < \nu/u < -3.7 \times 10^{-4}$$

The physical interpretation of the results is that the distance for the temperature of the slab to drop from its maximum of 1685°K to room temperature is greater than 90 cm. Cooling by heat transfer along the slab is very small compared to the heat loss through the upper or lower surface.

Fast Pulse Heating

The assumption of a 0.015-sec pulse width was based on a sheet electron beam width of 4.5 mm (30 cm/sec x 15 msec). The electron beam could be focused to about 0.5 mm for a pulse width of 1.66 msec. The effect of this shorter pulse will be computed assuming negligible heat transfer along the slab in the $\hat{x}$ direction. The problem is again one-dimensional (heating a semi-infinite slab) in the $\hat{z}$ direction. The surface temperature is given by W.R. Neal, Spire Corporation, in Report No. TR-78-02:

$$T \cong \dot{F}\, x(t)/\sqrt{\pi \kappa}$$

where κ is the thermal conductivity and x is given by Equation (1). Here $x = 0.0386$ cm, about equal to the substrate thickness, and the fluence F to reach melt is about 51 joules/cm^2. The reduction of a factor of 2 for part (1) is due to not heating the entire substrate uniformly throughout its thickness. Recommended beam parameters form this calculation are:

Fluence:	51 joules/cm^2
Energy:	20 keV
Length:	20 cm
Width:	0.5 mm
Current:	1.5 A/cm^2

Some relaxation of the beam current density may be possible by expanding the width of the line beam to 10 mm; however, 45-mm electron beam line widths would not allow sufficient current density for the required temperature rise.

The important distinction of annealing by scanned DC electron beams as contrasted to pulsed electron beam annealing is the physical mechanism responsible for lattice regrowth. Scanned DC electron beam power densities are limited to temperature increases below the melting point because the entire silicon sheet is uniformly heated and cannot be allowed to melt. Because there would not be a thermal gradient under these heating conditions, any solid phase regrowth occurs extremely rapidly at 1100-1400°C, and polycrystallite formation can be expected to occur in amorphous, implanted layers as the transition occurs to the crystalline phase. In addition, rapid thermal quenching of the silicon material from 1100-1400°C to 25°C will induce recombination centers, decrease minority-carrier lifetime, and lower the solar cell performance.

SECTION 3
ECONOMIC ANALYSIS

Economic analyses have been performed to assess the cost effectiveness of ion implantation as a large-scale manufacturing process. Phase one of the contract emphasized use of JPL's Solar Array Manufacturing Industry Costing Standard (SAMICS) and a desk top calculator to estimate add-on prices for ion implantation and pulse annealing based on existing hardware and projected machine costs for 100 MW per year throughputs.

A summary of the specifications for existing implanters and the Spire design are included in Table 3-1. The results of these SAMICS estimates are shown in Table 3-2 and 3-3. Input data in JPL Format A's are explained in greater detail in the Spire Interim Report No. 78/06 for this contract.

Under phase two of the contract, JPL's Solar Array Manufacturing Industry Simulation (SAMIS) was used to study the cost effectiveness of ion implantation and furnace annealing for junction formation in the following process sequence:

1. Phosphorus Implant Junction
2. Aluminum Implant BSF
3. Furnace Anneal
4. Plasma Etch to Remove Oxide

3.1 SAMIS ESTIMATES FOR JUNCTION FORMATION

The SAMIS III computer model was used to estimate the manufacturer's add-on prices for each of the four process elements listed. Input data was prepared using a standard Format A. The annual production quantities that were considered ranged from 25 through 100 MW per year based on capital equipment designed with a throughput of 100 MW per year (Section 2.[illegible] reviews the implanter design and Section 2.2.5 reviews the belt furnace design). The parameters selected for each of the four junction processing steps are listed below:

1. Phosphorus Implant - Based on the device development efforts of the contract 2.5×10^{15} $^{31}P^{+}$ cm^{-2} dose was used with a tolerance of ±10 percent and at 10 keV. A 100 mA implanter with mass analysis and a throughput of 500 cm^2/sec was utilized in the Format A statements.

TABLE 3-1. SAMICS ION IMPLANTER INPUT DATA

	Implanter		
	Varian/Extrion 200-1000 WF	NOVA NV-10	Spire Design
Beam Current (mA)	4	10	100
Purchase Price K$	350	410	1200
Floor Space (ft^2)	210	72	328
Processing Rate*			
- 3" wafers/hour	300	270	35,000
- m_2/min	0.023	0.021	3.0
Uptime (%)	85	85	85
Purchase Price (1978 $)	350	410	1500
Direct Labor (PRSN*YRS)			
- A3096D (Operator)	1.0	1.0	1.0
- A3704D (E. Tech.)	0.1	0.1	0.1
- 3736D (M. Tech.)	0.1	0.1	0.1

TABLE 3-2. SUMMARY OF SAMICS ANALYSIS FOR ION IMPLANTED JUNCTIONS

Implanter	Ion Beam Current (mA)	Production Year	IPEG Annual Amount (m^2)	Price ($\$/m^2$) Production Year Dollars	Price ($\$/m^2$) 1980 Dollars
Varian Extrion 200-20A	0.1 - 0.2	1978	5.6×10^3	1.01×10^3	1.13×10^3
Varian/Extrion Model 200-1000WF	2 - 4	1982	8.0×10^4	55.67	49.55
		1986	1.7×10^6	68.35	48.17
Automated Production System	100	1982	8.0×10^4	16.58	13.64
		1986	1.7×10^6	2.46	1.73

TABLE 3-3. SUMMARY OF SAMICS ANALYSIS FOR STAND-ALONE PULSED ELECTRON BEAM ANNEALING

Processor	Production Year	IPEG Annual Amount (mA)	Price ($\$/m^2$) Production-Year Dollars	Price ($\$/m^2$) 1980 Dollars
Existing Laboratory Facility	1978	6.6×10^3	530.79	596.54
Automated Production System	1986	1.7×10^6	2.11	1.49

2. Aluminum Implant - A dose of 5 x 10^{15} $^{27}Al^+$ cm^{-2} was selected to replace the $^{11}B^+$ ions used throughout most of this contract. Aluminum was selected for SAMIS analysis because of the inherently higher ion beam currents that are obtainable — at least with Freeman type ion sources. Because of the higher implant dose, the machine throughput was decreased to 250 cm^2/sec.

3. Furnace Anneal was based on a belt furnace capable of a throughput of 500 cm^2/sec with a 550/850/550°C temperature profile and a capital equipment cost of $80K (1979$).

4. Plasma etch was considered a necessary process following furnace anneal to remove any nonintentional SiO_2 prior to metallization. A capital equipment cost of $110K (1977$) was assumed.

The SAMIS company consisted of only three processes with the following referents:

P-IMP 500:	Phosphorus junction implant at 500 cm^2/sec in one machine
A-IMP 250:	Aluminum p^+ implant at 250 cm^2/sec in one machine
FURNACE:	Belt furnace implant anneal
ETCH:	Plasma etch

The results of the SAMIS III simulations are shown in Figure 3-1. For a nonvertically integrated company, the overhead rates are extremely high. For example, at a production rate of 25 MW per year, a company which only implants and anneals has an overhead rate of 7.87 according to the SAMIS III model. At 100 MW/year, the overhead rate drops to 4.4 and the total, add-on price is about $0.041 (1980$) for junction, p+, anneal, and plasma etch.

The cost components for this simulated company are shown in Table 3-4. The major element for implant is the capital equipment cost. In contrast, both direct labor and capital costs are approximately equal for furnace anneal. The product assumed for this company was 7.5 x 10 cm ribbon or sheet material with AM1-28°C efficiencies corresponding to the measured CZ cell performance for the particular anneal cycle being evaluated.

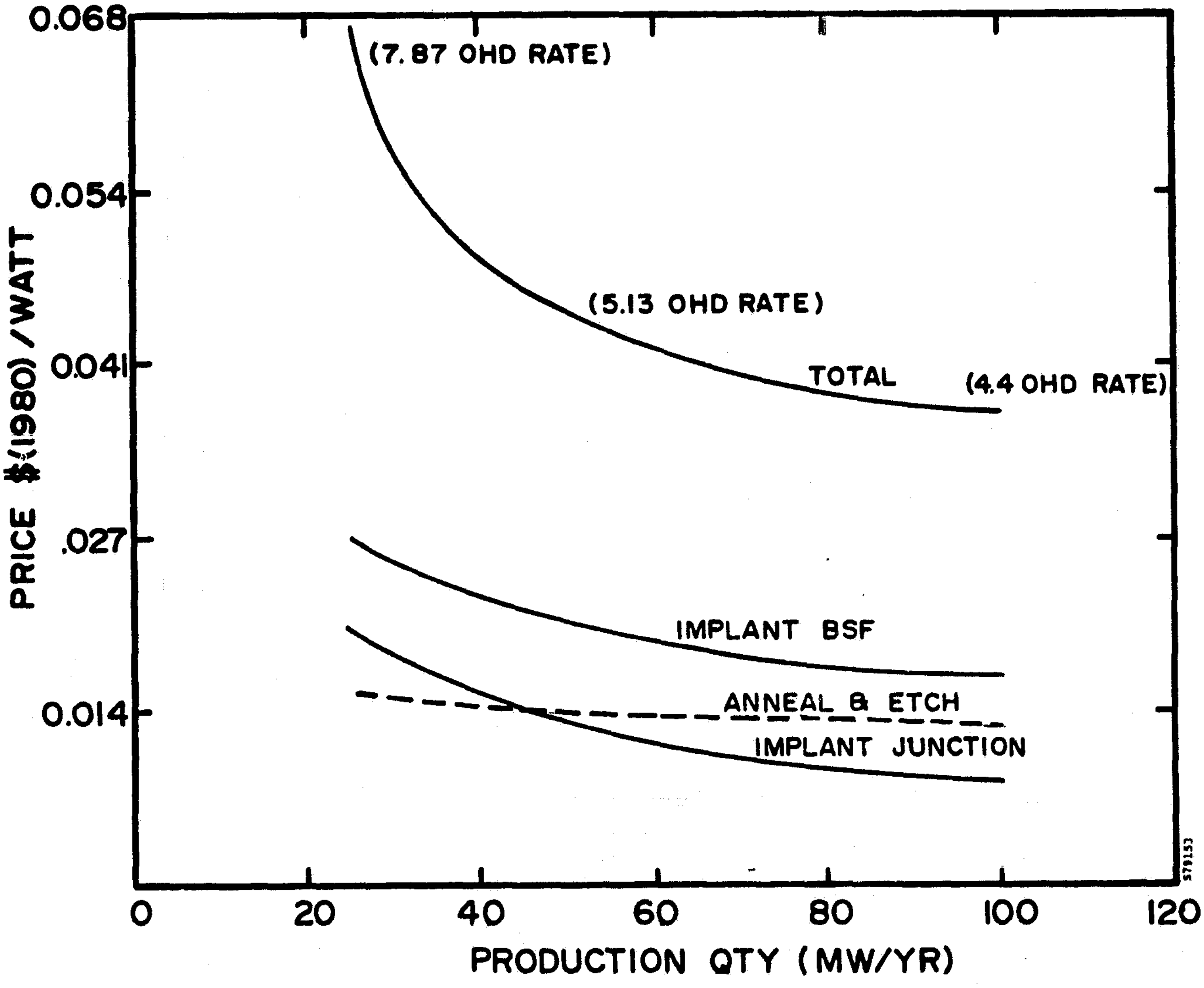

FIGURE 3-1. SAMIS III COST ESTIMATES FOR JUNCTION AND BSF FORMATION

TABLE 3-4. SAMIS III COST ELEMENTS FOR JUNCTION AND BSF FORMATION

Process Element	Cost (1980$/Watt) Capital	Direct Labor	Materials	Utilities	Indirect	Total
Phosphorus Junction Implant	0.0072	0.0005	0.0016	0.0004	0.0037	0.0134
Aluminum P$^+$ Implant	0.0082	0.0011	0.0020	0.0008	0.0016	0.0138
Furnace Anneal	0.0012	0.0005	—	—	0.0012	0.0030
Plasma Etch	0.0037	0.0003	—	0.0001	0.0047	0.0088

Notes: Based on 100 MW per year production rate and 7.5x10cm sheet material.

Additional reductions in add-on price for junction and BSF formation would result by integration of the two ion implanters required into a common vacuum system. The effect on the total add-on price would be reduced capital equipment costs.

3.2 SAMIS ANALYSIS OF FURNACE ANNEALING

The add-on price per peak-watt for furance-annealing and etching 7.5 x 10 cm cells was calculated using the SAMIS III Program. Eight different anneal types which produced cells of varying efficiencies were considered. (Refer to Section 2.2.4 for a discussion of the junction implantation anneal cycles).

The equipment cost, floor space, personnel, utility and commodity requirements for producing a cell of anneal type-2 with an efficiency of 14.7 percent were used as the standard. Since only the processing cost was studied, the initial cost for the annealed wafer was considered to be zero. The personnel requirements were not changed for the different anneal types. All of the other requirements and the equipment cost were scaled as a function of the anneal time (i.e., if the time doubled, the capital equipment costs doubled).

The prices were calculated for industries producing 25, 50, and 100 megawatts per year. Table 3-5 gives a summary of the efficiency, and price per watt-peak for the eight anneal types used. Figure 3-2 shows the same information graphically. Figure 3-3 shows the general trend of processing add-on price for increasing anneal time. Both efficiency and anneal time naturally affect the price per watt. Anneal types 2, 3, and 5 give very similar cost, particularly for the largest industry size. However, at very low production rates it appears that shortening the anneal time is a more effective means of cutting the price than is increasing the cell efficiency by longer anneal times.

A sample SAMIS computer simulation is included in Appendix E. The industry, company and process information used as the input to the simulation is in the listing.

TABLE 3-5. ADD-ON PRICES ($1980/WATT) FURNACE ANNEAL AND PLASMA ETCH PROCESSES

Anneal Type	Anneal Time (Minutes)	CZ Cell Efficiency (%)	Annual Amount		
			25 MW	50 MW	100 MW
STD	225	14.6	0.0210	0.0151	0.0114
1	135	14.6	0.0165	0.0130	0.0101
2	75	14.7	0.0134	0.0114	0.0093
3	15	13.0	0.0108	0.1041	0.0092
4	272	13.4	0,0230	0.0165	0.0122
5	45	14.1	0.0120	0.0108	0.0092
6	135	13.8	0.0169	0.0132	0.0104
7	75	14.2	0.0137	0.0115	0.0095

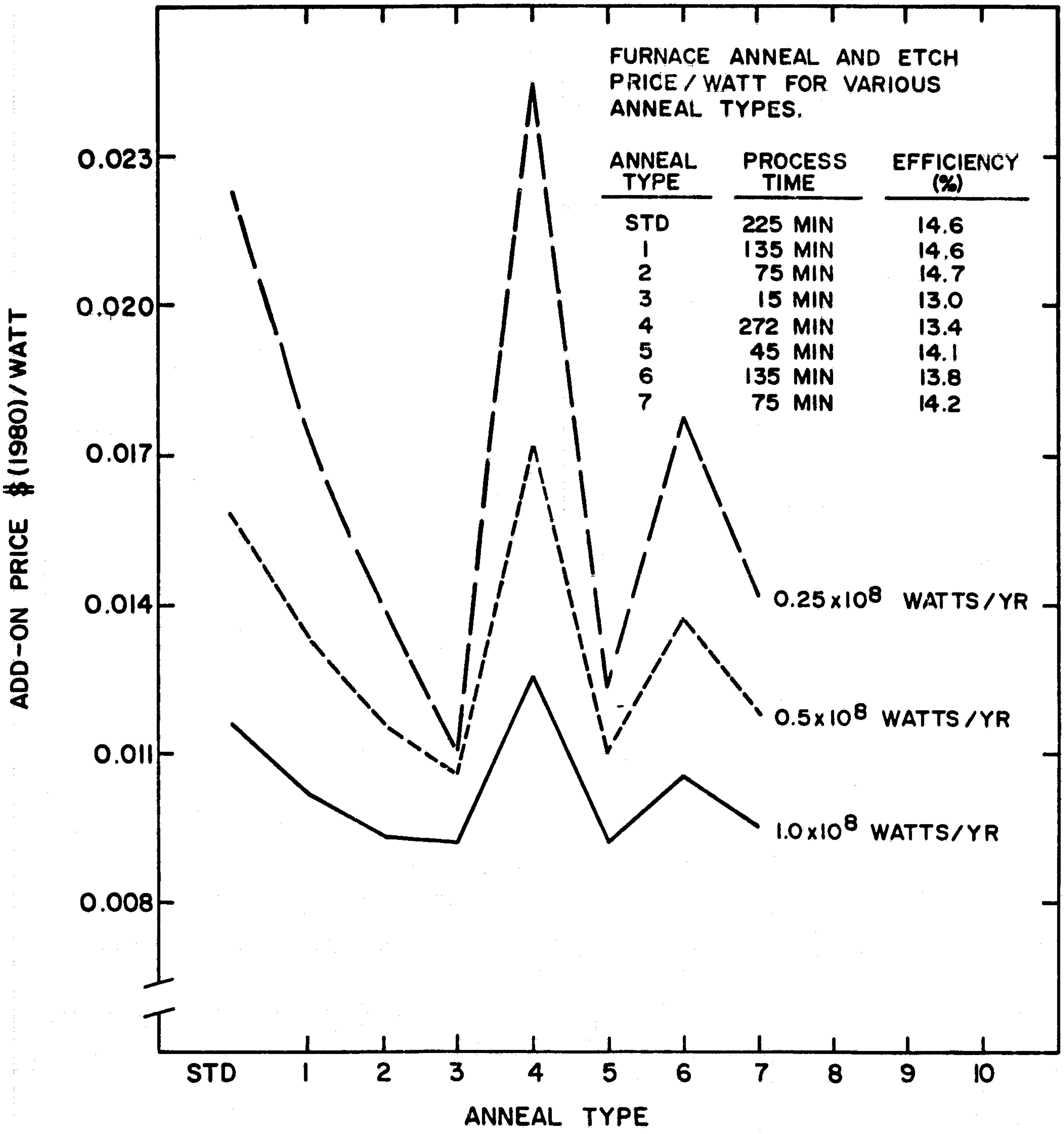

FURNACE ANNEAL AND ETCH PRICE / WATT FOR VARIOUS ANNEAL TYPES.

ANNEAL TYPE	PROCESS TIME	EFFICIENCY (%)
STD	225 MIN	14.6
1	135 MIN	14.6
2	75 MIN	14.7
3	15 MIN	13.0
4	272 MIN	13.4
5	45 MIN	14.1
6	135 MIN	13.8
7	75 MIN	14.2

FIGURE 3-2. SAMIS ADD-ON PRICE FOR VARIOUS FURNACE ANNEAL CYCLES AND PLASMA ETCHING

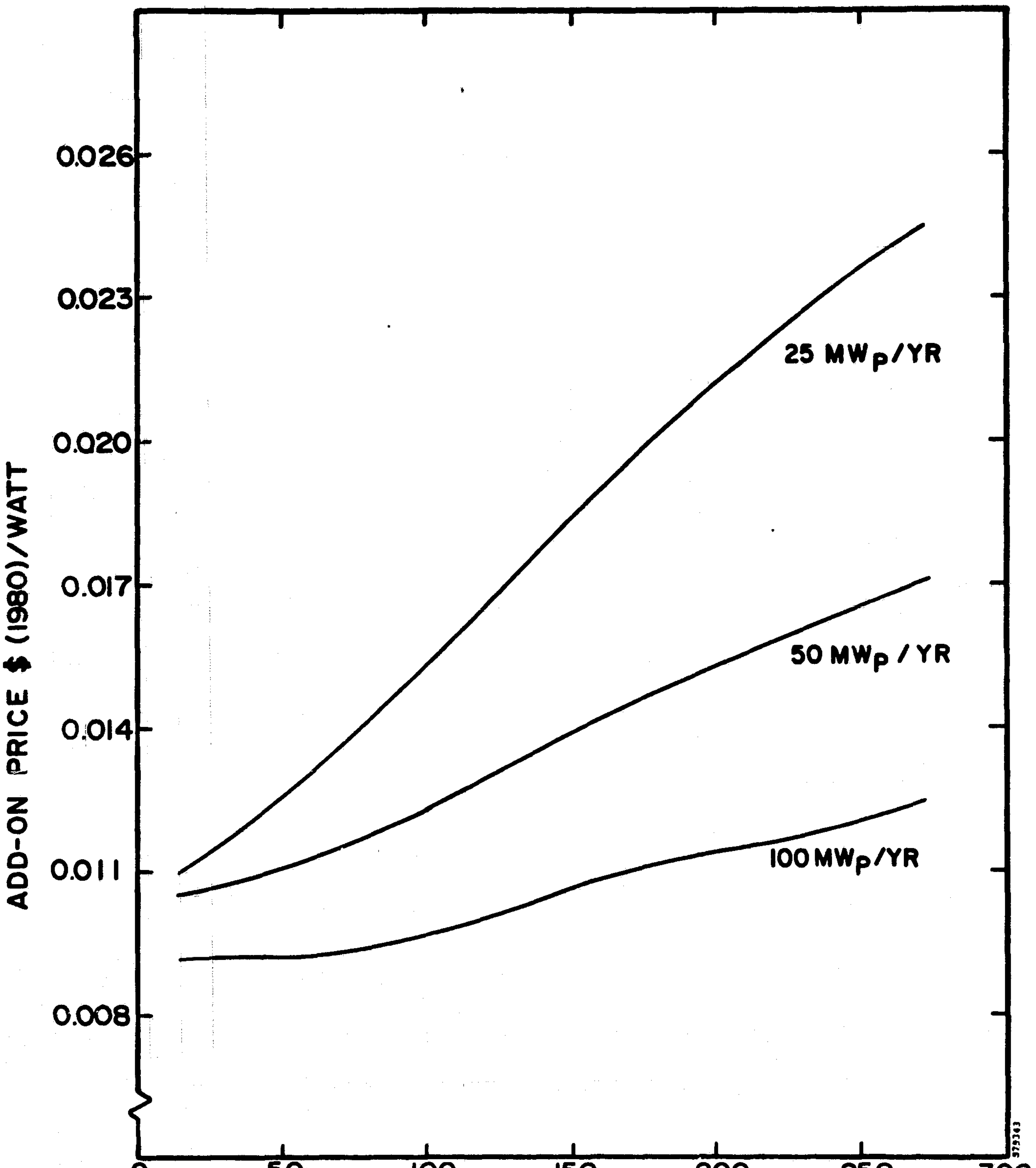

FIGURE 3-3. SAMIS ADD-ON PRICE VERSUS TIME FOR FURNACE ANNEALING AND PLASMA ETCHING

3.3 SAMICS ANALYSIS OF IMPLANTATION HARDWARE

As shown in Table 3-2 and Figure 3-1, ion implantation can be an economical process for junction formation if very large throughput machines are built, and if the annual production quantity is large enough to utilize these high-throughput machines.

To assess the possibility of near term use of ion implantation, a SAMICS analysis was performed for 1978-1984 production levels. For this analysis machine's functional requirements were defined as follows:

Throughput: 900 - 1800 5" wafers per hour
Production Rate: 0.19 - 0.38 m^2/minute
Machine Up-Time: 85%
Machine Cost: 200-250 K (1979 $)
Floor Space: 24 square feet

These data were entered into a Format A process description as shown in Table 3-6 and the SAMICS cost per watt was calculated for annual production quantities of 0.85 through 12 MW per year.

The results of this analysis are shown in Table 3-7 and demonstrate that implantation may be utilized for near term (1980-1982) production providing an implanter can be purchased for approximately $250K (1979$). The relative cost of this type of implanter is shown in Figure 3-4 which shows implanter cost per unit of beam current. The required low-cost per unit beam current necessitates a implanter dedicated to a single ion species and energy.

TABLE 3-6. PROCESS DESCRIPTION FOR SPIRE IMPLANTER

FORMAT A

JET PROPULSION LABORATORY
California Institute of Technology
4800 Oak Grove Dr. / Pasadena, Calif. 91103

PROCESS DESCRIPTION

Note: Names given in brackets [ ] are the names of process attributes requested by the SAMICS III computer program.

A1 Process [Referent] Implant

A2 [Descriptive Name] Spire Implanter (8-10 MW/YR)

PART 1 – PRODUCT DESCRIPTION

A3 [Product Referent] Implant Slice

A4 Descriptive Name [Product Name] Implant Slices @ 2.5 x 10^{15} P^+

A5 Unit Of Measure [Product Units] M^2 (5"ϕCZ = 127.6 cm^2 each)

PART 2 – PROCESS CHARACTERISTICS

A6 [Output Rate] (Not Thruput) 0.190 M^2/Min — Units (given on line A5) Per Operating Minute

A7 Average Time at Station [Processing Time] 1 Min — Calendar Minutes (Used only to compute in-process inventory)

A8 Machine "Up" Time Fraction [Usage Fraction] 0.85 — Operating Minutes Per Minute

PART 3 – EQUIPMENT COST FACTORS [Machine Description]

A9	Component [Referent]	@ ~~15 mA~~	15 mA	
A9a	Component [Descriptive Name] (Optional)	Implanter	Implanter	
A10	Base Year For Equipment Prices [Price Year]	1979	1979	1979
A11	Purchase Price ($ Per Component) [Purchase Cost]	$250K	$200K	$250K
A12	Anticipated Useful Life (Years) [Useful Life]	5	5	
A13	[Salvage Value] ($ Per Component)	$25K	$25K	
A14	[Removal and Installation Cost] ($/Component)	$2.5K	$2.5K	

Note: The SAMICS III computer program also prompts for the [payment float interval], the [inflation rate table], the [equipment tax depreciation method], and the [equipment book depreciation method]. In the LSA SAMICS context, use 0.0, (1975, 4.0), DDB, and SL.

Format A: Process Description (Continued)

A15 Process Referent (From Page 1 Line A1) ____________________

PART 4 – DIRECT REQUIREMENTS PER MACHINE (Facilities) OR PER MACHINE PER SHIFT (Personnel)
[Facilities and Personnel Requirements]

A16 Catalog Number [Expense Item Referent]	A18 Amount Required Per Machine (Per Shift) [Amount per Machine]	A19 Units	A17 Requirement Description
A 2064D	24	Sq. Ft.	Mfg. Space Type A
B 3096D	1.0	PRS*YRS	Semiconductor Assembler
B 3704D	0.07	PRS*YRS	Mechanical Technician

PART 5 – DIRECT REQUIREMENTS PER MACHINE PER MINUTE
[Byproduct Outputs] and [Utilities and Commodities Requirements]

A20 Catalog Number [Expense Item Referent]	A22 Amount Required Per Machine Per Minute [Amount per Cycle]	A23 Units	A21 Requirement Description
C 1032B	0.167	KWHR/Min	Electricity
C 1128D	0.23	KWHR/Min	Cooling Water
D 1016B	200	CFM	Fumes
E 3000X	0.0167	gm/Min	Red Phosphorus
E 1608D	0.042	$/Min	Spare Parts

PART 6 – INTRA-INDUSTRY PRODUCT(S) REQUIRED [Required Products]

A24 [Product Reference]	A26 Usable Output Per Unit of Input Product	A27 Units	A25 Product Name
		/	
		/	None
		/	

Prepared by J.M. **Date** 11/1/79

REVERSE SIDE JPL 3037–S R 7/78

TABLE 3-7. SAMICS ADD-ON PRICE FOR JUNCTION ION IMPLANTATION

Machine	Production Year	1 Peg Quantity		No. of Machines	$/watt Add-On Price	
		(m^2/yr)	(MW/yr)		(1975 $)	(1980 $)
900 wafers/hour 5" CZ $200 K, 15% AM1 cells	1978	5.66×10^3	0.85	1	0.231	0.312
	1980	2.12×10^4	3.18	1	0.087	0.118
	1982	8.08×10^4	12.1	2	0.056	0.075
900 wafers/hour 5" CZ $250 K, 15% AM1 cells	1978	5.66×10^3	0.85	1	0.254	0.343
	1980	2.12×10^4	3.18	1	0.093	0.126
	1982	8.08×10^4	12.1	2	0.059	0.080
900 wafers/hour 5" CZ $250 K, 15% AM1 cells	1978	5.66×10^3	0.85	1	0.247	0.334
	1980	2.12×10^4	3.18	1	0.086	0.116
	1982	8.08×10^4	12.1	1	0.035	0.047

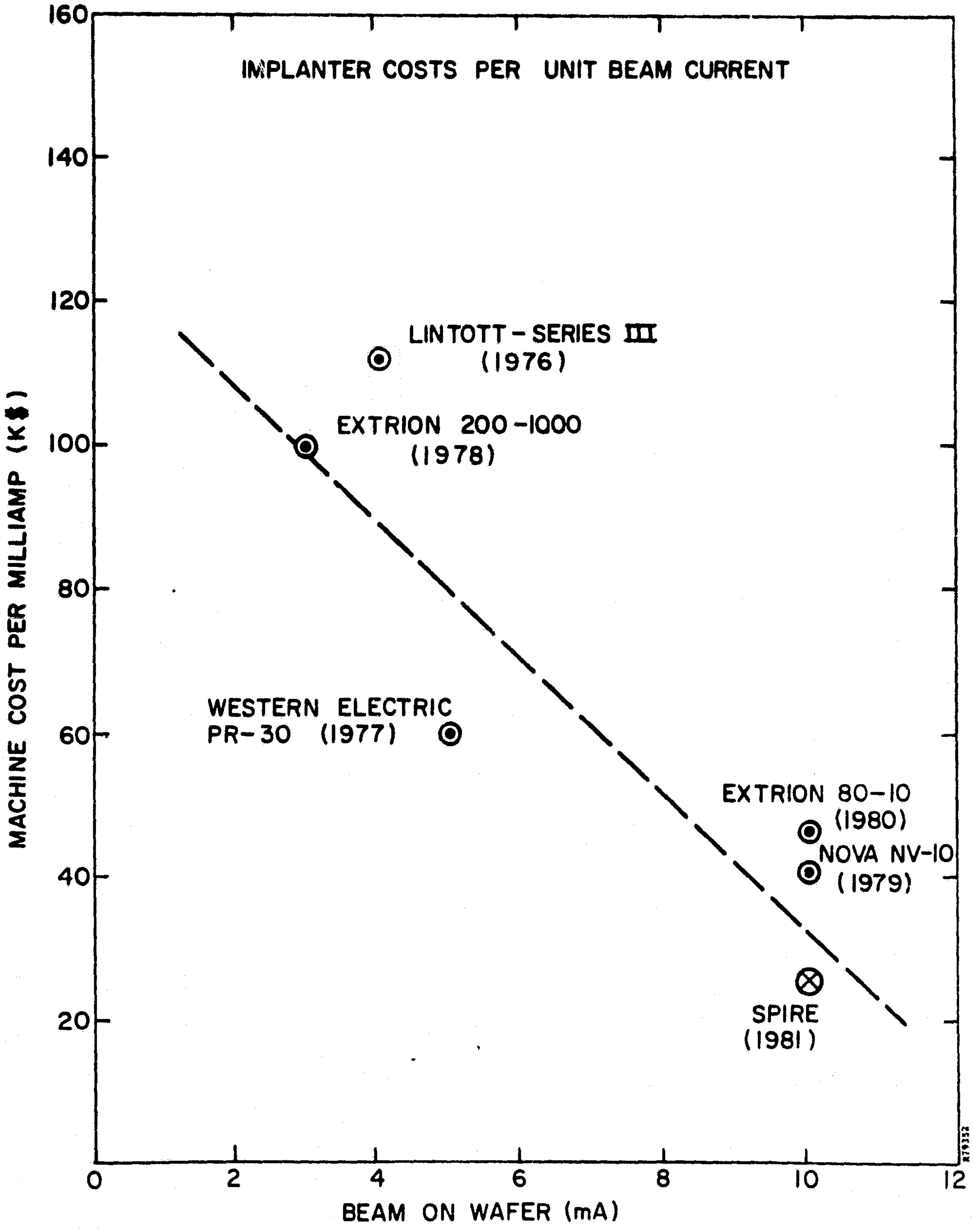

FIGURE 3-4. ION IMPLANTATION MACHINE COSTS PER UNIT BEAM CURRENT

SECTION 4
CONCLUSIONS

This report has described the results of an 18-month program to develop ion implantation and associated processing for automated production of solar cells. Significant accomplishments of this contract include:

1. Operation of a dedicated, state-of-the-art solar cell implanter for 16 months. Implanter setup parameter procedures have been defined for implant uniformities better than ±10 percent. Throughputs of 300 wafers per hour have been achieved at doses of 2.5×10^{15} $^{31}P^{+}$. Cells processed using these implant specifications and thermally annealed using the standard sequence have average efficiencies of 15 percent AM1 and peak efficiencies as high as 16.5 percent AM1 for 3-inch diameter cells.

2. Completion of the design of a 100-MW_e/yr automated production ion implantation machine. This implanter will deliver 100 mA of a mass-separated ion beam onto silicon wafer, sheet, or ribbon material transported through the machine in carriers. Analysis, using JPL's Solar Array Manufacturing Industry Costing Standards (SAMICS) methods, shows that the cost for solar cell junction implants will be only $0.01 per peak watt if 100-mA facilities are available.

3. Development of a reproducible back surface field (BSF) process using high-dose boron implantation. Open-circuit voltages averaged 0.595V for 10-ohm-cm BSF cells delivered to JPL. The advantages of implanted BSF structures include compatibility with thin CZ wafers due to the absence of wafer distortion and the characteristics of line-of-sight processing, which eliminates temporary diffusion masks in the process sequence.

4. Development of functional requirements for a pulsed electron beam system for single-pulse annealing of high-dose implants. Both the throughputs and operational mode of the pulsed electron beam annealer (PEBA) are compatible with the ion implanter.

5. Identification of a physical mechanism and development of a computer model for pulse annealing of ion implantation in semiconductors. The liquid phase, epitaxial regrowth annealing model was developed under this contract.

6. Selection of a manufacturing process sequence based on ion implantation for junction and back surface field formation. The process sequence also includes pulse annealers which can be integrated with ion implanters in a junction formation processor.

7. Identification of a cost-effective annealing schedule which can be specified for belt furnace hardware. The anneal schedule effectively anneals phosphorus junction implants and boron BSF implants simultaneously. The cycle requires only 75 minutes compared to 265 minutes for the performance optimized anneal cycle developed during Phase I of the contract.

8. Demonstration of step and repeat pulse annealing using either solid phase or liquid phase epitaxial regrowth. The application of step and repeat annealing allows annealing of rectangular geometry, sheet silicon materials with dimensions of up to 20 x 20 cm.

9. Development of large-area pulsed electron beams for annealing 7.6-cm wafers with a single pulse. The advantages of pulse annealing of ion implantation damage include simplified process sequences due to the absence of wet chemistry, and throughputs — compatible with high current implanters — that are easily scaled.

10. Delivery of 2,000 high-efficiency solar cells to JPL. The 7.6-cm diameter deliverable cells included implanted/furnace annealed, implanted/pulse annealed, and diffused junctions. For comparison, implanted/laser and implanted/electron beam pulse annealed junctions were assessed, using a 2 x 2-cm solar cell structure.

In general, the higher efficiency cells — both peak and on average — were manufactured using implantation and furnace annealing. Cell efficiency was found independent of cell sizes from 2 x 2-cm to 7.6-cm round wafers. Slightly lower peak efficiencies and less reproducible results were obtained by pulse annealing. This performance deficiency was attributed to three causes: (1) nonuniformity within the 7.6-cm diameter pulsed electron beam, (2) less than adequate reproducibility from pulse to pulse, and (3) limitations of the laboratory pulser which constrained the average electron energy to 25 keV for 7.6-cm diameter pulses. Higher efficiency 2 x 2-cm cells were obtained with 5.0-cm diameter pulses with an average electron energy of only 12 keV.

In summary, this contract has resulted in development of solar cell processing based on ion implantation, pulse annealing, and absence of wet chemistry. The process is compatible with state-of-the-art efficiencies and is attractive for low-cost production of solar cells from either Czochralski or sheet silicon materials.

SECTION 5
NEW TECHNOLOGY

No new technology has been developed to completion during this contract.

SECTION 6
RECOMMENDATIONS

Dedicated ion implanters should be designed and fabrication costs estimated for single-ion, single-energy machines with throughputs of 1,800 wafers per hour. Satisfactory pulse processors for annealing ion implantation damage in silicon should be designed and built with throughput rates of 1,800 wafers/hour. As a part of this development, requirements should be identified for long-term, high repetition rate operation. Ultimately, both ion implantation and pulse annealing should be carried out in a common vacuum by integration of these component machines into a junction processor.

Further machine and process-sequence development should now be directed toward the possibility of ion implantation without mass analysis. This development should include SAMICS analysis of non-mass-analyzed processing. Selection of hardware should be made so that the hardware can be integrated in a pulse processor. The junction formation processing sequence would include:

1. p^+ introduction by charged particle deposition
2. pulse anneal
3. ion implantation for junction with or without mass-analysis
4. pulse anneal.

REFERENCES

1. A. R. Kirkpatrick, et al., "Development of Methods and Procedures for High-Rate Low-Energy Expenditure Fabrication of Solar Cells", JPL Document No. 954289-76/4. Spire Corporation, Bedford, Masschusetts (1976).

2. J. A. Minnucci, "Development of Pulsed Processes for the Manufacture of Solar Cells", JPL Document No. 954786-78/06, Spire Corporation, Bedford, MA (1978).

3. Nova Associates, Beverly, Massachusetts.

4. R. Handy, Solid-State Electron. **10**, 765 (1976).

5. M. Wolf, Proc. IRE **48**, 1246 (1960).

6. W. Matzen, et al., 12th IEEE Photovoltaic Specialists Conf. Proc., 340 (1976).

7. M. Y. Tsai and B. G. Streetman, J. Appl. Phys. **50**(1), 183 (1979).

8. J. D. Gerson, et al., J. Appl. Phys. 48(11), 4821 (1977).

9. W R. Runyan, Silicon Semiconductor Technology, McGraw-Hill (1965).

APPENDIX A

SYSTEM DETAIL DRAWINGS FOR AUTOMATED ION IMPLANTER WITH 500-cm^2/sec THROUGHPUT

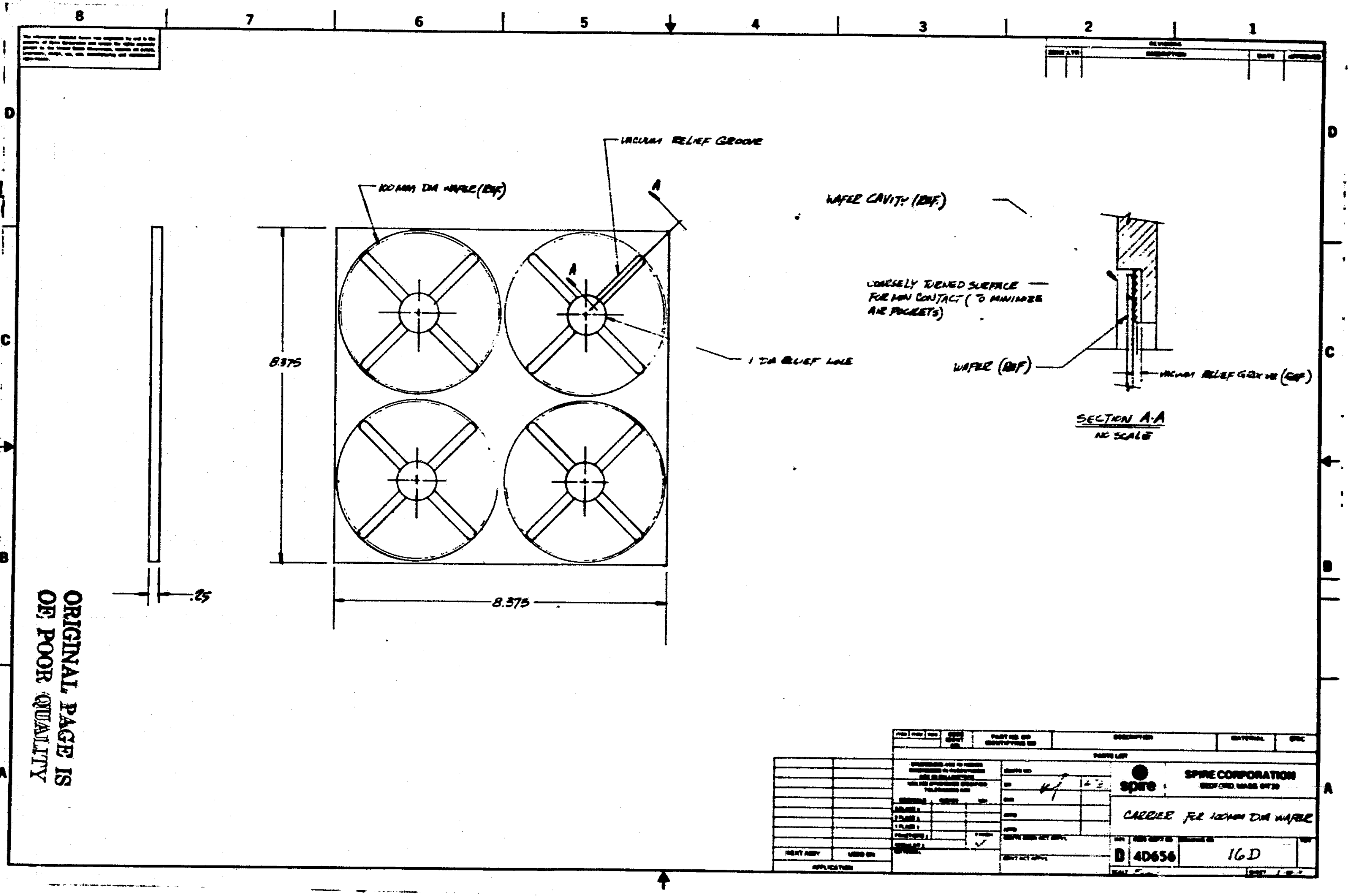

ORIGINAL PAGE IS
OF POOR QUALITY

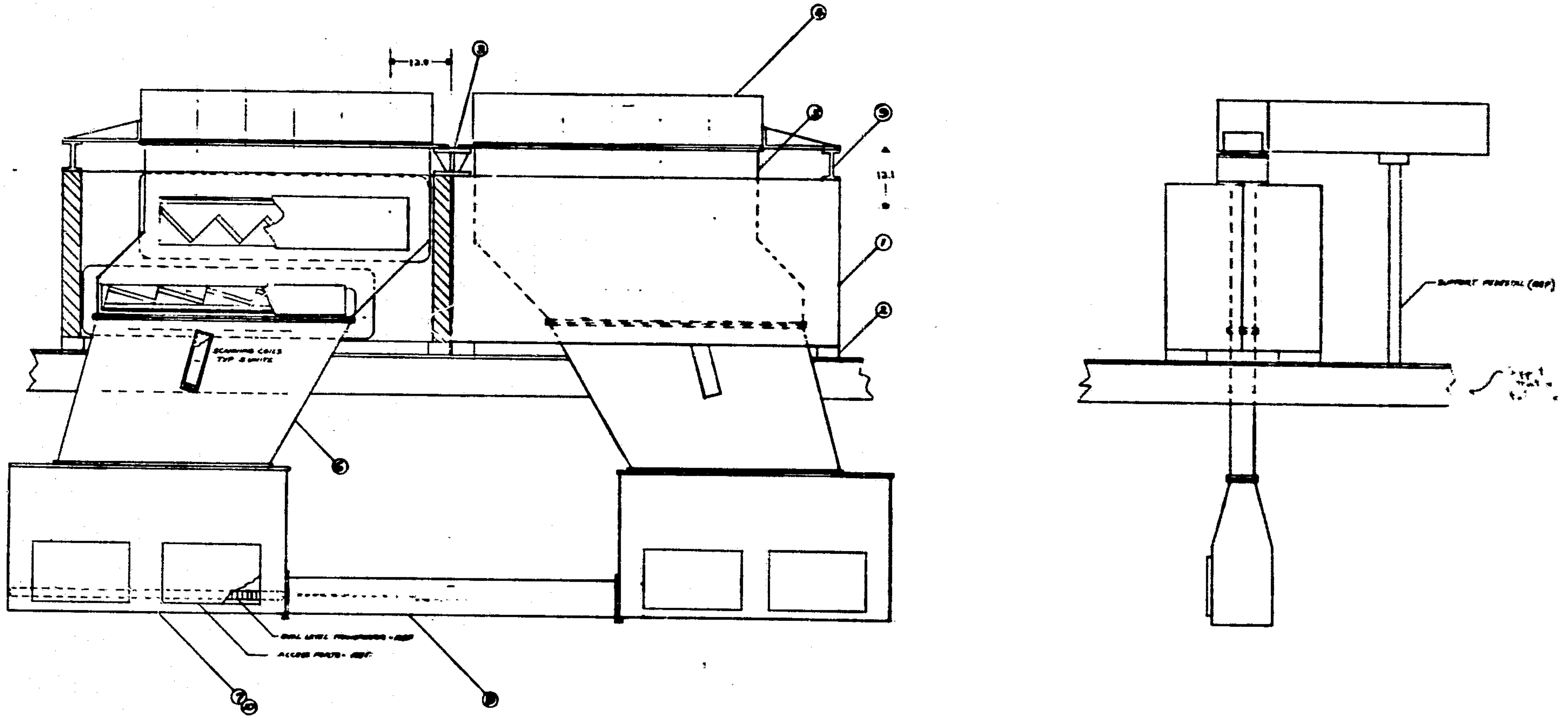

SPIRE CORPORATION
BEDFORD, MASS 01730

ANALYZING MAGNET
& MAIN VACUUM CHAMBER ASSY

PARTS LIST

B 4D656 3D 0

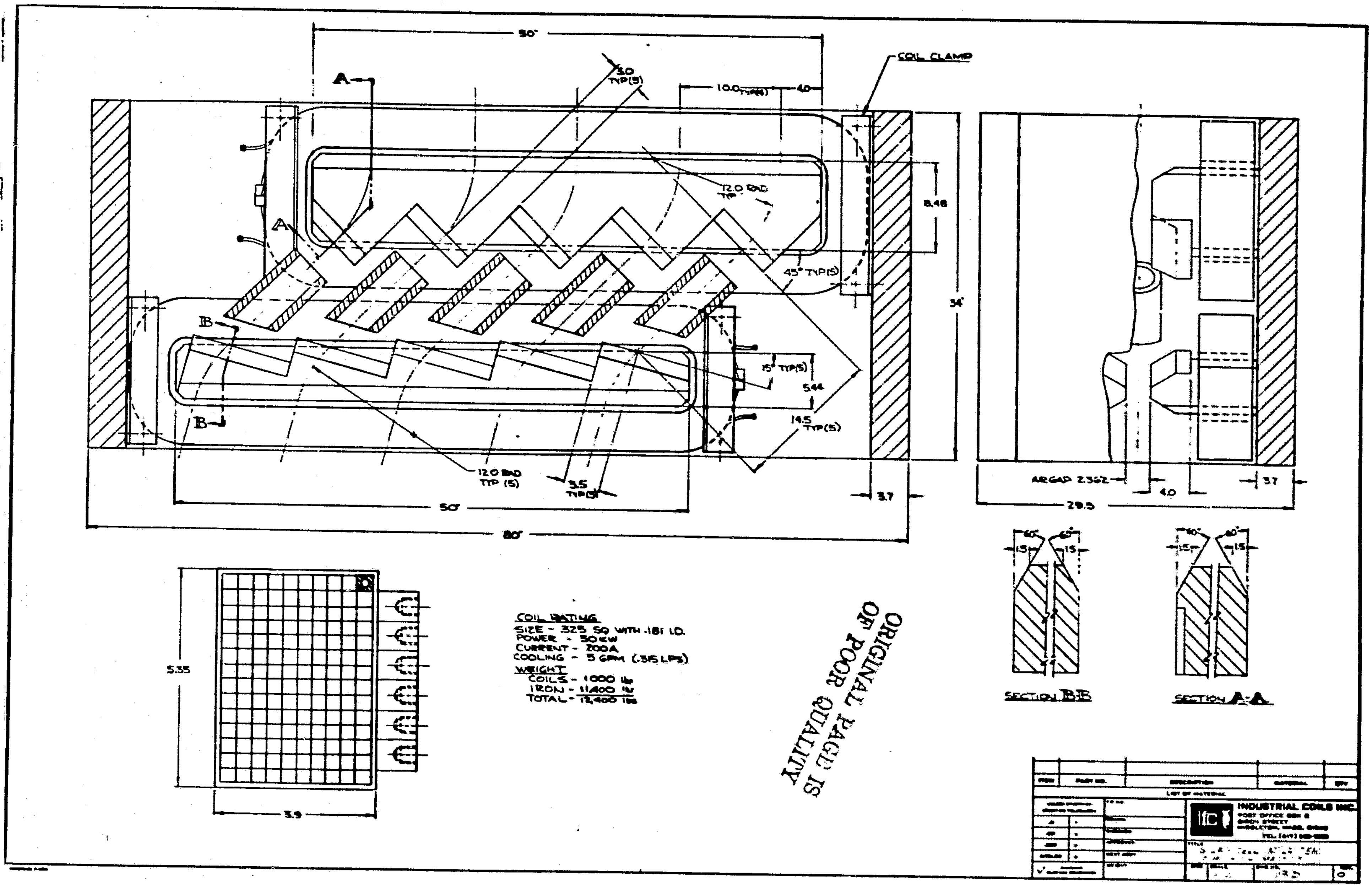

COIL RATING
SIZE - .325 SQ WITH .181 I.D.
POWER - 50 KW
CURRENT - 200A
COOLING - 5 GPM (.315 LPS)
WEIGHT
COILS - 1000 lbs
IRON - 11,400 lbs
TOTAL - 12,400 lbs

ORIGINAL PAGE IS
OF POOR QUALITY

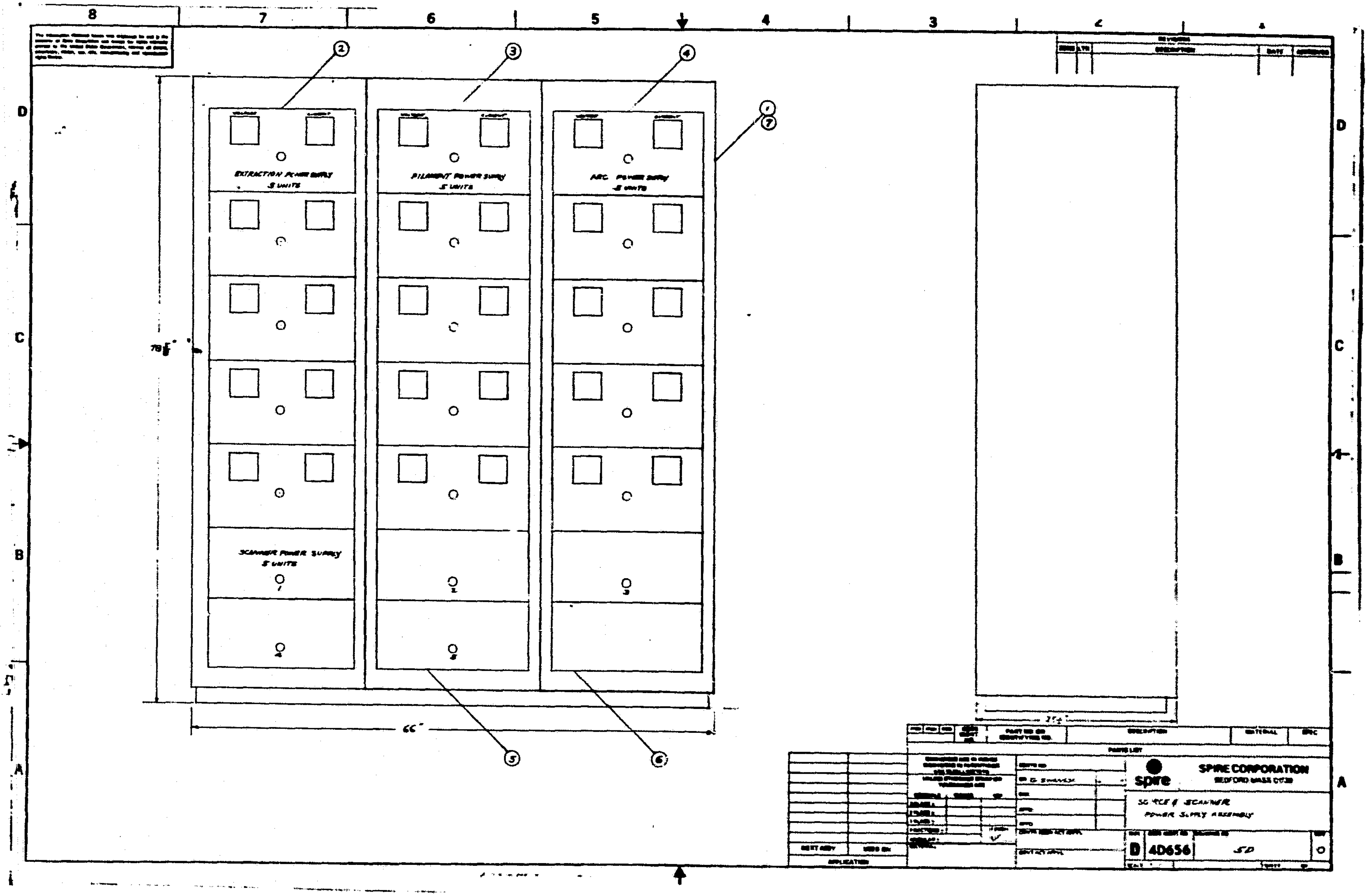
EXTRACTION POWER SUPPLY
5 UNITS
FILAMENT POWER SUPPLY
5 UNITS
ARC POWER SUPPLY
5 UNITS
SCANNER POWER SUPPLY
5 UNITS
VOLTAGE
CURRENT
1
2
3
4
5
②
③
④
⑤
⑥
①
⑦
78"
66"
27½"
PARTS LIST
PART NO. OR IDENTIFYING NO.
DESCRIPTION
MATERIAL
SPEC
REVISIONS
spire
SPIRE CORPORATION
BEDFORD MASS 01730
SOURCE & SCANNER
POWER SUPPLY ASSEMBLY
D
4D656
SD
0
APPLICATION
NEXT ASSY
USED ON

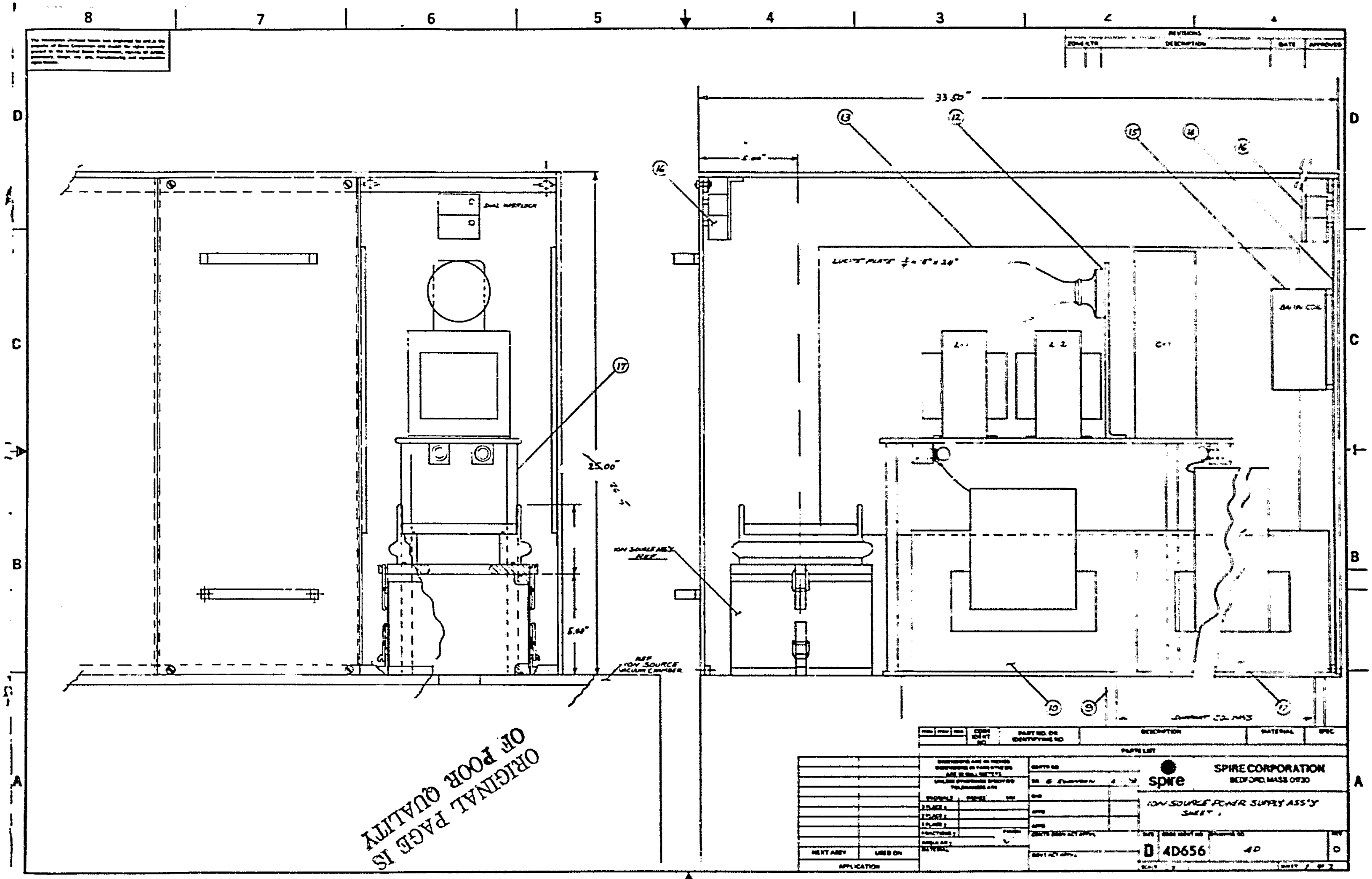

SPIRE CORPORATION
BEDFORD, MASS 01730

ION SOURCE POWER SUPPLY ASS'Y
SHEET 1

D 4D656 4D
0
SHEET 1 OF 2

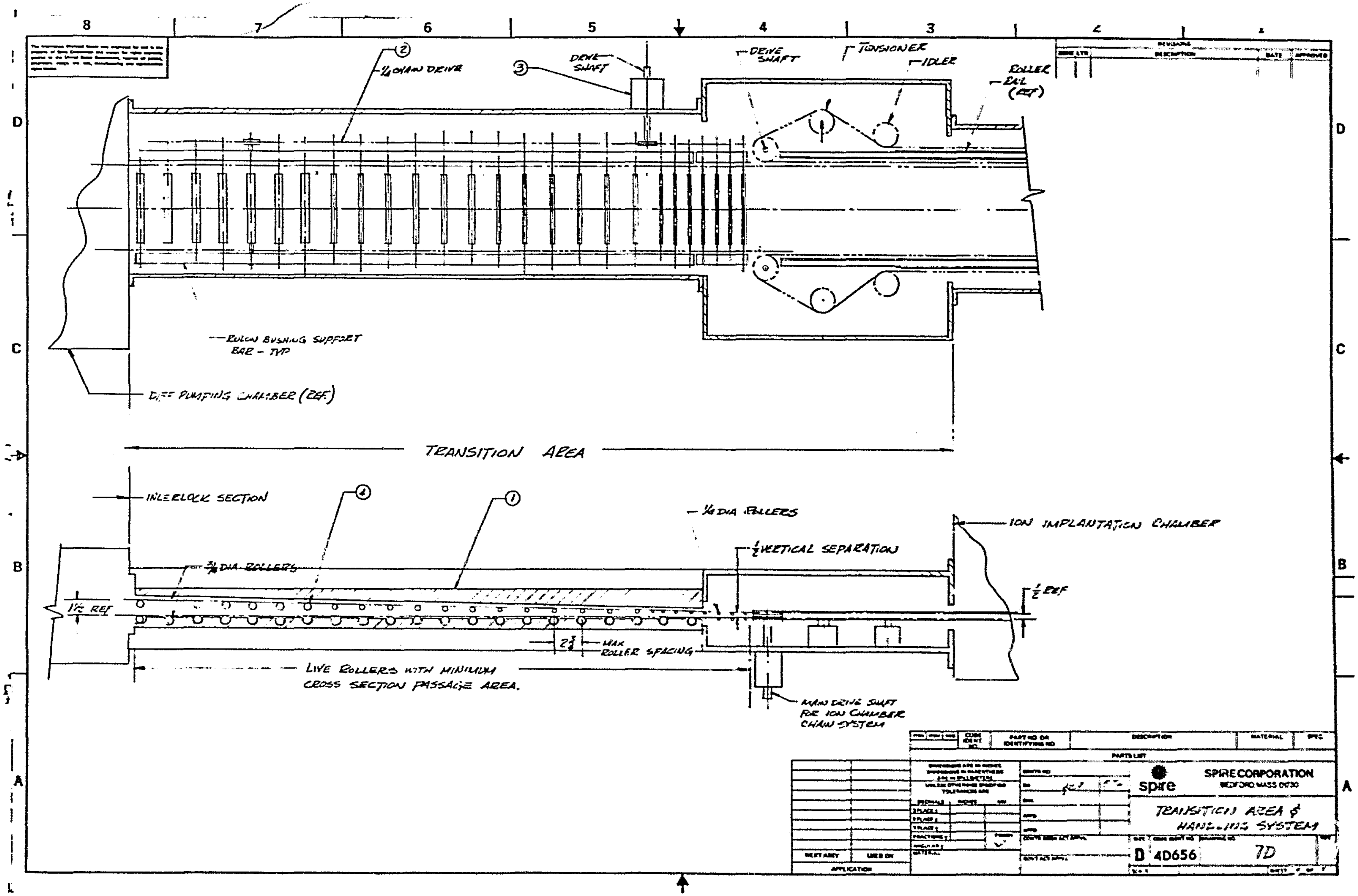
② 1/4 CHAIN DRIVE
③ DRIVE SHAFT
DRIVE SHAFT
TENSIONER
IDLER
ROLLER BAIL (REF)
ROLON BUSHING SUPPORT BAR - TYP
DIFF PUMPING CHAMBER (REF)
TRANSITION AREA
INTERLOCK SECTION
④
①
1/4 DIA ROLLERS
ION IMPLANTATION CHAMBER
1/2 VERTICAL SEPARATION
3/4 DIA ROLLERS
1 1/2 REF
1/2 REF
2 3/4 MAX ROLLER SPACING
LIVE ROLLERS WITH MINIMUM CROSS SECTION PASSAGE AREA.
MAIN DRIVE SHAFT FOR ION CHAMBER CHAIN SYSTEM
spire
SPIRE CORPORATION
BEDFORD MASS 01730
TRANSITION AREA & HANDLING SYSTEM
D 4D656
7D
PARTS LIST
DESCRIPTION
MATERIAL
SPEC
REVISIONS
NEXT ASSY
USED ON
APPLICATION
8
7
6
5
4
3
2
1
D
C
B
A

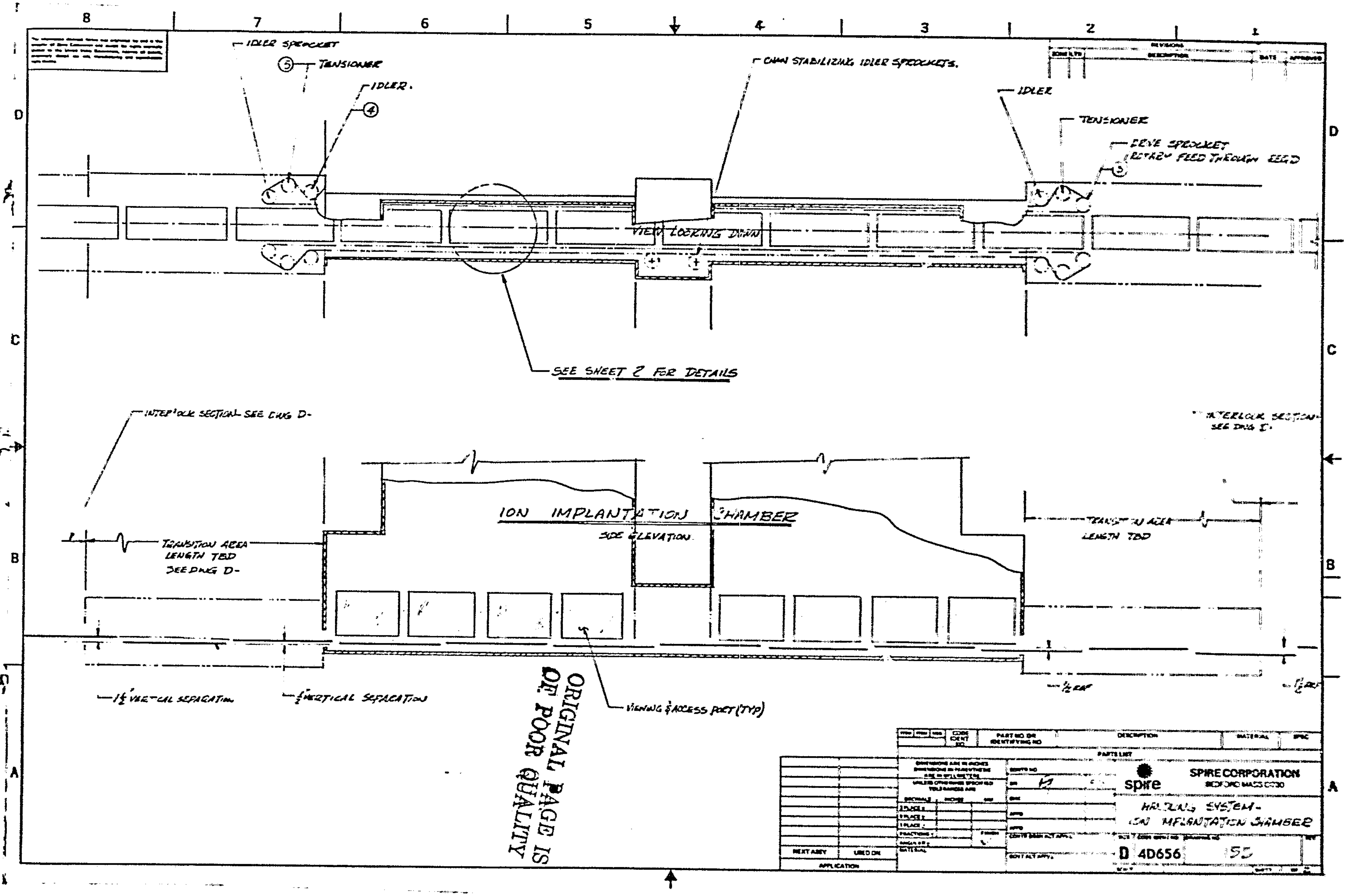

ORIGINAL PAGE IS
OF POOR QUALITY

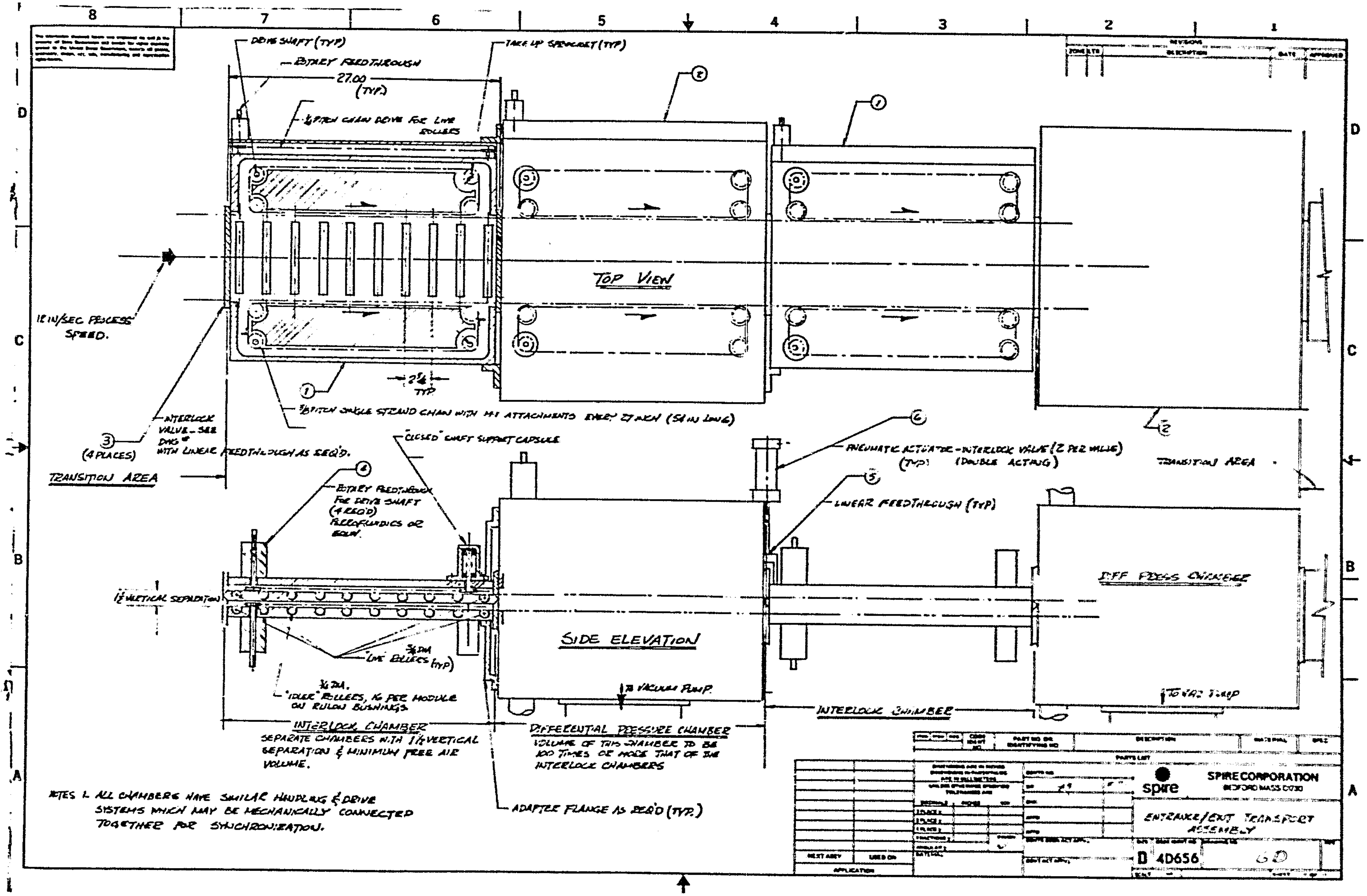DRIVE SHAFT (TYP)
ROTARY FEEDTHROUGH
27.00 (TYP)
TAKE UP SPROCKET (TYP)
1/2 PITCH CHAIN DRIVE FOR LIVE ROLLERS
②
①
TOP VIEW
12 IN/SEC PROCESS SPEED.
2 1/4 TYP
3/8 PITCH SINGLE STRAND CHAIN WITH M-1 ATTACHMENTS EVERY 27 INCH (54 IN LONG)
③ (4 PLACES)
INTERLOCK VALVE – SEE DWG # WITH LINEAR FEEDTHROUGH AS REQ'D.
TRANSITION AREA
"CLOSED" SHAFT SUPPORT CAPSULE
④
ROTARY FEEDTHROUGH FOR DRIVE SHAFT (4 REQ'D) FERROFLUIDICS OR EQUIV.
⑥
PNEUMATIC ACTUATOR – INTERLOCK VALVE (2 PER VALVE) (TYP) (DOUBLE ACTING)
⑤
LINEAR FEEDTHROUGH (TYP)
TRANSITION AREA
2
1 1/2 VERTICAL SEPARATION
3/4 DIA "LIVE" ROLLERS (TYP)
1/2 DIA. "IDLER" ROLLERS, 16 PER MODULE ON RULON BUSHINGS
SIDE ELEVATION
TO VACUUM PUMP
DIFF PRESS CHAMBER
TO VAC PUMP
INTERLOCK CHAMBER
SEPARATE CHAMBERS WITH 1 1/2 VERTICAL SEPARATION & MINIMUM FREE AIR VOLUME.
DIFFERENTIAL PRESSURE CHAMBER
VOLUME OF THIS CHAMBER TO BE 100 TIMES OR MORE THAT OF THE INTERLOCK CHAMBERS
INTERLOCK CHAMBER
ADAPTER FLANGE AS REQ'D (TYP.)
NOTES 1. ALL CHAMBERS HAVE SIMILAR HANDLING & DRIVE SYSTEMS WHICH MAY BE MECHANICALLY CONNECTED TOGETHER FOR SYNCHRONIZATION.
PARTS LIST
NEXT ASSY
USED ON
APPLICATION
spire
SPIRE CORPORATION
BEDFORD MASS 01730
ENTRANCE/EXIT TRANSPORT ASSEMBLY
D 4D656
6D
8 7 6 5 4 3 2 1
D C B A

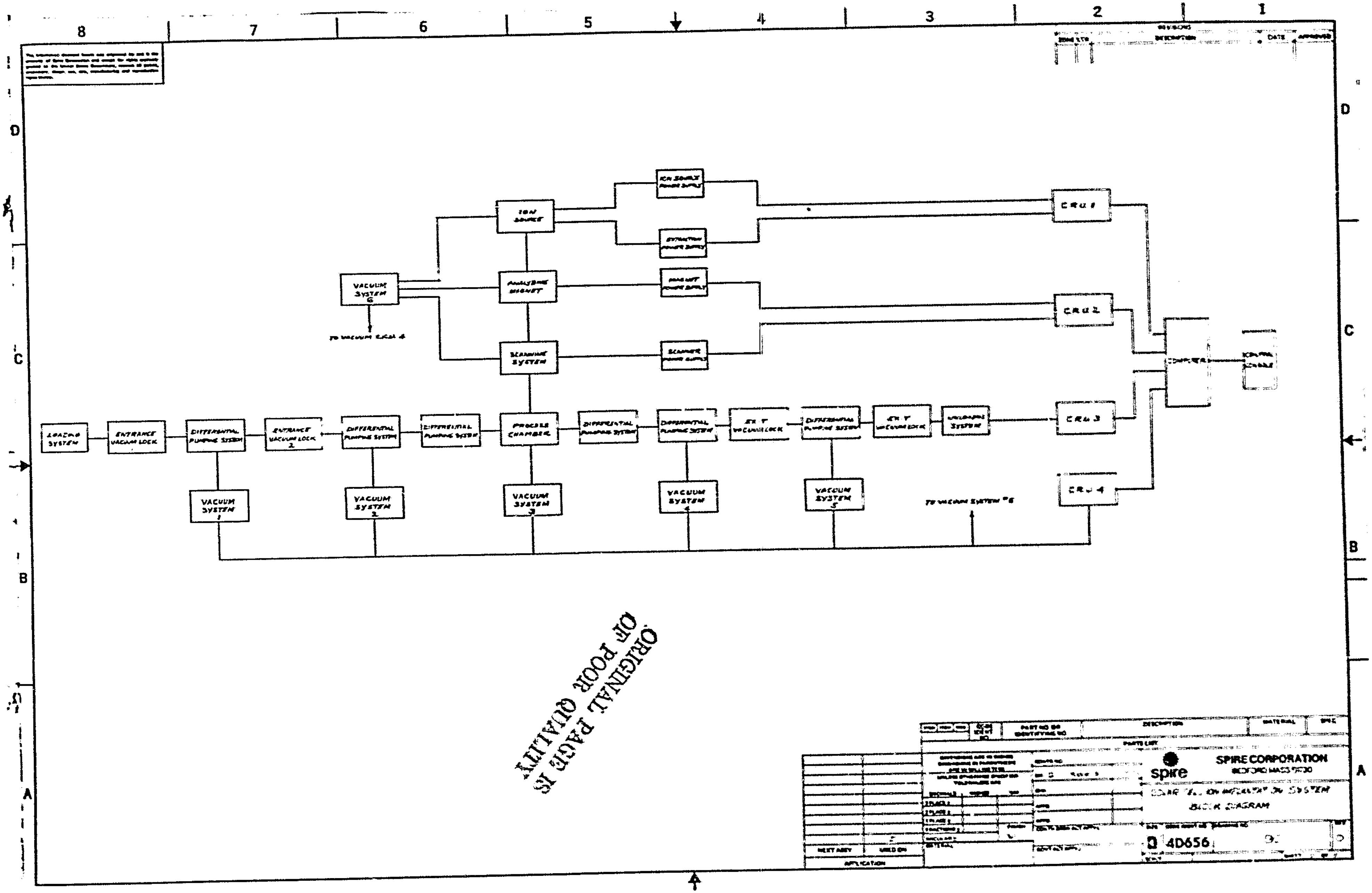
LOADING SYSTEM
ENTRANCE VACUUM LOCK
DIFFERENTIAL PUMPING SYSTEM
ENTRANCE VACUUM LOCK 2
DIFFERENTIAL PUMPING SYSTEM
DIFFERENTIAL PUMPING SYSTEM
PROCESS CHAMBER
DIFFERENTIAL PUMPING SYSTEM
DIFFERENTIAL PUMPING SYSTEM
EXIT VACUUM LOCK
DIFFERENTIAL PUMPING SYSTEM
EXIT VACUUM LOCK
UNLOADING SYSTEM
VACUUM SYSTEM 1
VACUUM SYSTEM 2
VACUUM SYSTEM 3
VACUUM SYSTEM 4
VACUUM SYSTEM 5
TO VACUUM SYSTEM #6
VACUUM SYSTEM 6
TO VACUUM C.R.U. 4
ION SOURCE
ANALYZING MAGNET
SCANNING SYSTEM
ION SOURCE POWER SUPPLY
EXTRACTION POWER SUPPLY
MAGNET POWER SUPPLY
SCANNER POWER SUPPLY
C R U 1
C R U 2
C R U 3
C R U 4
COMPUTER
CONTROL CONSOLE
8
7
6
5
4
3
2
1
D
C
B
A
REVISIONS
ZONE
LTR
DESCRIPTION
DATE
APPROVED
PARTS LIST
PART NO OR IDENTIFYING NO
DESCRIPTION
MATERIAL
SPEC
SPIRE CORPORATION
BEDFORD MASS 01730
spire
SOLAR CELL ION IMPLANTATION SYSTEM
BLOCK DIAGRAM
D 4D656
NEXT ASSY
USED ON
APPLICATION

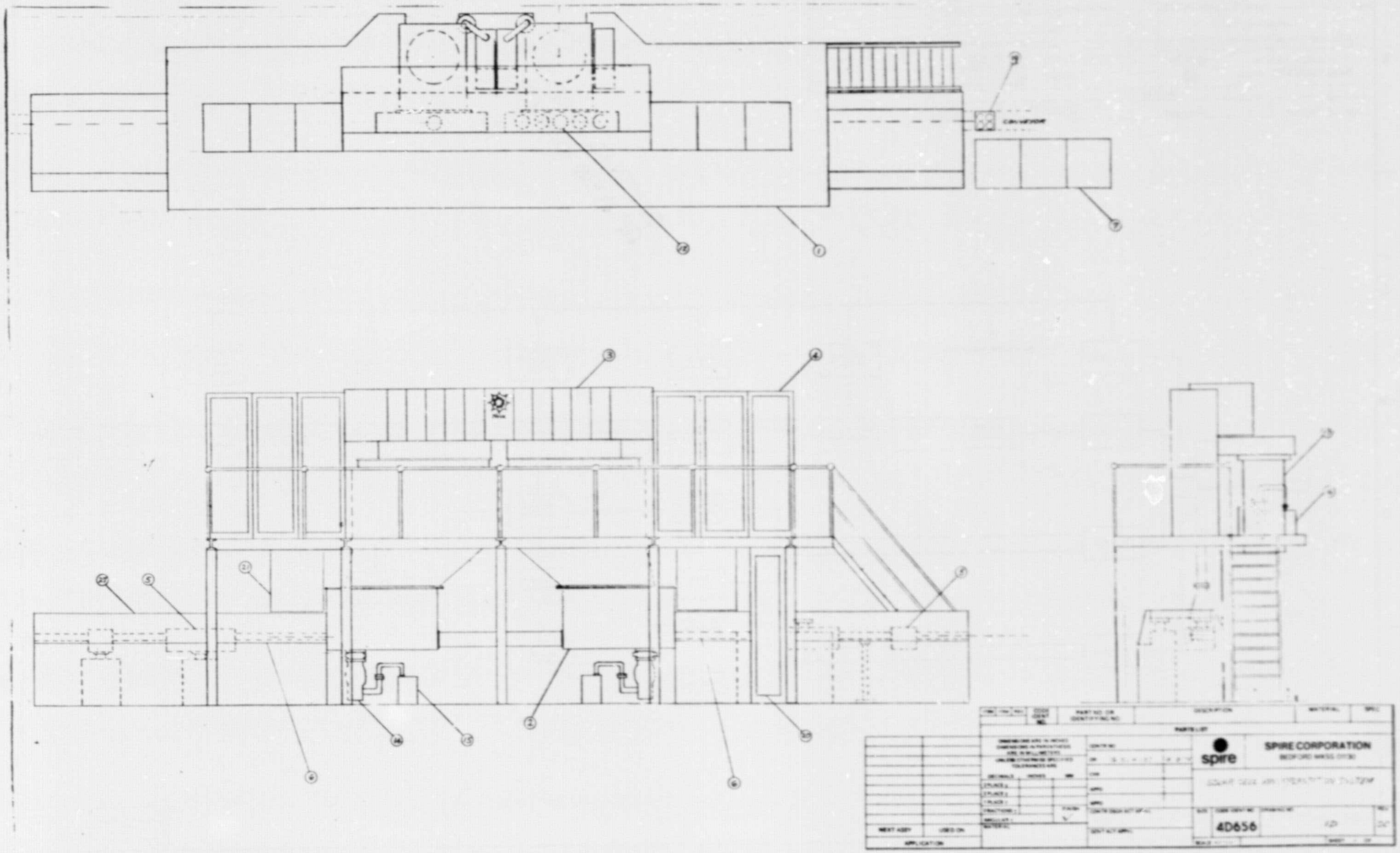
PART NO. OR IDENTIFYING NO.
DESCRIPTION
MATERIAL
PARTS LIST
spire
SPIRE CORPORATION
BEDFORD MASS 01730
4D656
NEXT ASSY
USED ON
APPLICATION

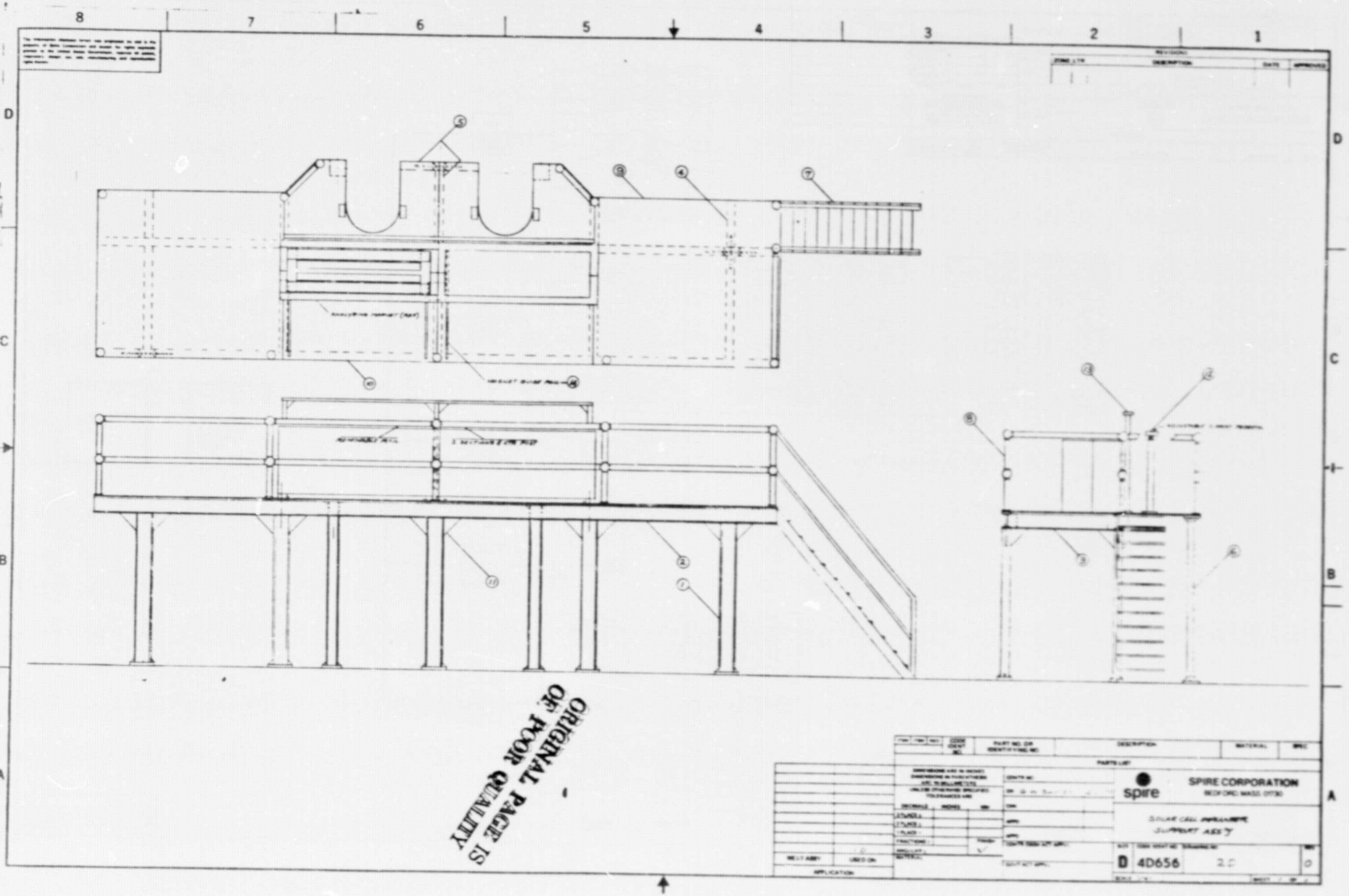

ORIGINAL PAGE IS
OF POOR QUALITY

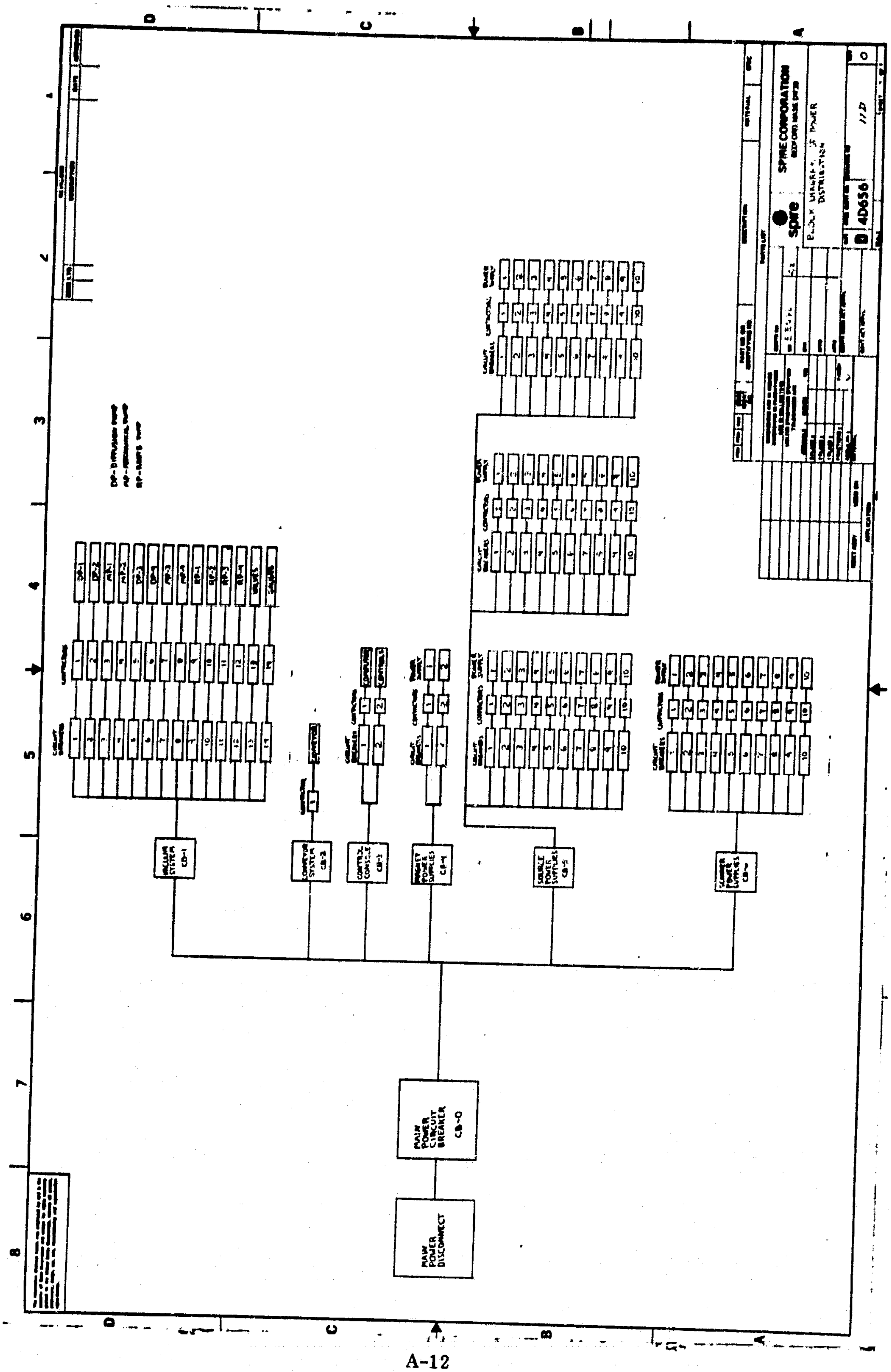
MAIN POWER DISCONNECT
MAIN POWER CIRCUIT BREAKER CB-0
VACUUM SYSTEM CB-1
CONVEYOR SYSTEM CB-2
CONTROL CONSOLE CB-3
MAGNET POWER SUPPLIES CB-4
SOURCE POWER SUPPLIES CB-5
SCANNER POWER SUPPLIES CB-6
CIRCUIT BREAKERS
CONTACTORS
POWER SUPPLY
CONTROLLER
CONVEYOR
CONTROLS
DP-1
DP-2
MP-1
MP-2
DP-3
DP-4
MP-3
MP-4
RP-1
RP-2
RP-3
RP-4
VALVES
GAUGES
DP - DIFFUSION PUMP
MP - MECHANICAL PUMP
RP - ROUGHING PUMP
SPIRE CORPORATION
BEDFORD MASS 01730
spire
BLOCK DIAGRAM OF POWER DISTRIBUTION
D
4D656
11D
0
1
2
3
4
5
6
7
8
A
B
C
D

ORIGINAL PAGE IS OF POOR QUALITY

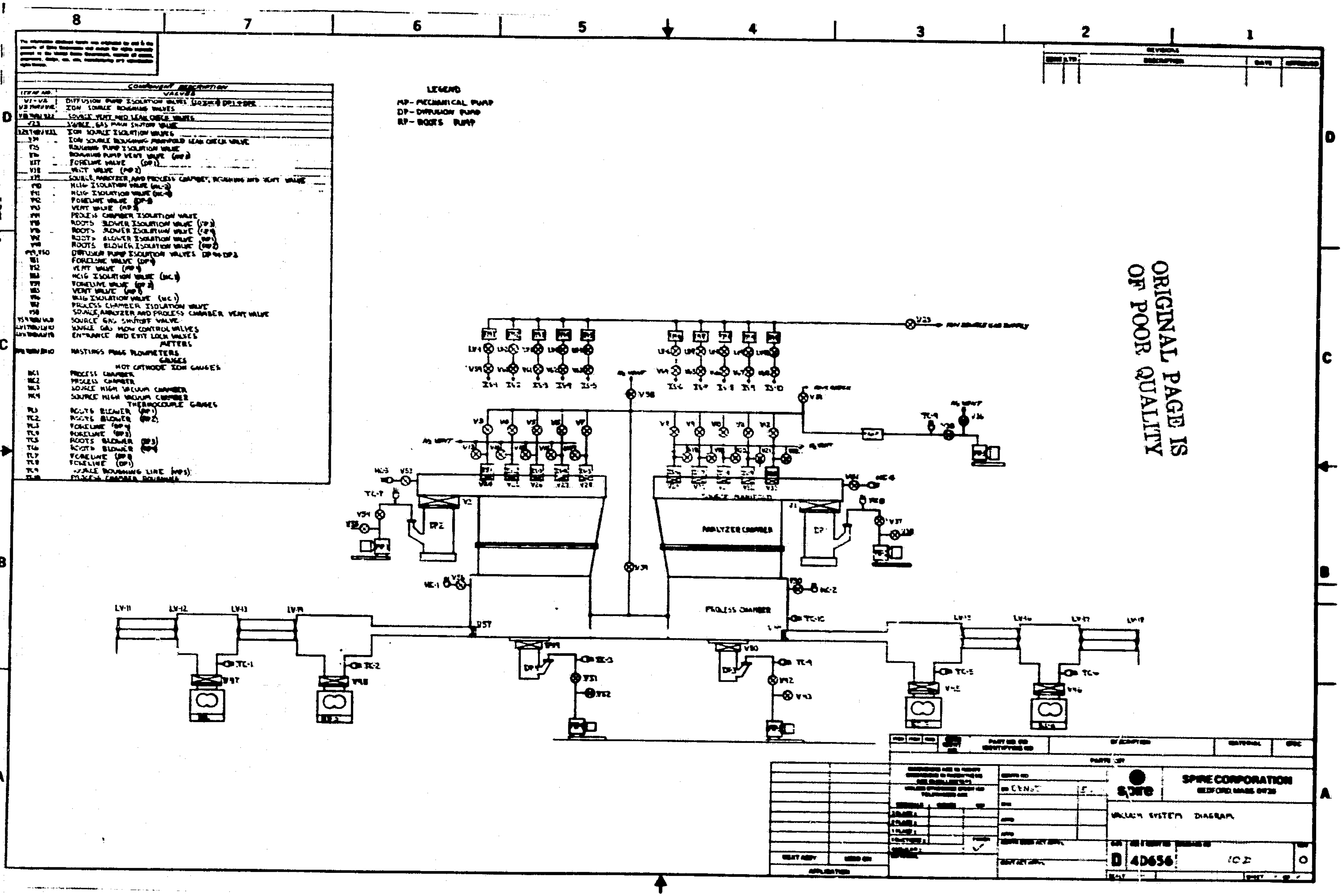

LEGEND
MP- MECHANICAL PUMP
DP- DIFFUSION PUMP
RP- ROOTS PUMP

ITEM NO.	COMPONENT DESCRIPTION
	VALVES
V1-V4	DIFFUSION PUMP ISOLATION VALVES [illegible]
V5 THRU V8	ION SOURCE ROUGHING VALVES
V9 THRU V12	SOURCE VENT AND LEAK CHECK VALVES
V23	SOURCE GAS MAIN SHUTOFF VALVE
V13 THRU V22	ION SOURCE ISOLATION VALVES
V24	ION SOURCE ROUGHING MANIFOLD LEAK CHECK VALVE
V25	ROUGHING PUMP ISOLATION VALVE
V26	ROUGHING PUMP VENT VALVE (MP 2)
V37	FORELINE VALVE (DP 1)
V38	VENT VALVE (MP 2)
V39	SOURCE, ANALYZER, AND PROCESS CHAMBER, ROUGHING AND VENT VALVE
V40	HCIG ISOLATION VALVE (HC-2)
V41	HCIG ISOLATION VALVE (HC-4)
V42	FORELINE VALVE (DP-3)
V43	VENT VALVE (MP 3)
V44	PROCESS CHAMBER ISOLATION VALVE
V45	ROOTS BLOWER ISOLATION VALVE (RP 3)
V46	ROOTS BLOWER ISOLATION VALVE (RP 4)
V47	ROOTS BLOWER ISOLATION VALVE (RP 1)
V48	ROOTS BLOWER ISOLATION VALVE (RP 2)
V49, V50	DIFFUSION PUMP ISOLATION VALVES DP4 & DP3
V51	FORELINE VALVE (DP 4)
V52	VENT VALVE (MP 4)
V53	HCIG ISOLATION VALVE (HC 3)
V54	FORELINE VALVE (DP 2)
V55	VENT VALVE (MP 5)
V56	HCIG ISOLATION VALVE (HC 1)
V57	PROCESS CHAMBER ISOLATION VALVE
V58	SOURCE, ANALYZER AND PROCESS CHAMBER VENT VALVE
V59 THRU V68	SOURCE GAS SHUTOFF VALVE
LV1 THRU LV10	SOURCE GAS FLOW CONTROL VALVES
LV11 THRU LV19	ENTRANCE AND EXIT LOCK VALVES
	METERS
FM1 THRU FM10	HASTINGS MASS FLOWMETERS
	GAUGES
	HOT CATHODE ION GAUGES
HC1	PROCESS CHAMBER
HC2	PROCESS CHAMBER
HC3	SOURCE HIGH VACUUM CHAMBER
HC4	SOURCE HIGH VACUUM CHAMBER
	THERMOCOUPLE GAUGES
TC1	ROOTS BLOWER (RP1)
TC2	ROOTS BLOWER (RP2)
TC3	FORELINE (DP4)
TC4	FORELINE (DP3)
TC5	ROOTS BLOWER (RP3)
TC6	ROOTS BLOWER (RP4)
TC7	FORELINE (DP2)
TC8	FORELINE (DP1)
TC9	SOURCE ROUGHING LINE (MP5)
TC10	PROCESS CHAMBER ROUGHING

PARTS LIST
PART NO. OR IDENTIFYING NO.
DESCRIPTION
MATERIAL
SPEC

SPIRE CORPORATION
BEDFORD MASS 01730

VACUUM SYSTEM DIAGRAM

D 4D656 ICE 0

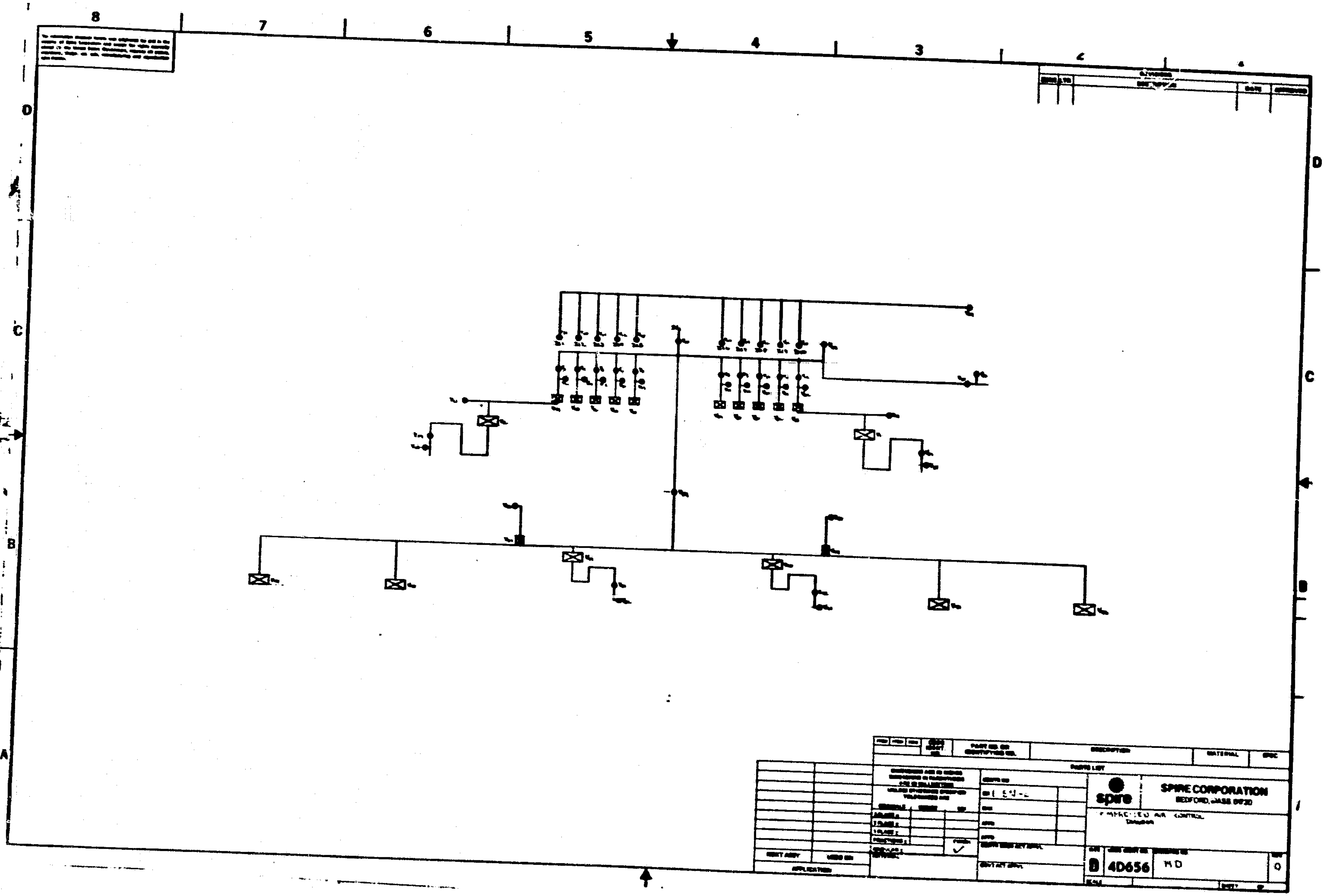
8
7
6
5
4
3
2
1
D
C
B
A
spire
SPIRE CORPORATION
BEDFORD, MASS 01730
COMPRESSED AIR CONTROL
PARTS LIST
DESCRIPTION
MATERIAL
SPEC
B
4D656
KD
0

APPENDIX B

SOLAR CELL PERFORMANCE DATA (HISTOGRAM FORMAT) FOR LASER, E-BEAM AND FURNACE ANNEALED JUNCTIONS

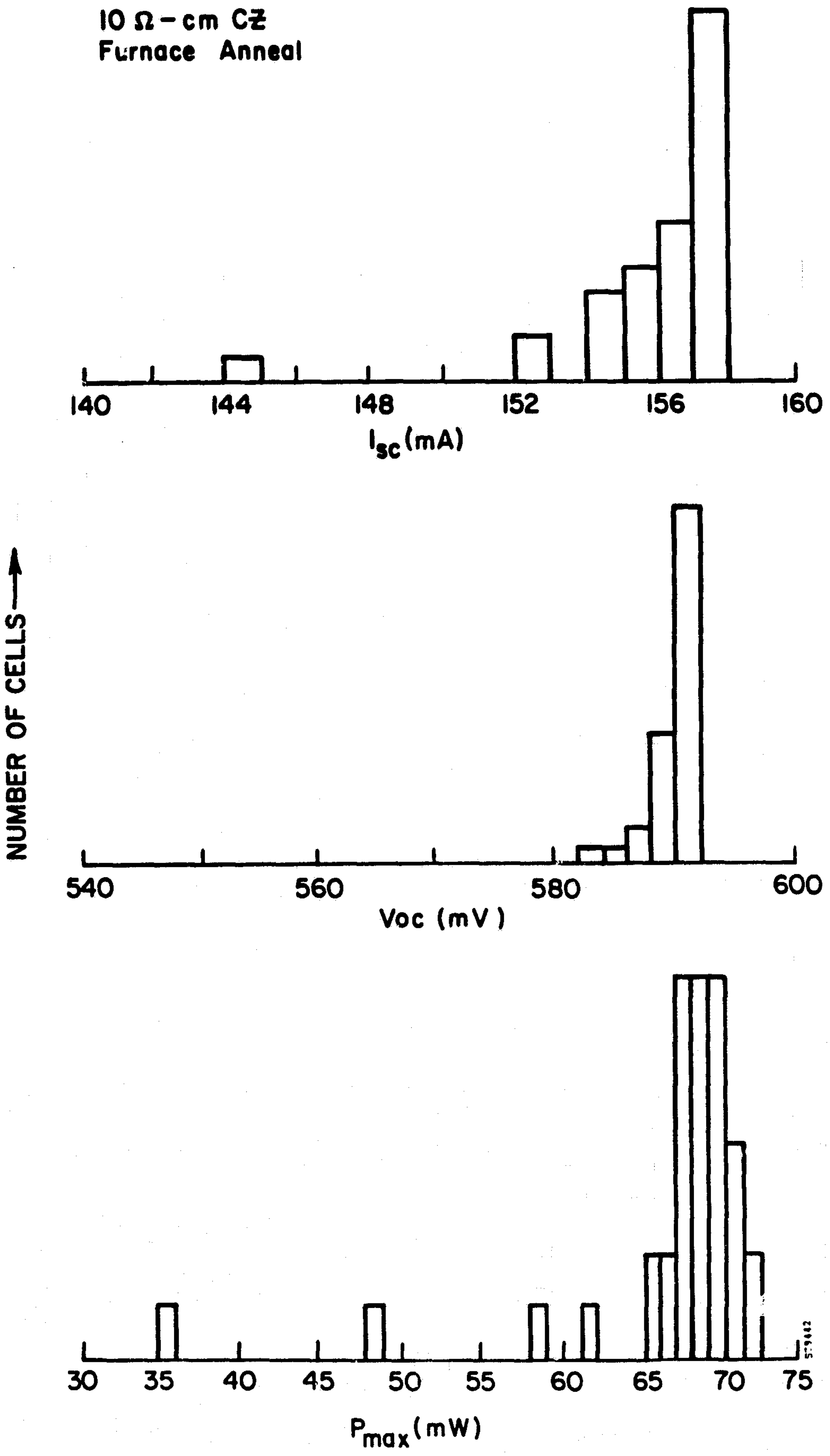

PERFORMANCE DISTRIBUTIONS FOR ION IMPLANTED/FURNACE ANNEALED SOLAR CELLS

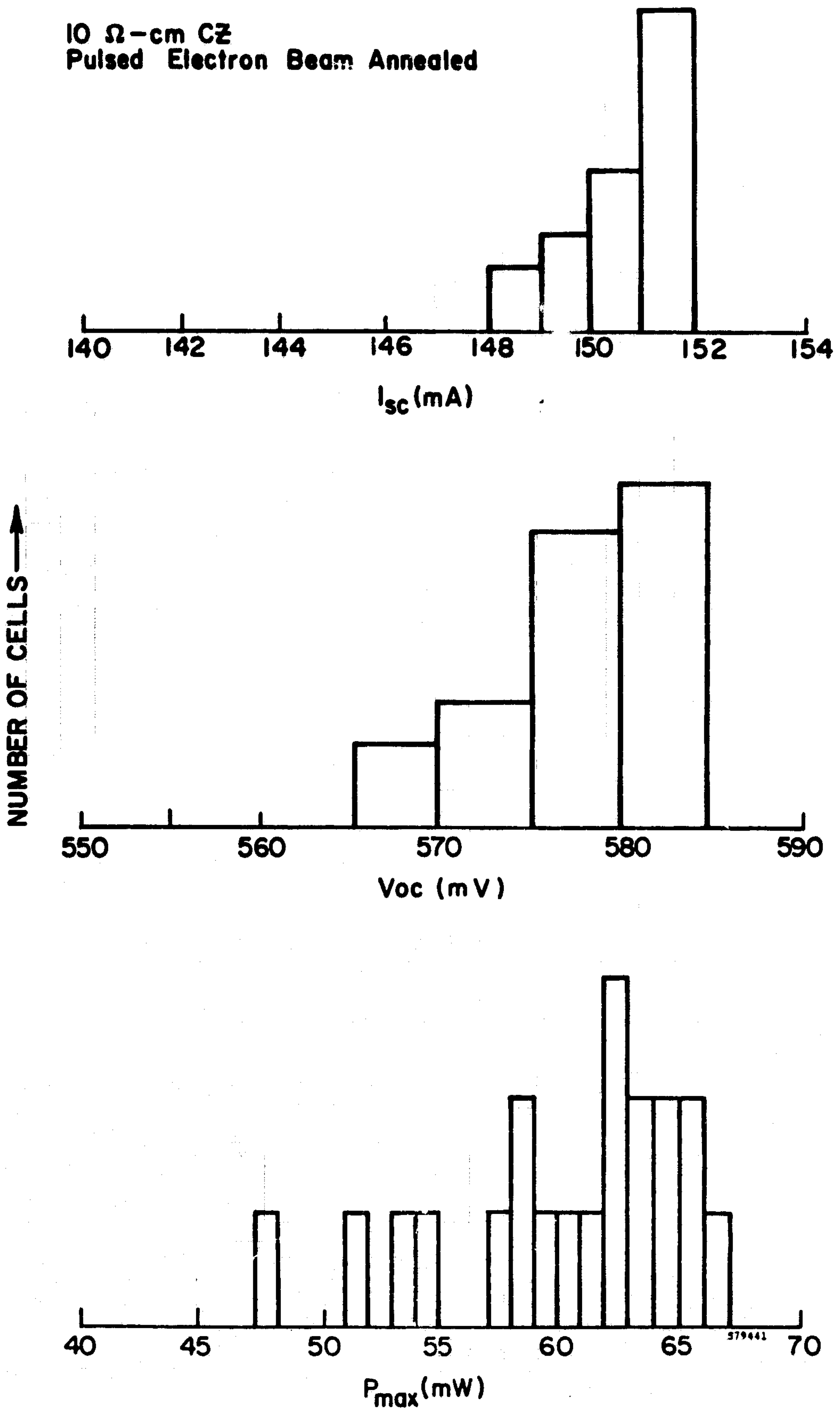

PERFORMANCE DISTRIBUTIONS FOR ION IMPLANTED/PULSED ELECTRON BEAM ANNEALED SOLAR CELLS

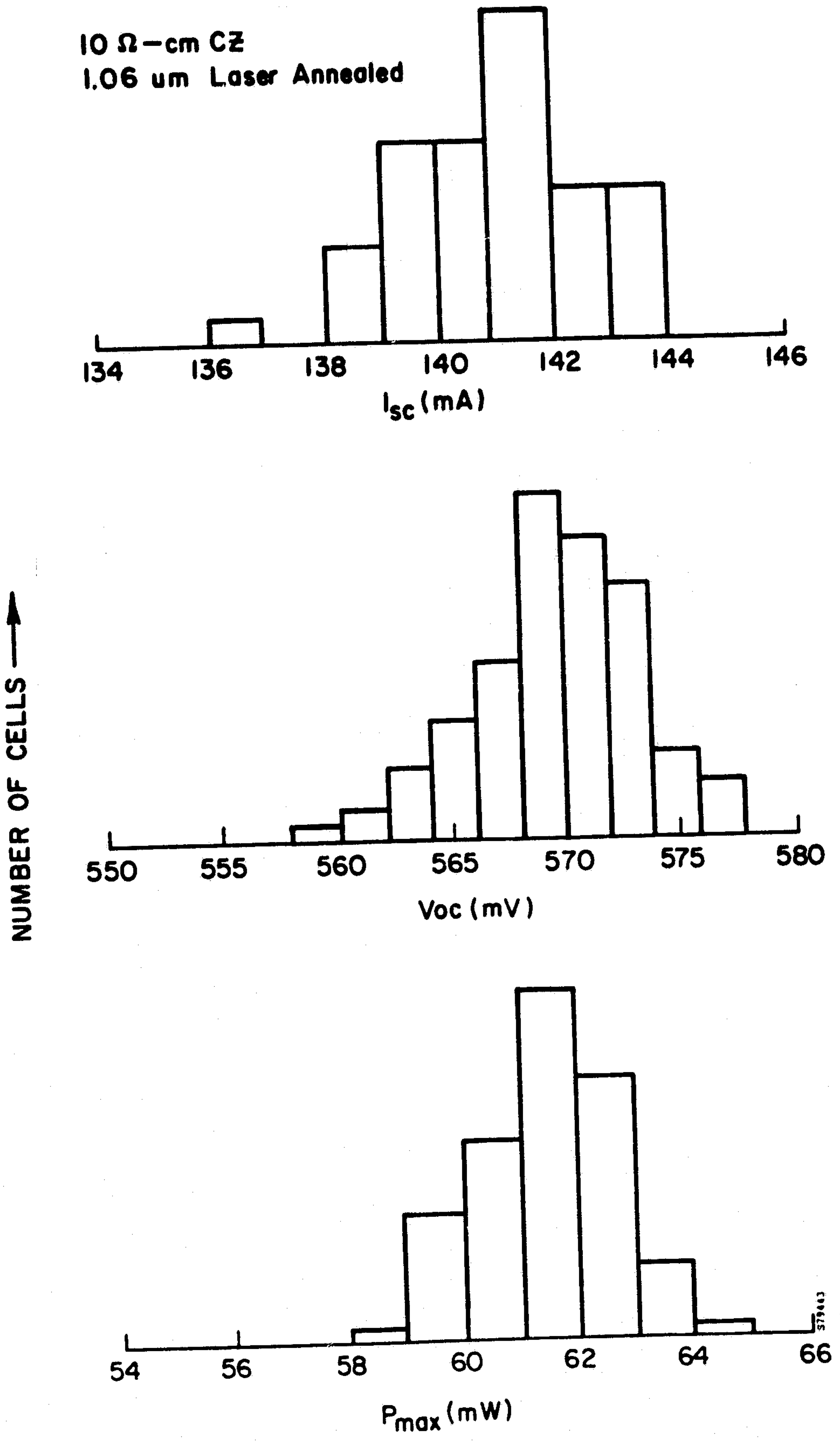

PERFORMANCE DISTRIBUTIONS FOR ION IMPLANTED/PULSED LASER ANNEALED SOLAR CELLS

APPENDIX C

PHYSICAL MODELS FOR PULSED ELECTRON BEAM ANNEALING PROCESSES

TR-78-26

PHYSICAL MODELS FOR PULSED ELECTRON BEAM ANNEALING PROCESSES

by

Neil C. Schoen
William R. Neal

SPIRE CORPORATION
Patriots Park
Bedford, MA 01730

TABLE OF CONTENTS

LIST OF ILLUSTRATIONS

PHYSICAL MODELS FOR PULSED ELECTRON BEAM ANNEALING PROCESSES

1.0 INTRODUCTION AND SUMMARY

This technical report summarizes work performed under JPL Contract 954786 covering Task I ("Pulsed Energy Process Analyses and Characterizations"). The subtasks covered by this work are listed below:

- I.1 Investigate Silicon Damage by Pulsed Energy Beams
- I.2 Analyze Silicon Thermal and Thermomechanical Responses to Ion Implantation and Pulsed Energy Beams
- I.3 Identify Mechanism of Pulsed Annealing
- I.6 Develop Computer Models of Pulsed Energy Effects
- I.7 Develop Theoretical Model of Pulsed Energy Processes

1.1 PROBLEM DEFINITION

The major analytical effort required by the subtasks listed above consisted of two phases. The initial work was directed towards the development of a one-dimensional thermal diffusion computer code so that accurate calculations of the temperature profiles produced by the pulsed electron beam could be obtained. The second phase of the analysis utilized the temperature profile predictions to devise theoretical models for both the annealing and damage mechanisms resulting from the PEBA processing. In addition to this analytical work, silicon damage thresholds were experimentally measured for comparison with predictions described in detail in the following sections of this report.

1.2 THERMAL ANALYSIS

The primary objective of the thermal analysis was the generation of a computer code (VXTEMP) to solve the time dependent heat flow problem in one dimension, with provisions for temperature dependent thermal properties and solid/liquid phase changes. The resultant finite element code also can handle multilayer configurations with time dependent energy deposition profiles, as well as a variety of boundary conditions at the exterior surfaces. An additional feature of VXTEMP is a variable spatial grid to speed execution of the code in regions where detailed resolution is not necessary. Several code runs were completed for various experimental configurations.

1.3 STRESS ANALYSIS

An analysis of several mechanisms responsible for stress generation resulting from pulsed electron beam processing of silicon was the primary approach taken to solve the fracture problems created by overlapping annealing pulses. The three potential damage mechanisms that were investigated are: (1) temperature induced thermoelastic stress, (2) pressure wave generation, and (3) ion implant stress effects. Calculations of the normal and shear components of the induced stress were performed using simple physical models and the basic equations describing the physical processes. Correlations and comparisons of calculated parameters with experimentally determined values were made and an explanatory model of the damage sequence has been formulated.

1.4 SUMMARY OF SIGNIFICANT CONCLUSIONS

The VXTEMP computer calculations indicate that front surface melt occurs as a result of pulsed electron beam annealing. The only variable of importance which is not well known is the heat of fusion of the amorphous implant layer. If the heat of fusion is assumed to be small compared to crystal silicon, then VXTEMP predicts front surface melting at fluences of 0.2 cal/cm^2, which agrees well with experimental anneal thresholds. If the heat of fusion is identical to the crystal silicon value, then fluences approaching 0.25-0.3 cal/cm^2 are needed for front surface melt. These fluences are in the range below fracture and above the anneal threshold. Uncertainties in the deposition profile in the 0.1-0.5μm range preclude determination of the actual value of the amorphous layer heat of fusion from the data presently available. The model that has been developed to explain the effects associated with pulsed electron beam annealing does not depend critically on the value of the heat of fusion of the amorphous layer, since it has become clear from both our own experiments and those reported in the literature(12) that melting is required for proper annealing.

With regard to stress generation and damage mechanisms, the data and calculations indicate that shear stresses, created by the large temperature gradients due to electron irradiation, are the primary cause of fracture in pulsed electron beam processing of silicon. The variation in fracture thresholds with crystal orientation of unimplanted silicon has been explained on the basis of the difference in the value of Young's modulus for the respective orientations. In addition, the increased fracture resistance of (111) silicon after implantation is attributed to the increased fracture strength of the amorphous layer created by implantation, which coincides with the region of maximum temperature gradients. As the incident energy density is increased, the large temperature gradients are shifted to the single crystal silicon region below the implant layer, thus causing fracture. This implies that it may be possible to alter electron beam parameters to eliminate fracture when overlapping annealing pulses.

2.0 THERMAL ANALYSIS

The following sections contain information describing the development, testing, and use of the VXTEMP time dependent thermal diffusion code.

2.1 CODE DEVELOPMENT

The finite element approach from a previously existing diffusion code (J. Uglum's XTEMP) served as the basis for the more versatile code VXTEMP written under subtask I.6. The fundamental equation to be solved is(7)

$$\nabla^2 T - \frac{1}{K}\frac{\partial T}{\partial t} = -\frac{A(x,y,z,t)}{k}$$

where K is the thermal diffusivity, k is the thermal conductivity, and A is the heat supplied per unit time per unit volume. The thermal diffusivity is

$$K(T) = \frac{k(T)}{\rho C(T)}$$

where ρ is the density and C is the specific heat. This equation was derived from considerations of energy flow into a small volume element. The same approach, as described below, is used to generate the algorithm employed in the VXTEMP code.

Consider the two slabs of material shown in Figure 1. The heat flow per unit area across any surface is

$$\dot{Q} = k \frac{dT}{dx} ,$$

The temperature rise of a given mass depends on the heat input and can be written as

$$Q = mCdT .$$

Using the midpoint surface of each slab and the principle of conservation of heat energy, the temperature rise T of a point on the slab interface can be written as

$$k_1(\mathrm{TMAV}) \left[\frac{(\mathrm{TM1}-\mathrm{TC})}{\Delta X1}\right] - k_2(\mathrm{TPAV}) \left[\frac{(\mathrm{TC}-\mathrm{TP1})}{\Delta X2}\right]$$

$$+ D(x) \left(\frac{\Delta X1}{2} \rho 1 + \frac{\Delta X2}{2} \rho 2 \right) + \mathrm{ADD}$$

$$= \left(\rho 1 \frac{\Delta X1}{2} (\mathrm{CP1}) + \rho 2 \frac{\Delta X2}{2} (\mathrm{CP2})\right) \frac{\Delta T}{\Delta t}$$

The quantity D(x) is the dose deposited (j/g-sec) and the variable ADD depends on the boundary conditions if either slab is an exterior surface. The value of ADD under varying boundary conditions is as follows:

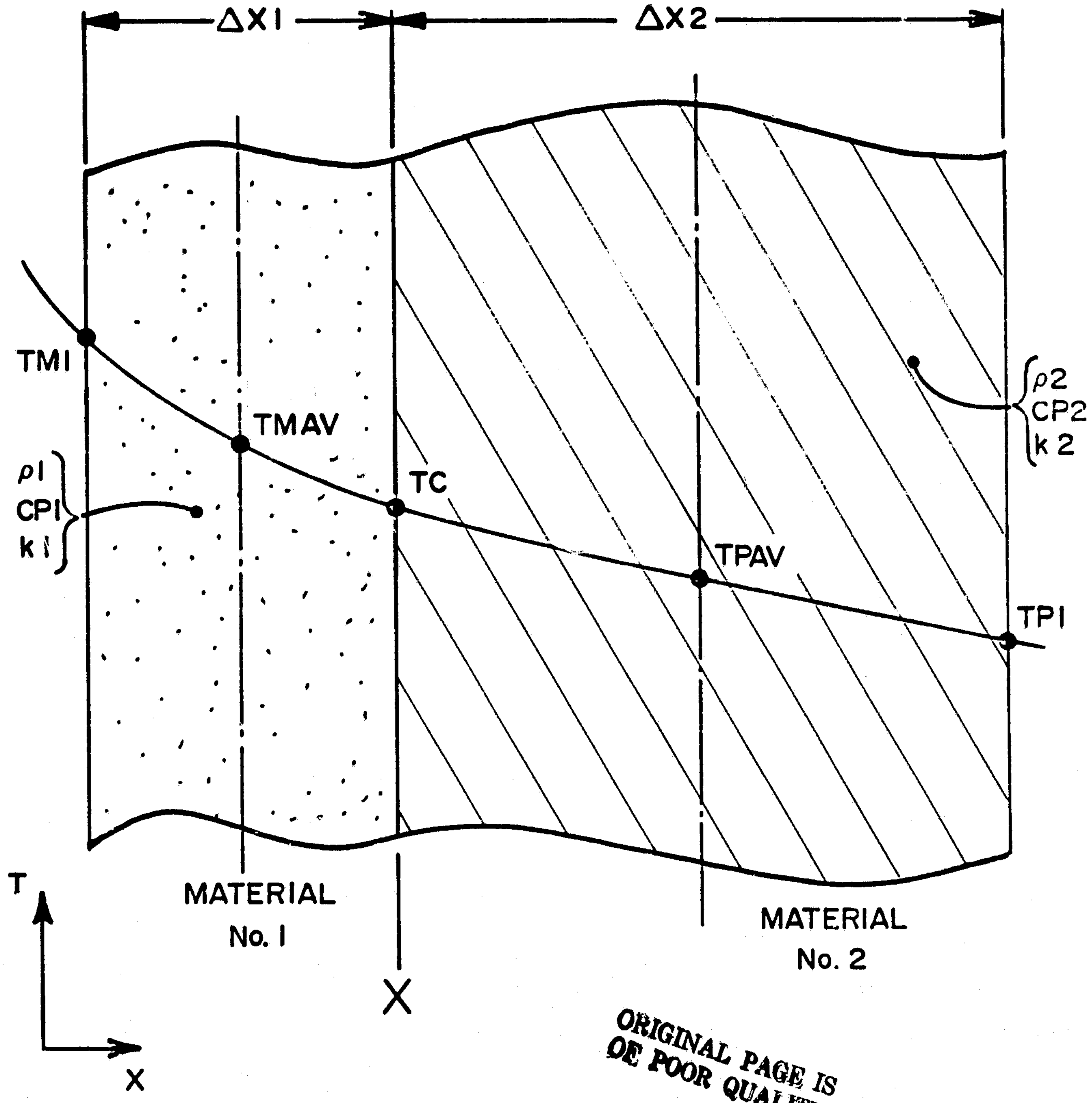

ORIGINAL PAGE IS OF POOR QUALITY

Figure 1. VXTEMP Grid Definitions

	Value	Condition
ADD =	$\sigma\varepsilon(TC)^4$	Radiation front/rear surface
	H(TP1-TC)	Conduction/convection interface
	0	No heat loss (or interior condition)

The temperature at x at time t + Δt depends on the previous temperature values at time t at points $X-\Delta X1$, X, and $X+\Delta X2$ and thus a direct iteration procedure is possible on a digital computer. The time and spatial increments must be chosen such that

$$\frac{K\Delta t}{(\Delta X)^2} < 0.5$$

to insure convergence.

To handle the solid/liquid phase change, the temperature change of a slab that has reached melt temperature is set to zero until the heat of fusion has been supplied for that particular slab. At this point the material is considered a liquid and the thermal parameters appropriate to the liquid state are used in the algorithm. Similar bookkeeping is done on change from liquid to solid phase.

At the present time, the following additional features are incorporated in the VXTEMP code:

- Deposition profile input in histogram or fitted polynomial format.
- Up to five different regions with different thermal properties can be input.
- Variable spatial increments in each region.
- Variable output format allows selected printout of data.

2.2 CODE TESTS

Several test runs were performed using configurations which allowed analytical solutions to be calculated for comparison with code predictions. The first test consisted of a two-material composite with a uniform electron beam deposition profile penetrating through half of the first material. This problem can be easily solved analytically for the equilibrium temperature distribution and the result was compared with the VXTEMP output for very long times (i.e, steady state or equilibrium conditions).

The closed form solution obtained from the differential equation

$$\nabla^2 T = \frac{-A}{k}$$

where A is the energy deposited per unit time and volume, and k is the thermal conductivity. For the one dimensional case the equation becomes

$$\frac{d^2T}{dX^2} + \frac{A}{k} = 0$$

for each of three regions:

Region I: deposition region ($A \neq 0$),
Region II: remainder of material one ($A = 0$),
Region III: all of material two ($A = 0$).

By matching the temperatures and temperature gradients at each boundary the solutions can be obtained and are listed below:

$$\text{Region I:} \quad T_I = AX_d \left[\left(X_1\left(\frac{1}{k_1} - \frac{1}{k_2}\right) + \frac{X_2}{k_2}\right) - \frac{X_d}{2k_1} - \frac{X^2}{X_d 2k_1}\right] + T0$$

where $(0<X<X_d)$

$$\text{Region II:} \quad T_{II} = AX_d \left[X_1\left(\frac{1}{k} - \frac{1}{k_2}\right) + \frac{X_2}{k_2} - \frac{X}{k_1}\right] + T0$$

where $(X_d<X<X_1)$

$$\text{Region III:} \quad T_{III} = \frac{AX_d}{k_2} (X_2 - X) + T\phi$$

$$\text{where } (X_1 < X < X_2)$$

The front surface temperature $T_I(X = 0)$ was calculated using this analytical technique and compared with the VXTEMP computer solution shown in Figure 2. The two values agree within 4%. This error can be reduced by using smaller grid spacings if higher accuracy is needed. Note that the change in slope at the material boundary is in agreement with the calculated value equal to k_1/k_2.

The next test involved "elevating" the material temperature into the melt range to check the phase change routines of VXTEMP. The material geometry and thermal properties are the same as those used in the first test with the addition of liquid phase data for the two materials including heat of fusion values. In this test, the energy deposition profile shape remained the same as that in the first test, but the dose values were scaled up to levels that result in a rapid melting of the material in the region where energy is deposited. Figure 3 shows the temperature profiles shortly after the end of the pulse ($T_{pulse} = 2.0 \times 10^{-6}$sec) and at several subsequent times. Initially the region subjected to energy deposition melts. As the heat flows outward, the surface temperature drops slightly while the melt interface moves outward even though the energy deposition has ceased. The thermal conductivity of the liquid state was arbitrarily chosen to be 2.5 times lower than that of the corresponding solid, so that the change in slopes at the melt interface could be easily determined and checked. After a short interval, the melt zone retreats as heat is lost to the solid. The two tests just described completed the preliminary verifications of the new code.

2.3 INPUT DATA FOR THE PEBA PROBLEM

The VXTEMP code has been used to determine the temperature profile generated by the standard PEBA beam at a fluence of 0.2 cal/cm^2, which is the threshold energy density for annealing. The deposition profile as used in this calculation is shown in Figure 4. The actual deposition profile varies as a function of both time and depth due to the changing electron beam energy and current levels. For purposes of this calculation, the depth-dose profile was

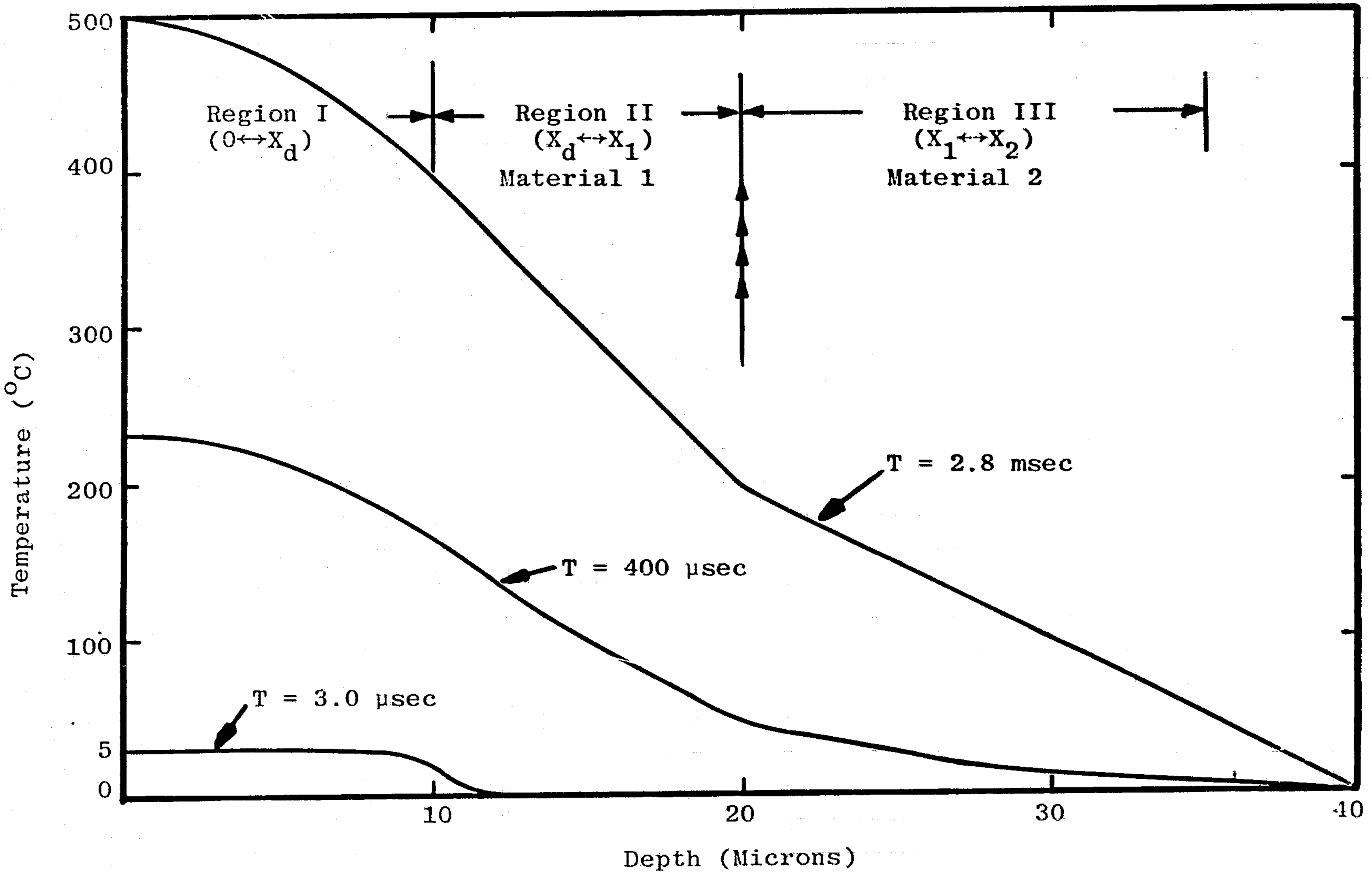

Figure 2. Calculated Temperature Profile Following Pulsed Energy Deposition in a Composite Material Without Melting.

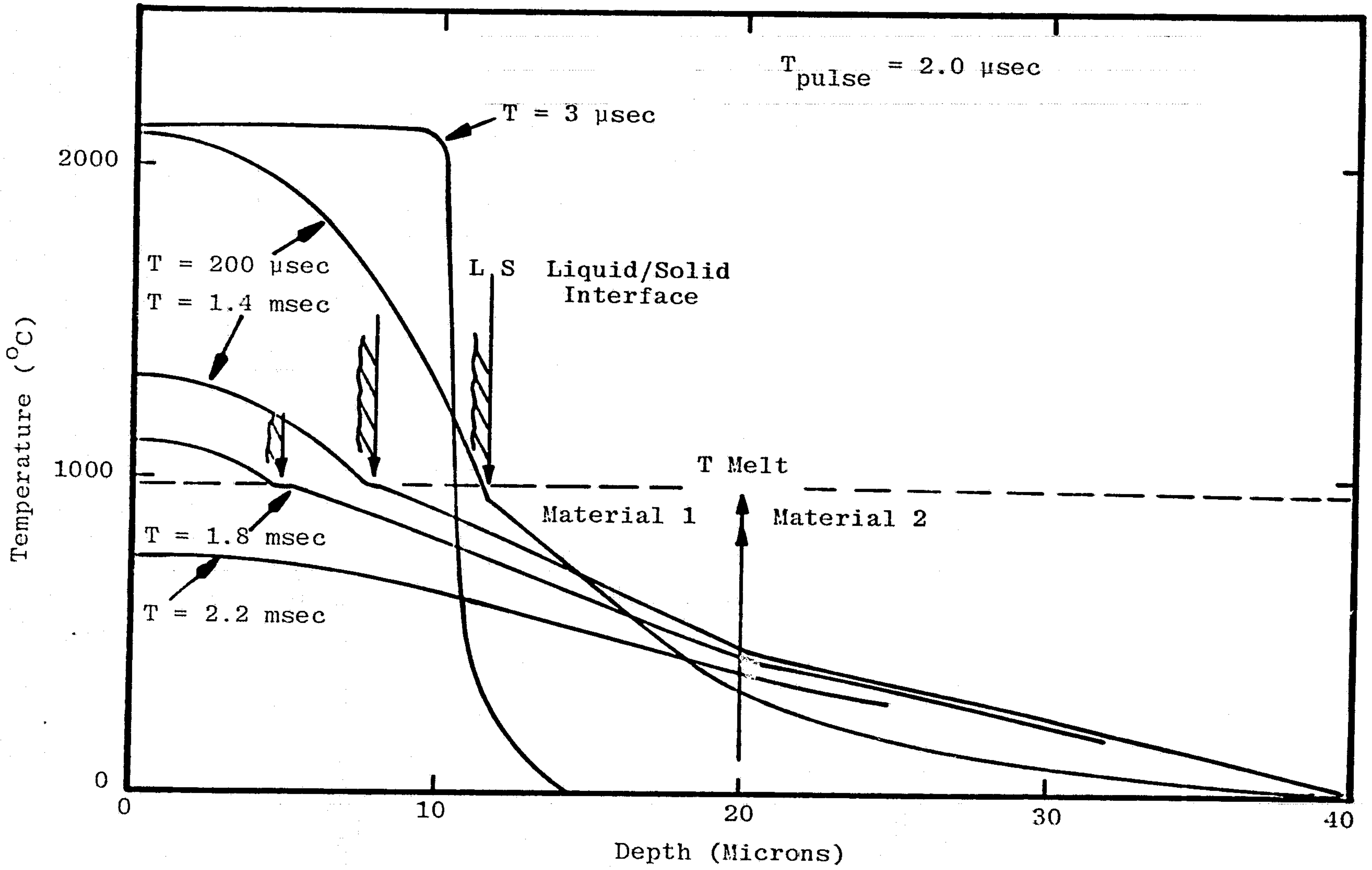

Figure 3. Calculated Temperature Profiles Following Pulsed Energy Deposition in a Composite Material with Melting.

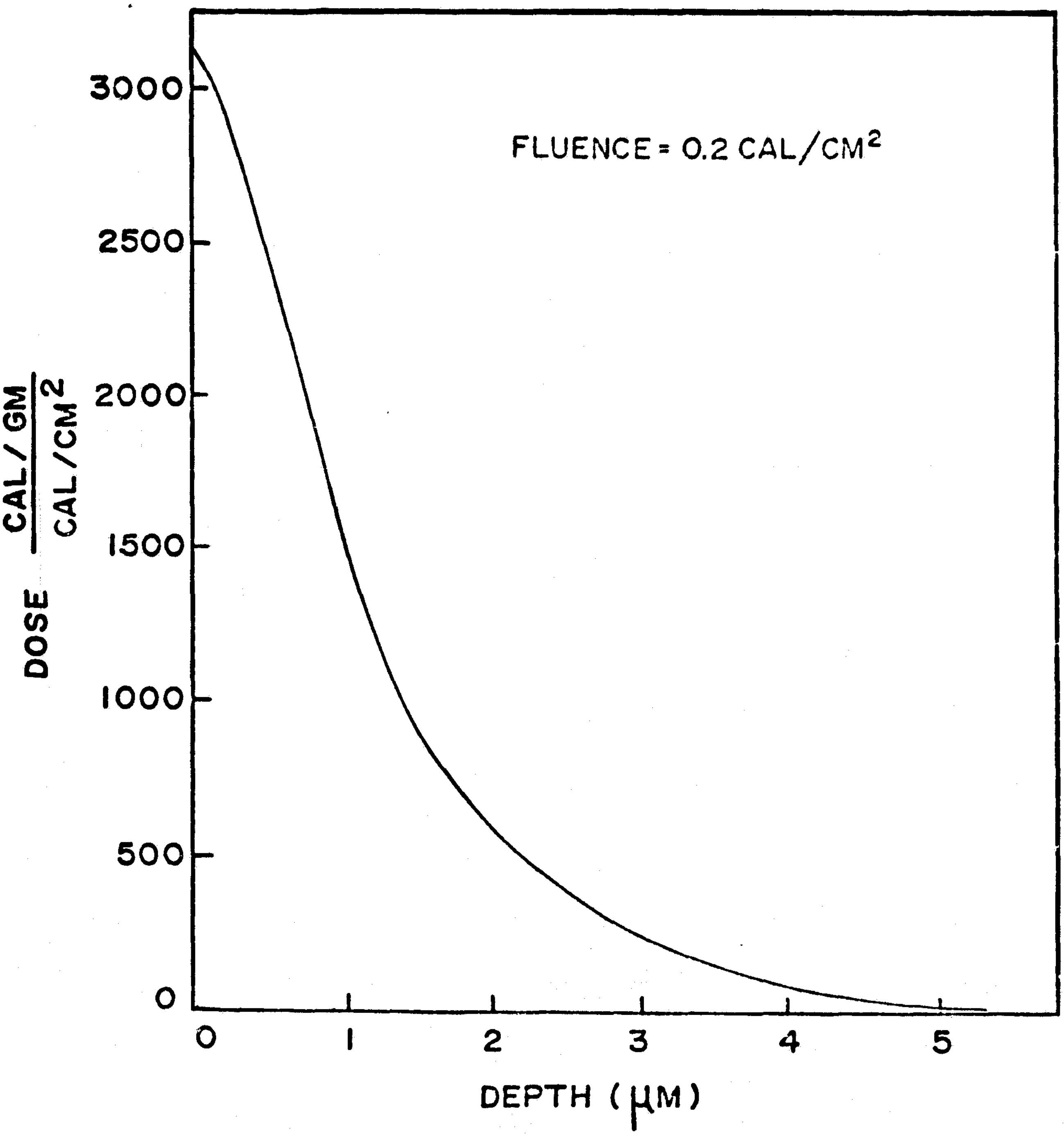

Figure 4. Energy Deposition vs. Depth Profile in Silicon for Pulsed Electron Beam.

assumed not to change in shape and to vary in amplitude in a Gaussian fashion, i.e.

$$\text{Dose} = D(x)\ e^{-(t-t_o)^2/2\sigma^2} = D(x,t)$$

where $\int_0^\infty D(x,t)dt$ is shown in Figure 4. This approximation is supported by experiments performed earlier in the program.

The thermal parameters used in this study are as follows. The specific heat as a function of temperature, C(T), of both crystalline and amorphous silicon was assumed to vary as the crystalline value with

$$C(T) = 0.8628 + 8.3452 \times 10^{-5}T - (1.6243 \times 10^4)/T^2$$

where C(T) is in Joules/gram-°K and T is the temperature in degrees Kelvin. The variation of the thermal conductivity of the various silicon states is shown in Figure 5, with the amorphous values being estimated from fused quartz and crystal quartz analogs.(13) Since we are assuming a glassy, amorphous layer with no heat of fusion during phase change, the melt and "pre-melt" thermal conductivity values for the amorphous layer were assumed equal.

The remaining thermal input data is listed below.(4)

PARAMETER	CRYSTAL	LIQUID	AMORPHOUS
H_{fusion}(j/gram)	1803	1803	0
ρ (gram/cm^3)	2.33	2.213	2.33
ϵ (emiss.)	0.5	0.46	0.5
k (j/sec-cm-°K)		.0750	
C (j/gram-°K)		.2433	

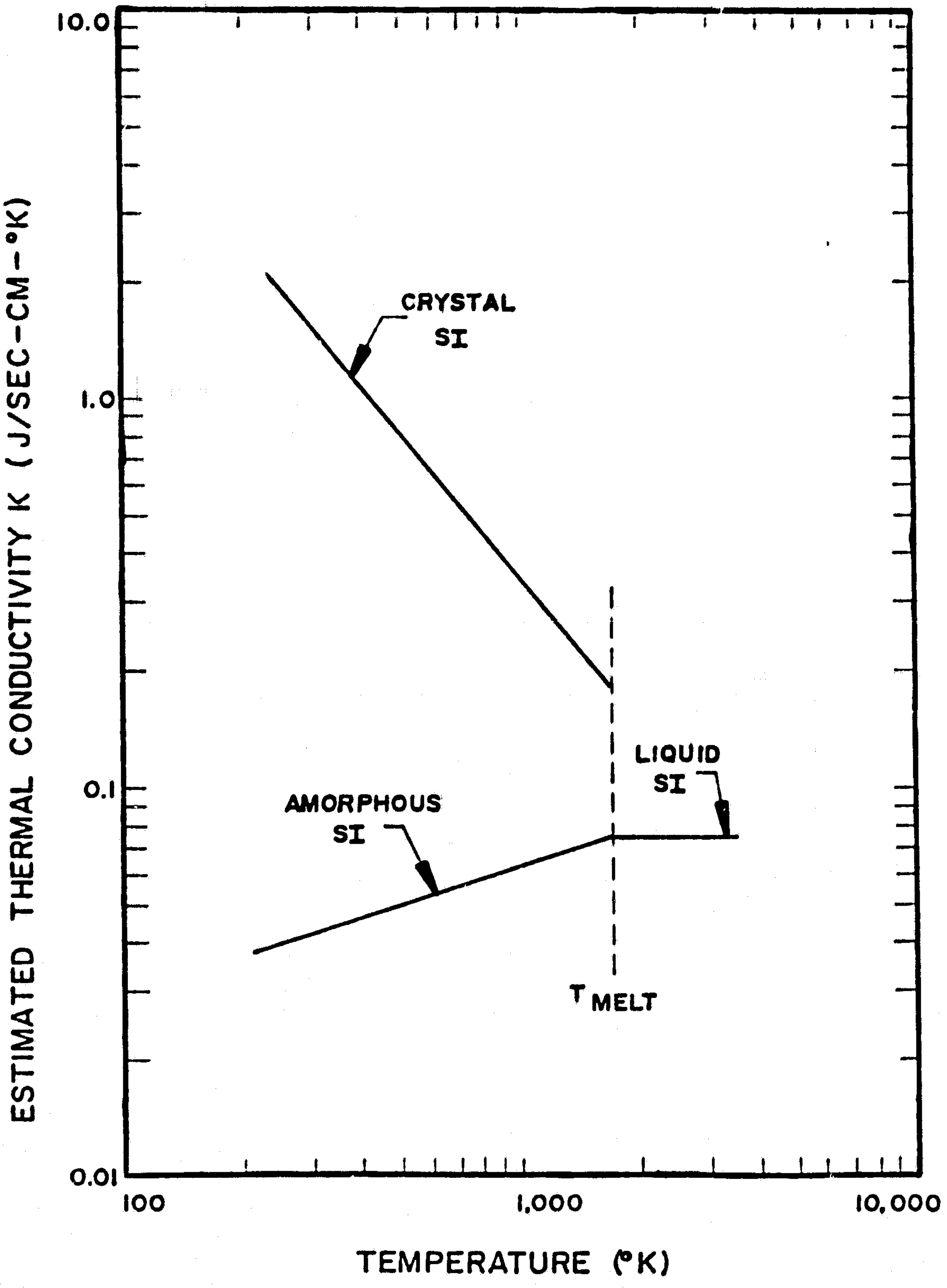

Figure 5. Variation of Thermal Conductivity with Temperature for Amorphous and Crystalline Silicon.

It should be noted that some of this data has been estimated since exact literature data is not always available. The errors induced by these uncertainties have little effect on the qualitative model developed from the VXTEMP predictions.

2.4 RESULTS AND INTERPRETATIONS

The physical models developed to explain some of the electron beam annealing processes are based on two VXTEMP runs. The first run, at an energy density of 0.2 cal/cm^2, was used to illucidate the annealing mechanism. The second run, at 0.3 cal/cm^2, provided information to develop a damage mechanism model. The code outputs are shown in Figures 6 - 7. Notice that front surface melt takes place at about 0.2 cal/cm^2, which is the annealing threshold. If the heat of fusion of the amorphous layer is assumed the same as crystal silicon, then front surface melt occurs around 0.25 - 0.27 cal/cm^2. It should be noted that the deposition profile was never measured below 1μ m and thus the energy deposited in the first few tenth-microns could be in error, allowing front surface melt at lower fluences. Recent private communications (6) indicate that the heat of fusion of the amorphous layer may be no larger than 60% of the crystal silicon value and thus melt should occur in the range of 0.2 - 0.25 cal/cm^2, which is in good agreement with Spire data.

The thermal conductivity of the amorphous layer is another input parameter whose value is not well known. Because the amorphous layer remains a solid for only 50 - 100 nsec, the temperature changes in the thin layer induced by changes in the assumed value of the thermal conductivity should be small. The effects of variation in thermal conductivity will be investigated with VXTEMP in the near future.

Evidence which qualitatively confirms the temperature profiles generated by VXTEMP will be presented in following sections of this report.

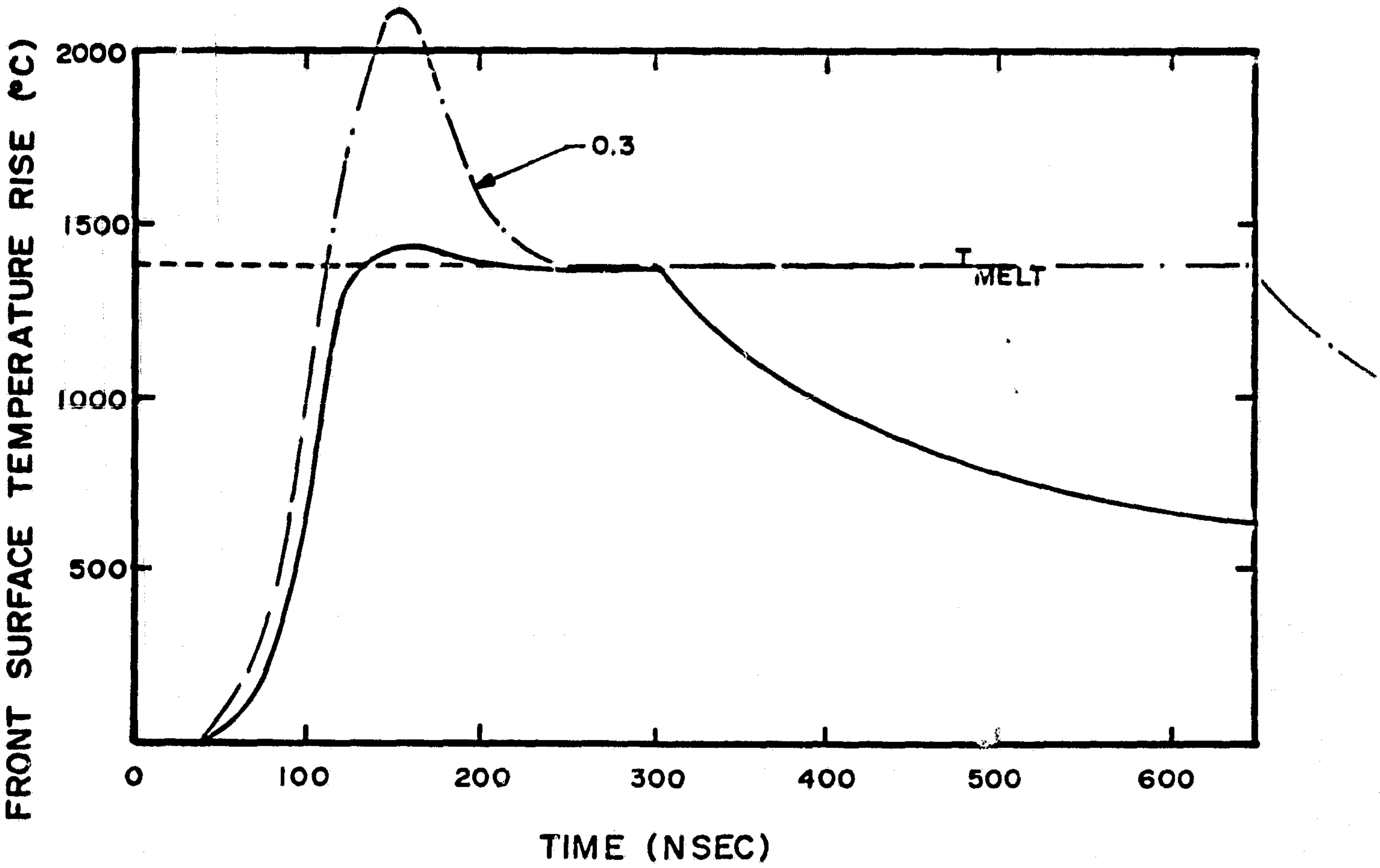

Figure 6. Front Surface Temperature versus Time for 0.2 and 0.3 cal/cm^2 Incident Energy Density.

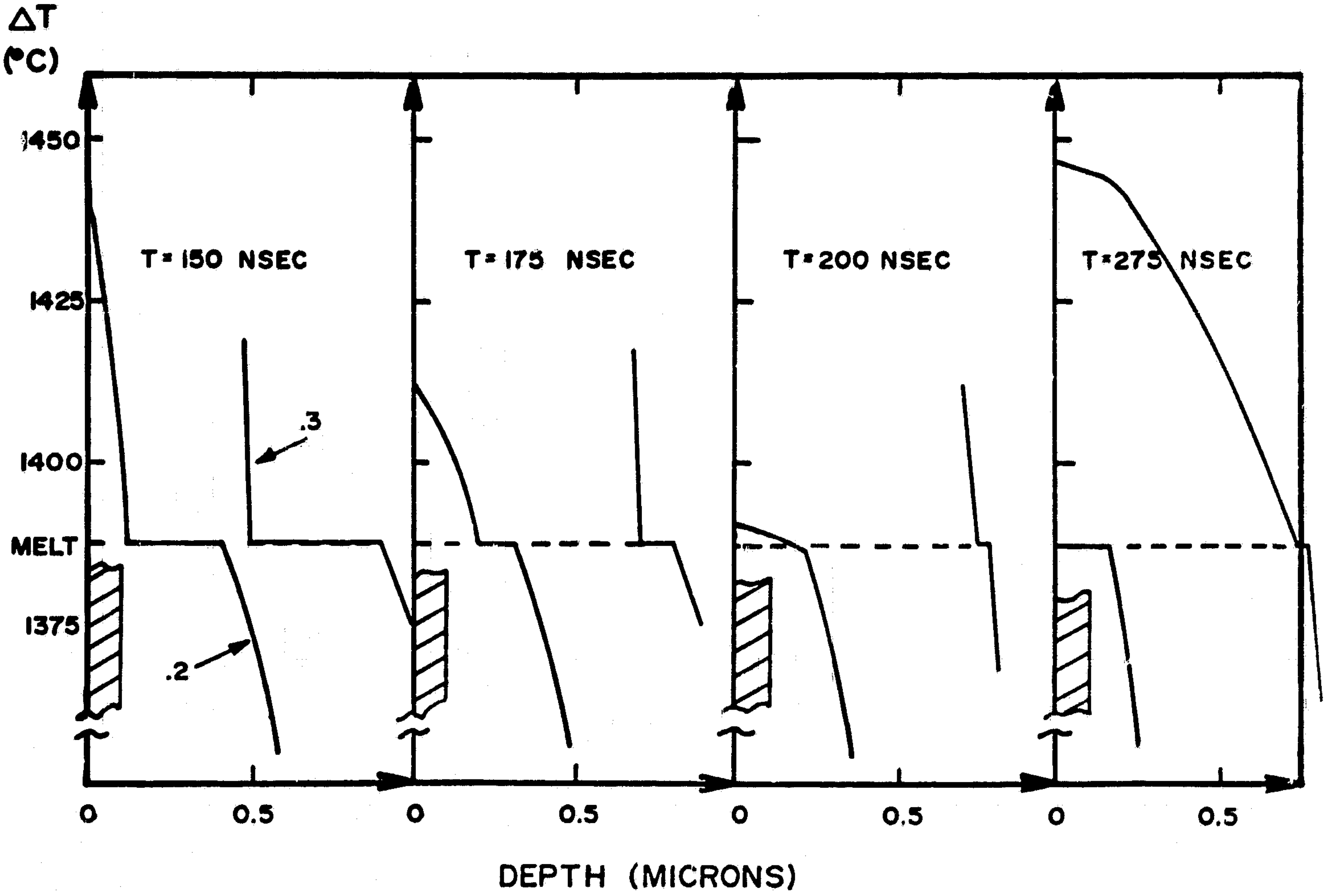

Figure 7( ). Temperature Profiles at Selected Time Intervals for 0.2 and 0.3 cal/cm^2 Incident Energy Density.

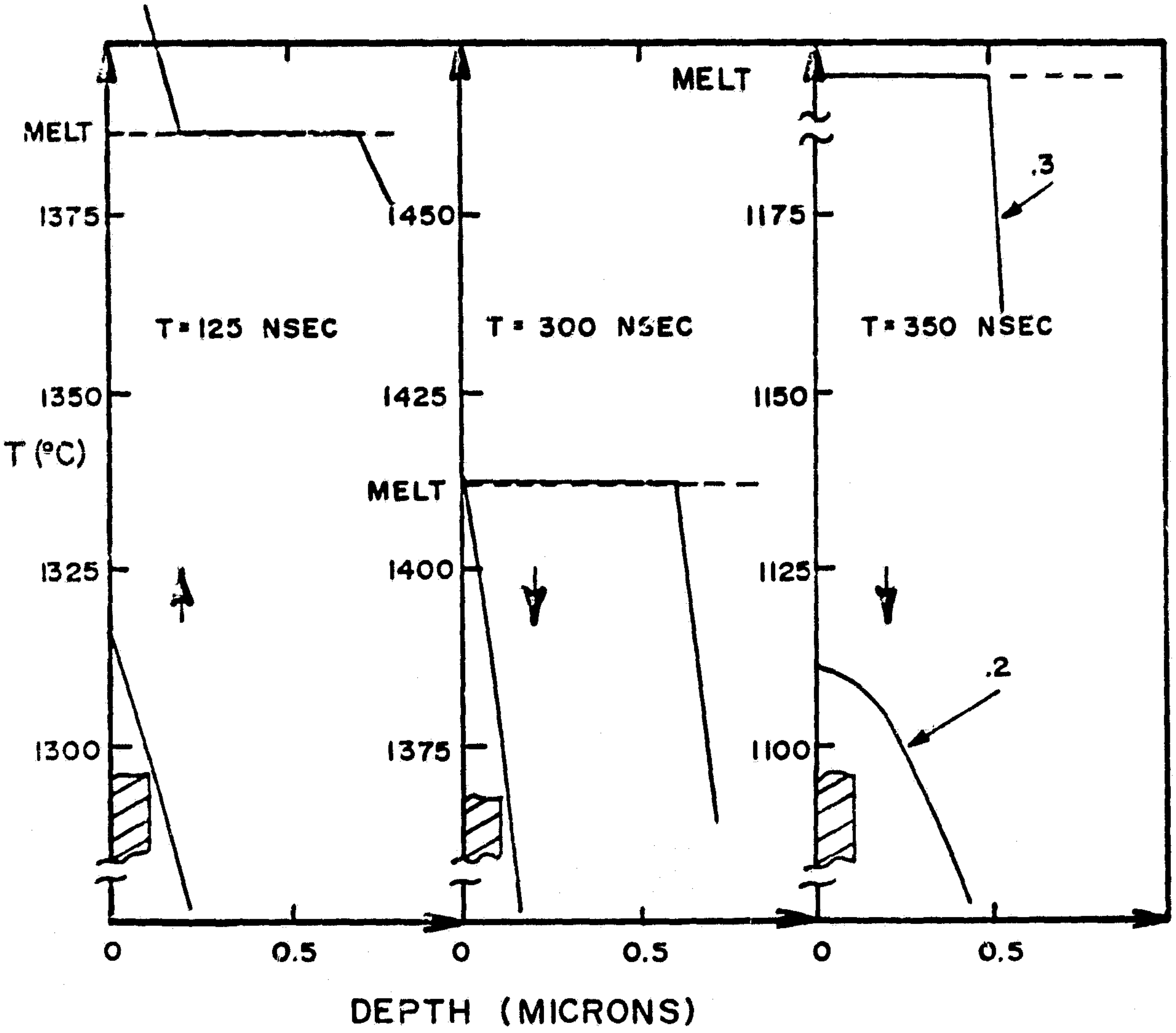

Figure 7(b). Temperature Profiles at Selected Time Intervals for 0.2 and 0.3 cal/cm^2 Incident Energy Density.

3.0 STRESS ANALYSIS

A description of the stress analysis and results related to damage mechanisms in pulsed electron beam processing is contained in the following sections.

3.1 THERMOELASTIC STRESS GENERATION

The stresses generated by variations in temperature within a medium can be determined by the equation of motion and the relation between stress and strain (displacement) in the material. Hooke's Law for the relationship between stress and strain in a homogeneous, isotropic medium can be written as (14):

$$S_{ij} = \lambda \theta \delta_{ij} + 2\,\mu \varepsilon_{ij} - \frac{E\alpha_v T}{3(1-2\nu)}\,\delta_{ij}$$

where:

$$\varepsilon_{ij} \equiv \frac{1}{2}\left(\frac{\partial u_i}{\partial x_j} + \frac{\partial u_j}{\partial x_i}\right)$$

and:

$$\theta = \varepsilon_{11} + \varepsilon_{22} + \varepsilon_{33}$$

and λ and μ are the Lamé constants, E is Young's modulus, α_v is the volume coefficient of expansion, and ν is Poisson's ratio. The quantity T represents the temperature change in a given region of the medium, the ε_{ij} are strains, and the quantity $\overline{u}$ is a displacement vector which we ultimately wish to determine. The equation of motion for a volume element in the material can be written as:

$$\rho\,\frac{\partial^2 x_j}{\partial t^2} = \rho X_j + \frac{\partial S_{ij}}{\partial x_i}$$

where X_j are due to body forces (i.e gravity) and S_{ij} are stresses acting on the volume surfaces. If we consider the case of no body forces with the volume element remaining in equilibrium, then the above equation reduces to

$$\frac{\partial S_{ij}}{\partial x_j} = 0$$

If Hooke's Law for the stresses S_{ij} is inserted in the above equation, it is possible to arrive at the differential equation for the displacement vector components$^{(10)}$

$$\frac{3(1-\nu)}{1+\nu} \ \nabla \ (\nabla \ \ \vec{u}) - \frac{3(1-2\nu)}{2(1+\nu)} \ \nabla \times \nabla \times \vec{u} = \alpha_v \nabla T$$

Once $\vec{u}$ is determined, subject to appropriate boundary conditions, then the stresses and strains can in principle be determined.

3.1.1 Calculation of Normal Stresses

The normal stresses induced in the silicon wafer in the directions parallel to the surface (x, y) have been calculated using a model which does not allow bending. The effects of bending on the magnitude of the stresses will be addressed after the results of the simple planar model are presented. The derivation of the normal stress produced by the PEBA temperature profile is as follows.

The planar constraint requires that $u_z = f(z)$ only since no curvature or bending of the wafer is allowed. If there are no external forces on the wafer and the above conditions hold, then it is reasonable to assume that there will be no shear forces, or $u_x = f(x)$ only and $u_y = f(y)$ only. Under these conditions, the equations for the components of the displacement vector reduce to

$$\frac{d^2u_x}{dx^2} = 0$$

$$\frac{d^2u_y}{dy^2} = 0$$

$$\frac{d^2u_z}{dz^2} = K \frac{dT(z)}{dz}$$

Solving these for the strains results in the following

$$\varepsilon_{xx} = \varepsilon_{yy} = A$$

$$\varepsilon_{zz} = B + K\,T(z)$$

where A and B are constants to be determined and $K = \frac{1+\nu}{3(1-\nu)}$. Since the silicon is free to expand in the z direction, and the wafer is unconstrained, $S_{zz} = 0$ and using Hooke's law one obtains the relation

$$A = -\frac{(\lambda+2\mu)}{\lambda}\,\frac{B}{2}$$

Using the above relation and Hooke's Law for S_{xx}, we find:

$$S_{xx} = -\frac{E\alpha_v T(z)}{3(1-\nu)}$$

This stress distribution does not produce zero stress at the ends of the wafer for an arbitrary temperature distribution T(z), nor does it allow a zero net force and moment at the surface. Saint-Venant's principle(14) allows the addition of stress terms X + Wz which yields

$$S_{xx} = X + Wz - \frac{E\alpha_v T(z)}{3(1-\nu)}$$

The values of X and W are chosen so that $\int S_{xx}\,dz = \int S_{xx}\,z\,dz = 0$; i.e. there is no net force or torque present at the ends of the wafer, while the effects of these additional stresses will be negligible at distances from the wafer ends comparable to the wafer thickness. For very shallow temperature profiles the maximum normal stress approaches

$$S_{xx}^{\text{max.}} \simeq \frac{E\alpha_v T_{\text{max}}}{3(1-\nu)}$$

For silicon just below melt temperature with values of $\alpha_v = 15 \times 10^{-6}/^oC$, $\nu = .25$, $E = 1.9 \times 10^{12}$ dynes/cm, and $T_{max} = 1385^oC$, the calculated normal stress approaches a maximum of 17.5×10^9 dynes/cm^2 for the (111) orientation. Data on fracture stress in silicon(4) shows that the stress necessary for fracture rises rapidly above 1000°C and approaches 8×10^9 dynes/cm^2 at 1200°C. Small silicon whiskers are reported as having breaking strengths in excess of 20×10^9 dynes/cm^2(4). Since plastic deformation starts at about 600°C for silicon(4), the calculated stresses are probably two or three times higher than the actual stresses generated by the electron beam pulse. In addition, if bending of the silicon wafer is allowed, the stress levels are reduced by factors of three to four(5). Therefore, it seems likely that the normal stresses generated by the temperatures near melt are not the primary cause for the observed fractures. A more thorough discussion of this hypothesis is presented later in this report.

3.1.2 Calculation of Shear Stresses

A straight forward solution of the differential equations for the displacement vector previously presented is difficult when arbitrary shear forces are included in the problem. Therefore, a solution by inspection was chosen in an attempt to estimate the magnitude of shear forces that would be produced by the temperature gradients predicted by VXTEMP. For a region with a linear temperature gradient $g = dT/dz$, a simple solution which satisfies the differential equations for u and allows for shear forces is

$$U_x = Axz, \; U_y = Ayz, \; U_z = Bz^2$$

Substitution of this solution into the differential equation yields the relation

$$2B + 2A\,(1-K) = K^1 g$$

where

$$K = \frac{1}{2}\,\frac{(1-2\nu)}{(1-\nu)} \quad \text{and} \quad K^1 = \frac{\alpha_v(1+\nu)}{3(1-\nu)}$$

Using the conditions of zero force and moment at the wafer ends plus Hooke's Law, the additional relation

$$2A(\lambda + \mu) + \lambda 2B - \frac{E\alpha_v g}{3(1-2\nu)} = 0$$

is obtained. The solution for A is

$$A = \frac{\alpha_v g}{3} \frac{(1+\nu)}{(1-2\nu)}$$

and therefore the shear stress is

$$S_{xz} = 2\mu \, \varepsilon_{xz} \approx \mu \frac{\alpha_v}{3} g \frac{(1+\nu)}{(1-2\nu)} x$$

where μ is the modulus of rigidity and x is the position from the center of the wafer. Note that the shear stress depends on the temperature gradient and modulus of rigidity for a given position. For the short deposition times used in PEBA, the temperature gradient is roughly proportional to the incident energy density, since the induced temperature profile is almost identical to the deposition profile because very little heat flow is possible during the electron beam pulse. In addition, the modulus of rigidity is related to Young's modulus by the relation

$$\mu = \frac{E}{2(1+\nu)}$$

Thus shear stresses produced by the pulsed electron beam should be proportional to the incident energy density and the value of Young's modulus for the appropriate orientation. This proportionality is evident in data presented in the final sections of this report.

3.2 PRESSURE WAVE GENERATION

The technical aspects of pressure generation by the rapid deposition of energy in a material has recently been examined (Spire TR-78-02). The peak pressure developed for a gaussian energy deposition profile has been shown to be

$$\Delta P_{max} = \frac{GF_o}{2V_o t_p}$$

where G is the Grueneisen parameter, F_o is the fluence, V_o the velocity of sound in the medium, and t_p is the pulse width. Using the values G = 1.9 dyne-cm/erg F_o = 1.25 j/cm^2, V_o = 1.3 x 10^6 cm/sec, and t_p = 60 x 10^{-9} sec, a maximum pressure of about 1.5 x 10^8 dynes/cm^2 is predicted. This level is ten times lower than the fracture stress for silicon(4) at room temperatures and thus pressure waves are not considered as a primary fracture mechanism. The calculation was checked with a hydrodynamic code, PUFF (memo 78413) which gave similar results.

3.3 IMPLANT STRAIN

Lattice strain may be produced by impurities placed in the silicon during the doping procedure, depending on the nature of the implant ion. The strain can be calculated from(4)

$$\varepsilon = 1 + f(\gamma^3 - 1)^{1/3} - 1$$

where f is the atom fraction of the dopant and γ is the ratio of the Pauling covalant radii of the two different atoms. Using $\gamma = 0.932$ and a dopant concentration of 10^{19} atoms/cm^3, strains of the order of $\varepsilon = 10^{-6}$ are produced. Stresses of the order of $^{\varepsilon}E$ are produced which for silicon is the order of 2 x 10^6 dynes/cm^2, which is three orders of magnitude below fracture levels. These stress levels may, however, be responsible for lattice slips(4) which could alter the ultimate fracture strength of the amorphous material.

4.0 PROPOSED MODELS FOR PULSED ANNEALING PROCESSES

The following sections contain descriptions of proposed physical models for several effects associated with the pusled electron beam treatment of silicon. The two major phenomena covered are the recrystallization of the ion-implanted silicon, and the fracture of the silicon under high fluence irradiation.

4.1 ANNEALING BY RECRYSTALLIZATION

The VXTEMP calculation makes apparent the mechanism responsible for the annealing of the ion implantation damage. It is clear from the work described earlier and recent literature reports(12) that melting of the amorphous layer created by ion implantation occurs and is necessary for the re-formation of very large single crystal silicon regions and the subsequent optimum electrical response characteristics. The question of whether or not the amorphous layer has a lower heat of fusion than the single crystal silicon does not affect the mechanism proposed in this report. The value of the heat of fusion will determine to a certain extent the location of the liquid-solid interface, but does not rule out the existence of a liquid zone because of uncertainties in the deposition profile shape and magnitude in the critical tenth-micron region. Based on the data shown in Figure 6, recrystallization takes place rapidly at the solid-liquid interface, which begins in the single crystal region below the implant layer where a good single crystal substrate exists. As heat is lost to the crystal, the interface recedes toward the front surface at which time the process is complete. Experimental evidence supporting this hypothesis appears in the following section.

4.1.1 Support Data for Melt Model

The most unequivocal evidence supporting the hypothesis of a melted layer has been SEM photographs presented by Spire in recent papers(2). Figure 8 shows before and after SEM pictures of a silicon wafer surface treated with a pulsed electron beam. The smoothing shown on formerly sharp crystal edges is indicative of surface layer melting.

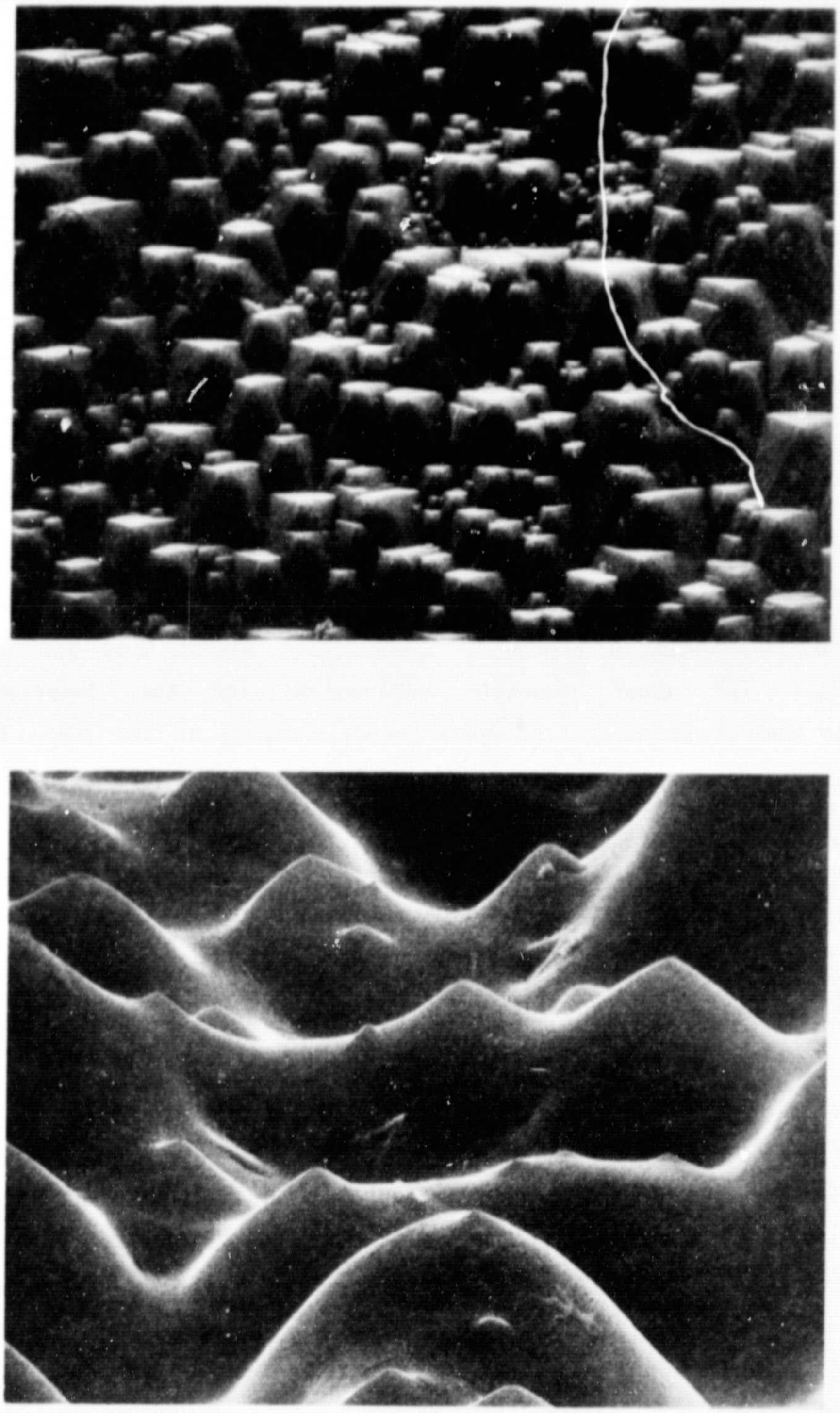

Figure 8. Texturized (100) Silicon Surface Before (a) and after (b) Pulsed Electron Beam Heating.

The results of diffusion calculations(7) of the before and after dopant profiles of an implanted wafer subjected to pulsed electron beam annealing are shown in Figure 9 along with experimentally determined profiles obtained by helium ion backscattering(8). A uniform implant profile was assumed to simplify the calculation. The results suggest that the melted layer must remain as a liquid for the order of 100 nsec in order to account for the observed dopant diffusion based on the reported diffusion coefficient for arsenic in liquid silicon(9). This agrees with the code predictions of 50 - 100 nsec shown in Figure 6.

4.2 DAMAGE MECHANISMS

Several fracture mechanisms were investigated analytically in earlier sections of this report: thermoelastic stress, pressure wave stress, and ion implantation induced stress. The most plausible explanation for the observed fracture phenomenon is that it is caused by shear forces created by the large temperature gradients produced by the electron beam pulse. Data and interpretation supporting this hypothesis is as follows.

4.2.1 Support Data for Shear Model

The experimentally measured fracture thresholds for pulsed electron beam heating of silicon wafers is shown in Table I. An interpretation of this data is as follows. An incident energy density of 0.2 cal/cm^2 will anneal an implanted wafer and thus causes the front surface to melt. Within the errors of the measurement, a comparable energy density (0.22 cal/cm^2) causes an unimplanted wafer cut in the (111) orientation to fracture. One might conclude from this fact and the previously calculated normal stress that at the melt temperature the fracture stress for silicon is exceeded, thus explaining the (111) fracture data. However, the (100) unimplanted wafer does not fracture at this level, presumably because the Young's modulus is lower and thus the stress generated is lower. Increasing the incident energy density should not increase the stress since it is already at its maximum value as soon as front surface melt takes place. Increasing the incident energy

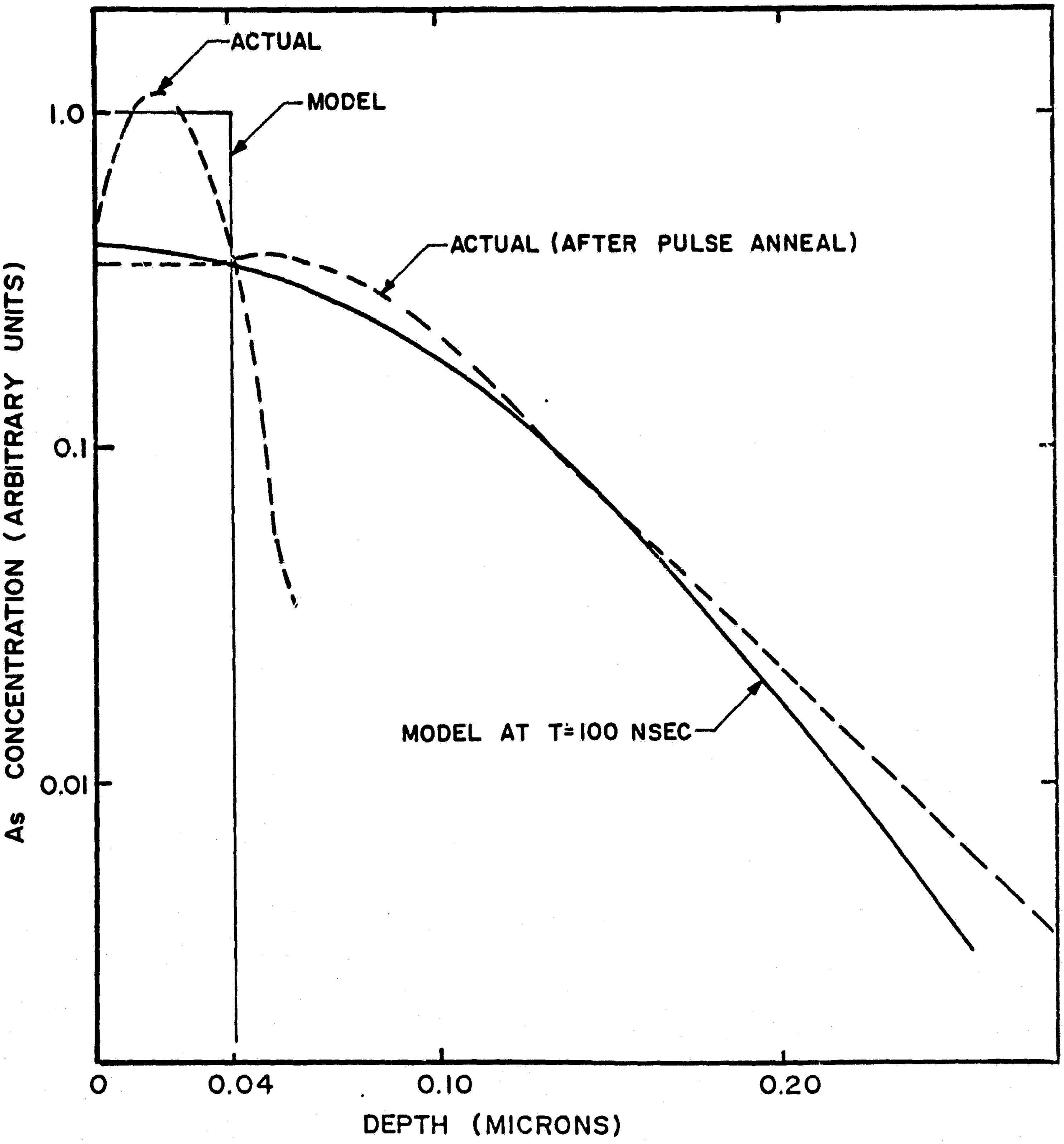

Figure 9. Predicted and Measured Dopant Diffusion Profile in Liquid Silicon.

TABLE I

Summary of Measured Fracture Thresholds for Pulsed Electron Beam Heating as a Function of Silicon Crystallographic Orientation

Parameter	Crystallographic Orientation	
	J (111)	J (100)
Microfracture of Unimplanted Wafer	0.22 ± 0.02 (cal/cm^2)	0.30 ± 0.02 (cal/cm^2)
Microfracture of Junction Implanted Wafer	0.27 ± 0.03 (cal/cm^2)	0.30 ± 0.03 (cal/cm^2)
Implant Anneal	>0.2 (cal/cm^2)	>0.2 (cal/cm^2)
Young's Modulus	1.9 x 10^{12} dynes/cm^2	1.3 x 10^{12} dynes/cm^2

Notes: Si: 7.6 cm Diameter, 250-500 μm thick p-type,
3 ± 1 ohm/cm

Implant: 10^{15} $^{31}P^+$ cm^{-2} at 10 keV should cause the melt region to penetrate further into the wafer causing the region of maximum stress to shift further into the wafer without increasing the magnitude of the stress. The fact that the (100) unimplanted wafer fractures at 0.3 cal/cm^2 implies that the damage mechanism does not initially involve the normal components of the stress. This leads to the investigation of shear forces as the primary cause of fracture.

It has been previously shown that the shear stress depends on the temperature gradient. For the short pulse durations involved in electron beam recrystallization, the temperature profile is the same as the incident energy density profile and therefore the temperature gradient is proportional to the incident energy density. Thus, the magnitude of shear stress produced is proportional to the incident energy density which explains the (100) unimplanted wafer fracture dependence on incident energy once the melt temperature has been reached. Moreover, since the modulus of rigidity is related to Young's modulus by the relation $\mu = E/ 2(1 + \nu)$ the shear stresses generated in the two crystallographic orientations should depend on the product of Young's modulus and the temperature gradient if variations in ν are neglected. If the silicon fracture stress under shear is independent of orientation then

$$S_{\text{shear}}^{\text{fracture}} \ \alpha \ E_{(111)} \ g_{J_{(111)}} = E_{(100)} \ g_{J_{(100)}}$$

Therefore, the ratio of the incident energy densities of fracture for the two orientations should equal the inverse of the ratio of the two Young's moduli. From the data in Table I, $E_{(100)}/E_{(111)} = 0.68$ and $J_{(111)}/J_{(100)} = 0.73$ which shows good agreement. Figure 10(a) and (b) show SEM photographs of the damage produced at threshold for a (111) implanted wafer. The curling of the "platelet" edges is indicative of shear-induced failure in the region of maximum temperature gradients followed by surface cracking initiated in the regions of shear failure.

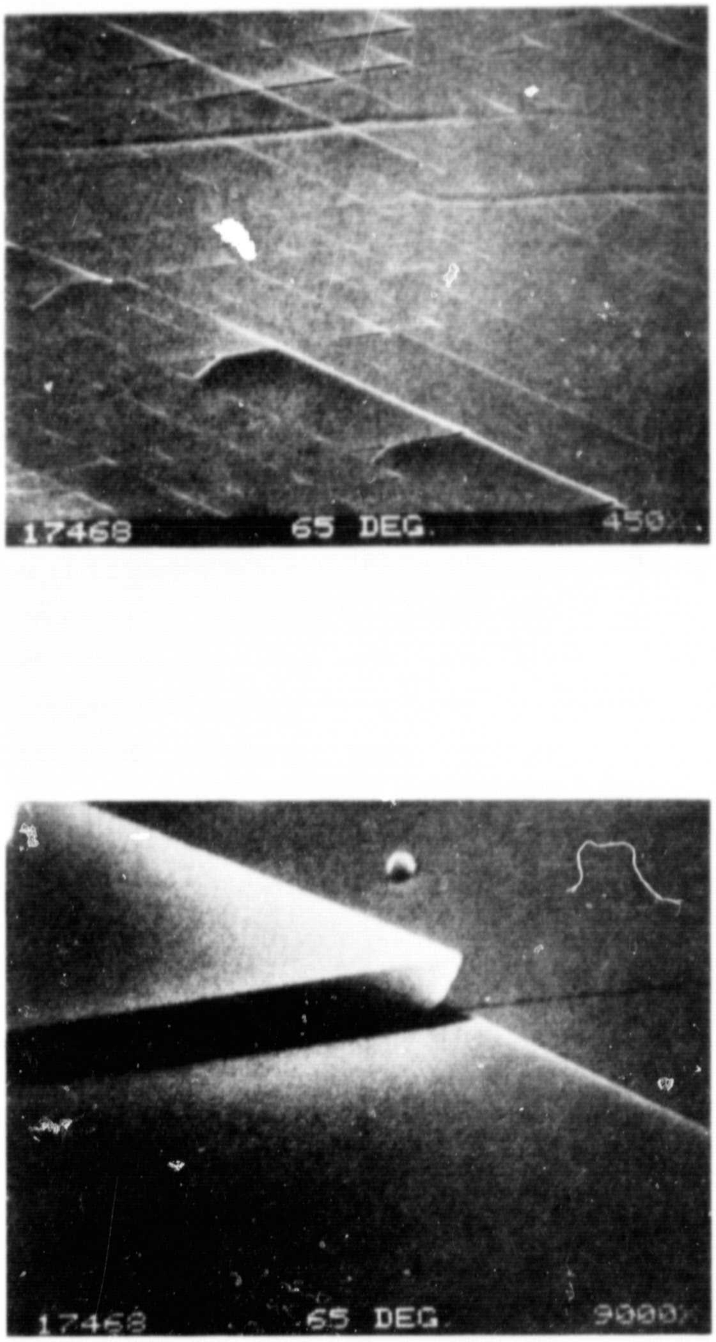

ORIGINAL PAGE IS
OF POOR QUALITY

Figure 10. SEM Photographs Showing Fracture of Implanted (111) Silicon Wafer after 0.27 cal/cm^2 Electron Beam Pulse. Magnification in (a) is 450 X, and in (b) is 9000 X.

The increase in fracture resistance of the (111) oriented silicon due to implantation is explained as follows. At the threshold for annealing (0.2cal/cm^2) the maximum temperature gradient appears in the amorphous region, which may extend out to 0.3 μ m depending on the implant ion species and energy. It is believed that this layer is able to withstand larger stresses before failure due to the absence of long range bonding caused by ion bombardment. The fracture does not occur until the incident energy density is sufficiently high to cause the region of maximum temperature gradients to extend into the underlying crystal silicon region, thus causing failure. Estimates made from Figure 7(a),(b) indicate fracture at depths of about 1 μm for the incident energy density of 0.27 cal/cm^2, which agrees with code predictions of a maximum gradient at 0.9 m for 0.3 cal/cm^2.

4.3 CONCLUSION

The time and spatial dependence of the temperature rise produced in ion implanted silicon subjected to pulsed electron beam bombardment has been numerically calculated. The computer generated temperature profiles have been used to calculate the thermoelastic stresses produced by the deposited energy. Experimental measurements of the incident energy density thresholds for fracture of the silicon have been made, and damage thresholds in the range of 1.1 - 1.25 J/cm^2 have been recorded. The temperature calculations have been qualitatively verified by diffusion profile measurements as compared with calculated profiles based on dopant diffusion in liquid silicon. The shear forces produced by the large temperature gradients have been proposed as the primary cause of fracture.

REFERENCES

1 A. R. Kirkpatrick, J. A. Minnucci, and A. C. Greenwald, IEEE Trans. Electron Devices, ED-24 (4), 429 (1977).

2. A. C. Greenwald, A. R. Kirkpatrick, R. G. Little, and J. A. Minnucci, J. Appl. Phys. (to be published).

3. R. Lowell and R. Little, Tech. Report 73-09, Spire Corp., Bedford, MA 01730 (1973) (unpublished).

4. W. R. Runyan, Silicon Semiconductor Technology, McGraw Hill (1965), Chap. 10.

5. J. R. Dennis and E. B. Hale, J. Appl. Phys., 49 (3), 1119 (1978).

6. D. H. Turnbull (private communication). The value may be as large as 60-70% of the single crystal heat of fusion.

7. H. S. Carslaw and J. C. Jaeger, Conduction of Heat in Solids, Oxford University Press (1959), p. 54.

8. S. S. Lau, W. Teng, and J. Mayer, provided helium ion backscatter data.

9. J. C. Brice, Solid State Electronics, 6, 673 (1963).

10. L. D. Landau and E. M. Lifshitz, Theory of Elasticity, Pergamon Press Ltd. (1959), p. 19.

11. H. M. Westergaard, Theory of Elasticity and Plasticity, Dover Publications (1964), p. 116.

12. P. Baeri, S. V. Campisano, G. Foti, and E. Rimini, Appl. Phys. Lett., 33 (2), 15 July 1978.

13. C. Kittel, Introduction to Solid State Physics, John Wiley & Sons (1971), p. 271.

14. R. R. Long, Mechanics of solids and Fluids, Prentice Hall (1963).

15. Solar Cell Array Design Handbood, Vol. I, JPL SP 43-38 (1976), Pg. 9.7 - 5.

APPENDIX D

TABULAR PERFORMANCE DATA FOR ION IMPLANTED/PULSE ANNEALED SOLAR CELLS

ION IMPLANTED/PULSE ANNEALED CELL PERFORMANCE

	AM0-25°C			AM1-28°C
Cell Number	I_{sc}(A)	V_{oc}(V)	P_{max}(W)	%
1801-16	1.670	0.564	0.598	11.4
1801-10	1.648	0.557	0.619	11.8
1801-7	1.646	0.557	0.625	12.0
1801-4	1.660	0.562	0.675	12.9
1801-13	1.649	0.557	0.619	11.8
1944-3	1.580	0.526	0.552	10.5
1944-4	1.618	0.525	0.576	10.9
1944-5	1.591	0.533	0.580	11.0
1944-6	1.571	0.514	0.532	10.1
1945-1	1.628	0.546	0.647	12.3
1945-2	1.602	0.550	0.632	12.0
1945-3	1.598	0.549	0.631	12.0
1945-4	1.613	0.546	0.640	12.2
1945-5	1.603	0.544	0.624	11.9
1945-6	1.596	0.543	0.635	12.1
1945-7	1.611	0.539	0.622	11.8
1945-8	1.602	0.548	0.602	11.4
1945-9	1.592	0.546	0.626	11.9
1945-10	1.596	0.542	0.585	11.1
1946-1	1.598	0.550	0.623	11.8
1946-3	1.567	0.545	0.592	11.2
1946-5	1.559	0.540	0.562	10.7
1946-6	1.558	0.541	0.598	11.4
1946-7	1.603	0.546	0.605	11.5
1946-8	1.578	0.538	0.589	11.2
1946-10	1.579	0.542	0.561	10.7
1946-11	1.569	0.540	0.596	11.3
1946-12	1.599	0.547	0.616	11.7
1946-13	1.603	0.547	0.606	11.5

ION IMPLANTED/PULSE ANNEALED CELL PERFORMANCE (Continued)

	AM0-25°C			AM1-28°C
Cell Number	I_{sc}(A)	V_{oc}(V)	P_{max}(W)	%
1946-14	1.569	0.546	0.593	11.3
1946-15	1.586	0.547	0.600	11.4
1946-16	1.600	0.549	0.618	11.7
1946-17	1.615	0.542	0.619	11.8
1946-18	1.591	0.547	0.605	11.5
1946-19	1.578	0.546	0.609	11.6
1947-1	1.608	0.561	0.669	12.7
1947-2	1.640	0.553	0.634	12.1
1947-3	1.585	0.554	0.632	12.0
1947-4	1.553	0.543	0.629	12.0
1947-5	1.608	0.553	0.642	12.2
1947-6	1.608	0.560	0.642	12.2
1947-7	1.620	0.567	0.676	12.8
1947-8	1.598	0.556	0.634	12.1
1947-9	1.597	0.555	0.619	11.8
1947-10	1.636	0.551	0.584	11.1
1947-11	1.594	0.557	0.630	12.0
1947-13	1.608	0.555	0.636	12.1
1949-1	1.640	0.554	0.669	12.7
1949-2	1.609	0.558	0.574	10.9
1949-3	1.637	0.569	0.644	12.2
1949-4	1.680	0.568	0.628	11.9
1949-5	1.654	0.562	0.602	11.4
1949-6	1.682	0.552	0.576	10.9
1949-7	1.620	0.553	0.549	10.4
1949-8	1.625	0.563	0.605	11.5
1949-9	1.640	0.563	0.614	11.7
1949-10	1.668	0.557	0.584	11.1
1949-11	1.625	0.558	0.585	11.1

ION IMPLANTED/PULSE ANNEALED CELL PERFORMANCE (Continued)

	AM0-25°C			AM1-28°C
Cell Number	I_{sc}(A)	V_{oc}(V)	P_{max}(W)	%
1949-12	1.643	0.558	0.576	10.9
1949-13	1.677	0.568	0.657	12.5
1949-15	1.620	0.559	0.588	11.2
1949-17	1.640	0.568	0.639	12.1
1949-18	1.650	0.573	0.684	13.0
1949-19	1.607	0.559	0.574	10.9
1949-22	1.654	0.559	0.602	11.4
1949-23	1.620	0.569	0.634	12.1
1949-14	1.649	0.548	0.540	10.3
1949-16	1.609	0.537	0.524	10.0
1951-1	1.618	0.549	0.647	12.3
1951-2	1.590	0.552	0.625	11.9
1951-3	1.588	0.541	0.624	11.9
1951-4	1.581	0.552	0.611	11.6
1951-5	1.578	0.550	0.642	12.2
1951-6	1.592	0.551	0.642	12.2
1951-7	1.572	0.556	0.648	12.3
1951-8	1.623	0.559	0.661	12.6
1951-9	1.639	0.556	0.660	12.6
1951-10	1.630	0.558	0.654	12.4
1951-11	1.605	0.566	0.612	11.6
1951-12	1.608	0.541	0.624	11.9
1951-13	1.630	0.572	0.662	12.6
1964-1	1.643	0.560	0.616	11.7
1964-2	1.660	0.572	0.644	12.2
1964-3	1.662	0.573	0.676	12.8
1964-4	1.636	0.551	0.571	10.9
1964-5	1.656	0.569	0.624	11.9
1964-6	1.652	0.561	0.593	11.3

ION IMPLANTED/PULSE ANNEALED CELL PERFORMANCE (Continued)

	AM0-25°C			AM1-28°C
Cell Number	I_{sc}(A)	V_{oc}(V)	P_{max}(W)	%
1964-7	1.660	0.565	0.624	11.9
1964-8	1.632	0.571	0.603	11.5
1964-9	1.665	0.569	0.657	12.5
1964-10	1.653	0.568	0.644	12.2
1964-11	1.652	0.563	0.630	12.0
1964-12	1.637	0.558	0.588	11.2
1964-13	1.631	0.556	0.533	10.1
1964-14	1.666	0.572	0.634	12.1
1965-1	1.680	0.577	0.571	10.9
1965-2	1.636	0.567	0.653	12.4
1965-3	1.623	0.567	0.662	12.5
1965-4	1.620	0.562	0.639	12.1
1965-5	1.630	0.572	0.700	13.3
1965-6	1.669	0.568	0.633	12.0
1965-7	1.659	0.571	0.653	12.4
1965-8	1.660	0.574	0.676	12.8
1965-9	1.656	0.567	0.648	12.3
1965-10	1.679	0.570	0.671	12.7
1965-11	1.633	0.517	0.539	10.2
1965-12	1.642	0.572	0.588	11.1
1965-13	1.654	0.560	0.639	12.1
1965-14	1.662	0.576	0.653	12.4
1965-15	1.639	0.560	0.653	12.4
1965-16	1.652	0.572	0.680	12.9
1965-17	1.649	0.571	0.705	13.4
1966-1	1.635	0.568	0.653	12.4
1966-2	1.668	0.562	0.619	11.7
1966-3	1.688	0.580	0.705	13.4
1966-4	1.681	0.572	0.720	13.6

ION IMPLANTED/PULSE ANNEALED CELL PERFORMANCE (Continued)

	AM0-25°C			AM1-28°C
Cell Number	I_{sc}(A)	V_{oc}(V)	P_{max}(W)	%
1966-5	1.653	0.557	0.604	11.4
1966-6	1.650	0.562	0.662	12.5
1966-7	1.658	0.580	0.695	13.2
1966-8	1.658	0.577	0.676	12.8
1966-9	1.658	0.575	0.648	12.3
1966-10	1.644	0.569	0.639	12.1
1966-11	1.658	0.578	0.676	12.8
1966-12	1.654	0.574	0.662	12.5
1966-13	1.644	0.572	0.648	12.3
1966-14	1.648	0.576	0.676	12.8
1966-15	1.652	0.572	0.639	12.1
1966-17	1.643	0.575	0.672	12.7
1966-18	1.656	0.577	0.667	12.6
1966-19	1.651	0.574	0.648	12.3
1967-1	1.659	0.570	0.619	11.8
1967-2	1.658	0.564	0.624	11.9
1967-3	1.682	0.574	0.680	12.9
1967-5	1.661	0.568	0.619	11.8
1967-6	1.669	0.571	0.537	10.2
1967-7	1.678	0.573	0.662	12.6
1967-8	1.658	0.574	0.642	12.2
1967-9	1.669	0.571	0.636	12.1
1967-10	1.652	0.566	0.616	11.7
1967-11	1.645	0.554	0.596	11.3
1967-12	1.648	0.573	0.596	11.3
1967-13	1.642	0.565	0.630	12.0
1967-14	1.634	0.565	0.633	12.0
1967-15	1.622	0.563	0.639	12.1
1967-16	1.654	0.574	0.648	12.3

ION IMPLANTED/PULSE ANNEALED CELL PERFORMANCE (Continued)

	AM0-25°C			AM1-28°C
Cell Number	I_{sc}(A)	V_{oc}(V)	P_{max}(W)	%
1967-18	1.644	0.570	0.616	11.7
1968-1	1.652	0.577	0.690	13.1
1968-2	1.643	0.571	0.653	12.4
1968-3	1.632	0.565	0.627	11.9
1968-4	1.646	0.572	0.690	13.1
1968-5	1.633	0.570	0.653	12.4
1968-6	1.652	0.577	0.695	13.2
1968-7	1.649	0.569	0.657	12.5
1968-8	1.658	0.570	0.671	12.7
1968-9	1.615	0.568	0.598	11.4
1968-10	1.623	0.575	0.657	12.5
1968-11	1.624	0.572	0.663	12.6
1968-12	1.621	0.570	0.648	12.3
1968-13	1.609	0.576	0.671	12.7
1968-14	1.658	0.569	0.639	12.1
1968-15	1.613	0.576	0.676	12.8
1968-16	1.605	0.574	0.667	12.7
1968-17	1.591	0.568	0.625	11.9
1968-18	1.633	0.577	0.695	13.2
1970-1	1.637	0.573	0.662	12.6
1970-2	1.639	0.577	0.676	12.8
1970-3	1.621	0.574	0.648	12.3
1970-4	1.623	0.573	0.610	11.6
1970-5	1.620	0.571	0.630	12.0
1970-6	1.615	0.578	0.681	12.9
1970-7	1.572	0.538	0.524	10.0
1970-8	1.620	0.578	0.667	12.7
1970-9	1.594	0.552	0.565	10.7
1970-10	1.622	0.568	0.621	11.8

ION IMPLANTED/PULSE ANNEALED CELL PERFORMANCE (Continued)

	AM0-25°C			AM1-28°C
Cell Number	I_{sc}(A)	V_{oc}(V)	P_{max}(W)	%
1970-11	1.624	0.573	0.639	12.1
1970-12	1.632	0.568	0.642	12.2
1970-13	1.627	0.578	0.681	12.9
1970-14	1.637	0.577	0.676	12.8
1970-15	1.607	0.561	0.571	10.9
1970-16	1.633	0.566	0.630	12.0
1970-17	1.616	0.552	0.565	10.7
1970-18	1.593	0.556	0.662	12.6
1970-19	1.621	0.566	0.624	11.9
1971-2	1.650	0.566	0.648	12.3
1971-3	1.670	0.568	0.666	12.7
1971-4	1.680	0.567	0.695	13.2
1971-7	1.640	0.576	0.596	11.3
1971-8	1.650	0.563	0.671	12.8
1971-9	1.670	0.577	0.695	13.2
1971-10	1.690	0.582	0.733	13.9
1971-11	1.650	0.568	0.676	12.8
1971-12	1.660	0.572	0.648	12.3
1971-15	1.640	0.577	0.524	10.0
1971-16	1.700	0.575	0.710	13.5
2125-1	1.564	0.552	0.596	11.3
2125-3	1.598	0.572	0.639	12.1
2125-4	1.590	0.571	0.653	12.4
2125-8	1.586	0.572	0.662	12.6
2125-9	1.594	0.569	0.642	12.2
2125-10	1.614	0.570	0.662	12.6
2125-11	1.609	0.566	0.612	11.6
2125-12	1.584	0.569	0.625	11.9
2125-13	1.624	0.564	0.657	12.5

ION IMPLANTED/PULSE ANNEALED CELL PERFORMANCE (Continued)

	AM0-25°C			AM1-28°C
Cell Number	I_{sc}(A)	V_{oc}(V)	P_{max}(W)	%
2125-14	1.601	0.562	0.572	10.9
2125-16	1.591	0.561	0.619	11.8
2125-19	1.601	0.573	0.671	12.8
2125-21	1.586	0.624	0.567	10.8
2125-22	1.623	0.566	0.633	12.0
2125-24	1.622	0.568	0.593	11.3
2126-1	1.619	0.568	0.648	12.3
2126-2	1.606	0.569	0.657	12.5
2126-3	1.624	0.544	0.648	12.3
2126-4	1.625	0.569	0.625	11.9
2126-5	1.598	0.574	0.671	12.8
2126-6	1.609	0.568	0.657	12.5
2126-8	1.638	0.562	0.589	11.2
2126-9	1.622	0.570	0.662	12.6
2126-10	1.618	0.572	0.658	12.5
2126-11	1.634	0.571	0.671	12.8
2126-12	1.635	0.575	0.686	13.0
2126-13	1.647	0.571	0.644	12.2
2126-14	1.641	0.569	0.633	12.0
2126-16	1.638	0.573	0.680	12.9
2126-17	1.626	0.571	0.676	12.8
2126-18	1.654	0.567	0.607	11.5
2126-21	1.655	0.571	0.634	12.0
2126-22	1.666	0.571	0.657	12.5
2126-23	1.658	0.576	0.695	13.2
2126-24	1.628	0.573	0.676	12.8
2126-25	1.662	0.572	0.644	12.2
2127-1	1.642	0.570	0.644	12.2
2127-2	1.667	0.577	0.630	12.0

ION IMPLANTED/PULSE ANNEALED CELL PERFORMANCE (Continued)

Cell Number	AM0-25°C			AM1-28°C
	I_{sc}(A)	V_{oc}(V)	P_{max}(W)	%
2127-3	1.652	0.575	0.676	12.8
2127-7	1.654	0.571	0.632	12.6
2127-11	1.619	0.562	0.610	11.6
2127-12	1.662	0.573	0.666	12.7
2127-13	1.658	0.571	0.662	12.6
2127-14	1.624	0.564	0.607	11.5
2127-15	1.654	0.568	0.607	11.5
2127-16	1.672	0.574	0.648	12.3
2127-17	1.668	0.588	0.576	10.9
2127-19	1.664	0.517	0.653	12.4
2127-22	1.660	0.573	0.695	13.2
2127-24	1.663	0.571	0.648	12.3
2127-25	1.662	0.573	0.644	12.2
2128-1	1.661	0.567	0.657	12.5
2128-2	1.687	0.569	0.695	13.2
2128-3	1.633	0.572	0.686	13.0
2128-5	1.671	0.571	0.690	13.1
2128-6	1.631	0.572	0.695	13.2
2128-7	1.628	0.562	0.580	11.0
2128-8	1.676	0.573	0.690	13.1
2128-9	1.607	0.571	0.657	12.5
2128-11	1.615	0.572	0.644	12.2
2128-12	1.629	0.575	0.691	13.1
2128-14	1.668	0.568	0.671	12.8
2128-15	1.662	0.569	0.690	13.1
2128-18	1.666	0.570	0.671	12.8
2128-19	1.691	0.575	0.699	13.3
2128-20	1.667	0.570	0.680	12.9
2128-21	1.603	0.572	0.667	12.7

ION IMPLANTED/PULSE ANNEALED CELL PERFORMANCE (Continued)

	AM0-25°C			AM1-28°C
Cell Number	I_{sc}(A)	V_{oc}(V)	P_{max}(W)	%
2128-22	1.606	0.564	0.585	11.1
2128-24	1.662	0.575	0.695	13.2
2128-25	1.637	0.570	0.666	12.7
2138-1	1.705	0.578	0.714	13.6
2138-2	1.706	0.576	0.733	13.9
2138-4	1.688	0.572	0.690	13.1
2138-6	1.678	0.573	0.671	12.7
2138-7	1.688	0.578	0.699	13.0
2138-8	1.692	0.575	0.708	13.4
2138-9	1.699	0.574	0.714	13.6
2138-10	1.671	0.568	0.675	12.8
2138-11	1.681	0.573	0.671	12.8
2138-12	1.691	0.574	0.662	12.6
2138-13	1.684	0.580	0.739	14.0
2138-14	1.683	0.574	0.676	12.8
2138-15	1.664	0.571	0.680	12.9
2138-16	1.682	0.577	0.699	13.2
2138-17	1.695	0.576	0.699	13.3
2138-18	1.683	0.572	0.699	13.3
2138-19	1.698	0.578	0.705	13.4
2138-20	1.667	0.573	0.558	10.6
2138-21	1.673	0.574	0.705	13.4
2138-22	1.686	0.573	0.648	12.3
2138-23	1.679	0.574	0.686	13.0
2138-24	1.688	0.577	0.714	13.6
2139-2	1.574	0.551	0.546	10.4
2139-4	1.620	0.563	0.624	11.9
2139-6	1.628	0.565	0.639	12.1
2139-7	1.588	0.553	0.571	10.9

ION IMPLANTED/PULSE ANNEALED CELL PERFORMANCE (Continued)

	AM0-25°C			AM1-28°C
Cell Number	I_{sc}(A)	V_{oc}(V)	P_{max}(W)	%
2139-8	1.625	0.549	0.571	10.9
2139-11	1.620	0.562	0.607	11.5
2139-12	1.610	0.539	0.552	10.5
2139-13	1.570	0.547	0.537	10.2
2139-14	1.589	0.556	0.567	10.8
1952-1	1.612	0.548	0.619	11.8
1952-2	1.630	0.561	0.634	12.0
1952-3	1.612	0.560	0.642	12.2
1952-4	1.622	0.553	0.556	10.6
1952-5	1.626	0.559	0.642	12.2
1952-6	1.633	0.559	0.661	12.6
1952-7	1.625	0.555	0.641	12.2
1952-8	1.639	0.558	0.642	12.2
1952-9	1.644	0.556	0.661	12.6
1952-10	1.641	0.566	0.668	12.7
1953-2	1.700	0.578	0.733	13.9
1953-3	1.660	0.573	0.567	10.8
1953-4	1.670	0.571	0.629	11.9
1953-7	1.633	0.569	0.648	12.3
1954-1	1.633	0.557	0.593	11.2
1954-2	1.642	0.569	0.630	12.0
1954-3	1.653	0.562	0.636	12.1
1954-4	1.638	0.560	0.602	11.4
1954-5	1.642	0.572	0.662	12.6
1954-6	1.606	0.547	0.554	10.5
1954-7	1.610	0.559	0.624	11.9
1955-1	1.670	0.570	0.662	12.6
1955-2	1.680	0.577	0.705	13.4
1955-3	1.664	0.566	0.638	12.1

ION IMPLANTED/PULSE ANNEALED CELL PERFORMANCE (Continued)

	AM0-25°C			AM1-28°C
Cell Number	I_{sc}(A)	V_{oc}(V)	P_{max}(W)	%
1955-4	1.662	0.572	0.666	12.7
1955-5	1.676	0.569	0.644	12.2
1955-6	1.642	0.563	0.602	11.4
1955-7	1.669	0.573	0.657	12.5
1955-8	1.658	0.566	0.614	11.6
1955-9	1.665	0.564	0.633	12.0
1955-10	1.655	0.573	0.676	12.8
1955-11	1.688	0.577	0.686	13.0
1956-1	1.599	0.559	0.630	12.0
1956-2	1.672	0.573	0.667	12.7
1956-3	1.625	0.571	0.667	12.7
1956-4	1.613	0.566	0.620	11.8
1956-5	1.610	0.567	0.644	12.2
1956-7	1.617	0.570	0.616	11.7
1956-8	1.604	0.561	0.621	11.8
1956-9	1.620	0.564	0.625	11.9
1956-10	1.596	0.569	0.625	11.9
1956-11	1.589	0.550	0.592	11.2
1956-12	1.590	0.566	0.620	11.8
1956-13	1.605	0.553	0.541	10.3
1956-15	1.593	0.560	0.607	11.5
1956-16	1.608	0.559	0.612	11.6
1956-17	1.580	0.561	0.612	11.6
1956-18	1.610	0.559	0.616	11.7
1957-1	1.598	0.540	0.576	10.9
1957-2	1.690	0.575	0.690	13.1
1957-3	1.685	0.569	0.666	12.7
1957-4	1.695	0.573	0.648	12.3
1957-6	1.683	0.574	0.675	12.8

ION IMPLANTED/PULSE ANNEALED CELL PERFORMANCE (Continued)

	AM0-25°C			AM1-28°C
Cell Number	I_{sc}(A)	V_{oc}(V)	P_{max}(W)	%
1957-7	1.677	0.567	0.625	11.9
1957-8	1.664	0.556	0.588	11.2
1957-9	1.613	0.537	0.524	10.0
1957-10	1.682	0.570	0.671	12.8
1957-11	1.691	0.578	0.695	13.2
1957-12	1.661	0.548	0.578	11.0
1957-13	1.600	0.535	0.552	10.5
1958-1	1.548	0.526	0.538	10.2
1958-3	1.643	0.563	0.648	12.3
1958-4	1.639	0.570	0.657	12.5
1958-5	1.562	0.537	0.582	11.1
1958-6	1.621	0.565	0.615	11.7
1958-8	1.600	0.554	0.593	11.2
1958-9	1.566	0.529	0.552	10.5
1959-1	1.639	0.557	0.634	12.0
1959-2	1.590	0.530	0.546	10.4
1959-3	1.584	0.542	0.658	12.5
1959-4	1.578	0.525	0.532	10.1
1959-5	1.562	0.514	0.562	10.7
1959-6	1.611	0.553	0.586	11.1
1959-7	1.598	0.547	0.675	12.8
1959-9	1.577	0.541	0.544	10.3
1959-10	1.571	0.540	0.598	11.3
1959-11	1.603	0.542	0.582	11.1
1959-13	1.560	0.531	0.533	10.1
1960-1	1.665	0.572	0.662	12.7
1960-2	1.661	0.574	0.680	12.9
1960-3	1.662	0.574	0.604	11.5
1960-4	1.666	0.570	0.644	12.2

ION IMPLANTED/PULSE ANNEALED CELL PERFORMANCE (Continued)

	AM0-25°C			AM1-28°C
Cell Number	I_{sc}(A)	V_{oc}(V)	P_{max}(W)	%
1960-5	1.693	0.573	0.690	13.1
1960-6	1.667	0.563	0.552	10.5
1960-7	1.671	0.574	0.653	12.4
1960-8	1.681	0.563	0.588	11.2
1960-9	1.654	0.566	0.642	12.2
1960-11	1.673	0.565	0.680	12.9
1960-12	1.633	0.566	0.630	12.0
1960-13	1.670	0.571	0.653	12.4
1960-14	1.668	0.572	0.653	12.4
1960-15	1.618	0.548	0.623	11.8
1960-16	1.666	0.570	0.648	12.3
1961-1	1.630	0.567	0.533	10.1
1961-4	1.660	0.562	0.695	13.2
1961-5	1.680	0.566	0.720	13.7
1961-6	1.670	0.568	0.710	13.5
1961-7	1.660	0.561	0.588	11.2
1961-8	1.660	0.588	0.705	13.4
1961-9	1.650	0.561	0.699	13.3
1961-10	1.640	0.559	0.695	13.2
1961-11	1.640	0.558	0.671	12.7
1961-13	1.650	0.568	0.667	12.7
1961-15	1.640	0.564	0.676	12.8
1961-18	1.670	0.569	0.710	13.5
1963-1	1.666	0.565	0.675	12.8
1963-2	1.659	0.560	0.671	12.7
1963-3	1.655	0.550	0.675	12.8
1963-4	1.644	0.562	0.624	11.8
1963-5	1.616	0.561	0.633	12.0
1963-6	1.618	0.562	0.653	12.4

ION IMPLANTED/PULSE ANNEALED CELL PERFORMANCE (Continued)

	AM0-25°C			AM1-28°C
Cell Number	I_{sc}(A)	V_{oc}(V)	P_{max}(W)	%
1963-7	1.622	0.564	0.639	12.1
1963-8	1.672	0.564	0.680	12.9
1963-9	1.634	0.564	0.662	12.6
1963-10	1.662	0.566	0.680	12.9
1963-12	1.606	0.552	0.593	11.2
1950-1	1.604	0.549	0.625	11.9
1950-2	1.610	0.551	0.647	12.3
1950-3	1.640	0.550	0.651	12.4
1950-4	1.559	0.522	0.567	10.8
1950-5	1.638	0.543	0.619	11.8
1950-6	1.598	0.545	0.587	11.1
1950-7	1.608	0.546	0.672	12.8
1950-9	1.621	0.551	0.634	12.0
1950-10	1.619	0.548	0.629	11.9
1950-11	1.657	0.544	0.646	12.3
1950-12	1.650	0.549	0.645	12.2
1948-1	1.545	0.560	0.579	11.0
1948-4	1.600	0.549	0.532	10.1
1948-5	1.603	0.555	0.560	10.6
1948-6	1.568	0.568	0.639	12.1
1948-9	1.555	0.555	0.559	10.6
1948-13	1.600	0.562	0.544	10.3
1948-15	1.578	0.566	0.594	11.3
1948-18	1.567	0.571	0.644	12.2
2140-1	1.580	0.548	0.612	11.6
2140-2	1.610	0.564	0.653	12.4
2140-3	1.600	0.553	0.607	11.5
2140-4	1.623	0.575	0.680	12.9
2140-5	1.620	0.567	0.653	12.4

ION IMPLANTED/PULSE ANNEALED CELL PERFORMANCE (Concluded)

	AM0-25°C			AM1-28°C
Cell Number	I_{sc}(A)	V_{oc}(V)	P_{max}(W)	%
2140-6	1.647	0.575	0.695	13.2
2140-7	1.650	0.574	0.700	13.3
2140-8	1.640	0.573	0.633	12.0
2140-9	1.670	0.566	0.639	12.1
2140-10	1.610	0.567	0.667	12.7
2140-11	1.572	0.563	0.625	11.9
2140-12	1.637	0.569	0.648	12.3
2140-13	1.610	0.563	0.630	12.0
2140-14	1.630	0.575	0.705	13.4
2140-15	1.625	0.569	0.667	12.7
2140-16	1.619	0.568	0.648	12.3
2140-17	1.600	0.564	0.634	12.1

APPENDIX E

SAMPLE OF SAMIS III
SIMULATION FOR FURNACE ANNEAL AND PLASMA ETCH

```
>DONE

PLEASE ENTER A SAMIS COMMAND
>
 FIND INDUSTRY FURNACE
FURNACE HAS BEEN LOCATED IN CORE
ENTER A MANIPULATION COMMAND FOR INDUSTRY 'FURNACE'
>LIST ALL
REFERENT IS 'FURNACE'
DESCRIPTIVE.NAME IS
'FURNACE ANNEAL OF IMPLANTED LAYERS'
OBJECTIVE IS
'NEW PHOTOVOLTAIC POWER CAPABILITY'
PRODUCTION.UNITS ARE
'WATTS PEAK'
FINAL.PRODUCTION.REFERENCE IS 'CELLS'
FINAL.PRODUCT.UNITS ARE
'CELLS'
HARDWARE.PERFORMANCE =     1.10200
MAKERS.LIST:
'FURNACE'             MARKET.SHARE =      100.00

ENTER A MANIPULATION COMMAND FOR INDUSTRY 'FURNACE'
>DONE

PLEASE ENTER A SAMIS COMMAND
>FIND COMPANY FURNACE
'FURNACE' HAS BEEN LOCATED IN CORE
ENTER A MANIPULATION COMMAND FOR COMPANY 'FURNACE'
>LIST ALL
TO OBTAIN A LIST OF ACCEPTABLE ABBREVIATIONS, TYPE 'DISPLAY ABBREVIATIONS'.
REFERENT IS 'FURNACE'
DESCRIPTIVE.NAME IS
'COST OF FURNACE ANNEALING IMPLANTED WAFERS AND ETCHING SURFACE'
THE FOLLOWING PRODUCTS ARE MANUFACTURED BY THIS COMPANY:
 CELLS *
PERCENT.OF.CAPACITY =    100.0000
LEVERAGE =      1.2000
DEBT.INTEREST.RATE =      9.2500
OTHER.TAX.RATE =       2.0000
INSURANCE.RATE =       4.0000
FACILITY.LIFE =     40.0000
RATE.OF.RETURN.ON.EQUITY =      20.0000
MISC.EXPENSE.PERCENTAGE.OF.REVENUE =        3.0000
MISC.EXPENSE.PERCENTAGE.OF.OPERATING.EXPENSE =        4.0000
MISC.EXPENSE.PERCENTAGE.OF.BOOK.VALUE =       0.
FACILITIES.TAX.DEPRECIATION.METHOD = DDB
FACILITIES.BOOK.DEPRECIATION.METHOD = SL
FACILITIES.INFLATION.RATE.TABLE =
  1977.0000      8.0000  *
RAW.MATERIALS.INVENTORY.TIME =        .0400
PROCESSING.TIME.MULTIPLIER =       1.0000
FINISHED.GOODS.INVENTORY.TIME =        .0400
ACCOUNTS.RECEIVABLE.TURNOVER.TIME =        .0100
THIS COMPANY IS COMPRISED OF THE FOLLOWING PROCESSES:
 ETCH FURNACE-2 *
THE PURCHASED PRODUCTS OF THIS COMPANY FOLLOW. TO OBTAIN A LISTING OF THE S
PLIERS LIST OF A PARTICULAR PURCHASED PRODUCT, TYPE 'YES', ELSE, TYPE 'NO'.
PURCHASED PRODUCTS:
ENTER A MANIPULATION COMMAND FOR COMPANY 'FURNACE'
>DONE

PLEASE ENTER A SAMIS COMMAND
>FIND PROCESS ETCH
'ETCH' HAS BEEN LOCATED IN THE PROCESS FILE AND LOADED INTO CORE.
```

```
ENTER A MANIPULATION COMMAND FOR PROCESS 'ETCH'
>LIST ALL
TO OBTAIN A LIST OF ACCEPTABLE ABBREVIATIONS, TYPE 'DISPLAY ABBREVIATIONS'
REFERENT IS 'ETCH'
DESCRIPTIVE NAME IS
'PLASMA ETCH WAFERS AFTER FURNACE STEP'
PRODUCT REFERENT IS 'CELLS'
PRODUCT NAME IS
'CELLS WITH JUNCTION,ANNEAL, AND ETCH'
PRODUCT UNITS ARE
'CELLS'
OUTPUT RATE =     85.0000
PROCESSING TIME =      10.0000
USAGE FRACTION =         .9110
THE MACHINE DESCRIPTIONS OF THIS PROCESS FOLLOW.  TO DISPLAY THE VALUES OF
ATTRIBUTES OF A COMPONENT, TYPE 'YES'.  OTHERWISE, TYPE 'NO'
COMPONENTS:
'MACHINE' -- ATTRIBUTES?
>YES
DESCRIPTIVE.NAME IS
'PLASMA ETCH'
PRICE.YEAR = 1977
PURCHASE.COST =  110000.00
USEFUL.LIFE =       7.0000
SALVAGE.VALUE =          0.
REMOVAL.AND.INSTALLATION.COST =     2750.00
PAYMENT.FLOAT.INTERVAL =       0.
INFLATION.RATE.TABLE =
  1975.0000      6.0000  *
EQUIPMENT.TAX.DEPRECIATION.METHOD = DDB
EQUIPMENT.BOOK.DEPRECIATION.METHOD = SL


TO DISPLAY THE BYPRODUCT.OUTPUTS, TYPE "YES'.  OTHERWISE TYPE "NO".
>NO

TO DISPLAY THE FACILITIES.AND.PERSONNEL.REQUIREMENTS, TYPE 'YES'.  OTHERWI
TYPE 'NO'.
>YES
FACILITIES AND PERSONNEL REQUIREMENTS:
'A2064D' , AMOUNT PER MACHINE =   150.0000
'B3672D' , AMOUNT PER MACHINE =     1.0000
'B3736D' , AMOUNT PER MACHINE =      .0500

TO DISPLAY THE UTILITIES.AND.COMMODITIES.REQUIREMENTS, TYPE 'YES'.  OTHERW
TYPE 'NO'.
>YES
UTILITIES AND COMMODITIES REQUIREMENTS:
'EG1024D' , AMOUNT PER CYCLE =       .0000
'E1112D' , AMOUNT PER CYCLE =       .0100
'C1032B' , AMOUNT PER CYCLE =       .1060
'C2128B' , AMOUNT PER CYCLE =       .0087

TO DISPLAY THE REQUIRED.PRODUCTS, TYPE "YES'.  OTHERWISE, TYPE 'NO".
>YES
REQUIRED PRODUCTS:
'ANNEALWAF' , YIELD =       .9940_

ENTER A MANIPULATION COMMAND FOR PROCESS 'ETCH'
>DONE

PLEASE ENTER A SAMIS COMMAND
>FIND PROCESS FURNACE-2
'FURNACE-2' HAS BEEN LOCATED IN CORE
ENTER A MANIPULATION COMMAND FOR PROCESS 'FURNACE-2'
>LIST ALL
```

ORIGINAL PAGE IS
OF POOR QUALITY

```
DESCRIPTIVE NAME IS
'FURNACE ANNEAL - 2'
PRODUCT REFERENT IS 'ANNEALWAF'
PRODUCT NAME IS
'ANNEALED WAFER - 2 EFFICIENCY 14.7'
PRODUCT UNITS ARE
'WAFERS'
OUTPUT RATE =   400.0000
PROCESSING TIME =     75.0000
USAGE FRACTION =        .9230
THE MACHINE DESCRIPTIONS OF THIS PROCESS FOLLOW.  TO DISPLAY THE VALUES OF T
ATTRIBUTES OF A COMPONENT, TYPE 'YES'.  OTHERWISE, TYPE 'NO'
COMPONENTS:
'FURNACE-1' -- ATTRIBUTES?
>YES
DESCRIPTIVE.NAME IS
'500 CM2/SEC BELT FURNACE, 75 MIN 550/850/550 CYCLE'
PRICE.YEAR = 1979
PURCHASE.COST =    80000.00
USEFUL.LIFE =    15.0000
SALVAGE.VALUE =    10000.00
REMOVAL.AND.INSTALLATION.COST =     2000.00
PAYMENT.FLOAT.INTERVAL =      0.
INFLATION.RATE.TABLE =
  1975.0000     4.0000  *
EQUIPMENT.TAX.DEPRECIATION.METHOD = DDB
EQUIPMENT.BOOK.DEPRECIATION.METHOD = SL


TO DISPLAY THE BYPRODUCT.OUTPUTS, TYPE 'YES'.  OTHERWISE TYPE 'NO'.
>NO

TO DISPLAY THE FACILITIES.AND.PERSONNEL.REQUIREMENTS, TYPE 'YES'.  OTHERWIS
TYPE 'NO'.
>YES
FACILITIES AND PERSONNEL REQUIREMENTS:
'A2064D' , AMOUNT PER MACHINE =  1000.0000
'B3096D' , AMOUNT PER MACHINE =     1.0000
'B3704D' , AMOUNT PER MACHINE =      .1000
'B3736D' , AMOUNT PER MACHINE =      .0500

TO DISPLAY THE UTILITIES.AND.COMMODITIES.REQUIREMENTS, TYPE 'YES'.  OTHERWI
TYPE 'NO'.
>YES
UTILITIES AND COMMODITIES REQUIREMENTS:
'E1416D' , AMOUNT PER CYCLE =       .0900
'E1608D' , AMOUNT PER CYCLE =       .0020
'C1032B' , AMOUNT PER CYCLE =       .5500
'C1016B' , AMOUNT PER CYCLE =       .0000

TO DISPLAY THE REQUIRED.PRODUCTS, TYPE 'YES'.  OTHERWISE, TYPE 'NO'.
>YES
REQUIRED PRODUCTS:

ENTER A MANIPULATION COMMAND FOR PROCESS 'FURNACE-2'
>DONE

PLEASE ENTER A SAMIS COMMAND
>FIND RUN.CONTROL DEFAULT
DEFAULT HAS BEEN LOCATED IN CORE
ENTER A MANIPULATION COMMAND FOR RUN CONTROL 'DEFAULT'
>LIST ALL
TO OBTAIN A LIST OF ACCEPTABLE ABBREVIATIONS, TYPE 'DISPLAY ABBREVIATIONS'.
REFERENT IS 'DEFAULT'
DESCRIPTIVE.NAME IS
'RUN CONTROL FOR EIGHTH PIN 3 4/MPK STRAWMAN INDUSTRY 2/24/78'
```

```
INDUSTRY.SIZE.RANGE:
 100000000.00 *
QUANTITY.RECALCULATION.FLAG IS ON
INTEGRAL.MACHINES.FLAG IS ON
STEADY.STATE.FLAG IS OFF
LINE.LENGTH =  132
PROMPT.LEVEL.CODE =     3
MAX.NUMBER.OF.SCALE.ITERATIONS =  200
MAX.NUMBER.OF.PRICE.ITERATIONS =   20
EPSILON =     .00100000
REPORT.CHOICES:
           1             1             1             1             1             1
           1             1             1             1             1             1
           1             1             1 *
REPORT.OUTPUT.FILE =    6 (TERMINAL)
MAX.NUMBER.OF.PARTITION.RECURSIONS =    10
ENTER A MANIPULATION COMMAND FOR RUN CONTROL 'DEFAULT'
>DONE

PLEASE ENTER A SAMIS COMMAND
>SIMULATE
$$$$$$$$$$$$$$$$$$$




SAMIS III - RELEASE 1        INDUSTRY CONFIGURATION

INDUSTRY: FURNACE, FURNACE ANNEAL OF IMPLANTED LAYERS

NEW PHOTOVOLTAIC POWER CAPABILITY, EXPRESSED IN WATTS PEAK/YEAR
                         IS PROVIDED BY
CELLS, CELLS WITH JUNCTION,ANNEAL, AND ETCH, EXPRESSED IN CELLS/YEAR
                              OF WHICH
100.00% IS MADE BY FURNACE, COST OF FURNACE ANNEALING IMPLANTED WAFERS AND
ING SURFACE

COMPANY: FURNACE                PRODUCTS: CELLS
REQUIRED PRODUCT: (NONE)

ECONOMY OF SCALE CONVERGENCE OBTAINED IN  21 ITERATIONS FOR FIRM FURNACE




SAMIS III - RELEASE 1        INDUSTRY SIZE INDEX =  1

INDUSTRY: FURNACE, FURNACE ANNEAL OF IMPLANTED LAYERS

INDUSTRY OBJECTIVE: NEW PHOTOVOLTAIC POWER CAPABILITY
FINAL PRODUCT: CELLS, CELLS WITH JUNCTION,ANNEAL, AND ETCH
PRODUCING     1.10 WATTS PEAK PER CELLS

QUANTITY:  100000000. =  1.0E+08 WATTS PEAK/YEAR =>  9.074E+07 CELLS/YEAR

PRICE:     .0069 $(1975)/WATTS PEAK =>       .008 $(1975)/CELLS

   COMPANY: FURNACE, COST OF FURNACE ANNEALING IMPLANTED WAFERS AND ETCHING
FACE
   PRODUCTS: CELLS
   QUANTITY: 9.073E+07
   [illegible]
```

```
             $(1975)/
             CELLS
   ENERGY PAYBACK TIME =    .002 YEARS
   COMPANY MARKUP =    4.096 TIMES (DIRECT EXPENSES PLUS EXTERNAL PRODUCT C(
   COMPANY PROFIT =    5.1% OF PRICE

         ***************************************************************************
*******************************************************
         ***************************************************************************
*******************************************************
         ***************************************************************************
*******************************************************
```

ORIGINAL PAGE IS
OF POOR QUALITY

```
      PROCESS: ETCH      , PLASMA ETCH WAFERS AFTER FURNACE STEP
      PRODUCT: CELLS     , CELLS WITH JUNCTION,ANNEAL, AND ETCH
      PRODUCES:   85.0000 CELLS/MINUTE, TAKING    10.000 MINUTES/CYCLE
      OPERATES  .91 OF THE TIME THE FACTORY IS OPERATING
         COMPONENT: MACHINE, PLASMA ETCH
            COST:  110000. $(1977)    INSTALLATION:    2750. $(1977)
            SALVAGE VALUE:        0. $(1977) AFTER  7.0 YEARS

         QUANTITY 9.074E+07 CELLS/YEAR AT      .0076 $(1975)/CELLS
         NUMBER OF ETCH MACHINES =  3.000, OF WHICH  .641 ARE IDLE

         ALL EXPENSES ARE IN $(1986)
         DIRECT EXPENSES                          261139.
            DIRECT LABOR EXPENSES                           254669.
            DIRECT MATERIALS AND SUPPLIES                      361.
            BYPRODUCT EXPENSES                                   0.
            DIRECT UTILITIES EXPENSES                         6109.

         INDIRECT EXPENSES                        183298.
            INDIRECT LABOR EXPENSES                         155208.
            INDIRECT MATERIALS AND SUPPLIES                  21371.
            INDIRECT UTILITIES EXPENSES                       6719.

         BYPRODUCT INCOME                    (          0.)

         CAPITAL EXPENSES                         350773.
            EQUIPMENT REPLACEMENT                            81638.
            FACILITIES REPLACEMENT                            7475.
            AMORTIZED ONE-TIME COSTS                        166602.
            INTEREST ON DEBT                                  4761.
            RETURN ON EQUITY                                 51470.
            NON-INCOME TAXES                                  2960.
            INSURANCE PREMIUMS                               35867.

         INCOME TAXES                             206374.

         MISCELLANEOUS                             49353.

         EXTERNAL PRODUCT COST                         0.
         INTERNAL (IMPLICIT) PRODUCT COST         252933.

         VALUE ADDED:    .012 $(1986)/CELLS =    .011 $(1986)/WATTS PEAK
         PROFIT =  3.9% OF PRICE
         MARKUP = 2.536 TIMES (DIRECT EXPENSES PLUS INTERNAL AND EXTERNAL P
CT COSTS)
         THE ENERGY PAYBACK TIME FOR THIS PROCESS IS    .001 YEARS
```

```
          TO PRODUCE 7.074E+07 CELLS/YEAR, THE ETCH
          PROCESS REQUIRES:

              ALL DOLLARS ARE IN $(1986)

              DIRECT REQUIREMENTS

                  ACCOUNT A - FACILITIES
                      4.500E+02 SQ. FT. OF A2064D, MANUFACTURING SPACE (TYPE A
                            @     93.06 $(1986)/SQ. FT. . . . . . . . . . . . . . .
 . . . . . . . . . . . . . . IMPLIES     41876.  $(1986)

                  ACCOUNT B - PERSONNEL
                      1.109E+01 PRSN*YRS OF B3672D, CHEMICAL OPERATOR II
                            @  21697.17 $(1986)/PRSN*YRS. . . . . . . . . . . . .
 . . . . . . . . . . . . . . IMPLIES    240547.  $(1986)
                      5.543E-01 PRSN*YRS OF B3736D, MAINTENANCE MECHANIC II
                            @  25475.28 $(1986)/PRSN*YRS. . . . . . . . . . . . .
 . . . . . . . . . . . . . . IMPLIES     14122.  $(1986)

                  ACCOUNT C - UTILITIES
                      1.132E+05 KW HR. OF C1032B, ELECTRICITY
                            @       .05 $(1986)/KW HR.. . . . . . . . . . . . . .
 . . . . . . . . . . . . . . IMPLIES      6109.  $(1986)
                      9.288E+03 CU. FT. OF C2128B, VENTILATED ROOM SPACE
                            @       0.  $(1986)/CU. FT. . . . . . . . . . . . . .
 . . . . . . . . . . . . . . IMPLIES          .  $(1986)

                  ACCOUNT D - BYPRODUCTS
                  (NONE)

                  ACCOUNT E - COMMODITIES
                      1.068E+04 CU. FT. OF E1112D, ARGON GAS
                            @       .03 $(1986)/CU. FT. . . . . . . . . . . . . .
 . . . . . . . . . . . . . . IMPLIES       325.  $(1986)
                      2.135E+01 EACH OF E61024D, BLADE DRESSING, 1/2 X 1/2 X 6
 INA STICKS
                            @      1.72 $(1986)/EACH. . . . . . . . . . . . . . .
 . . . . . . . . . . . . . . IMPLIES        37.  $(1986)

                  ACCOUNT F - RESOURCES
                  (NONE)

              INDIRECT REQUIREMENTS

                  ACCOUNT A - FACILITIES
                      4.550E+02 SQ. FT. OF A2256I, TOILET AND LOCKER ROOM
                            @    138.48 $(1986)/SQ. FT. . . . . . . . . . . . . .
 . . . . . . . . . . . . . . IMPLIES     63004.  $(1986)
                      6.461E+02 SQ. FT. OF A2128I, OFFICE SPACE-ADMINISTRATION
                            @     67.77 $(1986)/SQ. FT. . . . . . . . . . . . . .
 . . . . . . . . . . . . . . IMPLIES     43781.  $(1986)
                      9.529E+02 SQ. FT. OF A2224I, SOLVENT AND CHEMICAL STORAGE
                            @     30.46 $(1986)/SQ. FT. . . . . . . . . . . . . .
 . . . . . . . . . . . . . . IMPLIES     29027.  $(1986)
                      5.708E+02 FT. OF A2040I, EXTERIOR WALLS
                            @     47.98 $(1986)/FT. . . . . . . . . . . . . . . .
 . . . . . . . . . . . . . . IMPLIES     27383.  $(1986)
                      9.899E+01 KW OF A1112I, ELECTRICAL SERVICE FACILITIES
                            @    166.40 $(1986)/KW. . . . . . . . . . . . . . . .
 . . . . . . . . . . . . . . IMPLIES     16471.  $(1986)
                      8.118E+01 SQ. FT. OF A2016I, CAFETERIA AND LUNCHROOM
                            @    129.94 $(1986)/SQ. FT. . . . . . . . . . . . . .
 . . . . . . . . . . . . . . IMPLIES     10548.  $(1986)
                      2.624E+02 SQ. FT. OF A2112I, MECHANICAL EQUIPMENT ROOM
                            @     36.78 $(1986)/SQ. FT. . . . . . . . . . . . . .
```

```
          ACCOUNT E - COMMODITIES
             1.068E+04 CU. FT. OF E1112D, ARGON GAS
                  @        .03 $(1986)/CU. FT. . . . . . . . . . . . . . .
. . . . . . . . . . . . . . . IMPLIES       325.  $(1986)
             2.135E+01 EACH OF E610240, BLADE DRESSING, 1/2 X 1/2 X 6 I
INH STICKS
                  @       1.72 $(1986)/EACH. . . . . . . . . . . . . . . .
. . . . . . . . . . . . . . . IMPLIES        37.  $(1986)

          ACCOUNT F - RESOURCES
          (NONE)

       INDIRECT REQUIREMENTS

          ACCOUNT A - FACILITIES
             4.550E+02 SQ. FT. OF A2256I, TOILET AND LOCKER ROOM
                  @     138.48 $(1986)/SQ. FT. . . . . . . . . . . . . . .
. . . . . . . . . . . . . . . IMPLIES     63004.  $(1986)
             6.461E+02 SQ. FT. OF A2128I, OFFICE SPACE-ADMINISTRATION
                  @      67.77 $(1986)/SQ. FT. . . . . . . . . . . . . . .

VP

>KT 10000
INVALID VP REQUEST.

>
>KT 10000
*                 @  17832.70 $(1986)/PRSN*YRS. . . . . . . . . . . . .
 . . . . . . . . . . . . . . . IMPLIES      2076.  $(1986)
             1.164E-01 PRSN*YRS OF B1048I, CLERK GENERAL OFFICE (ADMINI
ATIVE
VP

>
>KT10000
             1.803E-02 PRSN*YRS OF B3304I, VICE PRESIDENT, MANUFACTURIN
                  @ 113343.44 $(1986)/PRSN*YRS. . . . . . . . . . . . .
. . . . . . . . . . . . . . . IMPLIES      2043.  $(1986)
             3.880E-02 PRSN*YRS OF B3128B, CHEMICAL ENGINEER
K                 @  51814.14 $(1986)/PRSN*YRS. . . . . . . . . . . . .
 . . . . . . . . . . . . . . IMPLIES      2011.  $(
VP

>
>KT10000
                  @ 113343.44 $(1986)/PRSN*YRS. . . . . . . . . . . . .
. . . . . . . . . . . . . . . IMPLIES      1970.  $(1986)
             3.703E-02 PRSN*YRS OF B3496I, PRODUCTION SUPERINTENDENT (F
Y MANAGER)
                  @  50734.68 $(1986)/PRSN*YRS. . . . . . . . . . . . .
. . . . . . . . . . . . . . . IMPLIES      1879.  $(1986)
             2.567E-02 PRSN*YRS OF B1080I, DIRECTOR OFFICE ADMINISTRATI

VP

>
>KT 10000 PROCESS: FURNACE , FURNACE ANNEAL
*       PRODUCT: ANNEALWAF, ANNEALED WAFER
       PRODUCES:  400.0000 WAFERS/MINUTE, TAKING     75.000 MINUTES/CYCLE
       OPERATES  .92 OF THE TIME THE FACTORY IS OPERATING
          COMPONENT: FURNACE-1, 500 CM2/SEC BELT FURNACE, 75 MIN 550/850/550
LE
             COST:   80000. $(1979)     INSTALLATION:    2000. $(1979)
             SALVAGE VALUE:   10000. $(1979) AFTER 15.0 YEARS
```

```
        ALL EXPENSES ARE IN $(1986)
        DIRECT EXPENSES                                 57138.
           DIRECT LABOR EXPENSES                                  49443.
           DIRECT MATERIALS AND SUPPLIES                            918.
           BYPRODUCT EXPENSES                                         0.
           DIRECT UTILITIES EXPENSES                               6776.

        INDIRECT EXPENSES                               50294.
           INDIRECT LABOR EXPENSES                                42740.
           INDIRECT MATERIALS AND SUPPLIES                         5347.
           INDIRECT UTILITIES EXPENSES                             2206.

        BYPRODUCT INCOME                        (           0.)

        CAPITAL EXPENSES                                83991.
           EQUIPMENT REPLACEMENT                                   6316.
           FACILITIES REPLACEMENT                                  5702.
           AMORTIZED ONE-TIME COSTS                               40104.
           INTEREST ON DEBT                                        1436.
           RETURN ON EQUITY                                       15529.
           NON-INCOME TAXES                                        1181.
           INSURANCE PREMIUMS                                     13721.

        INCOME TAXES                                    49678.

        MISCELLANEOUS                                   11880.

        EXTERNAL PRODUCT COST                               0.
        INTERNAL (IMPLICIT) PRODUCT COST                    0.

        TO PRODUCE 9.129E+07 WAFERS/YEAR, THE FURNACE
        PROCESS REQUIRES:

           ALL DOLLARS ARE IN $(1986)

           DIRECT REQUIREMENTS

              ACCOUNT A - FACILITIES
                 1.000E+03 SQ. FT. OF A20640, MANUFACTURING SPACE (TYPE  A)
                      @      93.06 $(1986)/SQ. FT. . . . . . . . . . . . . . .
 . . . . . . . . . . . . . . IMPLIES     93057.  $(1986)

              ACCOUNT B - PERSONNEL
                 2.339E+00 PRSN*YRS OF B3096D, SEMICONDUCTOR ASSEMBLER (ELE
ONICS)
                      @  17487.27 $(1986)/PRSN*YRS. . . . . . . . . . . . .
 . . . . . . . . . . . . . . IMPLIES     40908.  $(1986)
                 2.339E-01 PRSN*YRS OF B3704D, ELECTRONICS TECHNICIAN, AUTO
ED PROCESSES
                      @  23748.14 $(1986)/PRSN*YRS. . . . . . . . . . . . .
 . . . . . . . . . . . . . . IMPLIES      5555.  $(1986)
                 1.170E-01 PRSN*YRS OF B3736D, MAINTENANCE MECHANIC II
                      @  25475.28 $(1986)/PRSN*YRS. . . . . . . . . . . . .
 . . . . . . . . . . . . . . IMPLIES      2980.  $(1986)

              ACCOUNT C - UTILITIES
                 1.255E+05 KW HR. OF C1032B, ELECTRICITY
                      @        .05 $(1986)/KW HR.. . . . . . . . . . . . . .
 . . . . . . . . . . . . . . IMPLIES      6776.  $(1986)
                 1.141E+01 CU. FT. OF C1016B, DOMESTIC WATER
                      @        .01 $(1986)/CU. FT. . . . . . . . . . . . . .
 . . . . . . . . . . . . . . IMPLIES          .  $(1986)

              ACCOUNT G - BYPRODUCTS
```

```
                (NONE)

                ACCOUNT E - COMMODITIES
                   4.565E+02 DOLLARS OF E1308D, SPARE PARTS
                         @       1.69 $(1986)/DOLLARS . . . . . . . . . . . . .
. . . . . . . . . . . . . . IMPLIES       771.  $(1986)
                   2.054E+04 CU. FT. OF E1416D, NITROGEN GAS, REGULAR FRE-F
ED
                         @        .01 $(1986)/CU. FT. . . . . . . . . . . . . .
. . . . . . . . . . . . . . IMPLIES       147.  $(1986)

                ACCOUNT F - RESOURCES
                (NONE)

             INDIRECT REQUIREMENTS

                ACCOUNT A - FACILITIES
                   7.390E+02 SQ. FT. OF A2224I, SOLVENT AND CHEMICAL STORAG
                         @      30.46 $(1986)/SQ. FT. . . . . . . . . . . . . .
. . . . . . . . . . . . . . IMPLIES     22512.  $(1986)
                   4.354E+02 FT. OF A2040I, EXTERIOR WALLS
                         @      47.98 $(1986)/FT. . . . . . . . . . . . . . . .
. . . . . . . . . . . . . . IMPLIES     20887.  $(1986)
                   1.138E+02 SQ. FT. OF A2256I, TOILET AND LOCKER ROOM
                         @     138.48 $(1986)/SQ. FT. . . . . . . . . . . . . .
. . . . . . . . . . . . . . IMPLIES     15763.. $(1986)
                   1.918E+02 SQ. FT. OF A2128I, OFFICE SPACE-ADMINISTRATION
                         @      67.77 $(1986)/SQ. FT. . . . . . . . . . . . . .

VP

>
>KT
$$$$"KT10000" IS NOT IN THE PROGRAM VOCABULARY
"KT10000" IS NOT IN THE PROGRAM VOCABULARY
>FIND RUN @.CONTROL DEFAULT
DEFAULT HAS BEEN LOCATED IN CORE
ENTER A MANIPULATION COMMAND FOR RUN CONTROL "DEFAULT"
>CHANGE ISR
PLEASE ENTER THE NEW VECTOR
>5.0E7 *
ISR CHANGED FROM:
 100000000.00 *
TO:
  50000000.00 *
ENTER A MANIPULATION COMMAND FOR RUN CONTROL "DEFAULT"
>DONE

PLEASE ENTER A SAMIS COMMAND
>SIMULATE
$$$$$$$$$
ECONOMY OF SCALE CONVERGENCE OBTAINED IN  21 ITERATIONS FOR FIRM FURNACE$$




SAMIS III - RELEASE 1        INDUSTRY SIZE INDEX =  1

INDUSTRY: FURNACE, FURNACE ANNEAL OF IMPLANTED LAYERS

INDUSTRY OBJECTIVE: NEW PHOTOVOLTAIC POWER CAPABILITY
FINAL PRODUCT: CELLS, CELLS WITH JUNCTION,ANNEAL, AND ETCH
PRODUCING     1.10 WATTS PEAK PER CELLS
```